Micro-Ultrasound Imaging of Tissue Dysplasia

By

Srikanta Sharma

Doctoral thesis submitted in fulfilment of the requirements for the degree of Doctor of Philosophy to the College of Medicine, Nursing and Dentistry, University of Dundee, Scotland, UK.

January 2015

Abstract

The second most common cause of cancer deaths in the developed world is bowel cancer. Improving the ability to detect and classify lesions as early as possible, allows treatment earlier. The work presented in this thesis is structured around the following detailed aims:

Development of high frequency, broadband µUS (micro-ultrasound) imaging transducers through optimization of ultra-thinning processes for lithium niobate (LNO) and fabrication of novel 'mass-spring' matching layers using carefully controlled vacuum deposition is demonstrated. The effectiveness of this technique was quantified by applying multiple matching layers to 3 mm diameter 45 MHz LNO µUS transducers using carefully controlled vacuum deposition. The bandwidth of single mass-spring layer µUS transducer was measured to be 46% with an insertion loss of 21 dB. The bandwidth and insertion loss of a multiple matching layer µUS transducer was measured to be 59% and 18 dB respectively. The values were compared with an unmatched transducer which had a bandwidth and insertion loss of 28% and 34 dB respectively. All the experimentally measured values were in agreement with unidimensional acoustic model predictions.

µUS tools that can detect and measure microscopic changes in precancerous tissue using a mouse small bowel model with an oncogenic mutation was developed. µUS transducer was used to test the hypothesis that the intestinal tissue morphology of WT (wild type) and $Apc^{Min/+}$ (adenomatous polyposis coli) diverges with progressing age intervals (60, 90 and 120 days) of mice. A high frequency ultrasound scanning system was designed and the experiments were performed *ex vivo* using a focused 45 MHz, f-# = 2.85, µUS transducer. The data collected by scanning was used to compute the backscatter coefficients (BSC) and acoustic impedance (Z) of WT and $Apc^{Min/+}$ mice. The 2D and 3D ultrasound images showed that µUS detects polyps < 500 µm in the scan plane. The measured values of BSC and Z showed differences between normal and precancerous tissue. The differences detected in precancerous murine intestine and human tissue using µUS were correlated with high resolution 3D optical imaging. This novel approach may provide a powerful adjunct to screening endoscopy for improved identification and monitoring, allowing earlier treatment of otherwise undetectable lesions.

Declaration

I hereby declare that this thesis titled “Micro-Ultrasound (µUS) Imaging of Tissue Dysplasia” has been prepared by me under the direct guidance of Prof. Sandy Cochran and Prof. Inke Näthke as a part of my study for the award of PhD degree at the University of Dundee, Dundee, Scotland. I have not submitted this thesis previously for the award of any degree or diploma at any other institution.

Signature: **Date: 08/01/2015**

Certificate

This is to certify that Mr. Srikanta Sharma has done his research under my supervision and complied with all the requirements for the submission of this Doctor of Philosophy thesis to the University of Dundee.

Signature: **Date: 08/01/2015**

Acknowledgements

I have been lucky to have been supervised by Profs. Sandy Cochran and Inke Nathke. They welcomed new research ideas and provided me with the independence to pursue them. They always provided very insightful, useful and constructive solutions at many critical junctures. I have learnt a good deal on proper research methods from my supervisors. They have nurtured me a great deal and I have learnt to think and act maturely (I think!). I sincerely thank both of them. Thanks to Prof. Jeremy Brown, from whom I learnt the wonderful field of making micro-ultrasound transducers. I was fortunate to have spent valuable time learning the techniques of fabrication from him and his group members in Canada. I also want to thank industrial partner to the project Mr. Jim McAneny (Crystapol International) for his advice. Thanks to Dr. Christine Demore for her useful insights and discussions.

I owe a great deal of thanks to my colleagues who made the lab a wonderful place to work. Thanks to Dr. Paul Appleton, Mr. Ian Newton, Dr. Scott Nelson, Dr. Aliya Fatehulla, Dr. Yongqiang Qiu, Dr. Zhen Qiu, Dr. Holly Lay, Dr. Muhammad Sadiq, Mr. Han Wang and Dr. Ben Cox, for their advice and support. I enhanced my understanding of ultrasound, mice dissection, simulations, optical imaging, and learnt very useful MatLab and Labview tricks from you all. Thanks to my friends Adi, Yogi, Joe and Satyam who have been a source of strength and much needed distraction.

I am grateful to my grandparents Late Mr. Umapathy and C. Lakshmi, my parents especially my Mother Nagarathna, and my sister Sheela, who encouraged me and taught me to value knowledge above all. They often put my interests ahead of theirs. Without your love and support I would not have been here. Special thanks to Mr. Raghuram and Sujatha, for their support and guidance. Thanks, to my wife Archana, for her patience, love, support, consideration and encouragement. You kept me sane during the final stages of this work. I look forward to welcoming our baby.

I dedicate this thesis to my grandparents Late Mr. Umapathy and C. Lakshmi.

The work reported here was funded by a Scottish university physics alliance (SUPA) prize studentship under the physics and life sciences theme and the Royal Society of Edinburgh.

Table of Contents

ABSTRACT ..... **I**

DECLARATION ..... **II**

CERTIFICATE ..... **III**

ACKNOWLEDGEMENTS ..... **IV**

TABLE OF CONTENTS ..... **V**

LIST OF FIGURES ..... **VIII**

LIST OF TABLES ..... **XVII**

CHAPTER 1: INTRODUCTION **1**

1.1 Overview 1
1.2 History of Ultrasound 1
1.3 High Resolution Ultrasound 3
1.4 Ultrasound Tissue Characterisation 4
1.5 Need for Early Detection of Colon Cancer 5
1.6 Objectives and Hypothesis 6
1.6.1 Rationale *6*
1.7 Contribution to Knowledge 8
1.8 Thesis Structure 9
1.9 Academic Grants Awarded 10
1.10 Publications 10
1.11 References 13

CHAPTER 2: COLORECTAL CANCER **14**

2.1 Overview 14
2.2 Epidemiology of Colorectal Cancer 15
2.3 Anatomy and Physiology of the Intestinal Tract 16
2.3.1 Small Intestine *17*
2.3.2 Large Intestine *19*
2.4 Screening and Diagnosis of Colorectal Cancer 20
2.4.1 Faecal Occult Blood Testing *21*
2.4.2 Colonoscopy *21*
2.4.3 Sigmoidoscopy *22*
2.4.4 Capsule Endoscopy *22*
2.4.5 Endoscopic Ultrasound *24*
2.4.6 Magnetic Resonance Imaging *27*
2.4.7 Computed Tomography *28*
2.5 Conclusion 29
2.6 References 29

CHAPTER 3: THEORY OF ULTRASOUND **33**

3.1 Introduction 33
3.2 Ultrasound Imaging 33
3.2.1 A-Scan *34*
3.2.2 B-Scan *35*
3.3 Interactions of Ultrasound with Tissue 37
3.4 High Resolution Ultrasound (HRUS) Imaging 44
3.5 Quantitative Ultrasound Tissue Characterisation 48
3.6 Design Considerations of μUS Transducer 50

3.7 Micro-ultrasound (μUS) Transducer 51
3.7.1 Active Element *53*
3.7.2 Backing layer *54*
3.7.3 Matching layer *55*
3.8 Conclusion 57
3.9 References 57

CHAPTER 4: FABRICATION OF μUS TRANSDUCERS 64

4.1 Overview 64
4.2 Active Element of μUS Transducer 65
4.3 μUS Transducer 67
4.3.1 Fabrication of Single Element μUS transducers *67*
4.3.2 Lapping and Polishing *69*
4.3.3 Dicing *71*
4.3.4 Vacuum Deposition of Parylene *73*
4.3.5 E-Beam Evaporation *75*
4.3.6 Electrode *76*
4.3.7 Focusing *77*
4.3.8 Backing Layer *78*
4.4 Quarter Wavelength Matching Layer 79
4.5 Theory of Mass-Spring Matching Layer 80
4.5.1 Mass-Spring Matching Layer *84*
4.6 KLM Model 86
4.7 Functional Transducer Characterisation 87
4.7.1 Electrical Impedance Spectroscopy *88*
4.7.2 Insertion Loss Measurements *88*
4.7.3 Pulse Shape *90*
4.7.4 Tungsten Wire Scanning *90*
4.7.5 Depth of Field and Line Spread Function *91*
4.8 Discussion 92
4.9 Conclusion 93
4.10 References 93

CHAPTER 5: RESULTS: μUS TRANSDUCERS 96

5.1 Overview 96
5.2 Ultra-thinning of LNO 97
5.3 High Resolution μUS Transducers 99
5.3.1 High Resolution μUS Transducer without Matching Layer *100*
5.3.2 Dual Quarter Wavelength Conventional Matched μUS Transducer *105*
5.3.3 Single Quarter Wavelength 'Mass-Spring' Matched High Resolution μUS Transducer *107*
5.3.4 Dual Quarter Wavelength Matched High Resolution μUS Transducer *111*
5.3.5 Dual Quarter Wavelength Matched Focused High Resolution μUS Transducer *113*
5.3.6 Commercial μUS Transducer *118*
5.3.7 Commercial μUS Transducer Characterisation *119*
5.4 Summary of Results 122
5.5 Discussion 124
5.6 Conclusion 125
5.7 References 126

CHAPTER 6: MATERIALS AND METHODS FOR μUS IMAGING AND TISSUE CHARACTERISATION 127

6.1 Overview 127
6.2 High Resolution Ultrasound Scanning System 128
6.2.2 Step-Repeat Scanning System *129*
6.2.3 High Speed Scanning System *133*
6.2.4 Visualisation of Data *135*

6.2.5 3D Imaging *137*
6.3 ULTRASOUND TISSUE CHARACTERISATION 138
6.3.1 Preparation of Murine Small Intestine *140*
6.3.2 Image Processing *141*
6.3.3 Attenuation Coefficients *143*
6.3.4 Acoustic Impedance *144*
6.3.5 Backscatter Coefficient (BSC) *145*
6.4 CONTROL EXPERIMENTS 147
6.4.1 Acoustic Impedance *148*
6.4.2 BSC Measurements using Beads *153*
6.4.3 Tissue Fixation *155*
6.5 CONCLUSIONS 157
6.6 REFERENCES 157

CHAPTER 7: RESULTS: EARLY DETECTION OF COLON CANCER BY µUS 159

7.1 OVERVIEW 159
7.2 B-SCAN IMAGING OF EARLY TISSUE DYSPLASIA 160
7.2.1 Ultrasound Imaging of Human Tissue *163*
7.3 3D ULTRASOUND IMAGING OF EARLY TISSUE DYSPLASIA 164
7.3.1 Correlation of µUS Images with Optical Images *166*
7.4 QUANTITATIVE ULTRASOUND TISSUE CHARACTERISATION 167
7.4.1 Backscatter Coefficient Measurements *167*
7.4.2 Acoustic Impedance Measurements *171*
7.4.3 Attenuation Coefficients *172*
7.5 DISCUSSION 173
7.6 CONCLUSION 175
7.7 REFERENCES 176

CHAPTER 8: CONCLUSIONS AND FUTURE WORK 178

8.1 OVERVIEW 178
8.2 DISCUSSION 178
8.3 CONCLUSION 182
8.4 FUTURE WORK 182
8.5 REFERENCES 183

APPENDIX – I CLXXXV

1. SCRIPT TO PRODUCE B-SCAN IMAGES CLXXXV

2. SCRIPT TO PRODUCE SERIES OF B-SCAN IMAGES FOR 3D CLXXXVI

IMAGING CLXXXVI

3. SCRIPT TO COMPUTE ATTENUATION COEFFICIENTS CLXXXVIII

4. SCRIPT TO COMPUTE ACOUSTIC IMPDANCE CLXXXIX

5. SCRIPT TO COMPUTE BSC CXCI

6. SCRIPT TO TO SEGEMENT B-SCAN IMAGES CXCII

7. SCRIPT FOR 1D INTERPOLATION OF B-SCAN IMAGES CXCVI

APPENDIX – II- MANUAL HRUS CXCVI

List of Figures

FIGURE 1.1: FIRST REPORTED ULTRASOUND IMAGE OF EARLY PREGNANCY AT 14 WEEKS. THE SHAPE IN THE LEFT SIDE OF THE IMAGE IS A LARGE CYSTIC CAVITY IN AN EARLY UTERUS (DONALD, MACVICAR, & BROWN, 1958). 2

FIGURE 2.1: AVERAGE NUMBER OF COLORECTAL CANCER CASES PER YEAR AND AGE SPECIFIC INCIDENCE RATES PER 100,000 POPULATIONS IN THE UK IN 2008-2010. (WWW.CANCERRESEARCHUK.ORG, 2013). 16

FIGURE 2.2: HUMAN GI TRACT, SHOWING UPPER GI, LOWER GI AND ACCESSORY ORGANS SUCH AS THE LIVER, GALL BLADDER AND PANCREAS (TRIALSIGHT MEDICAL MEDIA, 2008). 17

FIGURE 2.3: **A.** THE VARIOUS REGIONS OF SMALL INTESTINE. SMALL INTESTINE IS LOOPED AND FILLS UP THE ABDOMINAL CAVITY. SMALL INTESTINE IS SUB-DIVIDED INTO DUODENUM, JEJUNUM AND ILEUM. **B.** THE INSIDE LAYERS OF THE SMALL INTESTINE. THE UPPERMOST LAYER IS MADE UP OF FINGER LIKE PROJECTIONS CALLED VILLI, FOLLOWED BY MUCOSA, SUBMUCOSA, MUSCULARIS AND SEROSA. 19

FIGURE 2.4: LARGE BOWEL OR COLON IS THE FINAL SEGMENT OF THE GI. ABSORPTION OF NUTRIENTS AND WATER AND COMPACTION OF INDIGESTIBLE FOOD ARE ITS MAIN FUNCTIONS. (TRIALSIGHT MEDICAL MEDIA, 2008). 20

FIGURE 2.5: CAPSULE ENDOSCOPE, USED TO IMAGE PARTS OF THE GI TRACT THAT CANNOT BE VISUALIZED BY COLONOSCOPY AND SIGMOIDOSCOPY. CAPSULE ENDOSCOPES ARE ESPECIALLY USEFUL IN IMAGING THE SMALL INTESTINE. (MAHFOUZ ET AL. 2011). 23

FIGURE 2.6: CORRELATION OF HISTOLOGICAL AND ULTRASONOGRAPHY IMAGES OF THE GASTROINTESTINAL WALL. **A.** THE FIVE LAYER STRUCTURE OF THE GI WALL AND THE CORRESPONDING IMAGES THAT CAN BE VISUALIZED USING AN ULTRASOUND PROBE. THE DARK AND THE WHITE BANDS REPRESENT HYPERECHOIC AND HYPOECHOIC REGIONS RESPECTIVELY. **B.** FIVE LAYERED STRUCTURE OF THE GI WALL VISUALIZED WITH A EUS PROBE (ØDEGAARD ET AL. 2012). 26

FIGURE 3.1: BASIC ULTRASOUND PULSE ECHO IMAGING TECHNIQUE, AN ULTRASOUND SIGNAL IS TRANSMITTED INTO THE TISSUE AND THE REFLECTED ULTRASOUND WAVE THAT IS TIME SHIFTED AND

ATTENUATED IS RECEIVED BY THE SAME TRANSDUCER, THE TIME AND THE AMPLITUDE OF THE SIGNAL CORRESPONDS TO THE POSITION AND THE STRENGTH OF THE REFLECTOR. 34

FIGURE 3.2: ILLUSTRATION OF A B-SCAN SYSTEM SETUP. THE TRANSDUCER IS MOUNTED ON TO AN X-Y STAGE WHICH ENABLES THE TRANSDUCER TO MOVE IN USER DEFINED STEPS, TO COLLECT A-SCANS AT VARIOUS POINTS ACROSS THE TISSUE SAMPLES, WHICH ARE PRESENTED IN THE FORM OF A 2D IMAGE. THE SCAN STEP SIZES FORM THE AXES OF THE IMAGE WITH THE SCAN DEPTH AWAY FROM THE TRANSDUCER. 36

FIGURE 3.3: BLOCK DIAGRAM ILLUSTRATING B-SCAN IMAGE FORMATION SEQUENTIALLY FROM LEFT TO RIGHT. 37

FIGURE 3.4: A. SPECULAR REFLECTION, WHERE THE SOUND WAVE IS REFLECTED FROM A SMOOTH BOUNDARY, IN A STRAIGHT LINE. B. DIFFUSIVE REFLECTION, DUE TO CELLULAR STRUCTURES OF VARYING DIMENSIONS IN TISSUE RESULTING IN UNEVEN SURFACES AND REFLECTIONS RETURNING TO THE TRANSDUCER FROM DIFFERENT DIRECTIONS. 39

FIGURE 3.5: DESIGN CONSIDERATIONS FOR FABRICATION OF μUS TRANSDUCERS FOR PULSE ECHO TISSUE IMAGING 51

FIGURE 3.6: SUMMARY OF FABRICATION STEPS FOR A SINGLE ELEMENT μUS TRANSDUCER WITH A CONVENTIONAL Λ/4 MATCHING LAYER. 51

FIGURE 3.7: THREE PORT NETWORK REPRESENTATION OF AN ULTRASOUND TRANSDUCER, SHOWING THE MECHANICAL AND ELECTRICAL PORTS. 52

FIGURE 3.8: CROSS SECTION OF A PLANAR SINGLE ELEMENT ULTRASOUND TRANSDUCER SHOWING DIFFERENT COMPONENTS. 52

FIGURE 3.9: SCHEMATIC REPRESENTATION OF THE EFFECT OF BACKING LAYER IN A TRANSDUCER ASSEMBLY ON THE PULSE LENGTH. A. ACTIVE ELEMENT WITHOUT BACKING SHOWS EFFECTS OF RINGING IN THE PULSE. B. ACTIVE ELEMENT WITH BACKING LAYER SHOWING A SHORT PULSE DUE TO REDUCED RINGING. 55

FIGURE 4.1: A. DIAGRAM ILLUSTRATING STEPS (TOP TO BOTTOM) INVOLVED IN FABRICATING A SPHERICALLY SHAPED SINGLE ELEMENT μUS TRANSDUCER OF FREQUENCY 45 MHZ WITHOUT MATCHING LAYERS. B. CROSS SECTIONAL VIEW OF THE SINGLE ELEMENT μUS TRANSDUCER IN A BRASS CASING WITH SMA CONNECTION, THE FOCAL LENGTH OF THE TRANSDUCER IS 7 MM. 68

FIGURE 4.2: SCHEMATIC OF LAPPING AND POLISHING MACHINE USED FOR THINNING OF ACTIVE AND PASSIVE MATERIALS (BERNASSAU ET AL. 2012). 70

FIGURE 4.3: CONTACT GAUGE USED FOR MONITORING THE THICKNESS OF LNO DURING AND AFTER LAPPING. 71

FIGURE 4.4: MICROACE 66 DICING SAW IN OPERATION. 72

FIGURE 4.5: A. SCHEMATIC DESCRIBING THE ANGLES WHICH WERE USED TO DICE THE PIEZOELECTRIC SAMPLE INTO SIXTEEN SIDED POLYGONS. DOTTED LINES IN STEP 2 SHOW THE POSITION OF CUTS MADE WHEN THE SAMPLE WAS ROTATED AT 45^0 ANGLE IN POSITIVE AND NEGATIVE AXIS. IN STEP 3 THE SAMPLE WAS FURTHER ROTATED AND DICED AT 22.5^0 AND 67.5^0 IN THE POSITIVE AND NEGATIVE ROTATION DIRECTIONS RESPECTIVELY TO OBTAIN A SIXTEEN SIDED POLYGON. B. DICED SAMPLE WITH ALL THE CUTS. C. SIXTEEN SIDED POLYGON OF 3 MM WIDTH AFTER ALL THE EDGES WERE REMOVED. 73

FIGURE 4.6: SCS PARYLENE COATING MACHINE. A. VAPOUR DEPOSITION PROCESS OF PARYLENE ALLOWS PARYLENE TO BE UNIFORM IN THICKNESS AND PINHOLE FREE. B. CALIBRATION CURVE FOR THE PARYLENE COATING MACHINE DEVELOPED BY INCREASING THE PARYLENE DIMER LOAD IN THE MACHINE IN STEPS OF 1G UP TO 20 G. PARYLENE WAS COATED ON A GLASS SLIDE AND THE THICKNESS WAS MEASURED USING A CONTACT GAUGE. 74

FIGURE 4.7: A. SCHEMATIC OF E-BEAM EVAPORATION PROCESS B.E-BEAM EVAPORATOR USED FOR THE DEPOSITION OF CU ELECTRODES AND CU MASS LAYER. C. LNO μUS TRANSDUCERS BONDED TO A GLASS SUBSTRATE AND READY TO BE PLACED INTO THE E-BEAM EVAPORATOR FOR CU ELECTRODING. D. SAMPLES WITH EVAPORATED THIN FILM OF CU. 76

FIGURE 4.8: CIRCULAR DISK OF LNO OF DIAMETER 3MM IS PRESSED ON TO A STEEL BALL BEARING AT 75^0C, TO FORM A FOCUSED STRUCTURE. AFTER THE BALL BEARING COOLED, A BACKING LAYER WAS CAST ON THE SURFACE. THE SAMPLE RETAINED THE CURVED STRUCTURE AFTER IT WAS DISMOUNTED FROM THE BALL BEARING. 78

FIGURE 4.9: DIFFERENT LAYERS FOR Λ/4 MATCHED μUS TRANSDUCER. THIN LAYERS OF SILVER EPOXY AND PARYLENE APPROXIMATE A DUAL Λ/4 MATCHING LAYER ON THE FRONT FACE OF THE PIEZOELECTRIC SUBSTRATE. 79

FIGURE 4. 10: A. MASS-SPRING MODEL FOR POLYMER (SPRING) METAL LAYER (MASS) SHOWING THE TIMING RELATION AT RESONANCE. B. EQUIVALENT INDUCTANCE AND CAPACITANCE (LC) CIRCUIT REPRESENTATION OF MASS-SPRING LAYER ALONGSIDE A MULTILAYER MODEL OF METAL AND POLYMER (TODA & THOMPSON 2010). 81

FIGURE 4.11: A 45 MHZ SINGLE ELEMENT LNO μUS TRANSDUCER WITH AN EFFECTIVE SINGLE Λ/4 MASS-SPRING MATCHING LAYER. THIN LAYER OF PARYLENE FOLLOWED BY A THIN LAYER OF CU APPROXIMATE A SINGLE Λ/4 MATCHING LAYER. 85

FIGURE 4.12: A 45 MHZ SINGLE ELEMENT LNO μUS TRANSDUCER WITH A DUAL Λ/4 MASS-SPRING MATCHING LAYER. 86
FIGURE 4.13: A SCHEMATIC OF KLM MODEL (OAKLEY 1997). 86
FIGURE 4.14: ELECTRICAL IMPEDANCE ANALYSER WITH FIXTURE FOR TESTING THE IMPEDANCE AND PHASE RESPONSE OF μUS TRANSDUCERS AND ACTIVE ELEMENT. 88
FIGURE 4.15: SET-UP USED TO MEASURE INSERTION LOSS OF TRANSDUCERS IN PULSE ECHO MODE. THE TRANSDUCER EXCITATION WAS ACHIEVED WITH MULTI-CYCLE SINE WAVE BURST USING A PULSE GENERATOR (BP1, DAXSONICS INC., HALIFAX, NS) WITH 50 Ω COUPLING AND REFLECTING PULSE FROM AN X-CUT QUARTZ FLAT SITUATED AT THE FOCAL POINT OF THE TRANSDUCER. 89
FIGURE 4.16: DIAGRAM OF WIRE PHANTOM USED FOR THE EVALUATION OF BEAM PROFILE, DOF AND POINT SPREAD FUNCTION OF TRANSDUCERS. A. SOLIDWORKS DESIGN OF WIRE PHANTOM, B. MEASUREMENT OF SEPARATION DISTANCE BETWEEN EACH STEP WAS MAINTAINED AT 1MM. C. TUNGSTEN WIRE PHANTOM FRAME FABRICATED BY RAPID PROTOTYPING. 91

FIGURE 5.1: LAPPED SAMPLES OF LNO AS SEEN UNDER AN OPTICAL MICROSCOPE. A. LAPPED LNO SAMPLE OF THICKNESS 20 μM, EXHIBITS DARK SPOTS AND A HIGHER SURFACE ROUGHNESS CAUSED BY LAPPING. B. LNO SAMPLE AS IN A AFTER POLISHING, SHOWS A SPECULAR AND SMOOTH SURFACE, FREE FROM LAPPING DAMAGES, THICKNESS = 10 μM. 97
FIGURE 5.2: THE SURFACE ROUGHNESS OF LNO SAMPLES MEASURED BY A SURFACE PROFILER. A. AFTER LAPPING, R_A = 260 NM. B. AFTER POLISHING, R_A = 0.69 NM. NOTE THAT THE Y-AXIS IN A AND B IS SCALED DIFFERENTLY. 98
FIGURE 5.3: μUS TRANSDUCERS WITH AN OPERATION FREQUENCY OF 45 MHZ. A. SINGLE ELEMENT PLANAR μUS TRANSDUCER WITHOUT MATCHING LAYER. B. FOCUSED SINGLE Λ/4 WAVELENGTH MATCHED μUS TRANSDUCER. C. FOCUSED μUS TRANSDUCER WITH A DUAL Λ/4 'MASS-SPRING' MATCHING LAYER. 100
FIGURE 5.4: COMPARISON OF KLM MODEL TO EXPERIMENTAL RESULTS FOR A PLANAR TRANSDUCER WITHOUT MATCHING LAYERS OPERATING AT A CENTRE FREQUENCY OF 47 MHZ. A. PULSE ECHO RESPONSE AND B. ELECTRICAL MAGNITUDE AND PHASE. 101
FIGURE 5.5: THE RESULTS FROM THE KLM MODEL AND EXPERIMENTAL ELECTRICAL IMPEDANCE MEASUREMENTS FOR A PRESS FOCUSED SINGLE ELEMENT μUS TRANSDUCER WITHOUT MATCHING LAYERS. A. PULSE ECHO MEASUREMENTS. B. ELECTRICAL IMPEDANCE AND PHASE MEASUREMENTS.

Several low frequency modes are seen which could be due to micro-fractures resulting from press focusing. 102

Figure 5.6: Functional characterisation of 45 MHz focused μUS transducer without matching layers. A. Depth of field (DOF) measurement, around for a focal at a distance of 7 mm. 0 in the graph on the x-axis represents the focal point at 7 mm. B. Line spread function obtained by pulse-echo from a 5 μm tungsten wire. 103

Figure 5.7: B-scan images. B-scan image of a single 5 μm Tungsten wire at the focal point (7mm). 104

Figure 5.8: Comparison of KLM model to the experimental measurements for a focused single element μUS Transducer with traditional single matching layer. A. Pulse echo measurements. B. Electrical impedance and phase measurements 106

Figure 5.9: Comparison of KLM model to the experimental measurements for a focused single element μUS Transducer with single λ/4 'mass-spring' matching layers. A. Pulse echo measurements. B. Electrical impedance and phase measurements. 108

Figure 5.10: Functional characterisation of 45 MHz focused μUS transducer with single λ/4 'mass-spring' matching layers. A. Depth of filed (DOF) measurement, the focal point was determined to be at 7 mm. 0 in the graph on the x-axis represents the focal point at 7 mm. B. Line spread function obtained by pulse-echo from a 5 μm Tungsten wire. 109

Figure 5.11: B-scan images. A. B-scan image of a single 5 μm Tungsten wire at the focal point (7mm). 111

Figure 5.12: Comparison of KLM model and experimentally measured electrical impedance magnitude for LNO planar transducer with dual 'mass-spring' matching layer. A. Pulse echo measurements. B. Electrical impedance measurements. 112

Figure 5.13: Comparison of KLM model to the experimental measurements for a focused single element μUS transducer with dual λ/4 'mass-spring' matching layers. A. Pulse-echo measurements. B. Electrical impedance and phase measurements. 115

Figure 5.14: Functional characterisation of 45 MHz focused μUS transducer with dual λ/4 'mass-spring' matching layers. A. Depth of field (DOF) measurement relative to a focal depth of 7 mm. 0 in the graph on the x-axis represents the focal point at 7 mm. B. Line spread function obtained by pulse-echo from a 5 μm Tungsten wire. 116

Figure 5.15: B-scan images. A. B-scan image of a single 5 μm Tungsten wire at the focal point (7mm). 117

FIGURE 5.16: AFM TH-19 μUS TRANSDUCER. THIS DEVICE OPERATES AT 45 MHZ WITH AN F# = 2.85 AND PROVIDES A BEAM WIDTH OF 107 μM AT THE FOCUS. 118

FIGURE 5.17: FUNCTIONAL CHARACTERISATION OF AFM TH-19 FOCUSED μUS TRANSDUCER. A. PULSE ECHO MEASUREMENT, FROM A QUARTZ FLAT OF THICKNESS 500 μM AT THE FOCAL DISTANCE OF 4.25 MM. B. ELECTRICAL IMPEDANCE SPECTROSCOPY MEASUREMENT SHOWS A RESONANCE IN THE REGION OF 45 MHZ. 120

FIGURE 5.18: FUNCTIONAL CHARACTERISATION OF AFM TH-19 μUS TRANSDUCER. A. DEPTH OF FIELD (DOF) MEASUREMENT, WITH THE FOCAL DISTANCE DETERMINED TO BE AT 4.25 MM. 0 IN THE GRAPH ON THE X-AXIS REPRESENTS THE FOCAL POINT AT 4.25 MM. B. LINE SPREAD FUNCTION OBTAINED BY PULSE-ECHO FROM A 5 μM TUNGSTEN WIRE. 121

FIGURE 5.19: B-SCAN IMAGE OF A SINGLE 5 μM TUNGSTEN WIRE AT THE FOCAL POINT TO DETERMINE THE BEAM GEOMETRY OF AFM TH-19 TRANSDUCER, DYNAMIC RANGE = 35 DB. 121

FIGURE 6.1: BLOCK DIAGRAM OF THE STEP-REPEAT SCANNER USED FOR SCANNING OF TISSUE. A COMPUTER CONTROLS THE MOTION OF THE TRANSDUCER AND AN OSCILLOSCOPE COLLECTS THE PEAK AMPLITUDE DATA WHICH IS TRANSFERRED TO THE COMPUTER TO GENERATE B-SCAN IMAGES. ... 131

FIGURE 6.2: FLOW CHART FOR THE LABVIEW CONTROLLED STEP-REPEAT SCANNING SYSTEM. THE SCANNER IS AUTOMATED TO COLLECT RF DATA FROM THE TISSUE WHICH IS POST PROCESSED TO PRODUCE B-SCANS AND MEASURE TISSUE PROPERTIES. 131

FIGURE 6.3: BLOCK DIAGRAM OF HIGH SPEED SCANNER USED FOR SCANNING OF TISSUE. A LABVIEW CONTROLLED FPGA MODULE CONTROLS THE MOTION OF THE TRANSDUCER AND A FLEXRIO DIGITISER COLLECTS THE PEAK AMPLITUDE DATA WHICH IS TRANSFERRED TO THE COMPUTER VIA A HIGH SPEED PCI EXPRESS CARD TO GENERATE B-SCAN IMAGE. 134

FIGURE 6.4: FLOW CHART FOR THE LABVIEW CONTROLLED HIGH SPEED SCANNING SYSTEM. FPGA CONTROLS THE MOTION OF THE SCANNER AND THE DIGITISER TO COLLECT RF DATA FROM THE TISSUE WHICH IS POST PROCESSED TO PRODUCE B-SCANS AND MEASURE TISSUE PROPERTIES. 135

FIGURE 6.5: PROCEDURE TO PRODUCE B-SCAN IMAGES FROM RF DATA. A. FLOW CHART SHOWING THE STEPS INVOLVED IN PRODUCING A B-SCAN FROM THE RECORDED A-SCANS AT DIFFERENT POSITIONS ACROSS THE TISSUE. B. AN EXAMPLE OF A B-SCAN IMAGE PRODUCED BY SCANNING THE TRANSDUCER ACROSS A MURINE SMALL INTESTINE WITH MICRO POLYPS USING THE 45 MHZ PROBE. DYNAMIC RANGE OF THE IMAGE = 30 DB. 137

FIGURE 6.6: ILLUSTRATION OF METHOD USED FOR CREATING 3D VOLUMETRIC IMAGES FROM A SERIES OF B-SCAN IMAGES, USING THE IMAGEJ IMAGING SOFTWARE. 138

FIGURE 6.7: PULSE-ECHO MEASUREMENT CONDITIONS TO DETERMINE ATTENUATION, BSC'S AND ACOUSTIC IMPEDANCE OF MURINE SMALL INTESTINE. A 45 MHZ TRANSDUCER IS MECHANICALLY SCANNED ACROSS THE TISSUE SAMPLE PINNED ON AGAR (THICKNESS = 2 MM) AT A DISTANCE OF 5 MM, CLOSE TO THE FOCAL DISTANCE. THE REFERENCE SIGNAL FROM AGAR HAS PEAK AMPLITUDE OF A_0 AND TIME OF ARRIVAL T_0, WHILE THE SAMPLE RETURNING FROM THE TISSUE SAMPLE AT POSITION (X, Y) HAS A PEAK AMPLITUDE OF A(X, Y) AND TIME OF FLIGHT OF T(X, Y). A_0 IS USED AS THE REFERENCE SIGNAL FOR CALCULATING A. 139

FIGURE 6.8: A-SCAN ULTRASOUND SIGNAL MEASURED BY SCANNING AFM TH-19 PROBE OVER MURINE INTESTINE IN PULSE-ECHO MODE. THE SIGNAL IN RED IS THE REFERENCE SIGNAL (A_0) REFLECTED BACK FROM AGAR WITHOUT TISSUE AND THE SIGNAL IN BLACK IS AN EXAMPLE OF THE SIGNAL A(X,Y) OBTAINED WHEN THE TRANSDUCER MOVES ACROSS AND SCANS THE TISSUE. NOTICE THE REDUCED AMPLITUDE AND TIME SHIFTED SIGNAL DUE TO ATTENUATION OF SOUND AFTER INTERACTION WITH THE TISSUE. 140

FIGURE 6.9: ANATOMY OF MURINE GI TRACT. THE PORTION OF SMALL INTESTINE MARKED AS REGION-2 MEASURING APPROXIMATELY 3 CM IN LENGTH WAS USED FOR ULTRASOUND IMAGING AND CHARACTERISATION STUDIES. 141

FIGURE 6.10: ILLUSTRATION OF TISSUE SEGMENTATION ALGORITHM. A. STEP WISE PROCEDURE USED FOR SEGMENTING THE B-SCAN IMAGE AT DESIRED DEPTH OF THE TISSUE. B. SHOWS THE APPLICATION OF IMAGE SEGMENTATION ALGORITHM TO A B-SCAN IMAGE. STEP .5 SHOWS THE FINAL IMAGE, THE RF DATA FROM THIS SEGMENTED IMAGE WERE USED FOR QUANTITATIVE ANALYSIS OF TISSUE DATA. 142

FIGURE 6.11: STEPS INVOLVED IN COMPUTATION OF BSC FROM RF DATA. A. FLOW CHART OF THE ALGORITHM USED TO MEASURE BSC FROM TISSUE DATA. B. A-SCAN OF THE TISSUE TO ILLUSTRATE THE GATING PROCEDURE USED FOR COMPUTATION OF BSC, THE SIGNALS FROM AGAR AND MUSCLE WERE OMITTED AND ONLY THE REFLECTIONS FROM THE TOP LAYER OF THE TISSUE WERE CONSIDERED. 146

FIGURE 6.12: SCHEMATIC OF THE THROUGH-TRANSMISSION SET-UP FOR MEASUREMENT OF ATTENUATION COEFFICIENTS AND ACOUSTIC IMPEDANCES OF VARYING CONCENTRATIONS OF AGAR USING A 5 MHZ ULTRASOUND PROBE. 148

FIGURE 6.13: ACOUSTIC IMPEDANCE MEASUREMENTS. COMPARISON OF ACOUSTIC IMPEDANCES OF AGAR AT VARYING CONCEMTRATIONS USING PULSE-ECHO MEASUREMENTS (AT 45 MHZ) AND THROUGH-TRANSMISSION MEASUREMENTS (AT 5 MHZ).....152

FIGURE 6.14: ATTENUATION COEFFICIENT MEASUREMENTS. ATTEUNATION COEFFICIENTS FOR VARYING CONCENTRATIONS OF AGAR MEASURED IN THROUGH-TRANSMISSION MODE. THE GREAPH SHOWS A LINEAR RELATIONSHIP BETWEEN ATTENAUTAION AND DENSITY. 153

FIGURE 6.15: BSC MEASUREMENTS ON POLYSTYERENE BEADS. BEADS OF VARYING SIZES AND CONCETRATION SUSPENDED IN AGAR WERE SCANNED AND AVERAGE BSC IS SHOWN. 155

FIGURE 6.16: EFFECT OF FIXATION ON ACOUSTICAL PROPERTIES OF TISSUE. THE TISSUE WAS SCANNED OVER A PERIOD OF TIME AFTER FIXATION TO DETERMINE THE EFFECT OF FIXATION ON ACOUSTICAL PROPERTIES. 156

FIGURE 7.1: HRUS SCANS OF MURINE SMALL BOWEL. A. WT MOUSE INTESTINE AGED 60 DAYS. B. $APC^{MIN/+}$ MOUSE INTESTINE AGED 60 DAYS, ARROWS SHOWS INCREASED BACKSCATTER INDICATING TISSUE DYSPLASIA. C. WT MOUSE INTESTINE AGED 90 DAYS. D. $APC^{MIN/+}$ MOUSE INTESTINE AGED 90 DAYS, ARROWS SHOWS INCREASED BACKSCATTER INDICATING TISSUE DYSPLASIA AND THE NUMBER OF MICRO POLYPS IS MORE THAN IN IMAGE B. E. WT MICE INTESTINE AGED 60 DAYS. F. $APC^{MIN/+}$ MOUSE INTESTINE AGED 120 DAYS, NOTE INCREASED BACKSCATTER AND HIGH AMPLITUDE FEATURES CORRESPONDING TO POLYPS ON THE TOP SURFACE. SCALE BAR = 1MM, DYNAMIC RANGE = 35 DB. 162

FIGURE 7.2: CORRELATION OF μUS SCAN OF HUMAN POLYP FROM FAP PATIENT WITH OPTICAL IMAGE. A. B-SCAN IMAGE OF THE HUMAN POLYP SHOWING THREE DIFFERENT TISSUE ORGANISATIONAL LAYERS WITH VARYING SCATTERING INTENSITY WITHIN THE STRUCTURE. B. CROSS SECTION OF THE SAME POLYP STAINED WITH DAPI AND PHALLOIDIN TO REVEAL F-ACTIN (RED) AND NUCLEI (BLUE) SHOWING THE OVERALL STRUCTURE OF THE POLYP. (OPTICAL IMAGE WAS TAKEN BY DR. PAUL APPLETON). 164

FIGURE 7.3: 3-D ULTRASOUND IMAGING. A. CONFOCAL IMAGE OF $APC^{MIN/+}$ TISSUE PINNED ON AGAR TO PREVENT FROM CURLING VIEWED AT 10X MAGNIFICATION. B.3-D ULTRASOUND INTENSITY IMAGE OF TISSUE SHOWN IN A, IMAGED WITH AFMTH-19 SHOWS CORRELATION WITH THE OPTICAL IMAGE. SCALE BARS = 1MM. (OPTICAL IMAGE IN A WAS TAKEN BY DR. PAUL APPLETON). 165

FIGURE 7.4: CORRELATION OF μUS IMAGES WITH OPTICAL IMAGES. A. INTESTINAL TISSUE FROM $APC^{MIN/+}$ MOUSE PINNED ON AGAR VIEWED UNDER STEREOMICROSCOPE AT 10X MAGNIFICATION. THE ARROW MARKED AS 'I' AND 'II' SHOWS THE REGION OF POLYP THAT WAS RESECTED AND VIBRATOME SECTIONED. B. BRIGHT FIELD OPTICAL IMAGE OF THE CROSS SECTION OF THE RESECTED POLYP. C. B-SCAN IMAGE OF THE RESECTED POLYP, REGIONS 'I' AND 'II' ARE MARKED AND SEEN AS BRIGHT RED

spots indicating increased backscatter and density of the tissue in the polyp. D. Confocal image of the resected polyp in region 'II' stained with phalloidin and DAPI to visualise F-actin (red) and nuclei (blue). (Optical images were taken by Dr. Paul Appleton). 166

Figure 7.5: A. Apc heterozygous murine intestinal tissue showing the scanning path taken by the μUS transducer to produce B-scan images. B. B-scan image of tissue in A, showing the histological features of the tissue.....168

Figure 7.6: Backscatter Coefficients. WT and $Apc^{Min/+}$ tissue specimens from male and female mice at varying ages were prepared for μUS scanning. In male mice an increase in BSC is detectable at 60 days whereas female mice show a significant increase only at 90 days. 169

Figure 7.7: Images of crypts. a. WT and b. $Apc^{Min/+}$ tissue from region 2 of murine small intestine stained with DAPI to visualise nuclei (cyan) and phalloidin (yellow) to mark F-actin at the apical surface of cells revealing the packing of crypts in tissue. c. Crypt packing and size in human tissue were determined by measuring diameters of crypts and the distances between a selected crypt and its six closest neighbouring crypts. (Fatehullah et al., 2014).....170

Figure 7.8: Acoustic impedance measurements. Mean acoustic impedance from the tissue was determined for WT and $Apc^{Min/+}$ tissue using μUS transducer. In male mice there is an increase in Z at 60 days. The increase in Z for $Apc^{Min/+}$ mice at varying ages indicates differences in density and acoustical properties. 171

Figure 7.9: Attenuation coefficient measurements. Mean attenuation coefficients from the tissue was determined for WT and $Apc^{Min/+}$ tissue using μUS transducer at the centre frequency of 45 MHz. Indicated on the x-axis are the age of mice, the error bars indicate the positive range of the data.....172

Figure 8.1: Tissue from human small intestine. A. Normal human small intestine. B. FAP tissue. Straight crypts are seen in normal tissue and the crypts are curved in FAP tissue as indicated by coloured lines. The curvature index was calculated as the ratio between the length and depth of the crypts. (Picture taken by Dr. Paul Appleton) (Fatehullah et al., 2014).....180

List of Tables

TABLE 3.1: DENSITY, SPEED OF SOUND AND ACOUSTIC IMPEDANCE OF DIFFERENT TISSUES. SPEED OF SOUND WILL VARY WITH TEMPERATURE IN MOST CASES.(AZHARI 2010) 40

TABLE 3.2: EQUATIONS OF BSC FOR SINGLE ELEMENT ULTRASOUND TRANSDUCERS. 43

TABLE 4.1: MATERIAL PROPERTIES OF 36^0 Y-CUT LNO (G.S. KINO 1987). 66

TABLE 4.2: SUMMARY OF PROPERTIES OF MATERIALS USED FOR THE FABRICATION OF UNMATCHED AND MATCHED μUS TRANSDUCERS. 69

TABLE 4.3: PHYSICAL AND MECHANICAL PROPERTIES OF PARYLENE (C) WHICH WAS USED AS A SPRING LAYER FOR MASS-SPRING MATCHED TRANSDUCERS. 75

TABLE 5. 1: SUMMARY OF THICKNESS MEASUREMENTS AND MATERIAL REMOVAL RATES FOR ULTRA-THINNING OF LNO.....98

TABLE 5.2: PHYSICAL CHARACTERISTICS OF μUS TRANSDUCER WITHOUT MATCHING LAYER. 103

TABLE 5.3: STATISTICS OF FOCUSED μUS TRANSDUCER WITHOUT MATCHING LAYER IN PULSE-ECHO MODE. 104

TABLE 5.4: PHYSICAL CHARACTERISTICS OF μUS TRANSDUCER SINGLE Λ/4 'MASS-SPRING' MATCHING LAYER. 110

TABLE 5.5: STATISTICS OF FOCUSED μUS TRANSDUCER WITH SINGLE Λ/4 'MASS-SPRING' MATCHING LAYER IN PULSE-ECHO MODE.....110

TABLE 5.6: PHYSICAL CHARACTERISTICS OF μUS TRANSDUCER WITH DUAL MATCHING LAYER. 113

TABLE 5.7: STATISTICS OF PLANAR μUS TRANSDUCER WITH DUAL Λ/4 'MASS-SPRING' MATCHING LAYER IN PULSE-ECHO MODE.....113

TABLE 5.8: PHYSICAL CHARACTERISTICS OF μUS TRANSDUCER WITH DUAL Λ/4 'MASS-SPRING' MATCHING LAYER. 116

TABLE 5.9: STATISTICS OF FOCUSED μUS TRANSDUCER WITH DUAL Λ/4 'MASS-SPRING' MATCHING LAYER IN PULSE-ECHO MODE.....117

TABLE 5.10: PHYSICAL CHARACTERISTICS OF THE AFM TH-19 μUS TRANSDUCER.....119

TABLE 5.11: CHARACTERISTICS OF FOCUSED AFM TH-19 μUS TRANSDUCER IN PULSE-ECHO MODE. .122

TABLE 5.12: SUMMARY OF EXPERIMENTALLY DETERMINED CHARACTERISTICS OF μUS TRANSDUCERS TESTED IN PULSE ECHO MODE. 123

TABLE 6.1: ACOUSTICAL PARAMETERS OF AGAR MEASURED IN THROUGH TRANSMISSION MODE USING 5 MHZ PLANAR ULTRASOUND TRANSDUCER. 152

TABLE 7. 1: SUMMARY OF ULTRASOUND TISSUE PARAMETERS MEASURED FROM MALE MURINE INTESTINE. 173

TABLE 7.2: SUMMARY OF ULTRASOUND TISSUE PARAMETERS MEASURED FROM FEMALE MURINE INTESTINE. 173

Glossary

Symbol

$A\ (x,y)$	*Voltage Amplitude measured from tissue at positions x and y*
A_0	*Voltage amplitude measured using quartz*
c	*Speed of sound*
c^D_{ij}	*Elastic stiffness constant measured with constant displacement field*
c^E_{ij}	*Elastic stiffness constant measured with constant electric field*
d	*Distance*
D	*Diameter of transducer*
e_{ij}	*Piezoelectric stress constant*
ε^S	*Permittivity under constant strain*
ε^T	*Permittivity under constant stress*
f	*Frequency*
f_a	*Anti-resonant frequency*
f_r	*Resonant frequency*
k_t	*Thickness coupling coefficient*
l	*Thickness of Tissue*
N	*Near field distance*

p	***Pressure***
Q	***Quality factor***
Q_E	***Electrical quality factor***
Q_m	***Mechanical quality factor***
R	***Reflection Coefficient***
R_a	***Surface Roughness***
t	***Time***
T	***Transmission coefficient***
T_c	***Curie temperature***
V	***Volume***
v_L	***Longitudinal sound velocity***
v_w	***Sound velocity in water***
x	***Thickness of the piezoelectric material***
Z	***Acoustic Impedance***
Z_T	***Acoustic Impedance of tissue***
Z_w	***Acoustic Impedance of water***
α	***Attenuation coefficient***
α'	***Intensity attenuation coefficient***
Δt	***Time of flight***
θ	***Angle***
θ_t	***Half angle subtended by transducer at focus***
λ	***Wavelength***
$\lambda/4$	***Quarter wavelength***
ρ	***Density***

Abbreviations

µUS	**Micro-Ultrasound**
A-mode	**Amplitude Mode**
Apc	**Adenomatous Polyposis Coli**
B-mode	**Brightness Mode**
BSC	**Back Scatter Coefficient**
DOF	**Depth of Field**
FAP	**Familial Adenomatous Polyposis**

HRUS	**High Resolution Ultrasound**
KLM	**Krimholtz-Leedom Matthaei**
LNO	**Lithium Niobate**
LSF	**Line Spread Function**
Min	**Mice Intestinal Neoplasia**
NDT	**Non Destructive Testing**
PMN-PT	**PMN-PT**
PZT	**Lead Zirconate Titanate**
WT	**Wild Type**

Chapter 1: Introduction

"The greatest challenge to any thinker is stating the problem in a way that will allow a solution."

Bertrand Russell

1.1 Overview

This chapter gives a general overview of the history of medical ultrasound imaging, current trends and future developments. The rationale of the thesis is explained, detailing the hypothesis that was successfully confirmed during this research. The structure of the thesis, contributions to knowledge, patents and titles of publications are outlined.

1.2 History of Ultrasound

Ultrasound is one of the most widely used imaging modalities. Ultrasound imaging is commonly used in sonar, non-destructive testing and medical diagnosis. The piezoelectric effect demonstrated by Pierre and Jacques Curie in 1880 led to the development of ultrasound instrumentation. Quartz was the piezoelectric material incorporated into the first ultrasound device. This was a hydrophone developed by Langevin in the early 20^{th} century (Jaffe, 2012). This device was intended for sonar applications.

The use of ultrasound in medical imaging dates back to work done by Dussik and Ludwig in the 1940's. Dussik was able to use ultrasound for detection of intracranial tumours. Initially ultrasound was used in A-mode, to detect gallstones. The first conventional B-mode images were generated by Wild and Reid in 1954, using a mechanical scanning device to build a 2-D image based on A-scan measurements. This technique was used to detect breast and brain tumours (Dempsey, 2004). In the 1960's ultrasound was being used in obstetrics to measure foetal head size to determine growth. Prof. Donald and Tom Brown developed B-scan technology and investigated obstetric applications (Donald & Abdulla, 1967). A B-scan image is a cross sectional image that represents tissues and organ boundaries of the human body. It is constructed from echoes reflected and scattered at tissue boundaries due to irregularities within the tissue (Figure 1.1).

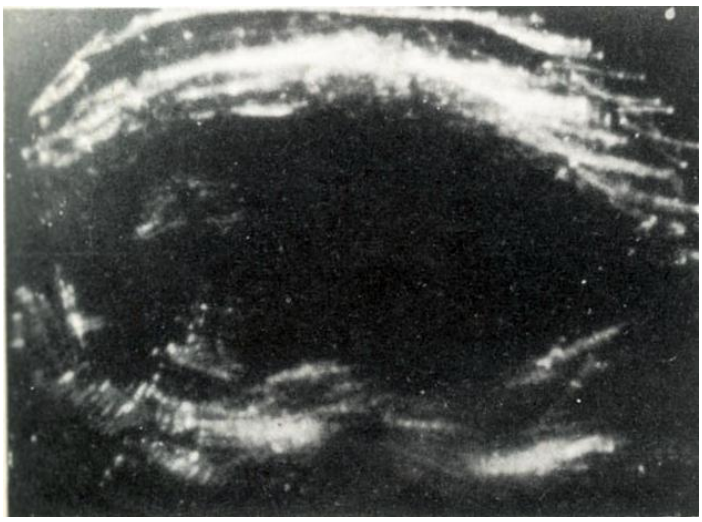

Figure 1.1: First reported ultrasound image of early pregnancy at 14 weeks. The shape in the left side of the image is a large cystic cavity in an early uterus (Donald, Macvicar, & Brown, 1958).

The invention of microchips in 1970s was a milestone in digital electronics and thus in ultrasound instrumentation. Microchips improved the processing power which led to the introduction of faster and more powerful ultrasound systems with digital beam-forming, signal processing and novel means for displaying images. This led to the development of electronically controlled arrays allowing for images to be obtained real time. A number of ultrasound imaging techniques such as: Doppler flow imaging, elastography and ultrasound contrast agent enhanced imaging have emerged. Doppler is used to detect movement of tissues and blood flow (Hoskins, 1997) and elastography to image and sometimes measure tissue stiffness.

Imaging modalities such as X-ray, computed tomography (CT), magnetic resonance imaging (MRI), positron emission tomography (PET) and optical coherence tomography (OCT) have also been developed in recent times. X-rays are relatively low cost and are widely used. However, they are a source of ionising radiation and cannot generate good images of soft tissue. CT produces excellent high resolution images but at the cost of large, though now decreasing doses of radiation exposure for patients. MRI also generates high resolution images but is very expensive and not portable. MRI, X-ray and CT are used for imaging either the full thickness of the human body or for imaging organs that lie deep within the human body (up to 10 cm). Optical computed tomography (OCT) uses optical backscatter from tissues to produce images, but has limited penetration (~ 1-3 mm). Hence it is less suited for imaging internal organs.

Most medical ultrasound transducers have an operational frequency between 1 and 15 MHz. Current medical diagnostic devices available commercially use arrays of piezoelectric transducers to produce 2D or 3D images of the regions of interest. The transducer is excited by a pulsed voltage and in response emits ultrasound pulses that travel through the tissue and organs. The reflected echoes from the tissue and organs are detected by the same transducer and the detected signals are displayed as an image. Clinical ultrasound is portable, inexpensive, safe and capable of producing images in real time but have relatively poor image resolution and signal to noise ratio. The need to produce images with greater resolution has triggered the development of high resolution ultrasound transducers.

1.3 High Resolution Ultrasound

High resolution ultrasound (HRUS), for the purpose of this thesis is defined as applications with a centre frequency exceeding 20 MHz. The resolution of an ultrasound imaging device is frequency dependant. The main advantage of HRUS is improved resolution, which is related to the wavelength of the emitted ultrasound. The shorter pulse length leads to improved axial resolution along the beam propagation direction and higher frequencies leads to better lateral resolution i.e. perpendicular to beam propagation (Lockwood, 1996). The resolution improves from approximately 1 mm to 100 μm when high frequency probes are used. The improved resolution helps in identifying smaller structures in the tissue such as micro-tumours which maybe just a few cells thick. Higher frequency devices provide increased resolution but have lower penetration depth. HRUS is commonly used to visualise small anatomical structures and its applications include ophthalmology, dermatology, intra vascular imaging and small animal imaging (Vogt & Wells, 2010).

Ultrasound transducer with a centre frequency of 45 MHz can provide both axial and lateral resolution in the order of 100 μm with a depth of penetration of 10 - 20 mm smaller than conventional ultrasound but sufficient to image the gut lumen when in proximity to it. High frequency ultrasound systems can be modified with appropriate matching and backing layer designs to achieve greater bandwidth and sensitivity when compared to unmatched transducers. HRUS also complements optical techniques such as confocal microscopy by providing full thickness information at a comparatively low resolution.

High resolution images from dysplastic regions for *in vivo* and *ex vivo* pathological applications would enable early detection and easy collection of biopsy samples, if smaller probes can be fabricated. The size of the ultrasound transducer tends to increase with the wavelength. High frequency leads to smaller dimensions of the transducers and fabrication of such µUS transducers present numerous challenges (Foster et al., 2000). With recent development of microfabrication techniques and advances in piezoelectric materials, it is now possible to explore the development of µUS transducers for imaging beyond sub-millimetre resolution.

1.4 Ultrasound Tissue Characterisation

Having described the potential of HRUS imaging, the need for quantitative ultrasound techniques to characterise tissue is described. B-scan images are created by envelope detection of backscattered echoes from tissue. They are in principle maps of the envelope of backscattered echoes from different regions of the tissue. The images represent partial information present in the echoes as information pertaining to frequency dependence of backscatter amplitude and phase is lost during computation.

When an ultrasound wave propagates through tissue, it is backscattered due to the size, shape and number of density of scatterers in tissue. The scatterers can be observed as discontinuities in the acoustical properties of the tissue. In the case of intestinal tissue the scatterers could be crypts, nuclei, sub-cellular components or villi. Analysis of the backscattered echoes provides quantitative information about the tissue which could be used for classifying pre-cancerous tissue from normal tissue (Oelze, & O'Brien, 2002). The other issue with ultrasound images is that identification of tissue structures using images relies on subjective interpretation of features and is also dependent on operator settings. Subjective interpretation is often difficult due to the presence of speckle in B-scan images. Speckle results from interference of sound waves from scatterers lying within the resolution cell (Foster et al., 1993).

The speed of sound in soft tissue is assumed to be 1540 ms^{-1} as speed does not vary with significantly with frequency. Attenuation coefficient is another acoustic parameter that can be computed. Attenuation is the loss of signal amplitude with propagation distance and is expressed in units such as dB mm^{-1}. Assuming constant speed of sound, acoustic impedance of tissue directly relates to the changes in the density of the tissue and is a useful parameter that can be derived from the rf data. BSC is the differential scattering cross section per unit volume at an angle of 180^0. BSC determines the

brightness of pixels in a B-scan image. In pulse-echo mode the recorded signals from tissue depends both on attenuation and BSC. Thus quantitative measurements have the potential to reduce bias and ambiguity in inferring tissue characteristics.

1.5 Need for Early Detection of Colon Cancer

A polyp or adenoma in the bowel is a small growth that usually develops in the colon or rectum. About 1 in 4 people over the age of 50 develop at least one bowel polyp. Polyps are benign and usually cause no problems. However, sometimes a benign polyp can turn cancerous, a polyp that has been present for 5-15 years and left untreated becomes cancerous. Most colorectal cancers (CRC) occur sporadically in > 95% of cases. In 5 to 10% they occur due to inherited causes such as: Familial adenomatous polyposis coli (FAP), Hereditary Non Polyposis Colorectal Cancer (HNPCC) and long standing history of inflammatory bowel disease (IBD) (Ellis et al., 2005).

Polyps in humans are characterized qualitatively based on size, colour, number and location. These characteristics of the polyp provide histological clues about the malignant potential. For example; Adenomas are large, red, multilobular and distributed through the colon, whereas hyperplastic polyps are small, pale, unilobular and situated in the rectum (Cappell 2005). Improving the ability to detect and classify lesions during screening visits is vital to make screening as effective as possible. This requires that the imaging modalities employed as part of the procedure utilize the most sensitive technologies to assist the endoscopist in detecting relevant changes.

Detection of changes in the tissue organisation is at the core of early diagnosis of colon cancer during endoscopy screening. When colon cancer is detected early it is readily treated but lack of symptoms until late in the disease means that most patients present too late. This has motivated a UK-wide screening program using colonoscopy on patients that present with blood in their stool (Steele et al., 2009).

Adding quantitative imaging modalities to histological examination has the potential to improve the ability to detect relatively subtle tissue abnormalities. Ultrasound has been successfully used to detect tissue abnormalities in clinical settings. Using higher frequencies (> 35 MHz) provides increased resolution and allows for characterization of tissue organization, making it suitable for identifying precancerous changes in patients. One of the primary goals of this thesis is early detection of colon cancer.

1.6 Objectives and Hypothesis

The project detailed in this thesis was driven by a biological aim, i.e. to detect early tissue dysplasia using µUS. The aims of the thesis are listed in order: The first is, to investigate the potential of novel 'mass-spring' matching layers to contribute to the ease with which broad bandwidth, high resolution µUS transducers can be made and thus to improve their availability by using carefully controlled vacuum deposition alone. Secondly to use µUS transducers fabricated, for the early detection of tissue dysplasia in mice models. The hypothesis investigated is that, the intestinal tissue morphology of WT (wild type) and $Apc^{Min/+}$ diverges with progressing age of mice. The divergence was measured using quantitative and qualitative ultrasound methods. Specifically, the quantitative technique was used to measure changes in the organisation of precancerous tissues which are irregular and denser than healthy tissue. The experiments were conducted *ex vivo* on murine small intestine.

1.6.1 Rationale

The rationale behind the technical and biological objectives stated in 1.6 as follows:

1. As a first step, to fabricate high resolution µUS transducers requires precise lapping techniques to thin the piezoelectric material. A reliable and repeatable process route for ultra-thinning of lithium niobate (LNO) was developed. Conventional ultrasound matching layers consists of one or more approximately quarter wavelength ($\lambda/4$) thick layers of bulk material with acoustic impedances intermediate between the piezoelectric substrate and water. The layers are a few tens of microns thick and therefore require precise lapping and bonding techniques to avoid degradation of bandwidth. Conventional quarter wavelength matching layers consist of loaded epoxy. Attenuation of ultrasound at high frequencies in loaded epoxy is high, due to scattering losses. Also fabrication of conventional matching layers is slow and cumbersome.

In this thesis an alternate approach is described by the use of 'mass-spring' matching layers for high frequency µUS transducers using vacuum deposition processes. The effectiveness of this technique was evaluated by applying single and dual matching layers to 3 mm diameter lithium niobate (LNO) planar and focused transducers operating at 45 MHz. The fabricated transducers were compared with a KLM model,

characterised and tested for their functionality to prove the advantages of vacuum deposition over conventional matching layers.

2. Altered tissue architecture is a hallmark of precancerous stage. The aim of this thesis was to image and quantitate changes induced by tumorigenic mutations in pre-cancerous stages of colon cancer, using a 45 MHz focused transducer and a step-repeat µUS scanner that was developed during this research.

The development of a custom design system has several reasons, principally that commercial ultrasound imaging systems operating at frequencies greater than 35 MHz are not commonly available and are expensive. Moreover, commercial systems have limitations when it comes to characterisation of tissues. For characterisation studies the raw backscatter signals are required and not just final images. Commercial systems lack the flexibility required for tissue characterisation. For example a VisualSonics systems operating at high frequency is commercially available that allows tissue characterisation but this system is expensive to buy, hence a a custom designed system on a research platform was built. The frequency of 45 MHz is compatible with a lateral resolution of approximately 100 µm, which makes it possible to resolve fine tissue structure of murine small intestine. Therefore a transducer with a centre frequency of 45 MHz was chosen.

The experimental study on colon carcinogenesis using mouse models dates back to eighty years (Krebs C. 1928). The advantages of studying mouse models include rapid and reproducible tumour induction which directly relates to the adenoma carcinoma sequence that occurs in humans (D. Rosenberg et al., 2009). The $Apc^{Min/+}$ mice is heterozygous for mutations in adenomatous polyposis coli (APC) and has been used as a model for familial adenomatous polyposis (FAP) as the individuals affected develop polyps in the small intestine. The $Apc^{Min/+}$ mice develop polyps in the small intestine and are the closest mice model to study CRC.

The data and interpretation presented in this thesis provides significant new insights in matching layer technology and early cancer detection. This work may well contribute to optimization of µUS transducer fabrication and improve patient outcomes during routine endoscopy screening for bowel cancer.

1.7 Contribution to Knowledge

The work described in the thesis has contributed to knowledge in three specific areas.

Ultra-thinning of LNO for high resolution ultrasound medical imaging

A potentially successful process route for ultra-thinning of LNO was established. The development of this process was motivated by the need to produce high resolution µUS transducers for imaging. The process route was implemented to fabricate µUS transducers operating at 45 MHz. It is expected that the success of this established process route will prove viability for wafer scale thinning of LNO wafers to produce µUS transducers at low cost and high yield. This part of the work was carried out in collaboration with Logitech Ltd. Kilpatrick, Glasgow, UK.

Mass – Spring Matching Layers for High- Frequency Ultrasound Transducers: A New Technique Using Vacuum Deposition

As noted previously, the matching layers used in high frequency transducers are conventional quarter wavelength thick layers. A new technique of matching layers called the 'mass-spring' matching layers has been implemented for high frequency ultrasound transducers. These vacuum based matching layers have many benefits. This type of matching layers allows for large volume production of µUS single element transducers and arrays. The vacuum deposition technique provides versatile material selection, uniformity of layers as the thickness can be well controlled, and application of matching layers to curved surfaces is easy and repeatable. Vacuum deposition avoids the need for adhesion of matching layers, thus providing low attenuation of the ultrasound signal and improved performance of the transducer. This work was carried out in collaboration with Prof. Jeremey Brown, Department of Biomedical Engineering, University of Dalhousie, Canada.

Detection of microscopic variations in precancerous tissue using microultrasound.

Colon cancer is the second most common cause of cancer deaths in the western world. The knowledge of molecular changes underpinning colorectal cancer has not yet translated into clinical benefit. In this research the potential of high resolution µUS for early detection of cancer was demonstrated. It was observed that µUS detects microscopic changes in precancerous tissue that are otherwise invisible. The acoustic properties of premalignant changes in the intestinal tissue were measured using high frequency µUS.

This provides novel means to detect microscopic abnormal regions in tissue independent of visual examination or biopsies. The approach developed during this research provides a powerful adjunct to screening endoscopy for improved identification and monitoring of microscopic lesions, which are undetectable with present imaging modalities. If it can be translated appropriately into clinical practice, this may improve patient outcomes. This part of the research was carried out in collaboration with Prof. Inke Nathke at the college of life sciences (CLS), Wellcome Trust, University of Dundee, UK.

1.8 Thesis Structure

This thesis is concerned with developing novel matching layers for high frequency µUS transducers and development of measurement techniques to detect early stages of colon cancer in murine models.

Chapter 2 is a review of the literature, explaining the pathophysiological, histological and molecular changes observed in colon cancer. The specific role Apc in colon cancer is explained. The chapter also reviews the diagnostic modalities that are currently used for screening, imaging and staging of colon cancer.

Chapter 3 explains the theoretical principles of ultrasound waves and ultrasound transducer design and fabrication. It also reviews the past and present research on HRUS imaging and ultrasound tissue characterisation, investigating the influence of clinical need that has led to the development of HRUS imaging.

Chapter 4 describes the experimental methodology used in this thesis, for fabrication, characterisation and testing of single element ‘mass-spring’ acoustically matched high resolution µUS transducers.

Chapter 5 presents the results from fundamental characterisation of ‘mass-spring’ matched µUS transducers. The results of the fabricated transducers were compared with a commercial transducer.

Chapter 6 explains experimental methodology utilised for imaging and measuring precancerous changes in tissue architecture of murine small intestine pre-disposed to bowel cancer, *ex vivo* using µUS transducer, to test the hypothesis stated above.

Chapter 7 presents results from high resolution ultrasound imaging and tissue characterisation of murine small intestine and human tissue.

Chapter 8 provides overall conclusions, highlighting successful results and those requiring further improvements. An overview of future work leading on from this thesis is also reported.

1.9 Academic Grants Awarded

The initial work on fabrication of single element µUS transducer successfully contributed to secure a SUPA Start grant of £ 5000 for project titled "Needle based ultrasound imaging device".

The results from tissue characterisation studies on murine small intestine contributed towards securing a grant worth £ 16,000 from the Dundee Cancer Centre (DCC). This money was used to build a high speed ultrasound scanner for imaging.

The work presented in this thesis on early detection of cancer, provided the pre-clinical data to successfully obtain an EPSRC grant, Sonopill (EPSRC Reference EP/K034537/1) for miniaturisation of ultrasound devices, specifically aiming to develop an ultrasonic capsule to aid in diagnosis of gastrointestinal diseases.

I was awarded the J.M. Lessells scholarship of £ 5,000 from the Royal Society of Edinburgh (RSE). This grant enabled collaboration and development of novel 'mass-spring' matching layers for high frequency ultrasound transducers along with Prof. Jeremy Brown at the University of Dalhousie, Halifax, Canada.

1.10 Publications

Published Article

J. Brown, **S. Sharma,** J. Leadbetter, S. Cochran and R. Adamson.

"Mass-spring matching layers for high-frequency ultrasound transducers: a new technique using vacuum deposition." *Ultrasonics, Ferroelectrics, and Frequency Control, IEEE Transactions on, 61*(11), 1911-1921.

Patents:

V. Seetohul, **S.Sharma,** J.Faerber and S.Cochran

"Sonarpill"

1. Patent number: Europe GB1405392.0, Patent filed on March 26, 2014.

S.Sharma, S.Cochran and I.Nathke

"Microultrasound macroscope for early detection of colon cancer"

2. Patent number: GB 1403025.8, Patent filed on February 20, 2014.

Journal paper in preparation

A.Fatheullah, **S.Sharma**, I.P.Newton, S.A.Nelson, R.K. McMahon, N.Mcllvenny, P.L.Appleton, S.Cochran and I.S.Näthke.

1. "Microultrasound detects microscopic variations in precancerous intestinal tissue" under review *Nature Communications.*

RT Ssekitoleko, **S Sharma**, C. Demore, S Cochran.

2. "Prediction of ultrasound imaging transducers performance through simulated resolution integral*" IEEE note or Ultrasonics.*

Conference Proceedings

Y. Qiu, D. A. Hughes, C. Demore, **S. Sharma**, K. Weijer, and S. Cochran.

1. "Multi-wavelength Ultrasonic Standing Wave Device for Non-invasive Cell Manipulation and Characterisation," *IEEE International Ultrasonics Symposium Proceedings, pp.188-191, 2011.*

Conference Presentation

J. Brown, **S. Sharma,** J. Leadbetter, S. Cochran and R. Adamson,

1. "Mass – Spring Matching Layers for High- Frequency Ultrasound Transducers: A New Technique Using Vacuum Deposition", *2014 IEEE International Ultrasonics Symposium Proceedings, Chicago, USA, September 2-10, 2014* (***Oral)***

S.Sharma, A.Fatheullah, P.Appleton, I.S.Näthke and S.Cochran

2. "High resolution ultrasound: Early Detection and Characterization of Colon Cancer",

CMDN Symposium, University of Dundee, Dundee, UK, June 2014 (***Oral, 2nd prize for best presentation)***

S.Sharma, A.Fatheullah, P.Appleton, C.Demore, I.S.Näthke and S.Cochran

3. "High Resolution Ultrasound Murine Bowel Characterization and Acoustic Microscopy of Murine Intestinal Dysplasia", *SUPA annual meet, Heriot Watt University, Edinburgh, UK, June 2013*.(***Poster, 1st prize for best poster and presentation)***

Christine E.M. Demore, Robert T. Ssekitoleko, Jack Hoyd-Gigg Ng, Yun Jiang, **S.Sharma**, Tim W. Button, Jeffrey C. Bamber, Marc P.Y. Desmulliez, and Sandy Cochran.

4. "Miniaturised transducer arrays for high resolution clinical imaging" *Ultrasonic Transducer Engineering Conference; 17-19 April 2013, Los Angeles, CA* ***(Oral)***
S.Sharma, P.Appleton, S.Nelson, I.S.Näthke and S.Cochran

5. "Ultrasound Microscopy: Quantitative Backscatter Imaging" *SUPA Annual meet, Heriot Watt University, Edinburgh, UK, September 3, 2012.* ***(Oral)***

R T Ssekitoleko, **S Sharma,** CEM Demore, and S Cochran.

6. "Prediction of ultrasound imaging transducers performance through simulated resolution integral". *IPEM, EMPEC2011 – 1st – 3rd September 2011, Dublin, UK* ***(Oral)***

Y. Qiu, D. A. Hughes, C. Demore, **S. Sharma**, K. Weijer, and S. Cochran.

7. "Multi-wavelength Ultrasonic Standing Wave Device for Non-invasive Cell Manipulation and Characterisation," *2011 IEEE International Ultrasonics Symposium Proceedings, Orlando, FL, October 18-21, 2011* ***(Oral)***
S.Sharma, J.McCrossan, J.McAnneny, and S.Cochran.

8. "Ultra-thinning of Lithium Niobate for High Frequency Ultrasonic Medical Imaging". *Fraunhofer EMFFT-Munich, 1st – 3rd August 2011, Munich, Germany.* ***(Oral)***

Malik. R, Madhwani. D, Fiabane. J, Kakchingbatam. D, O. Dogadkin., **S.Sharma**, Pancholi. K, P. Andre, R. Habeshaw, Wang. L, P. Prentice, S.Cochran, and A. Melzer.

9. "Formulations for ultrasound triggered image-guided targeted chemotherapy"

1st European Symposium, MR-guided Focused Ultrasound Therapy, Rome 2011. ***(Oral)***

1.11 References

Dempsey, P. J. (2004) "The history of breast ultrasound." *Journal of ultrasound in medicine*, *23*(7), 887-894.

Donald, I., & Abdulla, U. (1967) "Ultrasonics in obstetrics and gynaecology." *The British journal of radiology*, *40*(476), 604-611.

Donald, I., Macvicar, J., & Brown, T. G. (1958) "Investigation of abdominal masses by pulsed ultrasound." *The Lancet*, *271*(7032), 1188–1195.

Ellis, CN. (2005) " Inherited Colorectal Cancer Syndromes." *Clinics in Colon and Rectal Surgery*. 18(3):150-162.

Foster, F. S., Liu G., Mehi, J., Starkoski B. S., Adamson L., Zhou, Y., Zan L. (2000) "High frequency ultrasound imaging: from man to mouse." *IEEE Ultrasonics Symposium. Proceedings. 2*, 1633–1638.

Foster, F. S., Lockwood G. R., Ryan L. K., Harasiewicz K. a, Berube, L., & Rauth, A M. (1993) "Principles and applications of ultrasound backscatter microscopy." *IEEE Transactions on Ultrasonics, Ferroelectrics, and Frequency Control*, *40*(5), 608–17.

Hoskins, P. R. (1997) " Peak velocity estimation in arterial stenosis models using colour vector Doppler." *Ultrasound in Medicine & Biology*, *23*(6), 889–897.

Oelze M. L., Zachary, J. F., & O'Brien, Jr W. D. (2002) "Characterization of tissue microstructure using ultrasonic backscatter: Theory and technique for optimization using a Gaussian form factor." *The Journal of the Acoustical Society of America*, *112*(3), 1202-1211.

Rosenberg, D. W., Giardina, C., & Tanaka, T. (2009) "Mouse models for the study of colon carcinogenesis." *Carcinogenesis*, *30*(2), 183–196.

Steele, R. J. C., McClements P. L., Libby, G., Black, R., Morton, C., Birrell J., Fraser C. G. (2009) "Results from the first three rounds of the Scottish demonstration pilot of FOBT screening for colorectal cancer." *Gut*, *58*(4), 530–5.

Vogt, M., Opretzka, J., Perrey, C., Ermert, H., & Wells, P. N. T. (2010) "Ultrasonic microscanning." *Proceedings of the Institution of Mechanical Engineers, Part H: Journal of Engineering in Medicine*, *224*(2), 225–240.

Chapter 2: Colorectal Cancer

"In some ways disease does not exist until we have agreed that it does, by perceiving, naming, and responding to it"

C.E. Rosenberg

2.1 Overview

Colorectal cancer (CRC) is one of the leading causes of morbidity in the western world. Early detection of CRC is crucial to improve survival. Imaging modalities such as colonoscopy, MRI, CT have improved the detection of tumours, but the detection of pre-malignant dysplasia requires novel technologies. This thesis has aimed to the issue by developing qualitative and quantitative high resolution μultrasound techniques that can precancerous changes in the tissue.

In this chapter a brief review of physiological, anatomical and molecular precursors of CRC vis-à-vis current methods used for screening, diagnosis and staging of CRC have been discussed. The key concepts covered are:

- Section 2.1, reviews the epidemiology of CRC with emphasis on prevalence of CRC in the UK and the differences based on gender and demographics.
- Section 2.2, describes the basic anatomy and physiology of the GI tract, detailing the architecture of the small intestine and colon.
- Section 2.3, reviews current imaging modalities used for screening and detecting CRC and also imaging modalities currently used for staging and preoperative planning of CRC.

2.2 Epidemiology of Colorectal Cancer

Colorectal cancer (CRC) or bowel cancer is the third most leading cause of deaths with 35,000 new cases in the western world and 17,000 related deaths per annum in the UK. The highest estimated incidence rates are in Australia/New Zealand and the lowest in Western Africa (Globocan, 2012 (IARC)).

In the United Kingdom (UK), based on the latest available statistics, CRC is the fourth most common cancer with over 40,695 new cases, of which 22,834 cases (14%) are in males and 17,861 cases (11%) are in females. This means that there are around 75 new bowel cancer cases for every 10,000 males and around 56, for every 10,000 females in the UK. The European age-standardised incidence rates (ASR) show that the highest incidence rates in the UK are still in areas of Scotland, Northern Ireland, and north of England for males, which has been the trend from the 1990s. However, this divide is less clear in females. Bowel cancer incidence is strongly related to age, with the highest incidence rates being in older men and women. In the UK between 2008 and 2010, 73% of bowel cancer cases were diagnosed were in people aged over 65 years. Age specific incidence rate increases rapidly after the age of 50 (Figure 2.1). The life time risk of developing CRC is 5% and tends to increase dramatically with age. Almost 66% are cancers of the colon and over 34% are cancers of the rectum. Small bowel cancers are uncommon tumours of the gastrointestinal tract. As a result of their infrequency and variety, the accumulation of data regarding their clinical presentation, pathologic features, prognostic factors, treatment modalities, and outcome has been difficult.

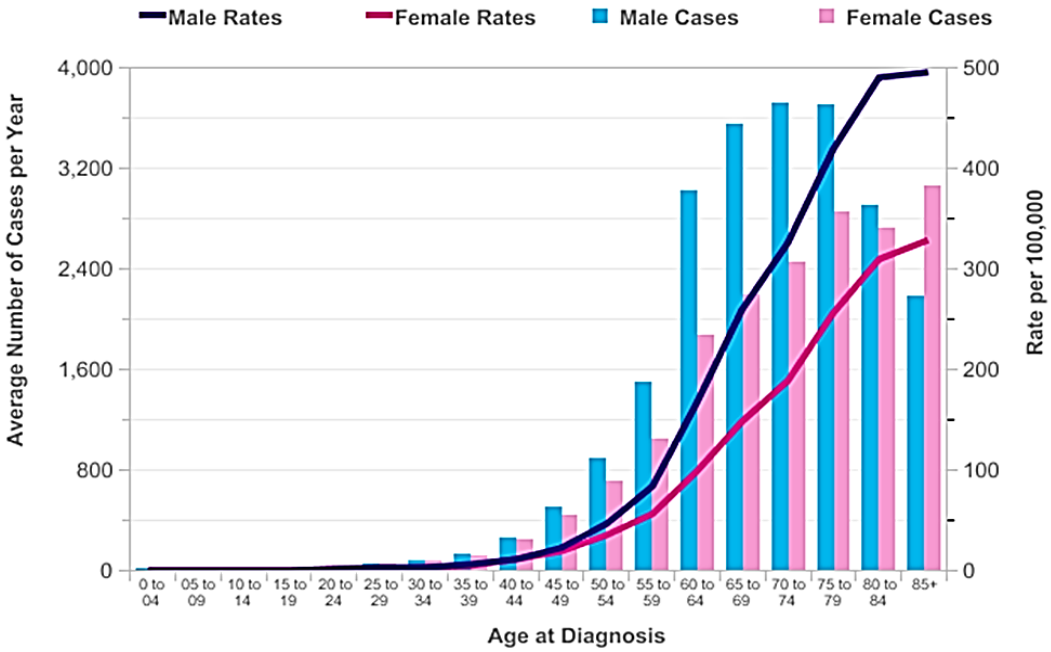

Figure 2.1: Average number of colorectal cancer cases per year and age specific incidence rates per 100,000 populations in the UK in 2008-2010. (www.cancerresearchuk.org, 2013).

2.3 Anatomy and Physiology of the Intestinal Tract

CRC arises through a gradual series of well characterized histological changes that are associated with specific gene mutations. An important fundamental step in understanding CRC is by understanding the anatomy and physiology of normal gut.

The gastrointestinal (GI) tract is a conduit that extends from the mouth to the anus. The main function of the intestinal tract is the digestion and absorption of nutrients. The human GI tract (Figure 2.2) can be divided into two distinct regions namely: the upper GI tract and lower GI tract. The upper GI tract includes the oesophagus, the stomach, the duodenum, the jejunum and the ileum. The rest form the lower GI tract which includes the ascending colon, the descending colon, the transverse colon, the sigmoid colon and the rectum. The caecum is considered to be the beginning of the large intestine. It connects the ascending colon of the large intestine.

The oesophagus carries food from the mouth to the stomach as bolus. This is then emptied into the small intestine after the action of gastric juices to form chyme, which has a low pH. The chyme then stimulates other accessory organs of digestion like the pancreas, the gall bladder, and the liver and smaller intestinal glands. As a result, some

more nutrients are absorbed in the small intestine. This is followed by its transit into the large intestine where mainly water is absorbed and waste products are compacted to form stool.

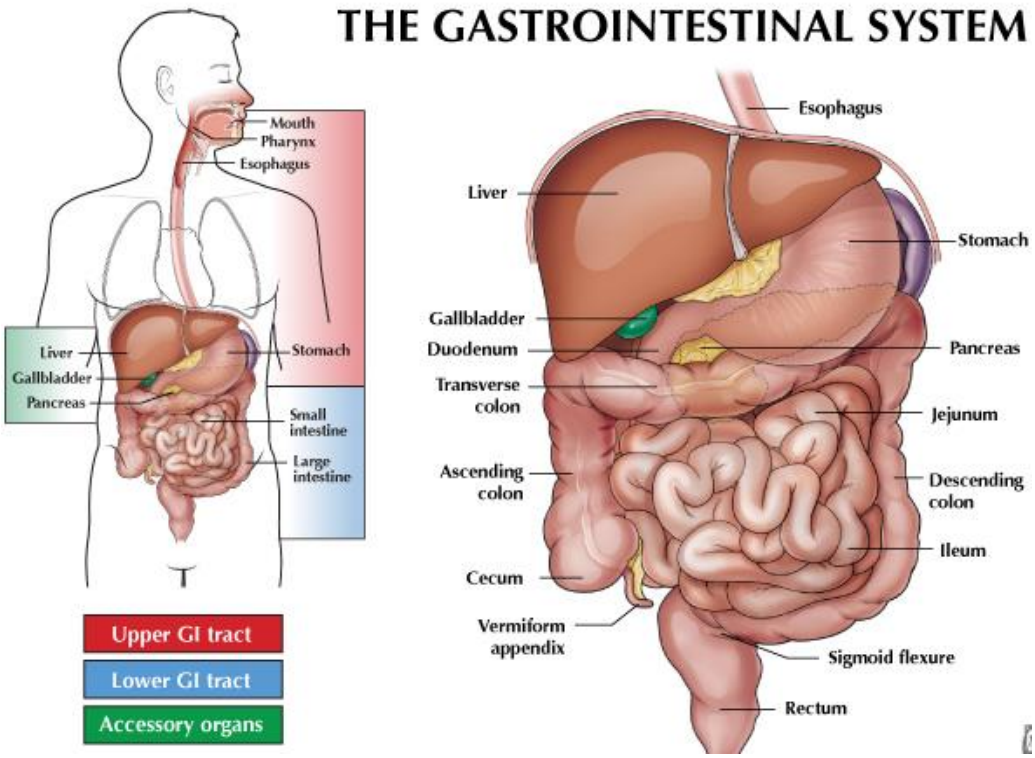

Figure 2.2: Human GI tract, showing upper GI, lower GI and accessory organs such as the liver, gall bladder and pancreas (Trialsight Medical Media, 2008).

2.3.1 Small Intestine

The small intestine is a convoluted tube, extends from the pylorus to the colic valve, and ends in the large intestine. It is about 7 meters in length and 2.5 cm in diameter. It gradually diminishes in size from its commencement to its termination. The small intestine is divided into three portions: the duodenum, the jejunum, and the ileum. Most of the digestion and absorption takes place in the small intestine.

The jejunum and the ileum are supported by a sheet of mesentery. Mesentery membrane suspends the small intestine from the back of the abdominal wall and supports blood vessels, nerves and lymph vessels that supply to the small intestine (Figure 2.3).

The wall of the small intestine (Fig. 2.3 B) is composed of four coats: serous, muscular, areolar or sub mucous and mucous. The serous coat (*tunica serosa*) is derived from the peritoneum. The muscular coat (tunica muscularis) consists of two layers of unstriped

fibres: an external, longitudinal, and an internal, circular layer. The longitudinal fibres are thinly scattered over the surface of the intestine, and are more distinct along its free border. The circular fibres form a thick, uniform layer, and are composed of plain muscle cells of considerable length. The areolar or sub mucous coat (tela submucosa) connects together the mucous and muscular layers. It consists of loose, filamentous areolar tissue containing blood vessels, lymphatics, and nerves. It is the strongest layer of the intestine. The mucosa includes the epithelial layer and loose connective tissue called the lamina propria. Villi are finger-like projections that protrude from the epithelial lining of the intestinal wall. The villi increase the absorptive capacity of the small intestine. The length of the villi decreases from duodenum to ileum and there are no villi in the colon.

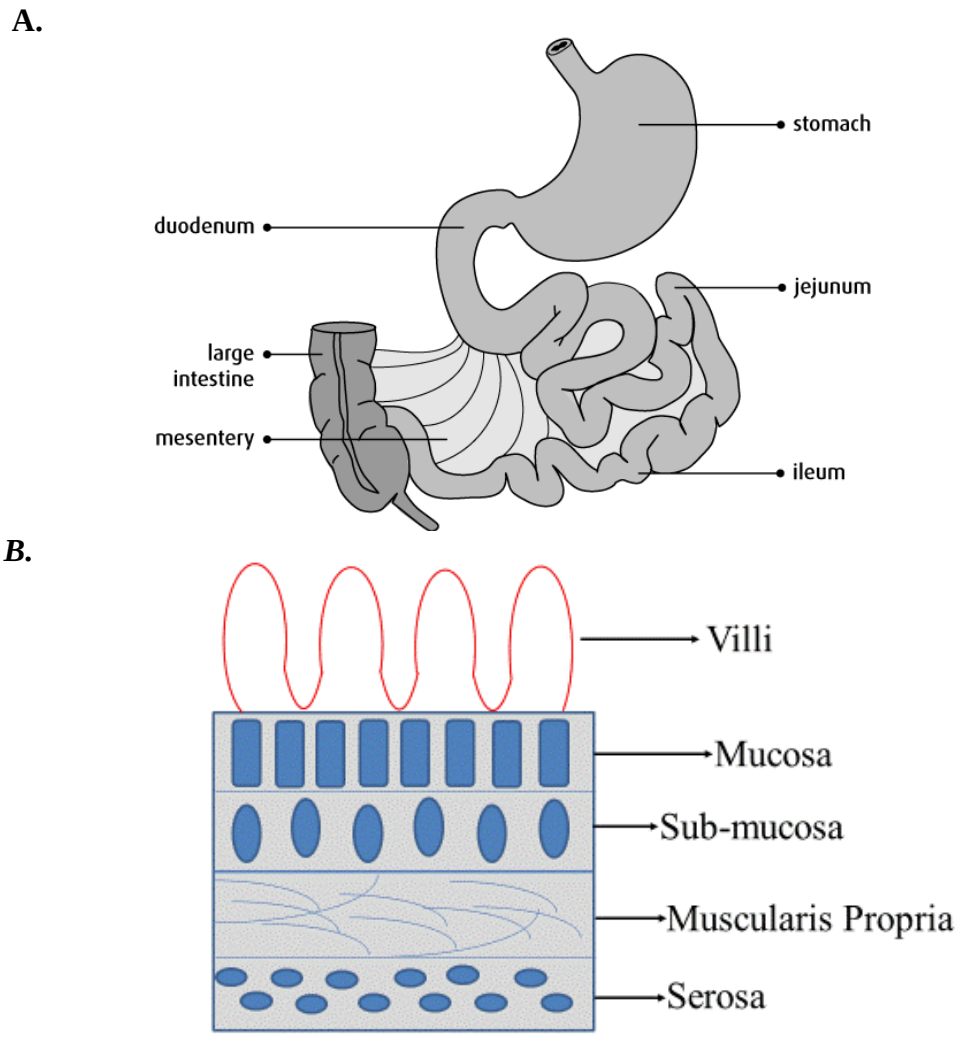

Figure 2.3: ***A.*** *The various regions of small intestine. Small intestine is looped and fills up the abdominal cavity. Small intestine is sub-divided into duodenum, jejunum and ileum.* ***B.*** *The inside layers of the small intestine. The uppermost layer is made up of finger like projections called villi, followed by mucosa, submucosa, muscularis and serosa.*

2.3.2 Large Intestine

The large intestine or colon joins the end of ileum and begins at the caecum. The large bowel is divided into four distinct parts namely: the ascending colon, the transverse colon, descending colon and sigmoid colon (Figure 2.4). The ascending colon starts at the caecum and travels along the right side of the body to the transverse colon. The transverse colon connects the ascending colon to the descending colon. The descending colon connects the transverse colon. The colon is made up of simple columnar epithelium and the anal canal is made up of stratified epithelium. A part of the colon is connected to the abdominal wall by mesentery. The epithelial layer in the colon is made up of goblet and absorptive cells. The absorptive cells absorb water and the goblet cells produce mucus.

The main function of the large bowel is bacterial digestion of food, absorption of water and nutrients and defecation. The colon receives partially digested food from the small intestine in liquid form. The bacterium in the colon breaks down the food. The epithelium layer absorbs food and nutrients. The remaining undigested food is made into stools and ejected through the anus. The epithelial layer produces mucus at the end of the digestive tract to make it easier for the stool to pass through colon and rectum.

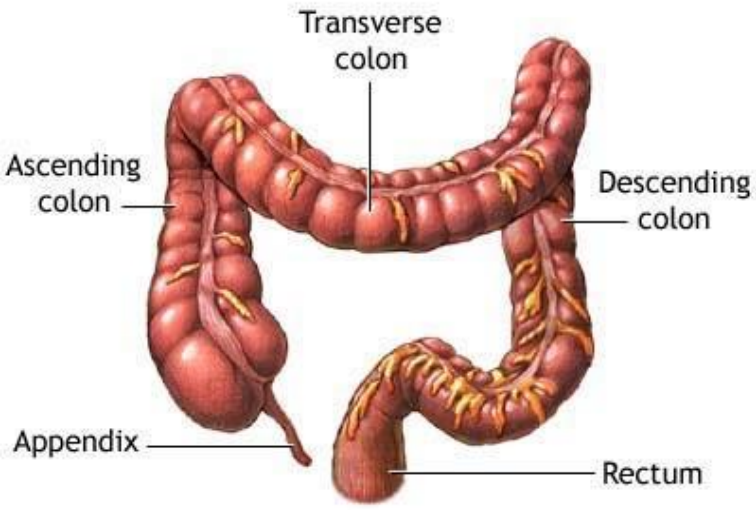

Figure 2.4: Large bowel or colon is the final segment of the GI. Absorption of nutrients and water and compaction of indigestible food are its main functions. (Trialsight Medical Media, 2008).

Gut tissue resides in chemically toxic and mechanistically stressful environments in the body. The cells have a limited residence of 3-5 days in this environment (Potten et al. 1997).

2.4 Screening and Diagnosis of Colorectal Cancer

Imaging of CRC can be divided into three basic areas: screening, regional evaluation of primary tumour and evaluation of metastatic disease. Modalities such as double contrast barium enema (DCBE), faecal occult blood test (FOBT) and colonography are commonly used for lesion detection in symptomatic individuals. The following sub-sections reviews the screening method and imaging modalities used to diagnose CRC.

Symptoms are prominent in CRC, symptomatic patients most commonly present with change of bowel habit which is due to the constriction of the bowel lumen due to enlargement of polyps. Low rectal tumours can bleed bright red blood and blood might be darker if the bleeding is from left side of the rectum and is usually mixed with stools. Iron deficiency or anemia is also an important mode of presentation and indicates right

sided tumours in the rectum. This is usually a symptom most prevalent in people over the age of 50 years.

2.4.1 Faecal Occult Blood Testing

As the incidence of CRC is most common in older people, a UK wide screening program was launched to screen for FOBT in population aged over 50 years (Steele et al. 2009; Nicholson et al. 2005). This involves testing three samples of faeces for blood. FOBT and FIT does not diagnose bowel cancer, but the results will indicate if further investigation (e.g. colonoscopy) is required. The guaiac based faecal occult blood testing (FOBT) is a screening technique that detects the peroxidase activity of haemoglobin, indicating the presence of occult blood in the stools. Guaiac turns blue after oxidation by peroxidases. The positive test result of FOBT is proportional to the quantity of blood in the stools, which in turn is related to the size and location of the lesion (Rockey 1999). The sensitivity of the FOBT to detect colorectal cancer is between 30 -50%, implying that around 50% of the colonoscopies done for positive FOBT showed no neoplasia. The sensitivity is dependent on the number of trials of the test and if the stool sample has been rehydrated. Faecal immunochemical test (FIT) uses antibodies specific for human haemoglobin. The combination of FIT and FOBT increases the sensitivity of detecting neoplasia (Nicholson et al. 2005).

2.4.2 Colonoscopy

Colonoscopy is the gold standard investigation procedure for CRC. Colonic polyps are usually in the range of 10 – 12 mm. Colonoscopy is highly sensitive in detecting colonic polyps larger than 10 mm. A video camera is attached to the end of the scope which is inserted through the rectum and pushed through the rectum, to enable visual inspection of the large bowel from the rectum to the caecum. The camera connects to a computer which can store and print images taken during the procedure. Colonoscopy can detect cancers and also allows biopsies to be taken (Hall 2007).

Polyps are characterized qualitatively based on size, colour, number and location. These characteristics of the polyp provide histological clues about the malignant potential. For example; Adenomas are large, red, multilobular and distributed through the colon, whereas hyperplastic polyps are small, pale, unilobular and situated in the rectum (Cappell 2005). A study conducted by Rockey et al., reported that sensitivity for polyps

of 10 mm or more in size was 98 % for colonoscopy (Rockey et al. 2005). It has been reported that colonoscopy is more sensitive and specific than barium enema.

Colonoscopy cannot distinguish between malignant and nonmalignant adenomatous polyps, as colonoscopic appearance is not definitive. Pathological biopsies of the colonic polys are usually diagnostic. However, colonic polyps can be missed around the sigmoid and hepatic flexures and in areas covered by stool due to poor colonic preparation and also, colonoscopy is expensive, invasive, and uncomfortable to the patient. Colonoscopy entails a significant risk of complications to the patient due to gastrointestinal bleeding and colonic perforation.

2.4.3 Sigmoidoscopy

A sigmoidoscope is used to investigate the cause of bleeding or pain in the rectum. A sigmoidoscope is circular tube with an attached light source. The sigmoidoscope is inserted through the anus and pushed slowly into the rectum and the sigmoid colon. Flexible sigmoidoscopy is usually recommended in conjunction with FOBT. Sigmoidoscopy is highly sensitive and specific for lesions within the reach of the instrument. Recent research studies conducted in the UK in 2010 found that a routine flexible sigmoidoscopy of patients in the age group of 55 and 64 had a reduced risk of developing colorectal cancer by about a third; this was because most polyps that were found during the test were removed.

In current clinical setting the use of sigmoidoscopy is becoming increasingly limited in screening and diagnosis of colon cancer. It is difficult to detect colonic polyps as the proximal half of the colon cannot be visualized. This effect in recent times has increased due to the shift of colonic polyps to the right side of the colon (Nicholson et al. 2005). Although sigmoidoscopy is not as thorough as colonoscopy, it is safer, cheaper and considered to be efficacious (Sandler 1990).

2.4.4 Capsule Endoscopy

The small intestine is a difficult organ to access through colonoscopy and endoscopy, and complete diagnosis and treatment can only be achieved with surgery. Capsule endoscopy allows painless imaging of diseases of the GI tract and small bowel. Some common examples of the diseases targeted by capsule endoscopy are angiodysplasias, Crohn’s disease and tumour of the small intestine (Neumann et al. 2013). Capsule endoscopy utilizes a small capsule, which contains a video camera, battery, light source

and a transmitter (Figure 2.5). The typical size of the capsule endoscope is around 10 - 30 mm. The camera acquires two pictures every two seconds for up to eight hours transmitting images to a data logger, which worn around the waist by the patients. Capsule endoscopy is useful in evaluating jejunoileal bleeding, which is usually caused by upper or lower GI lesions. Capsule endoscopy is attractive given its noninvasiveness and safety.

Figure 2.5: Capsule endoscope, used to image parts of the GI tract that cannot be visualized by colonoscopy and sigmoidoscopy. Capsule endoscopes are especially useful in imaging the small intestine. (Mahfouz et al. 2011).

At the end of the procedure after eight hours, the images are downloaded from the receiver to the computer and the images are reviewed by the surgeon. The capsule is passed by the patient into the toilet and disposed.

Capsule endoscopy is shown to have a positive diagnosis rate ranging from 45% to 76% compared to other methods such as push enteroscopy and MRI (Mylonaki et al. 2003). Hartmann et al., conducted a two center study comparing capsule endoscopy with enteroscopy and found that capsule endoscopy had high sensitivity and specificity to detect bleeding source in patients and hence recommended the use of capsule endoscopy as a routine work up for patients with GI bleeding (Hartmann et al. 2005). Pennazio et al., conducted a study on 100 patients with obscure GI bleeding and reported that the sensitivity and specificity of capsule endoscopy was 82%. It was also concluded that use of capsule endoscopy could shorten the time to diagnosis and lead to early treatment in patients with occult bleeding (Pennazio et al. 2004).

Although the capsule provides best noninvasive means to image the small intestine, there are limitations such as: the capsule does not allow therapy and is expensive. The

time taken to achieve complete imaging is long and cannot be used for diagnosis in emergencies (Lahat & Fidder 2014). Abnormalities in certain areas of the small intestine are missed due to the speed with which the capsule passes through the small intestine. The rapid passage of the capsule leads to blurred images. The images can be blurred due to poor preparation of the patient prior to capsule endoscopy (Viazis et al. 2004). Failure of the battery may lead to incomplete imaging of the small intestine. The failure of battery could be due to slow transit of the capsule through the small intestine. As most of the capsule endoscopes cannot record the position of where the image was captured, it is difficult for the surgeon to ascertain the location of the abnormality and thereby treat effectively. The presence of tumours in the small intestine leads to narrowing of the small intestine, the capsule can get stuck in the narrow area and cause obstruction of the intestine which may require surgical intervention (Pennazio et al. 2004). The volume of data produced is large and going through all the images is time consuming.

2.4.5 Endoscopic Ultrasound

Endoscopic ultrasound combines endoscopy and high resolution ultrasound (HRUS) to visualize the GI tract. The examination does not involve ionizing radiation. EUS is relatively inexpensive and readily accessible and causes no inconvenience to the patient. A HRUS linear array or a radial array transducer is placed on the tip of the endoscope. Radial array transducer is capable of producing 3D images of the GI tract similar to CT. linear array probes are mainly used for needle biopsies and also enable real time visualization of the GI tract along the axis of the endoscope. EUS is optimal for the evaluation of local extent of disease in rectal cancer. EUS examinations are quick when compared to CT and MRI, inexpensive and there is no risk of ionizing radiation or intravenous contrast agents. EUS has been shown through studies that, it can be used accurately for staging of rectal tumours (Tseng et al. 2002; Akahoshi & Chijiiwa 1997; Krakamp et al. 2004; Hünerbein et al. 2000).

EUS probes are in the frequency range of 12-20 MHz (Cysewska-Sobusiak et al. 2006). The high frequency of the probes provides greater resolution but have less tissue penetration. Nylund *et al.*, used probes ranging from 8 MHz – 12 MHz to image the GI wall in healthy individuals, the measured wall thickness ranged from 0.9 mm to 1.2 mm in areas ranging from jejunum to sigmoid colon (Nylund 2009). It was reported that GI

wall has normal stratification if five US layers are visible and there is a loss of stratification if one or more layers of the wall are missing.

Endorectal ultrasound had been used for assessment of patients after polypectomy of malignant rectal polyps in the colon (Haji et al. 2014). The sonographic image of the gastric wall appears as a five layered structure which is produced by the echoes and differences in the acoustic impedance of different layers (Figure 2.8). The first layer observed is the serosa. The interface echo is thicker than the serosa and extends into muscularis propria. The next echogenic layer corresponds to submucosa and the mucosa. Carcinoma is identified as a thickening of the layer and irregularities of the layers involved (Ødegaard et al. 2012). Kruskal *et al*., used EUS in 18 patients who had undergone polypectomy and were found to have carcinoma (Kruskal et al. 2000) and reported to be able to identify residual tumour with a sensitivity of 100%. However they were able to predict the stage of the tumour accurately in only 44% of the patients.

3D EUS has been found to be accurate in staging 78% of tumours in rectal cancers. In colonic tumours EUS showed 87%-94% T-staging accuracy and the treatment of patients based on EUs findings was accurate in 90% of the cases (Schizas et al. 2009). The EUS probes require proper coupling with the gastric wall and this is achieved by either inflating the bowel with water or by placing a balloon filled with water at the tip of the endoscope. It is important not to overinflate the balloon as it may cause compression of the rectal wall.

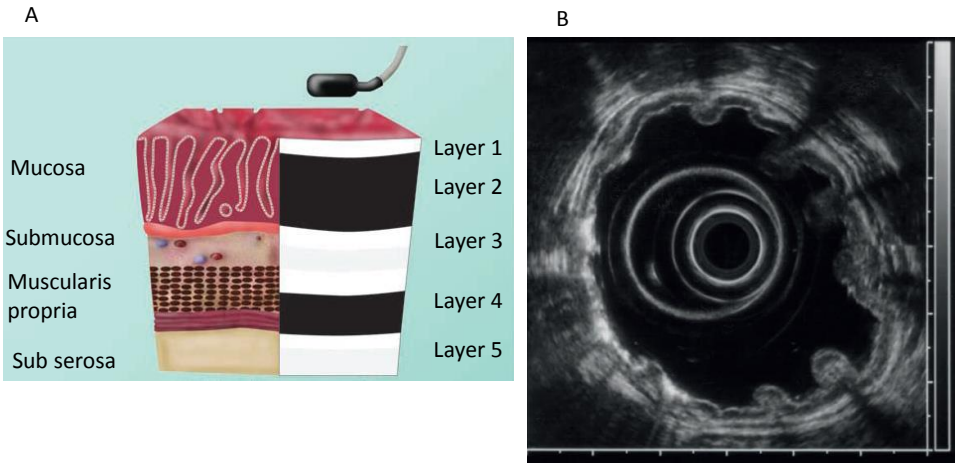

Figure 2.6: Correlation of Histological and ultrasonography images of the gastrointestinal wall. ***A****. The five layer structure of the GI wall and the corresponding images that can be visualized using an ultrasound probe. The dark and the white bands represent hyperechoic and hypoechoic regions respectively.* ***B.*** *Five layered structure of the GI wall visualized with a EUS probe (Ødegaard et al. 2012).*

Identification of sub-epithelial lesions is not possible with the current frequency of EUS probes and this can be overcome by using higher frequency probes (< 30 MHz). EUS is not suitable for evaluating very early rectal cancer. The intubation of EUS beyond the rectum is not possible due to limited oblique endoscopic view (Kongkam et al. 2014). EUS T staging following chemo radiation is found to be inaccurate. High frequency of the probes limits the depth of penetration it is not possible to depict the relationship between the edges of the tumour and the mesorectal fascia. Trapped air and stools will lead to shadowing in the images due to reverberation of ultrasound, which in turn may lead to poor images of the tumour (Kruskal et al. 2000).

Shadowing is also caused due to attenuation of ultrasound by the tumour which inhibits the ultrasound wave from passing through the tissue, beyond the tumour hence providing inadequate images. The need to have an acoustic coupling between the transducer and the tissue poses problems and movement of the patients also leads to image artifacts. The angle of the transducer also plays a critical role. If the transducer is not maintained at 90^0 angle to the tissue, diffraction artefacts in the image are seen that lead to over staging of the tumour. Refraction of the ultrasound beam due to oblique interfaces is also a cause of concern in EUS probes. EUS has limitations in staging of

colorectal cancer (Tsung et al. 2013). One of the ways to overcome this is by referring the patient to MRI.

2.4.5.1 Contrast enhanced US Imaging of GI wall

This method of imaging is mainly used as a follow up post treatment for colorectal cancer, to evaluate tumour induced angiogenesis (Ødegaard et al. 2012). Contrast enhanced imaging of the GI wall allows for imaging of the vascular regions of the bowel. The evaluation of vascularity is useful in characterising inflammation of the bowel and tissue properties. Ultrasound contrast agents are typically of size 1- 7 μm and mainly consist of microbubbles that are made up of phospholipid shells filled with gases.

The contrast agents are delivered to the patient intravenously. Contrast agents are known to improve the sensitivity and specificity of US imaging by increasing the blood flow signal intensity (Forsberg et al. 2002). This increase in the signal intensity leads to enhanced signal to noise ratios by up to 30 dB. When imaged using a high frequency US probe the contrast agents produce a non-linear, harmonic response that can be used to delineate the tissue signal using contrast harmonics. The frequency of the probes used for imaging of the GI tract is typically in the range of 7.5 MHz (Nylund 2009). The intestinal wall is observed using US Doppler after 30 s of injecting contrast agents. The RF data comprising signal intensity is obtained and analyzed. In the region of interest average intensity of the signal along the time axis is plotted. The pattern of circulation is different in malignancies as compared to inflammation and this is evaluated both qualitatively and quantitatively (Badea, Socaciu, et al. 2010). The phase inversion technique of imaging enables identification of polyps by creating a good contrast between the lumen and the mucosa (Badea, Ciobanu, et al. 2010).

2.4.6 Magnetic Resonance Imaging

Magnetic resonance imaging (MRI) is non-invasive compared to colonoscopy and EUS. MRI is widely used for diagnosis and staging in patients with colorectal tumours. MRI is capable of visualizing the intestinal wall and the surrounding pelvic anatomy. The MRI is used for detecting endoluminal polyps of size greater than 10 mm. MRI enables T-staging and nodal invasion and aids in preoperative decision making. MRI provides excellent soft tissue contrast. Initially MR imaging for colon cancer was performed with a body coil. The images obtained with the conventional body coil had poor resolution

and it was difficult to differentiate between the layers of the rectal wall (Klessen et al. 2007) . The introduction of endoluminal coils provided greater image resolution and it was possible to evaluate the layers of the rectal wall in greater detail. Thus, improving the consistency of T-staging with an accuracy ranging from 71%-91% (Pappalardo et al. 2000). Recently, MR imaging with iron oxide contrast agents has shown improved efficacy of the method for staging of nodal cancers.

The patient is exposed to radiation between 3-6 mSv in a single examination and multiple examination may increase the risk of radiation exposure to patients (Mettler et al. 2008). MRI is incapable of distinguishing pseudopolyps, adenomatous polyps and adenocarcinomas. In cases of rectal cancer MRI has limited field of view and only allows evaluation of early stages of rectal cancer as imaging of the surrounding pelvic anatomy is not possible (Klessen et al. 2007). Most staging failures with MRI occurs due to difficulty in differentiating between T2 and T3 stages and over staging is a cause of concern (Beets-Tan & Beets 2004). Therefore most patients after an MRI undergo colonoscopy for histological diagnosis (Hall 2007). The spatial resolution of MRI is inferior to that of colonoscopy which hampers the visualization of polyps less than 5 mm in size. Presence of air in the colon due to poor preparation and spillage of the contrast medium into the small intestine leads to poor images of the colon. MRI is not very cost effective when compared to colonoscopy.

2.4.7 Computed Tomography

Abdominal computed tomography (CT) is an important imaging modality for staging and planning surgery for colon cancer. CT usually takes 10 seconds for a scan and is easily accessible. CT is capable of demonstrating regional extension of tumour, size of the tumour, adenopathy and spread of cancer to distal organs. Complications of CRC such as obstruction, luminal narrowing, perforation and fistula can be visualized with CT. CT is mostly used for preoperative assessment of patients for identifying recurrences, evaluating postoperative anatomy and to confirm absence of new lesions.

However, CT has its limitations. Its accuracy for determining the presence of nodal involvement is low, with estimates of accuracy ranging from 23-73% (Horton et al. 2000). The accuracy of staging in the liver is 78%, hepatic involvement is 71%, and the overall accuracy of staging is 48-74% (Kinkel et al. 2002). Limitations of CT include accurate determination of the depth of tumour invasion through the gut wall and inability to identify nodes that may contain tumour. The other main disadvantage of CT

is the risk of radiation involved. The patient undergoing a CT is exposed to 15 mSv, of radiation dose in a single examination and multiple examinations poses a considerable risk of radiation damage to the patients.

2.5 Conclusion

The early detection of CRC is the endpoint of interest in this thesis. CRC ranks among the three most common cancers and cancer related deaths in the western world. In summary this chapter reviewed epidemiology, anatomy and physiology of small and large intestines and imaging modalities used for diagnosing CRC. The knowledge of molecular changes that accompany pre-malignant tumour initiation is important, as the molecular changes dictate the changes in tissue architecture at a microscopic level. This knowledge aided in development of ultrasound tissue characterization techniques to differentiate between normal and precancerous tissue. Understanding of the current trends in diagnosing CRC is crucial to this thesis, as this knowledge is required for devising methods using µUS to detect early tissue dysplasia. The next chapter describes the fundamentals of high resolution ultrasound imaging and its role in clinical diagnostics.

2.6 References

Badea, R., Ciobanu , L., (2010) "Contrast ultrasonography--a necessary procedure for a better characterization of digestive tract pathology" *Medical ultrasonography*, 12(1), 73–80.

Badea, R., Socaciu, M. (2010) "Contrast-enhanced ultrasonography (CEUS) for the evaluation of the inflammation of the digestive tract wall" *Journal of gastrointestinal and liver diseases : JGLD*, 19(4), 439–44.

Beets-Tan, R. & Beets, G. (2004) "Rectal Cancer: Review with Emphasis on MR Imaging" *Radiology*, (6), 335–346.

Cappell, M.S. (2005) "The pathophysiology, clinical presentation, and diagnosis of colon cancer and adenomatous polyps" *The Medical clinics of North America*, 89(1), 1–42, vii.

Cysewska-Sobusiak, A., Skrzywane, P., Sowier, A. (2006) "Utilization of Miniprobes in Modern Endoscopic Ultrasonography" *IEEE Sensors Journal*, 6(5), 1323–1330.

Forsberg, F., Rawool, N., Merton, D.A., Liu, J.B., Goldberg, B.B. (2002) "Contrast enhanced vascular three-dimensional ultrasound imaging." *Ultrasonics*, 40(1-8), 117–22.

Haji, A., Adams, K., Bjarnason, I., & Papagrigoriadis, S. (2014) "High-Frequency Mini Probe Ultrasound Before Endoscopic Resection of Colorectal Polyps–Is It Useful?." *Diseases of the Colon & Rectum*, *57*(3), 378-382.

Hall, N. (2007) "Colorectal cancer: features and investigation." *Medicine*, *35*(6), 302-305.

Hartmann, D., Schmidt, H., Bolz, G., Schilling, D., Kinzel, F., Eickhoff, A., & Riemann, J. F. (2005) "A prospective two-center study comparing wireless capsule endoscopy with intraoperative enteroscopy in patients with obscure GI bleeding." *Gastrointestinal endoscopy*, *61*(7), 826-832.

Horton, K., Abrams, R. & Fishman, E., (2000) "Spiral CT of Colon Cancer: Imaging Features and Role in Management" *Radiographics*, 21287, pp.419–430.

Hünerbein, M., Totkas, S., Ghadimi, B. M., & Schlag, P. M. (2000) "Preoperative evaluation of colorectal neoplasms by colonoscopic miniprobe ultrasonography." *Annals of surgery*, *232*(1), 46.

Kinkel, K., Lu, Y., Both, M., Warren, R. S., & Thoeni, R. F. (2002) "Detection of hepatic metastases from cancers of the gastrointestinal tract by using noninvasive imaging methods (US, CT, MR imaging, PET): a meta-analysis" *Radiology*, *224*(3), 748-756.

Klessen, C., Rogalla, P., Taupitz, M. (2007) "Local staging of rectal cancer: the current role of MRI" *European radiology*, 17(2), 379–89.

Kongkam, P., Linlawan, S., Aniwan, S., Lakananurak, N., Khemnark, S., Sahakitrungruang, C., & Rerknimitr, R. (2014) "Forward-viewing radial-array echoendoscope for staging of colon cancer beyond the rectum." *World journal of gastroenterology: WJG*, *20*(10), 2681.

Krakamp, B., M. Parusel, M. Weber, C. Brincker, LJ Tseng, and YTFN Jao. (2004) "Experience with ultrasound miniprobes in the staging of colorectal cancer. Authors' reply." *Endoscopy* 36, no. 4 (2004): 373-374.

Kruskal, J. B., Kane, R. A., Sentovich, S. M., & Longmaid, H. E. (1997) "Pitfalls and sources of error in staging rectal cancer with endorectal US".*Radiographics*, *17*(3), 609-626.

Kwee R.M., Kwee T.C. (2007) "Imaging in local staging of gastric cancer: a systematic review" *Journal of clinical oncology : official journal of the American Society of Clinical Oncology*, 25(15), pp.2107–16.

Lahat, A., & Fidder, H. H. (2014) "Bowel Imaging in IBD Patients: Review of the Literature and Current Recommendations." *J Gastroint Dig Syst*, *4*(189), 2.

Leslie, A., Carey, F. A., Pratt, N. R., & Steele, R. J. C. (2002) "The colorectal adenoma–carcinoma sequence." *British Journal of Surgery*, *89*(7), 845-860.

Mahfouz, M., To, G., & Kuhn, M. (2011). "*The future of ultra wideband systems in medicine: orthopedic surgical navigation*." INTECH Open Access Publisher.

McCartney, B. M., & Näthke, I. S. (2008) "Cell regulation by the Apc protein: Apc as master regulator of epithelia." *Current opinion in cell biology*, *20*(2), 186-193.

Mettler, Jr, F. A., Huda, W., Yoshizumi, T. T., & Mahesh, M. (2008) "Effective Doses in Radiology and Diagnostic Nuclear Medicine: A Catalog 1." *Radiology*,*248*(1), 254-263.

Mylonaki, M., Fritscher-Ravens, A., & Swain, P. (2003) "Wireless capsule endoscopy: a comparison with push enteroscopy in patients with gastroscopy and colonoscopy negative gastrointestinal bleeding." *Gut*, *52*(8), 1122-1126.

Neumann, H., Fry, L. C., & Neurath, M. F. (2013) "Review article on current applications and future concepts of capsule endoscopy." *Digestion*, *87*(2), 91-99.

Nicholson, F. B., Barro, J. L., Atkin, W., Lilford, R., Patnick, J., Williams, C. B., ... & Kamm, M. A. (2005) "Review article: population screening for colorectal cancer. "*Alimentary pharmacology & therapeutics*, *22*(11-12),1069-1077.

Nylund, K., Ødegaard, S., Hausken, T., Folvik, G., Lied, G. A., Viola, I., & Gilja, O. H. (2009) "Sonography of the small intestine." *World journal of gastroenterology: WJG*, *15*(11), 1319.

Ødegaard, S., Nesje, L. B., Lærum, O. D., & Kimmey, M. B. (2012) "High-frequency ultrasonographic imaging of the gastrointestinal wall." *Expert review of medical devices*, *9*(3), 263-273.

Pappalardo, G., Polettini, E., Frattaroli, F. M., Casciani, E., D'orta, C., D'amato, M., & Gualdi, G. F. (2000) "Magnetic resonance colonography versus conventional colonoscopy for the detection of colonic endoluminal lesions." *Gastroenterology*, *119*(2), 300-304.

Pennazio, M., Santucci, R., Rondonotti, E., Abbiati, C., Beccari, G., Rossini, F. P., & De Franchis, R. (2004) "Outcome of patients with obscure gastrointestinal bleeding after capsule endoscopy: report of 100 consecutive cases." *Gastroenterology*, *126*(3), 643-653.

Potten, C. S., Booth, C., & Pritchard, D. M. (1997) "The intestinal epithelial stem cell: the mucosal governor." *International journal of experimental pathology*, *78*(4), 219.

Rockey, D. C., Paulson, E., Niedzwiecki, D. E., Davis, W., Bosworth, H. B., Sanders, L., & Halvorsen, R. (2005) "Analysis of air contrast barium enema, computed tomographic colonography, and colonoscopy: prospective comparison." *The Lancet*, *365*(9456), 305-311.

Ransohoff, D. F., & Sandler, R. S. (2002) "Screening for colorectal cancer." *New England Journal of Medicine*, *346*(1), 40-44.

Schizas, A. M., Williams, A. B., & Meenan, J. (2009) "Endosonographic staging of lower intestinal malignancy." *Best Practice & Research Clinical Gastroenterology*, *23*(5), 663-670.

Specian, R. D., & Oliver, M. G. (1991) "Functional biology of intestinal goblet cells." *American Journal of Physiology-Cell Physiology*, *260*(2), C183-C193.

Steele, R. J., McClements, P. L., Libby, G., Black, R., Morton, C., Birrell, J., & Fraser, C. G. (2009) "Results from the first three rounds of the Scottish demonstration pilot of FOBT screening for colorectal cancer." *Gut*, *58*(4), 530-535.

Su, L. K., Kinzler, K. W., Vogelstein, B., Preisinger, A. C., Moser, A. R., Luongo, C., & Dove, W. F. (1992) "Multiple intestinal neoplasia caused by a mutation in the murine homolog of the APC gene." *Science*, *256*(5057), 668-670.

De Leon, M. P., & Di Gregorio, C. (2001) "Pathology of colorectal cancer." *Digestive and Liver Disease*, *33*(4), 372-388.

Tseng, L. J., Jao, Y. T., & Mo, L. R. (2002) "Preoperative staging of colorectal cancer with a balloon-sheathed miniprobe." *Endoscopy*, *34*(7), 564-568.

Tsung, P. C., Park, J. H., Kim, Y. S., Kim, S. Y., Park, W. W., Kim, H. T., & Moon, J. S. (2013) "Miniprobe endoscopic ultrasonography has limitations in determining the T stage in early colorectal cancer." *Gut and liver*, *7*(2), 163.

Viazis, N., Sgouros S., Papaxoinis, K., Vlachogiannakos, J., Bergele, C., Sklavos, P., Panani, A., and Avgerinos, A., (2004) "Bowel preparation increases the diagnostic yield of capsule endoscopy: a prospective, randomized, controlled study." *Gastrointestinal endoscopy* 60, no. 4 (2004): 534-538.

Chapter 3: Theory of Ultrasound

"The multitude of books is making us ignorant"

Voltaire

3.1 Introduction

High resolution ultrasound has become a well-established medical imaging modality over the past 20 years. As the aim of this thesis is to determine the use of high resolution μUS to image and measure tissue alterations in precancerous tissue and develop novel matching layers for high frequency transducer applications. It requires understanding of the principles governing ultrasound interaction in tissue. This chapter summaries physical and technical principle involved in fabrication and applications of high resolution μUS transducers for medical imaging and quantitative tissue characterisation.

- In Section 3.2, concepts of ultrasound imaging, Interaction of ultrasound waves with tissue and key concepts of acoustic impedance, attenuation and backscatter coefficient are explained.
- In Sections 3.3 - 3.4, a literature review on high resolution ultrasound imaging and quantitative tissue characterisation is presented.
- In Sections 3.5 - 3.6, the design considerations for high resolutions micro-ultrasound transducers, specific components of the transducer, with an emphasis on the theory of quarter wavelength matching layers are presented.

3.2 Ultrasound Imaging

Ultrasound imaging depends on the speed of sound and acoustic impedance of the material. These variables are influenced by the elastic moduli of the material. Most ultrasound imaging is based on this method of imaging commonly called the pulse-echo mode. This technique was first used clinically by Wild and Reid in 1952 (Dempsey 2004) to produce 2D images of breast tumours, by scanning a single element transducer at right angles to its propagating beam. Ultrasound waves propagated into the tissue are scattered, the scattered sound wave is recorded and, with the knowledge of the speed of

sound, the distance, *x*, to the reflecting structure can be determined by using Equation *(3.1)*:

$$x = \frac{ct}{2} \qquad (3.1)$$

Ultrasound imaging is widely used for imaging of internal structures of the human body. Commonly used modes of ultrasound imaging are explained below. The design and operation of slow and high-speed high-resolution ultrasound (HRUS) scanning system will be explained in Chapter 6. The technique of pulse-echo imaging from tissue is illustrated in Figure 3.1.

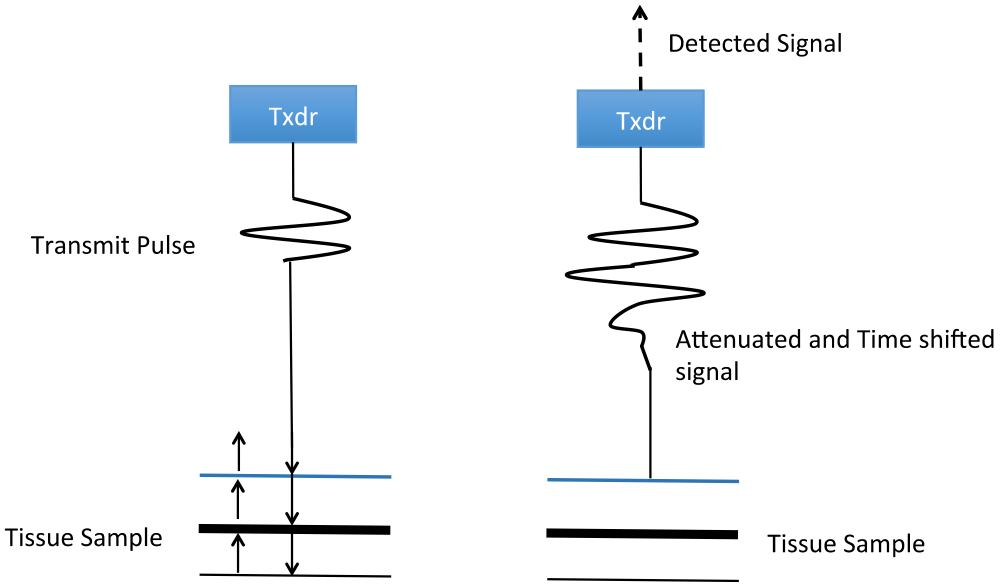

Figure 3.1: Basic ultrasound pulse echo imaging technique, an ultrasound signal is transmitted into the tissue and the reflected ultrasound wave that is time shifted and attenuated is received by the same transducer, the time and the amplitude of the signal corresponds to the position and the strength of the reflector.

3.2.1 A-Scan

Amplitude modulation scans, also known as A-scans results from the measurement at a single point by an ultrasound transducer and is the simplest representation of the waveform data. The two fundamental parameters of an A-scan are the amplitude and the position of the signal in time with respect to the transit pulse. A-scans are commonly used in NDT for detecting flaws in metal pipes and thickness measurements. A-scan biometry, is routinely used in ophthalmology for detection of thickness of ocular structures along the visual axis (Lizzi & Coleman 2004). In an A-scan, signals received

from the structures close to the transducer arrive earlier than from the structures farther away from the transducer.

3.2.2 B-Scan

Ultrasound waves propagated into the tissue are reflected off internal structures. With the knowledge of the speed of sound, the distance of the reflecting structure can be measured. This basic technique of imaging was first applied in oceanographic and NDT applications. Wild and Reid in 1952 first reported the use of this technique clinically.

B-scans imaging systems can be classified into two types: contact scanners, in which the transducers are in direct contact with the specimen, e.g. for skin, foetal imaging, etc., and non-contact scanners, in which the specimen is contained and a liquid coupling medium is used to conduct the sound from the transducer to the specimen. Small mismatches in the sound velocity between the specimen and the coupling medium (water / saline) eliminate the problem of beam distortion and enhances transmission of the beam though the specimen. More emphasis is laid on non-contact B-scan systems in this thesis.

B-scan means brightness mode scan; it represents a cross sectional 2D slice from a tissue within a volume, with the scan depth away from the transducer (Gan 2012). B-scan images are formed by scanning narrow a focused acoustic beam through a plane and the transverse dimension is obtained by mechanically moving the transducer in the case of a single element or electronically in the case of an array (Havlice & Taenzer 1979). The process of moving the transducer across the specimen is continued until the region of interest (ROI) is completely covered. A block diagram of a research platform based B-scan system is illustrated in Figure 3.2; note that this is not a clinical system.

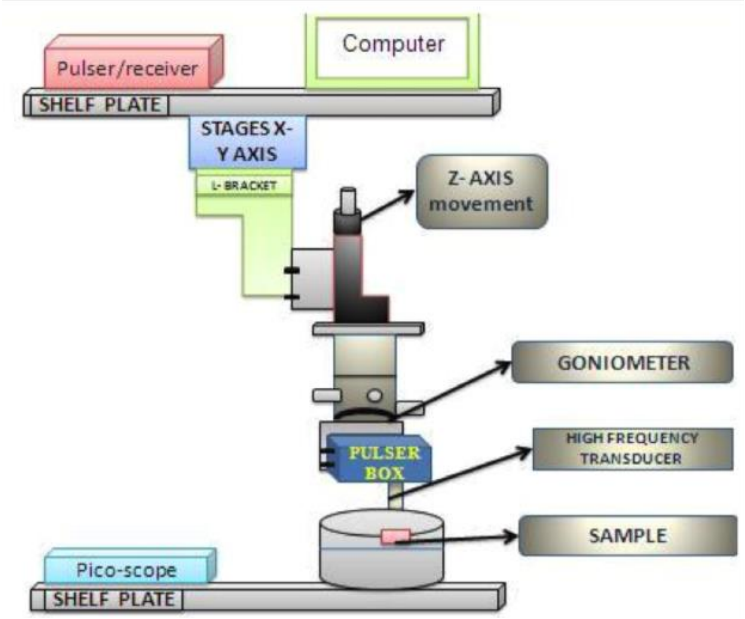

Figure 3.2: Illustration of a B-scan system setup. The transducer is mounted on to an x-y stage which enables the transducer to move in user defined steps, to collect A-scans at various points across the tissue samples, which are presented in the form of a 2D image. The scan step sizes form the axes of the image with the scan depth away from the transducer.

An electronic pulser excites the transducer, resulting in a short burst of ultrasound being produced and propagated into the tissue. The signals reflected from the tissue along the acoustic beam path are received by the transducer and converted to electronic signals (RF) and recorded. Envelope detection of the RF signal is performed using a Hilbert transform, which demodulates the signal. The demodulated signal is logarithmically compressed, which reduces its dynamic range so that both high and low intensity echoes are within the range of 60 dB, as this is required to display the subtle features of the tissue. B-scan images can be displayed in either grey scale or as RGB images. In a grey scale, there are usually 10 or more distinct brightness levels. The weaker echoes are displayed at lower brightness and the strongest echoes are displayed brightest. In RGB format the strongest echoes are represented as red and the weaker echoes at progressively darker shades of colour between green and blue.

3D images can be reconstructed by stitching the B-scans together using an image processing software (e.g. MatLab, ImageJ, Volocity, etc.). 3D images resemble the images obtained with microscopy and look more familiar and may be more easily interpretable by the clinicians than a simple B-scan image. The process of image formation from A-scans is illustrated in Figure 3.3.

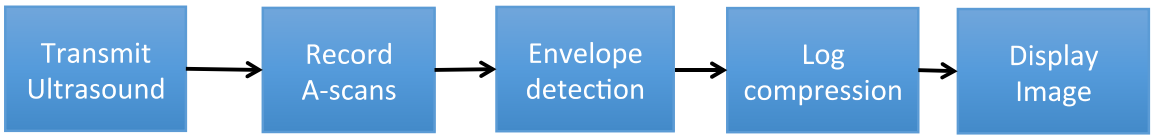

Figure 3.3: Block diagram illustrating B-scan image formation sequentially from left to right.

To improve the quality of a B-scan, the RF data is pre-processed before being displayed as an image. The most common of pre-processing involves logarithmic compression and time-gain compensation. Logarithmic compression of the ultrasound data is used to improve the image quality. Reflections from tissue boundaries are much greater than those caused by diffuse scattering and hence amplification of the returned signals is necessary which is achieved by logarithmic compression. Over-amplification of the returned signal leads to degradation of the image. Ultrasound beam intensity decreases with depth, causing distortion in images. To compensate for the loss of ultrasound beam intensity with respect to depth, time gain compensation can be applied.

Modern clinical ultrasound imaging systems possess electronics designed to detect Doppler shifted frequencies to identify the flow of blood or movement of organs. Recent developments include 3D imaging, harmonic imaging, elastography and contrast enhanced imaging (Shung 2009).

3.3 Interactions of Ultrasound with Tissue

Soft tissue is formed by cellular components of different shapes, spatial organisation and mechanical properties that are unique to the tissue type. In tissue, ultrasound waves are transmitted by propagation through molecular collision and vibration. The propagation of ultrasound through a material is dependent on the mechanical properties of that material. Tissues are normally modelled as liquids (Szabo 2004). The effects that occur when ultrasound travels through the tissue are: reflection, refraction, and absorption.

3.3.1 Reflection of Ultrasound

Reflection of ultrasound plays an important role in imaging. Ultrasound waves are reflected at the tissue boundaries when there is a difference in *Z* between the material and the coupling medium. These positions are called acoustic boundaries. The difference in *Z* is known as the impedance mismatch. A larger percentage of energy is reflected at the interface boundary, when the impedance mismatch is larger. If the *Z* of the materials on both sides of the boundary is known, the reflected energy of the ultrasound wave for perpendicular incidence can be calculated using Equation (*3.2*), in which the energy reflection coefficient, R_c, is the proportion of ultrasound energy reflected at the interface between two media with differing acoustic impedance.

$$R_c = \left(\frac{Z_1 - Z_2}{Z_1 + Z_2}\right)^2 \qquad (3.2)$$

Z_1 and Z_2 are the acoustic impedances of the two materials. The transmission coefficient, T_c, can be calculated using Equation *(3.3)* if the reflection coefficient is known. T_c, is a measure of ultrasound energy that has not been reflected by the tissue.

$$T_c = 1 - R_c = \frac{4Z_1Z_2}{(Z_1 + Z_2)^2} \qquad (3.3)$$

Specular reflections (Figure 3.4A) occur when the boundary is smooth and larger than the beam dimensions, while non-specular reflections occur when the interface is smaller than the beam. The intensity of the echo due to specular reflections depends on the angle of incidence and the difference in the acoustic impedance values of the differing media. The wavelength for most tissue structures is considerably smaller than the interface and therefore best reflection occurs when the transducer is at 90^0 to the interface.

Diffusive reflection occurs when the reflecting interface is irregular in shape and the dimensions are smaller than the ultrasound beam diameter. The dimension of the interface should be about one wavelength or less for the necessary scattering to happen. In high resolution imaging the wavelength is in the order of microns and within the

tissue there are many structures that have dimensions of a few microns, therefore scattered ultrasound provides information about the cellular architecture of the tissue. Scattering is frequency dependent and increases as the frequency is increased. Diffusive scattering or Rayleigh scattering intensity varies as the fourth power of the frequency. Diffusive scattering is independent of the angle of incidence of the ultrasound beam and it comprises of low amplitude reflections in many directions. Only a small amount of the incident energy is reflected back along the beam path of the transducer. Tissue is modelled as an aggregate of small sub wavelength point scatterers and this particular kind of scattering is important in characterisation of tissue. Doppler methods of blood flow measurement are dependent on scattering from small unresolved blood cells.

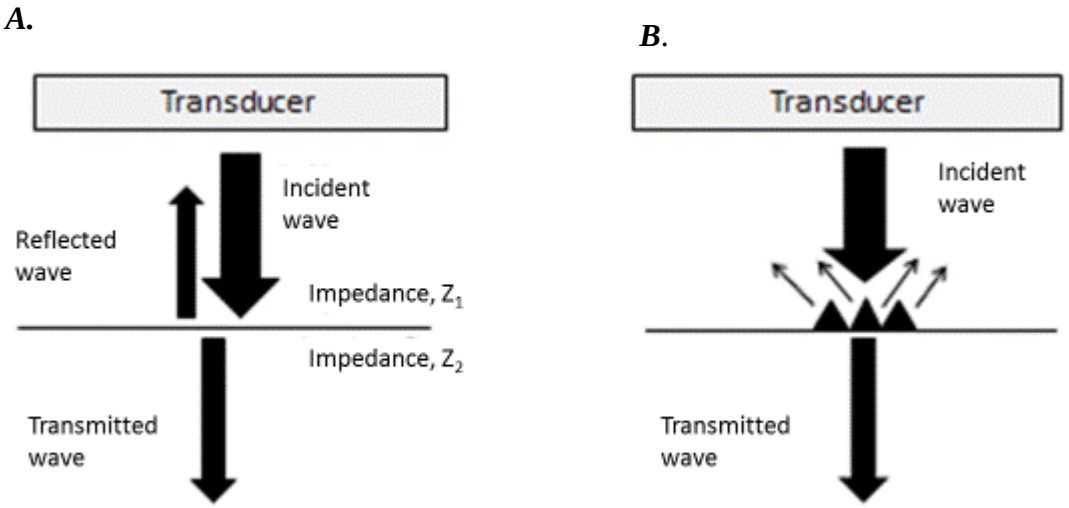

Figure 3.4: A. Specular reflection, where the sound wave is reflected from a smooth boundary, in a straight line. B. Diffusive reflection, due to cellular structures of varying dimensions in tissue resulting in uneven surfaces and reflections returning to the transducer from different directions.

3.3.2 Acoustic Impedance

If the acoustic pressure, *p*, and the particle velocity, *v*, are in phase then the specific acoustic impedance of the medium, *Z*, will be the ratio of *p* and *v*, which is numerically equal to the product of density, ρ, of the material and the speed of compressional wave in the material (Leighton 2010) and is given as:

$$z = \frac{p}{v} = \rho c \qquad (3.4)$$

The unit of acoustic impedance, *Z*, is Rayl (kg m^{-2} s^{-1}). The reflection of ultrasound at the interface between soft tissue and water is due to the mismatch in the acoustic impedance. Soft tissue have an acoustic impedance of 1.60 MRayl, when compared to fat which has an acoustic impedance of 1.38 MRayl and bone has an acoustic impedance of 6.36 MRayl (Szabo 2004). The interfaces wherein *Z* changes are called acoustic boundaries. In practise the differences in acoustic impedance means that the ultrasound beam suffers from losses in reflection when it propagates from one tissue surface to another, given that the angle of incidence is not at very large angles. This difference in *Z* is the main principle involved in pulse echo imaging. Table – 3.1 summaries the acoustic impedance, speed of sound and density of biological specimens.

Table 3.1: Density, speed of sound and acoustic impedance of different tissues. Speed of sound will vary with temperature in most cases.(Azhari 2010)

Tissue Material	**Density (g/cm^3)**	**Speed of Sound (m/s)**	**Z (MRayl)**
Water	1	1480	1.48
Blood	1.055	1575	1.66
Muscle	1.065	1575	1.68
Liver	1.06	1590	1.69
Skin	1.15	1730	1.99
Bone	1.9	2800	7.75
Fat	0.95	1450	1.38
Soft Tissue	1.05	1540	1.55

3.3.3 Attenuation

Ultrasound attenuation is the loss of acoustic energy as it travels through the medium, and is caused by the scattering and tissue absorption of the incident ultrasound beam. At low- MHz frequencies, scattering accounts to 10-15% of attenuation and absorption for the rest (Bamber et al. 1977). Absorption of the ultrasound beam is due to the viscous forces between the particles in motion that cause a lag between the particle pressure and velocity, resulting in energy loss. Absorption of ultrasound by soft tissues causes heating, and limits the penetration of the ultrasound beam through the body. Tissues with high water content show lower absorption when compared to tissues such as tendons and muscles. The attenuation coefficient term α, is defined as the ratio of the amplitude reflected from the tissue to the amplitude reflected from a perfect reflector,

e.g. quartz and is usually expressed on a logarithmic scale. α is expressed in dB cm^{-1} MHz^{-1}. Attenuation has a power law dependence on frequency (Thijssen 1987). Attenuation can be measured using either time domain or frequency domain methods. The spectral shift method and spectral difference method are employed in frequency domain. These methods neglect refraction and diffraction of the ultrasound beam through the tissue. Overall attenuation is characterised by an exponential decrease in the pressure amplitude, *p*, along the traveling distance of the wave, *x*. (Cobbold 2007).

$$p = p_0 e^{-\mu_A x} \qquad (3.5)$$

μ_A is the amplitude attenuation factor in Np-cm^{-1}

α, is dependent on frequency, temperature and pressure. The frequency dependent attenuation coefficient can be computed using the formula:

$$\alpha = \alpha_0 f^n \ \ dB\ cm^{-1}\ MHz^{-n} \qquad (3.6)$$

f, is the frequency of the ultrasound, n is an empirical constant for different materials, e.g. n = 2 for water and 1< n < 2 for biological tissues (Cobbold 2007). In this thesis the attenuation coefficients were measured using Equation *(3.7)*.

$$\alpha = \frac{20}{2l} log\left(\frac{A}{A_0}\right) \ \ dB\ cm^{-1} \qquad (3.7)$$

A is the reflected amplitude from the tissue and A_0 is the amplitude from a reflector, *l* is the travel distance of the ultrasound beam, The formula in *(3.7)* is valid at the centre frequency of the ultrasound transducer in pulse-echo mode.

Attenuation is important clinically as it affects the depth of penetration of an ultrasound beam into the tissue. Attenuation measurement can be helpful in separating various forms of diseased and normal tissue. This has been demonstrated in determining the various causes of enlargement of spleen and differentiating liver diseases and cell death (e.g. Ophir et al. 1984; Calderon et al. 1976; Oelze & O'Brien 2002; Kuc 1980; Tittmann et al. 2013; Bamber & Hill 1981).

At high frequency (>20 MHz) the contributions of absorption and scattering to attenuation have not been clearly understood. However in the low frequency range

(1-15 MHz) absorption has been shown to be a dominant mechanism (Parker 1988; Mimbs et al. 1980). Measuring attenuation coefficients *in vivo* require, comparison of the pulse echo signals through varying depths of the tissue, but the signals being compared at various depths will not only vary due to attenuation but also due to the changes in backscatter at various depths (Guittet et al. 1999). For this reason tissue is assumed to be a homogenous continuum. Attenuation governs the choice of frequency of the transducer and instrument settings such as time gain compensation (TGC) and system gain levels in clinical diagnostic instruments.

3.3.4 Backscatter Coefficient (BSC)

Another parameter that has been successfully used to characterise different aspects of the microstructure of the tissue is backscatter coefficient (BSC). BSC is defined as time-averaged scattered intensity of ultrasound from the tissue per unit solid angle per unit volume (Sr^{-1} mm^{-1}). Fundamental properties of the tissue such as size, shape, microstructure, and mismatch of impedance can be estimated by measuring the BSC (Mamou 2013). BSC is independent of operator and is a function of only tissue properties.

Various methods to compute BSC from single element transducers can be found in the literature (Table 3.2). Sigelmann and Reid were the first to have developed a method to measure BSC. They estimated BSC from a volume of randomly distributed scatters using a planar transducer. They measured the volumetric backscatter coefficient by calculating the ratio between the gated backscattered signals from the specimen and a rigid reflector (Sigelmann & Reid 1973). Insana et.al, used equations derived by the first order Born approximation to estimate the BSC from weakly scattering media and a planar reflector. They used a Hanning window approach to gate the RF data.

Table 3.2: Equations of BSC for single element ultrasound transducers.

	BSC (σ_b (ω))	Reference
1.	$\frac{4\alpha\varepsilon}{\Omega e^{-4\alpha r}[e^{\alpha c\tau} - e^{-\alpha c\tau}]}$	(Sigelmann & Reid 1973)
2.	$\frac{R_q}{2\pi(1-\cos\theta_T)} * \frac{\int_{Z_1}^{Z_2}\lvert V_{tissue}{}^2\rvert}{\int_{Z_1}^{Z_2}\lvert V_{Quartz}{}^2\rvert}$	(D'Astous & Foster, 1986)
3.	$\frac{0.36 * \gamma^2 R^2}{A_0 \Delta Z} \lvert S(\omega)\rvert^2$	(Insana & Hall 1990)
4.	$\frac{W_r}{W_i}\frac{2\eta R^2}{\beta^2 A}\left[\frac{\lambda_0}{\lambda}\right]^2 \frac{2\alpha}{e^{-2\alpha Z_1}[1 - e^{\alpha c\tau}]}$	(Nicholas et al. 1982)

The various approaches listed for calculation of BSC from single element transducers can explain some of the variations in measurements of BSC observed on tissue structures and reference phantoms. Due to the various methods of measuring BSCs there is a considerable lack of agreement between laboratories for estimation of BSC. In order to estimate the sources of error, BSC measurements from tissue mimicking phantoms embedded glass beads as scatterers were conducted between two laboratories. The aim of this study was to compare the theoretical model of scattering predicted by Faran (Faran 1951) to estimate BSCs in the frequency range of 1 – 12 MHz. BSC was measured using two different planar-reflector techniques. The results demonstrated good agreement between the two laboratories (Anderson et al. 2010). The inter-laboratory studies demonstrated that attenuation and diffraction correction have to be implemented for the accurate estimation of BSC.

The method described by Foster et al., has been used to compute BSC in this thesis (Foster et al. 1984; D'Astous & Foster 1986). Equation *(3.8)* uses a plane wave approximation at the focus to compute BSC. This approach is similar to the technique described by Nicholas et al.,(Nicholas 1982) except that a focused geometry is used.

$$\mu_{BSC} = \frac{R_q}{2\pi(1-\cos\theta_T)} * \frac{\int_{Z_1}^{Z_2}\lvert V_{tissue}{}^2\rvert}{\int_{Z_1}^{Z_2}\lvert V_{Quartz}{}^2\rvert}\frac{2\alpha}{e^{-2\alpha Z_1} - e^{-2\alpha Z_2}} \qquad (3.8)$$

In Equation *(3.13)*, R_q, is the intensity reflectance of the water-quartz interface, θ_T is the half angle subtended by the transducer at its focus. V_{tissue}, is the measured backscattered

and attenuation corrected signal from tissue, $V_{Quartz,}$ is the reference signal obtained from quartz surface and z_1 and z_2 are the axial length of the gated signal.

BSC from organs and tissues such as liver, prostrate, spleen, pancreas and heart (Nicholas 1982; Mimbs et al. 1980; Wagner et al. 1995; Lizzi et al. 2003; Bamber et al. 1977; Mamou 2005) have been studied by researchers in the past.

Mimbs et al., used BSC's to differentiate between normal heart and heart tissue with ischemic injury in canine models. It was observed that BSC was sensitive to concentration of collagen and the organisational state of the collagen content (Mimbs et al. 1980). They reported that there was a significant increase in BSC in ischemic heart due to the increase in the collagen content. Nicholas et al., reported BSC measurements from excised human spleen, liver and brain over a frequency range of 0.7 – 7 MHz noting that the scattering sites in these tissues was in the order of 20 – 40 μm (Nicholas 1982). Foster and D'Astous studied BSC measurements from three breast tumour tissues. They specifically reported BSC measurements from fat, parenchymal and infiltrating duct carcinoma. and reported that BSC measurements from fat were similar to that of tumour tissue at low frequencies but they could differentiate between fat and tumour site at higher frequencies (D'Astous & Foster 1986). Fat, which is macroscopically homogenous, displays low velocity, low attenuation and low scattering. Therefore using higher frequencies provided better contrast between breast masses and fat. The various methods of computing BSC have been tested by researchers (Wear & Stiles 2005) by testing BSC on reference phantoms with various scatterers.

BSC from diseased and normal, murine small intestine were measured during this project. BSC is a fundamental material characteristic that can be used to characterise tissues and monitor changes in the tissue architecture due to diseases. Various researchers have hypothesised that cells and nuclei maybe the dominant source of scattering in tissues and that the strength of scattering is related to acoustical properties of the tissue.

3.4 High Resolution Ultrasound (HRUS) Imaging

Medical ultrasound imaging uses pulse-echo techniques to form images of soft tissue structures. Imaging techniques should be capable of imaging tissues with good resolution to differentiate sub-layers of the tissue and to identify and isolate pathologies within the tissue. This is especially important for detecting early stages of colon cancer, where an accurate determination of lesion is important. Conventionally, the frequency

range from 1 - 15 MHz has been used for clinical imaging providing a minimum resolution of 300 µm. Ultrasound imaging is non-invasive diagnostic tool and real time B-mode scanners are used in various clinical applications. In comparison to clinical ultrasound imaging, high resolution ultrasound imaging (HRUS) is more sensitive to cell structure and changes in spatial distribution of cells in the given specimen (Tunis et al. 2005). HRUS imaging has less penetration depth than clinical ultrasound but greater image resolution, which makes it more sensitive to cell structure. Non-invasive *ex vivo* imaging using HRUS is performed by acquiring echo signals in a 2D plane along the surface of the specimen. Spherically focussed single-element transducer is mechanically scanned along the lateral direction and echo measurements are recorded. Water or saline is used as a coupling medium.

The pulse-echo method offers non-invasive imaging techniques on a microscopic scale. The pulse-echo methods of imaging tissue structure are extended into the domain of microscopy and commonly referred to as ultrasound backscatter microscopy (UBM) (Foster et al. 1984; Turnbull & Foster 2002; Vogt & Ermert 2007). Stavros et al., described a set of criteria such as echogenicity, shadowing and speckle for diagnosing breast lesions using B-mode images. Furthermore an algorithm was developed to encode these B-mode features for determining and classifying breast cancer (Drukker et al., 2002).

In pre-clinical areas the resolution is often a limitation as the subjects under question are usually small animals (e.g. mice.) or cells and the internal structures cannot be resolved as they are too small. To address this, new HRUS transducer techniques called micro-ultrasound (µUS) have been developed (Arasiewicz et al. 2002). µUS can provide images of subsurface structures with microscopic resolution. At higher frequencies higher spatial resolution, of up to 10 µm can be achieved but at the cost of penetration, due to attenuation of ultrasound. µUS is advantageous because of its resolution and is popular in intravascular catheter-based procedures, imaging of ensemble of cells, imaging of skin and eyes. Pre-clinically, µUS has become prevalent in small animal imaging and developmental cell biology for cancer research. Single element µUS transducers are widely used for imaging and tissue characterisation (Foster & Hunt 1978). Although there is a reduced penetration depth, in regions such as skin and eyes HRUS can be used for diagnosis of diseases (Barr et al. 1991). µUS scanners acquire images by mechanically scanning single element transducers across the medium of

interest. The resultant RF data is represented as a 2D image and the data is used to measure quantitative parameters of the tissue.

Intravascular applications of ultrasound are used for the detection of vascular plaque and stenosis. Lockwood et al., demonstrated the use of a single-element imaging system operating at 45 MHz to distinguish between the adventitia, media, intima (Lockwood & Ryan 1991). Endosonics, Inc. have developed a 20 MHz array based imaging system, which includes a real-time colour Doppler flow imaging, elasticity measurements and also monitors stent deployment (Donnell et al. 1997).

In the 1980s Alexander and Miller, and Rukinava and Mohar were the first to report their studies on skin using ultrasound (Alexander & Miller 1979; Rukavina & Mohar 1979). HRUS B-mode imaging of the skin delivers information about depth of tumours and the inflammatory processes. In cases of melanoma, HRUS imaging provides vital information prior to excision of the skin tumour (Kleinerman et al. 2012). Non-invasive imaging of skin is also useful in determining the size of the tumour, which is the single most important indicator of the stage of cancer. Unlike in the case of biopsies the skin can be examined and monitored over a period of time using ultrasound. Dermatological single element scanners working in the frequency range of 20 – 100 MHz were developed by Vogt et al., (Michael Vogt & Ermert, 2007). HRUS in the 100 MHz frequency range makes it possible to image near surface structures of the skin at greater resolution. Important contributions towards the development of B-scan ultrasound systems have increased the knowledge and experience aiding in differentiating normal and pathological skin.

HRUS is also used in ophthalmological applications (Knapik et al. 2000; Pavlin et al. 1990; Pavlin & Foster 1998; Silverman 2009), wherein a 50-100 MHz single element ultrasonic biomedical micro-scanning (UBM) system was used to produce high resolution images of the anterior segment of the eyes. The first system for ophthalmology applications was developed in 1989 (Sherar et al., 1989), and clinical usage of commercial eye scanning has been demonstrated operating at 50 MHz (Carl Zeiss Ltd.). The primary applications of the commercial scanning system are glaucoma investigation, imaging of lesions and measurement of corneal thickness and topography. Latest technological designs are concentrated on use of arrays for imaging. A five element annular array has been implemented to obtain improved depth of field (Ketterling & Silverman 2006).

Small animal imaging on mouse models, mainly for cancer research is another important application of HRUS. Turnbull et al was the first to report the use of fixed focus, single element HRUS for imaging of normal and mutant mouse embryos, at a frequency of 50 MHz (Turnbull 1995). Mechanically scanned single element transducers with a frequency range of 25 - 70 MHz and a system frame rate of 5 - 10 frames/second were designed for *in vivo* imaging of mouse (Foster et al. 2000).

Scanning acoustic microscopy (SAM) was pioneered by Lemons and Quate, SAM utilizes very high frequency (100 MHz to 2 GHz) single-element transducers to generate microscopic images. SAM uses 2D scanning of a thin sample in the focal plane of a spherically focussed transducer (Hildebrand et al. 1981). The ultrasound beam transmitted through the specimen is detected to create an image of attenuation of ultrasound in the specimen. Alternatively ultrasound can be reflected from the specimen and detected by the transmitting transducer. One of the major advantages of ultrasound for use in microscopy is its ability to penetrate the optically opaque specimen and image through the depth of the tissue. When compared to traditional optical imaging, no staining is required of the specimen. SAM's are usually limited to *in vitro* imaging and diagnostics. However Sherar et al., used a single element ultrasound microscope operating at 100 MHz to image the internal structures of a living tumour spheroids. In this case C-scan mode of imaging was applied to create images of the specimen, the authors were able to correlate the ultrasound images with optical images (Sherar et al. 1987).

Despite widespread applications of single element HRUS transducers, there are some limitations. The need to scan the transducer and electrical isolation to minimise noise has limited the use of single element μUS devices. Single element devices have a fixed focal distance and therefore the resulting image in the focus is in a narrow region (Lockwood 1996). Frame rates is a limiting factor of single element devices for real time imaging, but frame rates equal to pulse repetition frequency (PRF) can be used. This method of imaging has been incorporated in a commercial system manufactured by Visualsonics Inc., (Vogt et al. 2010; Chérin et al. 2006). Imaging of hard materials poses problems due to the mismatch in the sound velocity between the specimen and coupling medium, leading to beam distortion and poor transmission of the ultrasound beam (Sherar & Foster 1988). The difficulties can be overcome by incorporating arrays but the design of the array based systems is difficult due to factors such as: lack of suitable materials and fabrication limitations (Shung 2009).

3.5 Quantitative Ultrasound Tissue Characterisation

The field of quantitative ultrasound tissue characterisation (QUS) deals with methods of measurement that can yield quantitative tissue properties that are independent of the instrumentation and operator. Soft tissue is formed by tissue components having different shapes, spatial organisation and mechanical properties that are unique to the tissue type being investigated. Only a portion of the ultrasound backscattered echoes is used in displaying B-scan images, therefore it is a challenge to distinguish between normal and diseased tissue based on B-scan images (Oelze & Zachary 2006). For instance the benign and malignant lesions are both seen as hypoechoic regions with respect to healthy tissue this was shown by Fornage et al., while investigating skin tissue using a 20 MHz ultrasound scanner (Fornage et al. 1993).

QUS deals with the measurement methods that can provide tissue properties based on theories of how ultrasound interacts with tissue. QUS is strongly dependent on the frequency of the transducer as the frequency dictates the specific scale of the tissue structure that can be resolved. Tissue characterization is a methodology used to infer tissue properties from ultrasound measurements. One of the primary goals of QUS is to facilitate the development of signal processing techniques for raw RF data. This will allow the formation of quantitative sonograms.

Quantitative information of tissue properties provides better understanding of the contrast mechanism in the images and aids in the interpretation of the B-scan images. For example a malignant tumour often absorbs ultrasound at a higher rate than the surrounding tissue, the acoustic wave travelling through the malignant region is modified in both space and time domains and the resulting RF signal thus contains a signature of the diseased region. The effects of tissue structure on wave propagation were extensively studied by the researchers at the University of Rochester, who developed a technique to identify different tissue types in the abdominal wall. QUS technique such as elastography, which involves estimation of tissue stiffness, can be found in the literature (e.g. Arda, Ciledag, Aktas, Aribas, & Köse, 2011; Jonathan Ophir et al., 2002).

Characterization of tissue is based upon estimation of ultrasound velocity, acoustic impedance, attenuation and BSC. Lizzi et al. developed a theoretical model for the evaluation of spectral characteristics of a broadband pulse-echo clinical system (Lizzi et al. 1983). QUS has been used widely in understanding the properties of blood (Wang et

al. 2001), cells (Baddour et al. 2005; Tunis et al. 2005), tissue mimicking phantoms (Yang et al. 1991; Wear & Stiles 2005). QUS has been applied to pre-clinical cancer research to differentiate and characterise rat mammary fibroadenomas (Oelze et al. 2004). BSCs of normal ocular tissue were calculated to differentiate between different structures (Ye & Harasiewicz 1995; Lizzi & Coleman 2004) and the same techniques have been applied to prostate cancer (Feleppa et al. 1997), breast cancer (Sherar & Foster 1988), liver cancer (Bamber & Hill 1981) and skin cancer (Tittmann et al. 2013).

All these studies relied on measuring ultrasound parameters such as: attenuation coefficients, acoustic impedance *(Z)*, backscatter coefficient (BSC), spectral parameters and speed of sound *(c)* in diseased and normal tissue. The speed of sound in tissue is assumed to be at 1540 ms^{-1} in all soft tissues. The correct estimation of the speed of sound has been reported to indicate tissue abnormality and the speed of sound calculations for diseased and normal tissue has been described by Hachiya et al. (Hachiya et al. 1992). The measurements were conducted on a rabbit model, in which melanoma was implanted in the anterior segment of the eye. A BSC model called the 'inhomogeneous continuum' with a cylindrical Gaussian autocorrelation function was used to analyse the spectra. They concluded that the scatterer size is the most important factor is determining the spectral slope. However, one thing that needs to be noted is that with the Gaussian model is an oversimplification, as it considers the tumour to be filled with cells and does not account for the presence of blood vessels, which are highly reflective due to collagen (Romijn & Thijssen 1989). Insana et al., measured frequency dependent backscattering from structures in kidney and reported that the changes in effective length of the scatterers were responsible for the changes in the anisotropy of backscatter and not the scatter size (Insana et al. 1990). BSC from ensembles of cells treated with chemo toxic drugs, that induces apoptosis revealed that BSC increases during cell death and is due to the increase in the size of the nucleus in the cells, that contributed to increase in the reflected signal amplitude (Czarnota & Kolios 2010).

Another method for tissue characterisation is to model the ultrasonic signals as stochastic signals since the details of the scattering structures in the tissue are unknown *a priori*. The backscattered echo is modelled as a random process and probability density functions of this process depend on the number density of scatterers relative to the wavelength and spatial heterogeneity within the tissue. The number density has been used as a parameter for characterising tissues (Wagner et al. 1995; Lizzi et al. 2003).

QUS methods have been employed to classify normal and cancerous murine small intestine in this thesis. The methods and results of extracting BSC and Z from the small bowel of diseased and normal murine intestine are explained in chapters 6 and 7.

3.6 Design Considerations of µUS Transducer

The heart of every medical ultrasound imaging system is a transducer. An ideal medical imaging transducer requires high sensitivity and resolution. The design and fabrication of µUS transducers presents a multitude of challenges and which researchers have tried to simplify the challenges by adopting various process routes (Hunt et al. 1983) . The design considerations for fabrication of µUS transducers are summarised by the block diagram in Figure 3.5. Every step in the development of a transducer feeds back to previous steps and ultimately to the imaging objective.

It is important to design a transducer that is capable of providing a narrow beam while maintaining sufficient sensitivity to penetrate the desired depth of the tissue. The acoustic properties of the tissue such as attenuation, acoustic impedance and velocity, thus have to be considered.

For example, to improve the lateral resolution of the transducer a low *f-#* aperture needs to be considered but this result in reduced depth of field, which in turn degrades the images in regions away from the focal plane. The choice of a suitable frequency for imaging is also crucial to designing a µUS transducer. The main factors that affect the choice of frequency of the transducer are:

1. Tissue attenuation
2. Depth of penetration
3. Dynamic range
4. Resolution
5. Physical restrictions such as size and shape of the transducer

In principle, greater frequency provides better lateral resolution but this may not be realised in practise. The pulse length needed to obtain good axial resolution proves to be another challenge. A greater bandwidth of the transducer leads to reduced sensitivity. The design of µUS transducers must thus include: proper choice of active element, backing layers, matching layers, and packaging, along with simulation and modelling of performance of the µUS transducer prior to characterisation and testing.

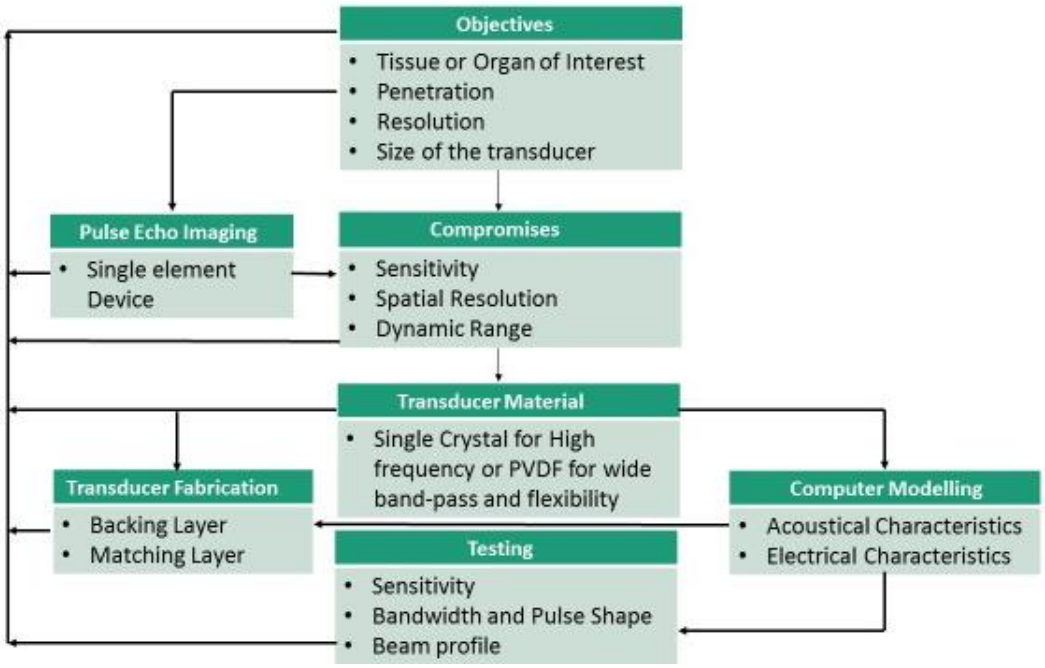

Figure 3.5: Design considerations for fabrication of µUS transducers for pulse echo tissue imaging.

The fabrication of transducers requires patience and care, and the final success of the system depends on the adoption and proposition of compromises in the design of transducers. The state of the art fabricating procedure of µUS transducers is shown in Figure 3.6.

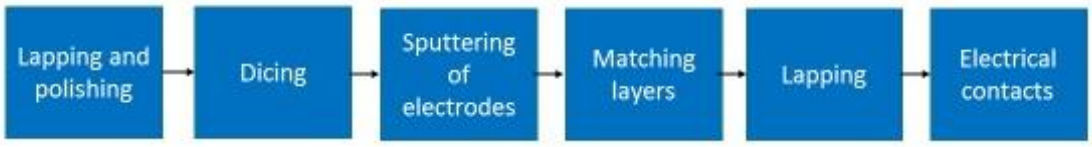

Figure 3.6: Summary of fabrication steps for a single element µUS transducer with a conventional λ/4 matching layer.

3.7 Micro-ultrasound (µUS) Transducer

The most important and indispensable part of an ultrasound imaging system is the transducer. Transducers come in many shapes, sizes and frequencies. A transducer can be treated as a three port network (Figure 3.7), with two ports acting as mechanical ports that represent the front and back surface of the active element and the electrical connection to the active element acting as an electrical port (K. Shung & Zippuro, 1999).

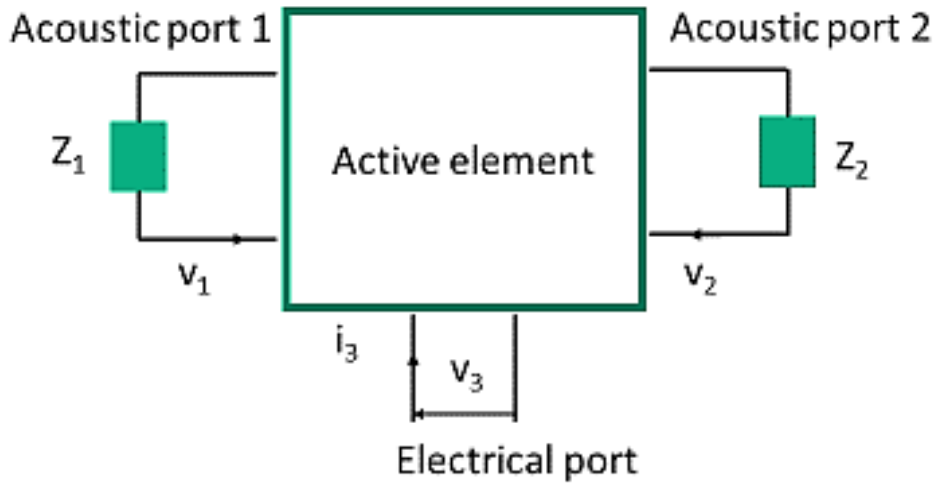

Figure 3.7: Three port network representation of an ultrasound transducer, showing the mechanical and electrical ports.

Single element µUS transducers are widely used in medical ultrasound applications in the range 30- 100 MHz, permitting visualization of tissue structures in the range 20 µm and less, with a penetration depth of around 4 mm (Foster et al. 1993). The work of this thesis mainly focused on fabrication, characterisation of µUS transducers and imaging and tissue characterisation with them.

A µUS transducer typically comprises a piezoelectric material also called the active element, backing layer, matching layer/s and cables to transmit power and information. A voltage pulse excites the active element, resulting in the expansion and contraction of the active element to emit ultrasound waves. The thickness of the active element determines the operating frequency of the transducer.

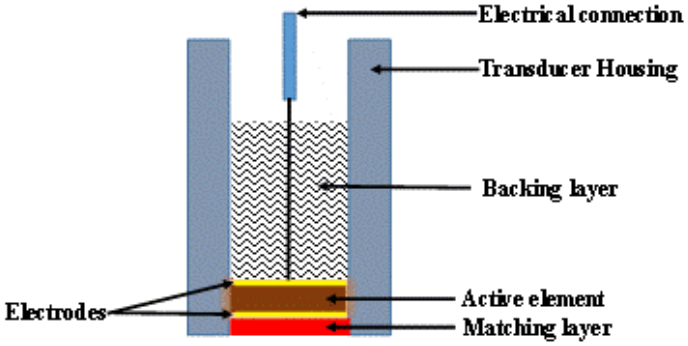

Figure 3.8: Cross section of a planar single element ultrasound transducer showing different components.

A single element transducer with its principal components is shown in Figure 3.10. Single element transducers, come with a fixed focal point and need to be mechanically scanned to produce a 2D image. As a result, the images have fixed depth which leads to poorer resolution at most depths and slow frame rates, limited by the speed of mechanical scanning (Shung 2009). Linear arrays allow electronic scanning and improved frame rates but limited dynamic depth focusing. Phased linear arrays allow dynamic depth focussing and beam steering, which increases the ultrasound diagnostic abilities. High frequency annular arrays allow dynamic 1D focusing and are a partial solution to mechanical scanning. The challenges in array fabrication are: need of small kerf width i.e. gap between elements, large electrical impedance and cross talk between the elements which leads to poor SNR. These challenges limit the fabrication of arrays to frequency up to 35 MHz, thus reducing the resolution of the imaging device.

The primary purpose of a μUS transducer is to produce excellent images and therefore an excellent pulse shape is the ultimate design goal. The design considerations to achieve this are discussed in the following sections.

3.7.1 Active Element

The active element of a transducer is the piezoelectric material. During transmission, it converts high voltage pulses into sound waves that travel through the tissue and converts displacements of the sound wave into voltage waveforms during reception. The piezoelectric element in a transducer is a resonant structure, which is designed to vibrate at half wavelength in the thickness mode. Commonly used materials for the active element include piezoceramics, piezoelectric polymers and single crystals.

Piezoelectric polymers have low acoustic impedance (Z ~ 4 MRayl) and are ideal for acoustic matching of the transducer with the human tissue (Z ~ 1.5 - 1.8 MRayl). Piezoelectric polymer materials can be easily made into thin films and can be easily press focused (Christopher & Turnbull 2000). However, these materials have a low dielectric constant and are ideal for low electrical matching, but their low thickness mode coupling coefficient (k_t = 0.32) renders them unsuitable for high frequency applications. Piezoceramics have higher k_t > 0.5 but have large dielectric constants (Smith & Auld 1991). Conventional piezoceramics such as PZT 5A and 5H analogues have been effective in applications such as intra-vascular ultrasound in 20 – 30 MHz frequency range. Piezoelectric composites use a combination of passive polymers and

piezoelectric material. The addition of polymer layers depending on volume fraction lowers the acoustic impedance of the active element from 34 MRayl to 17 MRayl.

Piezoelectric single crystals have been known since the discovery of single crystal quartz. However, no single crystals of useable size and properties could be grown successfully until recently and therefore, piezoceramics have dominated the commercial transducer market since the 1950s (Weis & Gaylord 1985). Single crystal material such as lithium niobate (LNO) has advantages over piezoceramics as they do not suffer from effects of grain structure. LNO has high electromechanical coupling coefficient and transmission coefficient. LNO has a lower dielectric constant than piezoceramics and are harder to shape. LNO has been used for fabricating transducers operating at 200 MHz for imaging applications (Knapik & Starkoski 1997). In this thesis LNO was used as in the devices developed.

3.7.2 Backing layer

Backing layers provide mechanical support to the active element and are usually made of acoustically lossy material. Backing layers minimise the reverberation or ringing within the active element, by absorbing the energy transferred. Effective damping leads to improved axial resolution and wider bandwidth. If the impedance of the backing layer is matched to the piezoelectric element, transducer sensitivity is reduced due to the absorption of most of the backward propagating energy. To maintain sufficient sensitivity with increased bandwidth, some reflection from the backing layer is necessary and therefore the acoustic impedance of the backing layer should be designed with appropriate impedance mismatch with respect to the active element.

There is a trade-off between the sensitivity, bandwidth and resolution. This can be overcome by using materials with lower Z than active element. The reduced Z of the backing improves the sensitivity of the transducer and the ringing of the transducer can be minimised further by using suitable matching layers. Most commonly used backing layers are polymers filled with heavy particles such as alumina, tungsten, silver, etc. Figure 3.9 illustrates the effect of backing on the pulse shape of the transducer.

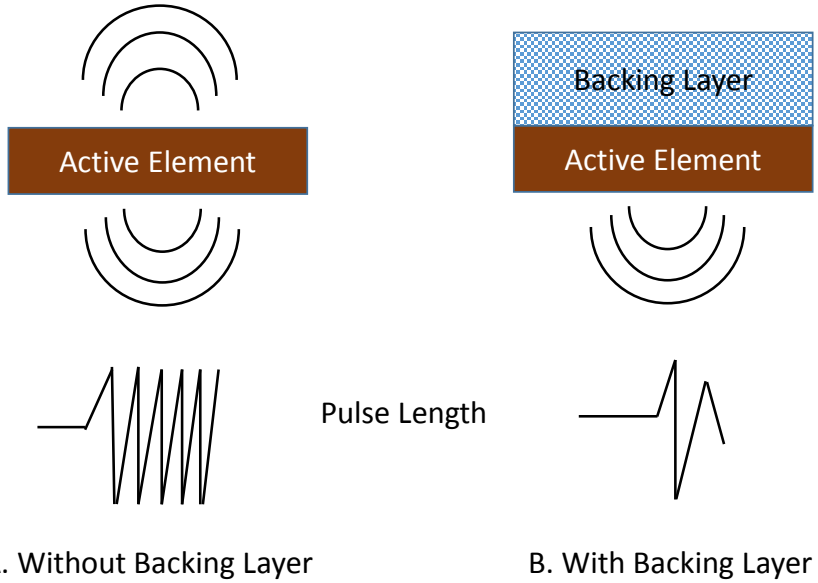

Figure 3.9: Schematic representation of the effect of backing layer in a transducer assembly on the pulse length. A. Active element without backing shows effects of ringing in the pulse. B. Active element with backing layer showing a short pulse due to reduced ringing.

3.7.3 Matching layer

Matching layers are used to improve the transfer of energy from the active element to the tissue. The acoustic impedance of soft tissue is 1.5 MRayl and the acoustic impedance of PZT is 30 MRayl. This mismatch in the acoustic impedance between the tissue and the PZT results in poor sensitivity and low transmission coefficient with approximately, 80 % of the energy generated by the transducer not being transmitted to the tissue. Loss in transmission energy leads to reduced sensitivity and bandwidth and hence results in poor images. In order to overcome this, a matching layer is designed with acoustic impedance, Z_m, which will maximise the energy transfer between the active layer with acoustic impedance, Z_p and the tissue with acoustic impedance, Z_t. The important condition that need to be considered for the design of the matching layers is: The thickness of the matching layer should be equal to a quarter wavelength at the operating frequency of the transducer, i.e. thickness (T) = $\lambda/4$.

A generally accepted formula for the ideal acoustic impedance of a single quarter wavelength matching layer is (Desilets et al. 1978):

$$Z_{\lambda/4} = \left(Z_p Z_w{}^2\right)^{1/3} \qquad (3.9)$$

Z_p is the acoustic impedance of the piezoelectric substrate and Z_w is the acoustic impedance of the coupling medium, usually water.

A transducer can have one or more matching layers, depending on the acoustic impedance mismatch between the active element and the imaging medium. It has been previously shown that multiple matching layers of graded acoustic impedances provides improved transmission between the active and material and the imaging medium. Equations used for the acoustic impedances of a dual quarter wavelength matching layer system are (Desilets et al. 1978):

$$Z_{\frac{1}{4}\lambda\#1} = \left(Z_p{}^4 Z_W{}^3\right)^{\frac{1}{7}} \qquad (3.10)$$

$$Z_{\frac{1}{4}\lambda\#2} = \left(Z_p Z_W{}^6\right)^{\frac{1}{7}} \qquad (3.11)$$

$Z_{1/4\lambda\#1}$, is the acoustic impedance of the first matching layer and $Z_{1/4}\lambda\#2$, is the acoustic impedance of the second matching layer. In Equations *(3.10)* and *(3.11)*, Z_p is the acoustic impedance of the piezoelectric substrate and Z_w is the acoustic impedance of the transmission medium typically taken as water in medical applications.

To achieve wider bandwidths and good acoustic coupling with piezoelectric substrates with high acoustic impedance, conventional quarter wavelength matching layer schemes have been used to date (e.g. Brown et al. 2007; Brown et al. 2004; Lukacs et al. 2006; Ritter et al. 2002). Traditional matching layer fabrication involves a mixture of high impedance particles with polymer to obtain impedance that can be used as a matching layer.

The basic principle of a quarter wavelength-matching layers is that constructive interference occurs as the wave fronts exit the transducer, and destructive interference occurs for waves reflected back into the piezoelectric substrate. This occurs because the quarter wavelength cavities generate appropriate phase shifts to generate the constructive and destructive interference at the different boundaries. The acoustic impedances of the matching layers are also carefully chosen so that the amplitude of the 'out of phase' waves theoretically combine to zero at the boundary reflecting back into

the piezoelectric substrate, resulting in a transmission coefficient close to one at the centre frequency of the transducer (Cobbold 2007; G.S. Kino 1987).

Precise lapping, grinding, and/or bonding high frequency matching layers is one of the most challenging aspects in fabricating transducers. For high frequency applications the matching layer thicknesses are in the order of 10 μm and therefore any variation in the precision of machining or thickness of bonding layer greater than around 1 μm can significantly degrade the performance of acoustic matching. The difficulty in precise machining increases with increasing number of matching layers. The process involved in producing a consistent bubble free mixture of metal-polymer is complicated due to the tendency of heavy metal powders to settle and create inhomogeneous mixtures (Toda & Thompson 2010). Thus, composite matching layers are not cost efficient and not well suited for mass production due to the lack of consistency with mixing and casting processes.

3.8 Conclusion

This chapter has covered topics including the principles of ultrasound wave propagation, HRUS imaging and ultrasound transducers. The review on HRUS demonstrated the diagnostic applications of single-element transducer technology. Quantitative ultrasound tissue characterisation has also been discussed. Particular emphasis was placed on matching layers. Particularly the concepts of matching layers is important as a novel mass-spring matching layers for μUS transducer was developed. Understanding of the topics discussed is crucial to this thesis, as this is required for fabrication and characterisation of μUS transducers for imaging of colon cancer models and quantitative tissue characterisation, which will aid in diagnosis of early tissue dysplasia. The next chapter describes the materials and methods used to fabricate and characterise high resolution μUS transducers with and without matching layers for imaging.

3.9 References

Alexander, H., & Miller, A. D. (1979) "Determining skin thickness with pulsed ultra sound." *Journal of Investigative Dermatology*, *72*(1), 17-19.

Anderson, J. J., Herd, M. T., King, M. R., Haak, A., Hafez, Z. T., Song, J., & Hall, T. J. (2010) "Interlaboratory comparison of backscatter coefficient estimates for tissue-mimicking phantoms." *Ultrasonic imaging*, *32*(1), 48-64.

Arda, K., Ciledag, N., Aktas, E., Arıbas, B. K., & Köse, K. (2011) "Quantitative assessment of normal soft-tissue elasticity using shear-wave ultrasound elastography." *American Journal of Roentgenology*, *197*(3), 532-536.Baddour, R.E. et al., 2005. High-frequency ultrasound scattering from microspheres and single cells. *The Journal of the Acoustical Society of America*, 117(2), 934.

Bamber, J. C., Fry, M. J., Hill, C. R., & Dunn, F. (1977) "Ultrasonic attenuation and backscattering by mammalian organs as a function of time after excision." *Ultrasound in medicine & biology*, *3*(1), 15-20.

Bamber, J.C. & Hill, C.R. (1981) "Acoustic properties of normal and cancerous human liver-I. Dependence on pathological condition." *Ultrasound in medicine & biology*, 7(2), 121–33.

Barr, R. J., White, G. M., Jones, J. P., Shaw, L. B., & Ross, P. A. (1991) "Scanning acoustic microscopy of neoplastic and inflammatory cutaneous tissue specimens." *Journal of investigative dermatology*, *96*(1), 38-42.

Brown, J., Foster, F. S., Needles, A., Cherin, E., & Lockwood, G. R. (2007) "Fabrication and performance of a 40-MHz linear array based on a 1-3 composite with geometric elevation focusing." *Ultrasonics, Ferroelectrics, and Frequency Control, IEEE Transactions on*, *54*(9), 1888-1894.

Brown, J., Morton-Démoré, C., Foster, F. S., & Lockwood, G. R. (2004, August) "Performance of a 50 MHz annular array based imaging system." In*Ultrasonics Symposium, 2004 IEEE* (Vol. 1, pp. 760-763). IEEE.

Bushberg, J. T., & Boone, J. M. (2011) "*The essential physics of medical imaging*." Lippincott Williams & Wilkins.

Calderon, C., Vilkomerson, D., Mezrich, R., Etzold, K. F., Kingsley, B., & Haskin, M. (1976) "Differences in the attenuation of ultrasound by normal, benign, and malignant breast tissue." *Journal of Clinical Ultrasound*, *4*(4), 249-254..

Chérin, E., Williams, R., Needles, A., Liu, G., White, C., Brown, A. S., & Foster, F. S. (2006) "Ultrahigh frame rate retrospective ultrasound microimaging and blood flow visualization in mice in vivo." *Ultrasound in medicine & biology*,*32*(5), 683-691.

Foster, F. S., Pavlin, C. J., Harasiewicz, K. A., Christopher, D. A., & Turnbull, D. H. (2000). "Advances in ultrasound biomicroscopy." *Ultrasound in medicine & biology*, *26*(1), 1-27.

Cobbold, R.S.C., (2007) "*Foundations of Biomedical Ultrasound*." Oxford University Press, Inc.

Czarnota, G. J., & Kolios, M. C. (2010) "Ultrasound detection of cell death." *Imaging in Medicine*, *2*(1), 17-28.

d'Astous, F. T., & Foster, F. S. (1986) "Frequency dependence of ultrasound attenuation and backscatter in breast tissue." *Ultrasound in medicine & biology*,*12*(10), 795-808.

Dempsey, P. J. (2004) "The history of breast ultrasound." *Journal of ultrasound in medicine*, *23*(7), 887-894.

Desilets, C., Fraser, J. & Kino, G. (1978) "The design of efficient broad-band piezoelectric transducers." *Sonics and Ultrasonics, IEEE*, (3), 115–125.

Donnell, M. O., Eberle, M. J., Stephens, D. N., Litzza, J. L., Vicente, K. S., & Shapo, B. M. (1997) "Synthetic phased arrays for intraluminal imaging of coronary arteries." *Ultrasonics, Ferroelectrics, and Frequency Control, IEEE Transactions on*, *44*(3), 714-721.

Feleppa, E. J., Liu, T., Kalisz, A., Shao, M. C., Fleshner, N., Reuter, V., & Fair, W. R. (1997) "Ultrasonic spectral-parameter imaging of the prostate." *International journal of imaging systems and technology*, *8*(1), 11-25.

Fornage, B. D., McGavran, M. H., Duvic, M., & Waldron, C. A. (1993) "Imaging of the skin with 20-MHz US." *Radiology*, *189*(1), 69-76.

Foster, F. S., Liu, G., Mehi, J., Starkoski, B. S., Adamson, L., Zhou, Y., & Zan, L. (2000, October) "High frequency ultrasound imaging: from man to mouse." In *Ultrasonics Symposium, 2000 IEEE* (Vol. 2, pp. 1633-1638). IEEE.

Foster, F. S., Zhang, M. Y., Zhou, Y. Q., Liu, G., Mehi, J., Cherin, E., & Adamson, S. L. (2002) "A new ultrasound instrument for in vivo microimaging of mice." *Ultrasound in medicine & biology*, *28*(9), 1165-1172.

Foster, F. S., & Hunt, J. W. (1978) "The design and characterization of short pulse ultrasound transducers." *Ultrasonics*, *16*(3), 116-122.

Foster, F. S., Strban, M., & Austin, G. (1984) "The ultrasound macroscope: initial studies of breast tissue." *Ultrasonic imaging*, *6*(3), 243-261.

Foster, F. S., Lockwood, G. R., Ryan, L. K., Harasiewicz, K. A., & Berube, L. (1993) "Principles and applications of ultrasound backscatter microscopy." *Ultrasonics, Ferroelectrics, and Frequency Control, IEEE Transactions on*,*40*(5), 608-617.

Kino, G. S. (1987). "*Acoustic waves: devices, imaging, and analog signal processing* (Vol. 107)." Englewood Cliffs, NJ: Prentice-Hall.

Gan, W. S. (2012) "*Acoustical Imaging: Techniques and Applications for Engineers*." John Wiley & Sons.

Guittet, C., Ossant, F., Vaillant, L., & Berson, M. (1999) "In vivo high-frequency ultrasonic characterization of human dermis." *Biomedical Engineering, IEEE Transactions on*, *46*(6), 740-746.

Hachiya, H., Ohtsuki, S., Tanaka, M., & Dunn, F. (1992) "Determination of sound speed in biological tissues based on frequency analysis of pulse response." *The Journal of the Acoustical Society of America*, *92*(3), 1564-1568.

Havlice, J. & Taenzer, J. (1979) "Medical ultrasonic imaging: An overview of principles and instrumentation." *Proceedings of the IEEE*, 6(4).

Hildebrand, J. A., Rugar, D., Johnston, R. N., & Quate, C. F. (1981) "Acoustic microscopy of living cells." *Proceedings of the National Academy of Sciences*,*78*(3), 1656-1660..

Hunt, J.W., Arditi, M. & Foster, F.S. (1983) "Ultrasound transducers for pulse-echo medical imaging." *IEEE transactions on bio-medical engineering*, 30(8), pp.453–81.

Insana, M. & Hall, T. (1990) "Parametric ultrasound imaging from backscatter coefficient measurements: image formation and interpretation." *Ultrasonic Imaging*, 267, pp.245–267.

Insana, M. F., Wagner, R. F., Brown, D. G., & Hall, T. J. (1990) "Describing small-scale structure in random media using pulse-echo ultrasound." *The Journal of the Acoustical Society of America*, *87*(1), 179-192.

Ketterling, J. & Silverman, R. (2006) "20-MHz Annular Arrays for Ophthalmic Imaging." *Ultrasonics Symposium, 2006.* 252–255.

Kleinerman, R., Whang, T. B., Bard, R. L., & Marmur, E. S. (2012) "Ultrasound in dermatology: Principles and applications." *Journal of the American Academy of Dermatology*, *67*(3), 478-487.

Knspik, D. A., Starkoski, B., Pavlin, C. J., & Foste, F. S. (2000) "A 100-200 MHz ultrasound biomicroscope." *Ultrasonics, Ferroelectrics, and Frequency Control, IEEE Transactions on*, *47*(6), 1540-1549.

Knapik, D. & Starkoski, B., (1997) "A realtime 200 MHz ultrasound B-scan imager." *Ultrasonics Symposium*, 1457–1460.

Kuc, R. (1980) "Clinical application of an ultrasound attenuation coefficient estimation technique for liver pathology characterization." *Biomedical Engineering, IEEE Transactions*, (6), 312-319.

Leighton, T. G. (2007) "What is ultrasound?." *Progress in biophysics and molecular biology*, *93*(1), 3-83.

Lizzi, F. L., Feleppa, E. J., Alam, S. K., & Deng, C. X. (2003) "Ultrasonic spectrum analysis for tissue evaluation." *Pattern Recognition Letters*, *24*(4), 637-658.

Lizzi, F. L., Greenebaum, M., Feleppa, E. J., Elbaum, M., & Coleman, D. J. (1983). "Theoretical framework for spectrum analysis in ultrasonic tissue characterization." *The Journal of the Acoustical Society of America*, *73*(4), 1366-1373.

Lizzi, F. L., & Coleman, D. J. (2004) "History of ophthalmic ultrasound." *Journal of ultrasound in medicine*, *23*(10), 1255-1266.

Lockwood, G. R., Turnball, D. H., Christopher, D. A., & Foster, F. S. (1996) "Beyond 30 MHz [applications of high-frequency ultrasound imaging]." *Engineering in Medicine and Biology Magazine, IEEE*, *15*(6), 60-71.

Lockwood, G. R., Ryan, L. K., Hunt, J. W., & Foster, F. S. (1991) "Measurement of the ultrasonic properties of vascular tissues and blood from 35–65 MHz." *Ultrasound in medicine & biology*, *17*(7), 653-666.

Lukacs, M., Yin, J., Pang, G., Garcia, R. C., Cherin, E., Williams, R., & Foster, F. S. (2006) "Performance and characterization of new micromachined high-frequency linear arrays." *Ultrasonics, Ferroelectrics, and Frequency Control, IEEE Transactions on*, *53*(10), 1719-1729.

Ghoshal, G., Oelze, M. L., & O'Brien Jr, W. D. (2013) "Quantitative ultrasound history and successes." In *Quantitative Ultrasound in Soft Tissues* (pp. 21-42). Springer Netherlands.

Mimbs, J. W., O'Donnell, M., Bauwens, D. A. N. I. E. L., Miller, J. W., & Sobel, B. E. (1980) "The dependence of ultrasonic attenuation and backscatter on collagen content in dog and rabbit hearts. " *Circulation Research*, *47*(1), 49-58.

Nicholas, D. (1982) "Evaluation of backscattering coefficients for excised human tissues: results, interpretation and associated measurements." *Ultrasound in Medicine & Biology*, 8(1), 17–28.

Nicholas, D., Hill, C.R. & Nassiri, D.K., (1982) "Evaluation of backscattering coefficients for excised human tissues: Principles and techniques." *Ultrasound in Medicine & Biology*, 8(1), 7–15.

Oelze, M. L., O'Brien Jr, W. D., Blue, J. P., & Zachary, J. F. (2004) "Differentiation and characterization of rat mammary fibroadenomas and 4T1 mouse carcinomas using quantitative ultrasound imaging." *Medical Imaging, IEEE Transactions on*, *23*(6), 764-771.

Oelze, M.L. & O'Brien, W.D. (2002) "Frequency-dependent attenuation-compensation functions for ultrasonic signals backscattered from random media." *The Journal of the Acoustical Society of America*, 111(5), p.2308.

Oelze, M.L. & Zachary, J.F. (2006) "Examination of cancer in mouse models using high-frequency quantitative ultrasound." *Ultrasound in medicine & biology*, 32(11), 1639–48.

Ophir, J., Shawker, T. H., Maklad, N. F., Miller, J. G., Flax, S. W., Narayana, P. A., & Jones, J. P. (1984) "Attenuation estimation in reflection: progress and prospects." *Ultrasonic imaging*, *6*(4), 349-395.

Ophir, J., Alam, S. K., Garra, B. S., Kallel, F., Konofagou, E. E., Krouskop, T., & Varghese, T. (2002) "Elastography: imaging the elastic properties of soft tissues with ultrasound." *Journal of Medical Ultrasonics*, *29*(4), 155-171.

Parker, K. J., & Lyons, M. E. (1988) "Absorption and attenuation in soft tissues. I. Calibration and error analyses." *Ultrasonics, Ferroelectrics, and Frequency Control, IEEE Transactions on*, *35*(2), 242-252.

Pavlin, C. J., Harasiewicz, K., Sherar, M. D., & Foster, F. S. (1991) "Clinical use of ultrasound biomicroscopy." *Ophthalmology*, *98*(3), 287-295.

Pavlin, C. J., Sherar, M. D., & Foster, F. S. (1990) "Subsurface ultrasound microscopic imaging of the intact eye." *Ophthalmology*, *97*(2), 244-250.

Ritter, T., Shrout, T. R., Tutwiler, R., & Shung, K. K. (2002) "A 30-MHz piezo-composite ultrasound array for medical imaging applications." *Ultrasonics, Ferroelectrics, and Frequency Control, IEEE Transactions on*, *49*(2), 217-230.

Romijn, R. L., Thijssen, J. M., Van Delft, J. L., de Wolff-Rouendaal, D., Van Best, J., & Oosterhuis, J. A. (1989) "In vivo ultrasound backscattering estimation for tumour diagnosis: an animal study." *Ultrasound in medicine & biology*, *15*(5), 471-479.

Rukavina, B., & Mohar, N. (1979) "An approach of ultrasound diagnostic techniques of the skin and subcutaneous tissue." *Dermatology*, *158*(2), 81-92.

Sherar, M. D., & Foster, F. S. (1989) "The design and fabrication of high frequency poly (vinylidene fluoride) transducers." *Ultrasonic imaging*, *11*(2), 75-94.

Sherar, M. D., Noss, M. B., & Foster, F. S. (1987) "Ultrasound backscatter microscopy images the internal structure of living tumour spheroids." *Nature*,*330*(6147), 493-495.

Sherar, M. D., & Foster, F. S. (1988, October). "Ultrasound backscatter microscopy." In *Ultrasonics Symposium, 1988. Proceedings., IEEE 1988* (pp. 959-966). IEEE.

Shung, K. K., & Zippuro, M. (1996) "Ultrasonic transducers and arrays." *Engineering in Medicine and Biology Magazine, IEEE*, *15*(6), 20-30.

Shung, K. K. (2009) "High frequency ultrasonic imaging." *Journal of medical ultrasound*, *17*(1), 25-30.

Sigelmann, R. & Reid, J. (1973) "Analysis and measurement of ultrasound backscattering from an ensemble of scatterers excited by sine-wave bursts." *The Journal of the Acoustical Society of America*, 53(5) 1351–1355.

Silverman, R.H. (2009) "High-resolution ultrasound imaging of the eye - a review." *Clinical & experimental ophthalmology*, 37(1), 54–67.

Smith, W. a & Auld, B. A. (1991) "Modeling 1-3 composite piezoelectrics: thickness-mode oscillations." *IEEE transactions on ultrasonics, ferroelectrics, and frequency control*, 38(1), pp.40–7.

Szabo, T.L. (2004) *Diagnostic ultrasound imaging: inside out* 2nd editio., Burglinton: Academic Press.

Thijssen, J. M. (1987) "Ultrasonic tissue characterization and echographic imaging." *Medical progress through technology*, *13*(1), 29.

Tittmann, B. R., Miyasaka, C., Maeva, E., & Shum, D. (2013) "Fine mapping of tissue properties on excised samples of melanoma and skin without the need for histological staining." *Ultrasonics, Ferroelectrics, and Frequency Control, IEEE Transactions on*, *60*(2), 320-331.

Tunis, A. S., Czarnota, G. J., Giles, A., Sherar, M. D., Hunt, J. W., & Kolios, M. C. (2005) "Monitoring structural changes in cells with high-frequency ultrasound signal statistics." *Ultrasound in medicine & biology*, *31*(8), 1041-1049.

Turnbull, D. H., Bloomfield, T. S., Baldwin, H. S., Foster, F. S., & Joyner, A. L. (1995) "Ultrasound backscatter microscope analysis of early mouse embryonic brain development." *Proceedings of the National Academy of Sciences*, *92*(6), 2239-2243..

Turnbull, D. H., & Foster, F. S. (2002) "In vivo ultrasound biomicroscopy in developmental biology." *Trends in Biotechnology*, *20*(8), S29-S33.

Vogt, M., Opretzka, J., Perrey, C., & Ermert, H. (2010) "Ultrasonic microscanning." *Proceedings of the Institution of Mechanical Engineers, Part H: Journal of Engineering in Medicine*, *224*(2), 225-240.

Vogt, M. & Ermert, H. (2007) "In vivo ultrasound biomicroscopy of skin: spectral system characteristics and inverse filtering optimization." *IEEE transactions on ultrasonics, ferroelectrics, and frequency control*, 54(8), 1551–9.

Wagner, R. F., Wear, K. A., Perez, J. E., McGill, J. B., Schechtman, K. B., & Miller, J. G. (1995) "Quantitative assessment of myocardial ultrasound tissue characterization through receiver operating characteristic analysis of Bayesian classifiers." *Journal of the American College of Cardiology*, *25*(7), 1706-1711.

Wang, S. H., Liao, J. D., Tsai, F. C., & Tsai, C. L. (2001) "Measurements of High Frequency Ultrasonic Backscattering from Blood-Frequencies Ranged from 5 to 42.5 MHz." *Journal of Medical and Biological Engineering*, *21*(2), 105-110.

Wear, K. & Stiles, T. (2005) "Interlaboratory Comparison of ultrasonic backscatter coefficient Measurements From 2 to 9 MHz." *journal of ultrasound in Medicine and Biology*,1235–1250.

Weis, R. S., & Gaylord, T. K. (1985) "Lithium niobate: summary of physical properties and crystal structure." *Applied Physics A*, *37*(4), 191-203.

Yang, J. N., Murphy, A. D., Madsen, E. L., Zagzebski, J. A., Gilchrist, K. W., Frank, G. R., & Gosset, F. R. (1991) "A method for in vitro mapping of ultrasonic speed and density in breast tissue." *Ultrasonic imaging*, *13*(1), 91-109.

Ye, S. G., Harasiewicz, K. A., Pavlin, C. J., & Foster, F. S. (1995) "Ultrasound characterization of normal ocular tissue in the frequency range from 50 MHz to 100 MHz." *Ultrasonics, Ferroelectrics, and Frequency Control, IEEE Transactions on*, *42*(1), 8-14.

Chapter 4: Fabrication of µUS Transducers

"Machines take me by surprise with great frequency"

Alan Turing

4.1 Overview

Having reviewed the basics of ultrasound imaging, ultrasound tissue characterisation and of µUS transducers in Chapter 3, the work presented in this chapter deals with materials and methods involved in modelling, fabricating and functional characterisation of single element lithium niobate (LNO) µUS transducers with and without matching layers. The transducers were fabricated to operate at a resonant frequency of 45 MHz, with a novel mass-spring matching layer configuration designed, modelled and fabricated in this thesis. The frequency of 45 MHz is compatible with a lateral resolution of approximately 100 µm, which makes it possible to resolve fine tissue structure and aid in diagnosis of early stages of colon cancer. This chapter has six further sections.

- In Sections 4.2 – 4.3, the steps involved in fabricating single element LNO focused and planar µUS transducers are explained. A Process route to thin LNO to a few micro meters (~ 10 µm) with sub-nano metre surface roughness for high frequency applications was established and is explained.
- In Section 4.4, the methods used for fabrication of conventional dual quarter wavelength (λ/4) matching layers for single element µUS transducers are explained.
- In Section 4.5, a scheme called the "mass-spring" matching layer, developed to overcome the drawbacks of conventional matching layers is explained. µUS transducers with mass-spring matching layers require very thin layers of mass (Cu)-spring (parylene) matching layers. A process of applying matching layers using vacuum deposition was implemented, and is described in Sections 4.5.4 and 4.5.5.
- In Section 4.6, a KLM model which was used to theoretically evaluate the performance of µUS transducers for various matching layer schemes is described.
- In section 4.7, the functional characterisation techniques to evaluate the performance of µUS imaging transducers are described.

4.2 Active Element of µUS Transducer

Lithium niobate (LNO) is a man-made dielectric material. It was first discovered to have ferroelectric properties in 1949 (Weis & Gaylord 1985). LNO was first synthesised in single crystal form at Bell Laboratories. The structure and properties of LNO were published in a series of papers in 1966 (Abrahams et al. 1966; Nassau et al. 1966a; Nassau et al. 1966b). LNO (Precision Micro-Optics, Woburn, MA) was used as an active element to fabricate µUS transducers in this project as it is an ideal single crystal material for large aperture single element transducers due to its high coupling coefficient and low dielectric constant.

LNO has a wide range of device applications that exploit its elastic, piezoelectric, dielectric and pyroelectric properties. LNO is an anisotropic crystal. LNO exhibits different piezoelectric properties with different orientations. Therefore the geometrical form, orientation, effective electromechanical coupling coefficient and the purity of the vibration modes play a key role in selecting the cut of LNO. The compressional cuts that are most widely used are the Z-cut and the rotated 36^0 Y-cut. The Z-cut (Y-90^0) gives a pure longitudinal mode but with a poor thickness mode coupling coefficient (k_t = 0.17). Y-cut (Y-36^0) has a coupling coefficient three times that of Z-cut. LNO exhibits low acoustic losses. The Curie temperature of LNO is 1150 ^{0}C, making it a suitable material for high temperature transducer applications (Kirk et al. 2001). LNO can easily be thinned to desired thickness to achieve a high frequency without disintegration as in ceramics.

LNO is also capable of sustaining high electric fields and low acoustic losses that allow the use of harmonics. The hardness of LNO is 5 on Mohs hardness scale and therefore thinning of LNO is cost effective and relatively easy, although care has to be taken due to the brittleness of the material and a faster removal rate when compared to other materials, e.g. quartz.

LNO was chosen as a material to fabricate µUS single element transducers for its high thickness mode coupling coefficient (k_t = 0.52) and relatively low clamped dielectric constant (ε^{s} = 39) (Cannata & Zhao 1999). The list of relevant properties to be considered for fabrication and KLM modelling purposes is listed in Table 4.1.

Table 4.1: Material properties of 36^0 Y-cut LNO (G.S. Kino 1987).

Property	**Value**
Electomechanical coupling coefficient (k_t)	0.49
Relative clamped dielectric constant ($\varepsilon^s/\varepsilon_0$)	39^2
Mechanical quality factor (Q_m)	10000
Electrical quality factor (Q_E)	1000
Longitudinal velocity (m/s)	7360
Acoustic Impedance (MRayl)	34.0
Curie temperature (^{0}C)	1150

Thickness mode coupling coefficient is a significant property of the material as it indicates as to how efficiently a material converts electrical energy to mechanical energy or vice versa. LNO transducers are relatively easy to match electrically to standard 50 Ω equipment. The second significant advantage of LNO is the thickness mode velocity of 7360 ms^{-1}, which is significantly faster than other alternative single crystal materials, with velocity of 2200 ms^{-1} for PVDF and 4800 ms^{-1} for PZT. For a given velocity of sound, *c*, and thickness, *x*, the mechanical resonant frequency, f_a, is given by the Equation *(4.1)*:

$$f_a = \frac{c}{2x} \qquad (4.1)$$

Materials with lower velocity require thinner active layers to achieve a given operational frequency, making the fabrication more complex and expensive. Incorporating an active material with better piezoelectric properties into a transducer can lead to devices with improved sensitivity and bandwidth that will improve the spatial resolution of ultrasound imaging systems.

One of the disadvantages of high thickness velocity is high acoustic impedance. The *Z* of LNO is ~30 MRayl and thus it is important to have matching layers, to obtain optimum performance of the imaging transducer.

It can be concluded from the above discussion that LNO Y-36^0 is ideal for large aperture single element µUS transducer because of low dielectric constant, high coupling coefficient (k_t = 0.49) and high resonant frequency constant (3.3 MHz/mm),

allowing thicker piezoelectric elements at high frequencies compared to conventional piezoceramics. Given its advantages, LNO Y-36^0 was used as the material of choice to fabricate high frequency µUS transducers for medical applications.

4.3 µUS Transducer

High frequency transducers are typically fabricated using materials such as PZT or single crystals such as LNO or PMN-PT. In order to achieve high frequency domain bandwidth and good coupling with tissue a conventional λ/4 matching layer scheme has been historically used to date (Desilets et al. 1978; Qian & Harris 2014; Kossoff 1966; Snook et al. 2002). Lapping, dicing or grinding and bonding of matching layers to the piezoelectric substrate precisely is challenging. This is because, the thickness of matching layer for µUS transducers is in the order of 10 µm and any variation in this thickness degrades the performance of the transducer. There is also the problem of using composite materials for matching layers, as it is difficult to predict the material performance, mixture ratios, size distribution, casting and curing process which is generally determined by a trial and error procedure (Toda & Thompson 2010).

To overcome these problems with conventional λ/4 matching layers a scheme of matching layers called the "mass-spring" configuration was designed and investigated for high frequency applications in this thesis. Three types of µUS transducers operating at a frequency of 45 MHz were fabricated and their performance was evaluated both, theoretically and experimentally. The three schemes investigated were:

1. Planar and focused single element transducers without matching layers
2. Single element LNO with dual λ/4 matching layers
3. Single element LNO with novel mass-spring matching layers

4.3.1 Fabrication of Single Element µUS transducers

An operating frequency of 45 MHz was chosen as devices, operating at this frequency were expected to produce acceptable imaging resolution to visualise fine structures of the murine intestine. The steps involved in fabrication of 45 MHz µUS transducers with conductive epoxy backing are illustrated sequentially in Figure 4.1 (A). These are similar to the technique developed by Lockwood et al., (Lockwood et al. 1994).

A bulk single crystal of LNO is lapped to a thickness of ~ 69 µm which corresponds to the desired frequency of 45 MHz the desired thickness for the known operating frequency was calculated using Equation in *(4.1)*. Lapping is followed by dicing the piezo substrate to circular disk of 3 mm diameter. A thin layer (~ 500 nm) of Cu electrode is cast on to the front face through E-beam evaporation. The sample is then gently heated to 70 ^{0}C and pressed onto a spherical ball bearing of 14 mm diameter to obtain a focal point at 7 mm. Heat is used to make the sample slightly flexible and makes it easier to shape the piezoelectric substrate. The piezoelectric substrate is then cooled to room temperature and dismounted from the spherical surface. A conductive silver epoxy backing layer of approximately 1 mm thickness is cast on to the back surface of the curved piezo substrate to provide additional support for the transducer to form an acoustically lossy but electrically conductive backing layer. An example of a spherically shaped 45 MHz single element LNO µUS transducer mounted in a SMA barrel connector is shown in Figure 4.3 B. The transducer is 3 mm diameter with a focal distance of 7 mm, electrical contact is made using the centre pin of the connector and by evaporating Cu electrode across the front face of the transducer and the SMA connector.

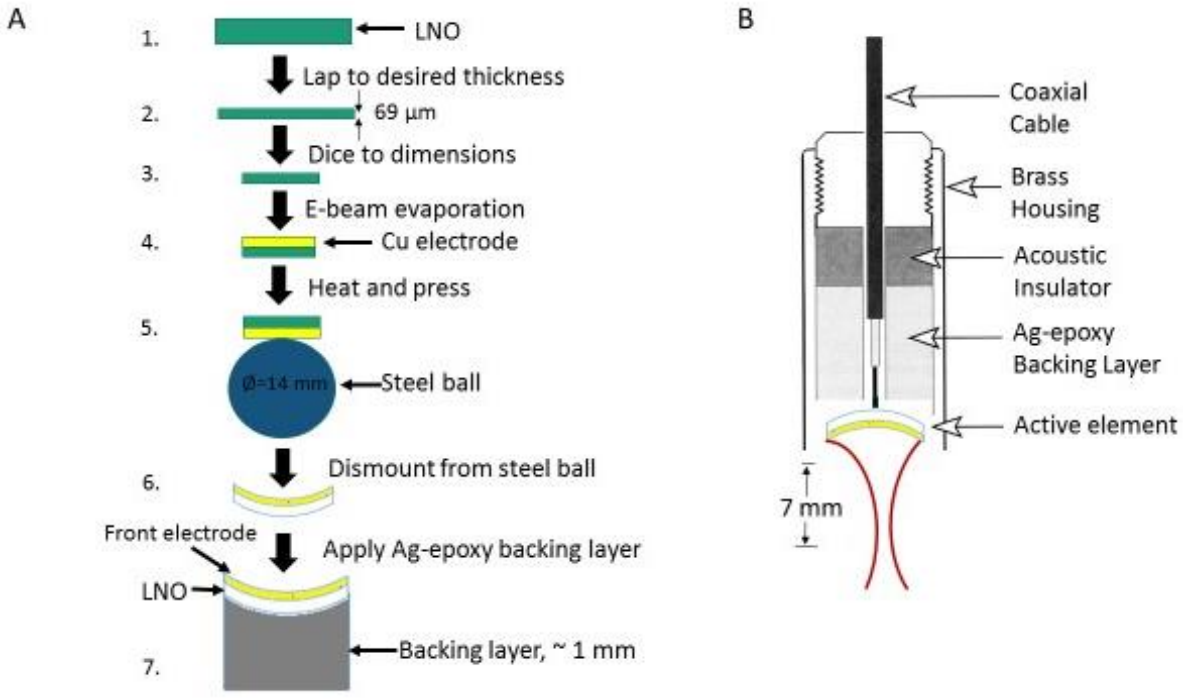

Figure 4.1: ***A.*** *Diagram illustrating steps (top to bottom) involved in fabricating a spherically shaped single element µUS transducer of frequency 45 MHz without matching layers.* ***B.*** *Cross sectional view of the single element µUS transducer in a brass casing with SMA connection, the focal length of the transducer is 7 mm.*

The acoustical properties and functions of the materials used for the fabrication of μUS transducers are summarised in Table - 4.2.

Table 4.2: Summary of properties of materials used for the fabrication of unmatched and matched μUS transducers.

Material	Manufacturer	Velocity (m/s)	Z (MRayl)	Function
Y-36^0 cut LNO	Precision Micro-Optics, Woburn, MA, USA	7360	34	Piezoelectric or Active Element
E- Solder	Van Roll, New Haven, CT, USA	1850	5.9	Backing Layer
Parylene C	SCS coatings, IN, USA	2135	2.75	Matching layer and Spring Layer
Copper	Kurt J. Lesker, Jefferson Hills, PA, USA	4660	41.6	Mass Layer and Front Electrode
Silver Epoxy	Epotek, MA, USA	2650	4.3	Traditional Matching Layer

The fabrication of dual λ/4 matched transducers is described in Section 4.4. For the application of mass-spring matching layers, Step 7 is followed by evaporation of the desired thickness of parylene followed by Cu. This is explained in further detail in Section 4.5. The fabricated μUS transducers were characterised and compared with the acoustical models built up using KLM, as explained in Section 4.6.

4.3.2 Lapping and Polishing

To obtain very high frequencies (> 30 MHz) the piezoelectric material has to be thinned to a desired thickness precisely and the best possible way to achieve this is by lapping and polishing. Thinning of single crystals such as LNO requires an accurate way to control the removal rate that is also repeatable and reliable. LNO has a lower removal rate than some other materials due to its hardness and is prone to scratches during lapping (Jeong et al. 2010). The sizes of the abrasive and lapping speed are critical in controlling the removal rate. When lapping single crystals it is important to avoid cleavages of the sample due to mechanical stresses, especially when reaching ultra-low thickness (Pinel et al. 1998). Earlier techniques for thinning of the piezoelectric material involved grinding and use of sand paper, which were not reliable as uniform flatness and thickness could not be ensured.

In this thesis, all lapping and polishing were performed with an LP-50/PM5 precision lapping and polishing machine (Logitech Ltd. Glasgow, UK). A schematic of the lapping and polishing system is shown in Figure 4.2. The removal rate and the surface roughness of the material can be controlled by choosing different lapping plates (grooved or non-grooved plates), loading forces on the lapping or polishing jig, rotational speed of the lapping plate, slurry drip rate, and particle size of the abrasive. Mechanical polishing followed lapping, to remove pitting caused by lapping and to ensure material flatness and sub-nano meter surface roughness.

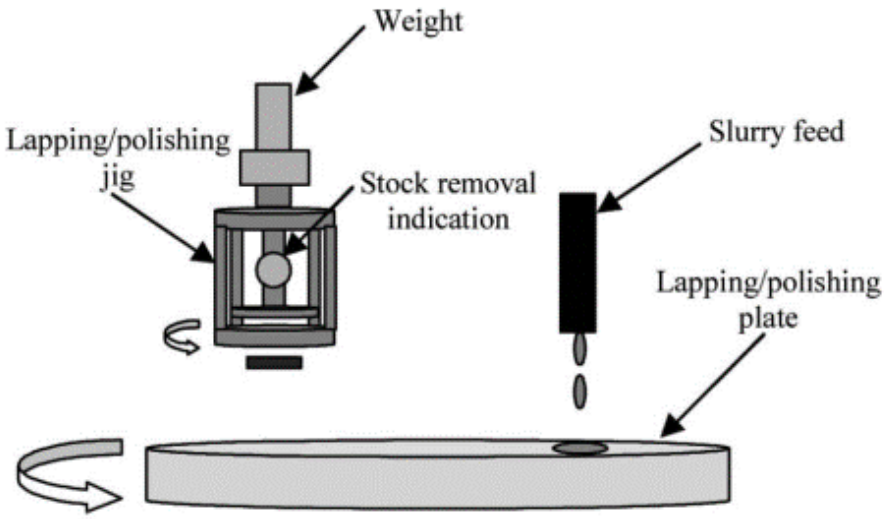

Figure 4.2: Schematic of lapping and polishing machine used for thinning of active and passive materials (Bernassau et al. 2012).

As an example, a 3 inch wafer of Y-36^0 cut LNO of thickness 500 µm was bonded to a glass substrate using quartz wax. The sample was lapped to 100 µm initially and then 50 µm subsequently on an non-grooved cast iron plate with abrasive slurries of 20 µm and 3 µm Al_2O_3 particles respectively. A non-grooved cast iron plate was used to prevent the sample from cracking at the edges. The plate speed was set at 50 rpm and the jig load at 950 g.

The sample was polished to achieve a final thickness of 10 µm using a polyurethane plate and SF1 alkaline colloidal silica polishing solution with a speed of 10 rpm and jig load of 250 g. The thickness of the sample through the process was monitored using the removal rate gauge on the lapping jig. The thickness of the sample was measured in intermediate steps at five different points on the sample using the contact gauge (CG-10, Logitech Ltd. Glasgow, UK) shown in Figure 4.3. The contact gauge has a

resolution of 0.0001 mm and can measure the thickness of a sample up to 10 mm. Monitoring the thickness in intermediate steps ensures uniform thickness and flatness of the sample.

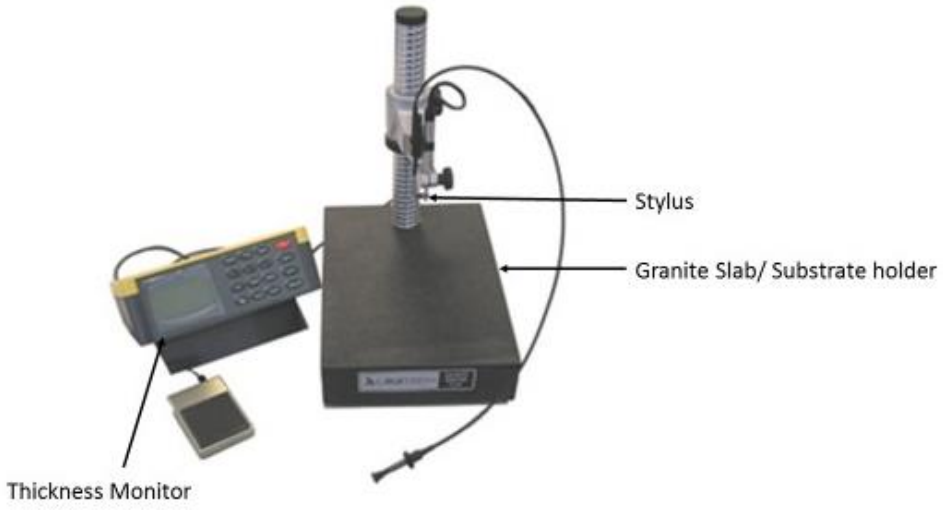

Figure 4.3: Contact gauge used for monitoring the thickness of LNO during and after lapping.

Lapping and polishing were carried out at low speeds to reduce vibration and surface scratching. The surface roughness of the finished sample was measured using a stylus based surface profiler (Veeco Dektak 150, Cambridge, UK). While surface roughness is needed to promote adhesion of thin film electrodes a smooth and a uniform surface is necessary for applications such as photolithography to deposit and pattern continuous electrodes. It should be noted that photolithography was not used in this work but most likely can be incorporated in the future designs of arrays with mass spring matching layers.

In this thesis 36^0 y-cut LNO disk of 3 mm^2 diameter was lapped to a thickness of 69 µm to fabricate 45 MHz µUS transducers. After achieving the desired thickness the square samples were diced into approximately circular disks.

4.3.3 Dicing

Dicing is extensively used in fabrication of arrays, to achieve kerfs between the elements. One of the most often used methods for creating kerfs is with a high precision dicing saw. For interested readers there are several papers on fabrication of diced arrays (e.g. Lukacs et al. 2006; Garland et al. 2011; Brown et al. 2009). The optimization of

these parameters is a process established by experience: in general, single crystal materials like LNO require higher spindle speed and lower feed rate to achieve chip free cuts.

High precision dicing was used to create sixteen-sided polygons of the active element to create approximate circular disks. Dicing was performed with a precision dicing saw (MicroAce 66, Loadpoint Ltd. UK). The dicing machine has a two point alignment system. The resolution of cutting is 100 µm in the X-axis and about 100 nm in Z and Y axes and 0.0004^0 in the rotational θ axis (Figure 4.4). The samples to be diced are fixed rings and vacuum mounted through a porous chuck. A coolant usually, water, is fed through the channels to cool the sample and the blade while dicing. The quality of the cut depends on some of the key parameters namely: hardness of the sample, spindle speed, feed rate, coolant rate, cut depth and the blade diameter. For dicing of LNO either resin bonded blades or metal blades with a high wear rate were used. The lower grit size of the metal blades gives a better finish.

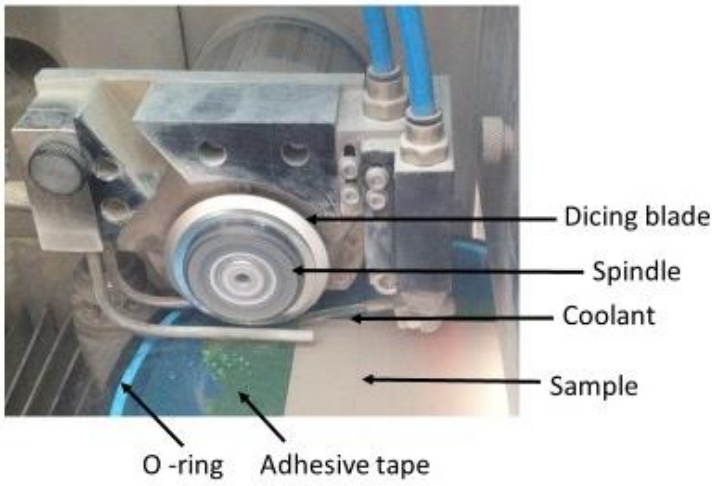

Figure 4.4: MicroAce 66 dicing saw in operation.

3 mm^2 samples of LNO were lapped, polished and were diced into sixteen sided polygons to obtain a structure very similar to a circle with a diameter of 3 mm. Techniques such as laser cutting can be employed to cut circles and laser cutting is more reliable and faster, but due to the lack of equipment traditional dicing was employed to make approximately circular transducers. The dicing was performed using a metal blade of thickness 10 µm, with a cut depth of 70 µm, spindle speed of 7000 rpm and a coolant

feed rate of 0.2 l/min. Sixteen sided polygons were diced by rotating the square sample at 45^0, 22.5^0 and 67.5^0 respectively in positive and negative axis. The angles and cuts which were used to make a sixteen sided polygon along with the finished sample are shown in Figure 4.5. The spindle speed and the feed rate were optimized, to avoid delamination of Cu electrodes on the substrate. The diced samples were then coated with desired thickness of Cu and parylene.

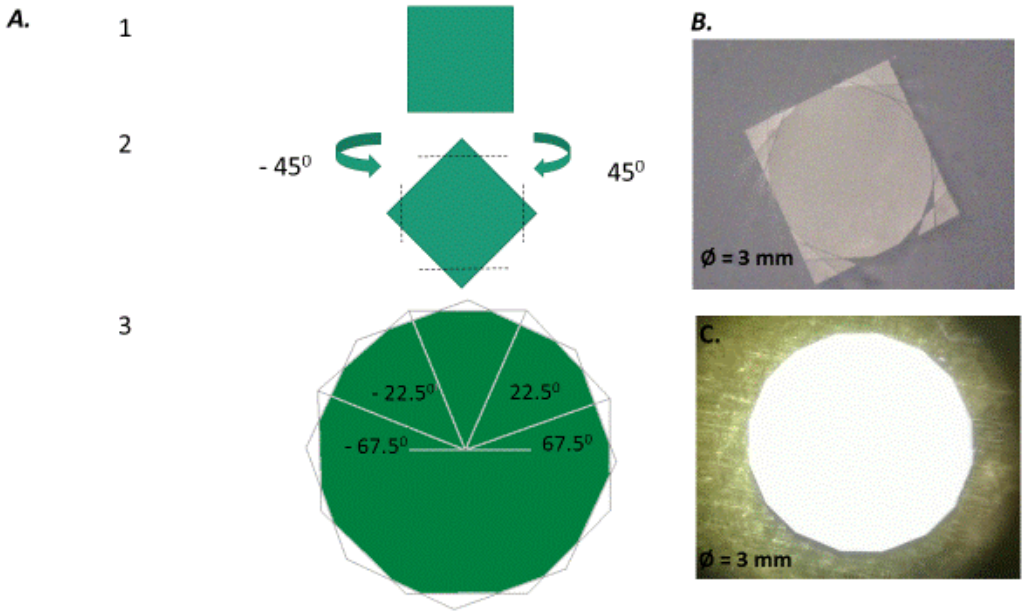

Figure 4.5: ***A****. Schematic describing the angles which were used to dice the piezoelectric sample into sixteen sided polygons. Dotted lines in step 2 show the position of cuts made when the sample was rotated at 45^0 angle in positive and negative axis. In step 3 the sample was further rotated and diced at 22.5^0 and 67.5^0 in the positive and negative rotation directions respectively to obtain a sixteen sided polygon.* ***B****. Diced sample with all the cuts.* ***C****. Sixteen sided polygon of 3 mm width after all the edges were removed.*

4.3.4 Vacuum Deposition of Parylene

Parylene is the generic name for polyparaxylylene. It was discovered in 1947 by a British chemist at the University of Manchester. For medical applications, parylene is a preferred coating material as it is bio-compatible. Parylene is an FDA approved class 6 material. The physical and mechanical properties of parylene are listed in Table - 4.3. A layer of parylene or a spring layer for mass-spring matched transducers was deposited on transducers with Cu mass layer using the SCS Labcoter parylene coater (SCS Coating Systems, Indianapolis, IN) (Figure 4.6). The parylene coating machine does not

have a thickness monitor and therefore there are no easy means of monitoring the thickness. In order to control the thickness of parylene, it was necessary to have a calibration curve of the parylene thickness inside the chamber for a given mass of parylene dimer. The calibration curve is shown in Figure 4.6 (B). The calibration curve was developed by increasing the mass of parylene dimer in steps of 1 g.

The mass of the dimer was increased up to 20 g. The thickness of the glass slide after deposition at every step was measured using a contact gauge (CG-10, Logitech Ltd. Glasgow, UK). The parylene calibration curve showed a linear relationship between the parylene dimer and parylene layer thickness. It was concluded that 1.9 g of parylene was required to deposit 1 µm of parylene with an error of ± 10%. The calibration curve will be dissimilar for different parylene coaters of the same model.

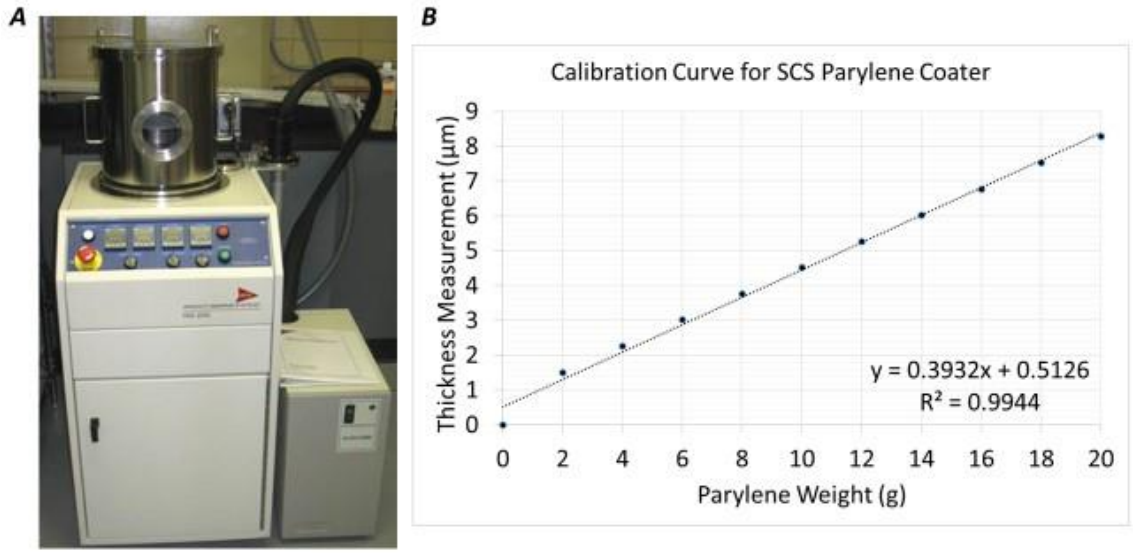

Figure 4.6: SCS parylene coating machine. ***A.*** *Vapour deposition process of parylene allows parylene to be uniform in thickness and pinhole free.* ***B.*** *Calibration curve for the parylene coating machine developed by increasing the parylene dimer load in the machine in steps of 1g up to 20 g. Parylene was coated on a glass slide and the thickness was measured using a contact gauge.*

Table 4.3: Physical and mechanical properties of parylene (C) which was used as a spring layer for mass-spring matched transducers.

Physical and mechanical properties	**Parylene (C)**
Tensile Strength, MPa	69
Density, g/cm^3	1.289
Acoustic Impedance, MRayl	2.75
Longitudinal Velocity, m/s	2135

4.3.5 E-Beam Evaporation

Electron beam (E-beam) evaporation is a process in which a target material is bombarded with an electron beam given off by a tungsten filament under high vacuum. The electrons dissipate their kinetic energy in the target material which causes the atoms to evaporate. The atoms in the gaseous phase precipitate into a solid form coating everything in the line of sight with a thin layer of the anode material. In the work described here, copper (Cu) target disc was placed at the bottom of the chamber (Figure 4.7). Prior to the process of evaporation, the chamber was closed and evacuated to ensure an oxygen free atmosphere. A high voltage of 1000 V was applied to the cathode. When the pressure of the chamber reached 0.8 µtorr, E-beam was made to strike the Cu target causing the Cu atoms near the surface to separate from the disk and create a thin film. The thickness of the coating was monitored using a precise thickness monitor.

The LNO samples to be coated with Cu electrodes were cleaned thoroughly using the two solvent method. Cleanliness of the sample ensures good adhesion of thin film. Solvents can clean organic and inorganic contaminants such as: oil, dust, and organic residues. These contaminants are mainly present from stains and finger prints. The LNO sample was first cleaned with acetone and the residual acetone was removed using isopropanol. The sample was then allowed to dry and wiped clean using cotton buds. The dried samples were rinsed with water and blow dried with compressed air to ensure a clean surface. The cleaned LNO sample was bonded onto a glass substrate and heated

to 50^0 C to remove any remaining water molecules and was placed in the sample holder of the E-beam evaporator.

Cu electrodes of thickness 500 ± 20 nm were coated on the front face of the transducer for unmatched and λ/4 matched transducer. Thin layer of Cu matching layer for the mass-spring matched transducers were deposited using the E-beam evaporator (Mantis Deposition LTD, Oxfordshire, UK). E-beam deposition technique was also used for applying novel matching layers for high frequency transducers. The thickness of the mass layer was 1.8 µm for transducers operating at 45 MHz and was controlled accurately using the thickness monitor. For coating the mass layer the transducers were first coated with Parlyene, bonded to a glass substrate and placed in the sample holder. The chamber was pumped down using a cryo pump. The vacuum pressure for deposition of mass layer and electrodes was maintained at 0.8 µtorr.

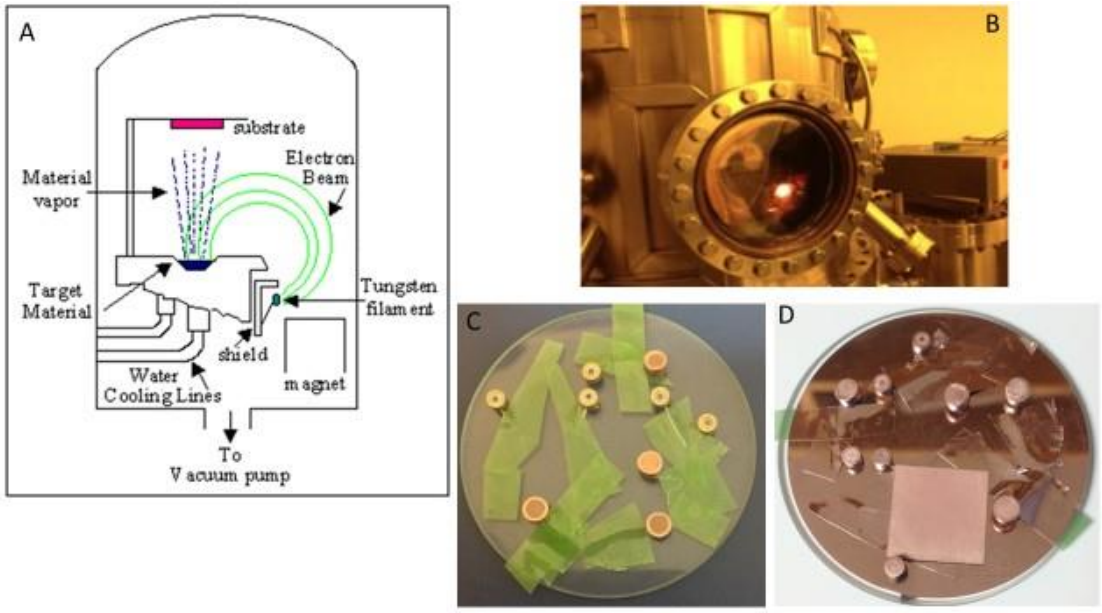

*Figure 4.7: **A**. Schematic of E-beam evaporation process **B.**E-Beam evaporator used for the deposition of Cu electrodes and Cu mass layer. **C.** LNO µUS transducers bonded to a glass substrate and ready to be placed into the E-beam evaporator for Cu electroding. **D.** Samples with evaporated thin film of Cu.*

4.3.6 Electrode

The surfaces of the active element were electroded by sputtering copper or gold. The electrode layer should be kept thin to avoid loading effects on the acoustical properties

(Knapik et al. 2000). Thin film electrodes of Cu were coated on one of the sides of the active element using E-beam deposition technique described previously.

The thin film coating on one of the sides of the active element was important for electrical linkage to driving electronics. E-beam deposition (Mantis Deposition LTD, Oxfordshire, UK) was used for the deposition of Cu electrode. The thickness of the Cu electrode was 500 ± 20 nm and the thickness was controlled using a very accurate thickness monitor. Using thin Cu electrodes provides a better connection when compared to silver paint electrodes. Cu has an acoustic impedance of 41 MRayl and a longitudinal sound velocity of 4660 m/s. Cu has a higher acoustic impedance relative to LNO (34 MRayl) therefore, it is important to have thin layers of electrode to avoid undesirable loading effects on the acoustic properties of the transducer.

4.3.7 Focusing

In the press focusing technique the active element is pressed onto heated spherical steel bearing of known diameter to form a focused structure. This technique is commonly employed for hard materials such as LNO. Press focusing usually leads to cracking of the active element, but no change in acoustic properties or deterioration in the performance of the transducer has been seen (Lockwood et al. 1994).

In the work reported here, unmatched and matched LNO transducers were curved using the press focusing technique to obtain a geometric focus at 7 mm. The technique used is similar to that described by Cannata et al., (Cannata et al. 2001). The active element was first diced into an approximately circular disk of 3 mm width and was then pressed on to a heated (75^0C) steel ball bearing 14 mm in diameter (Figure 4.8) to achieve a geometric focus of 7 mm.

Micro-fractures occur on the active element, given its thickness of 69 µm. The active element was then cooled to room temperature and a 1 mm thick backing layer of silver epoxy was cast onto the active element. The low f- # (f- # = 2.33) design results in high energy density of the ultrasound beam and good sensitivity of the transducers but a relatively shallow depth.

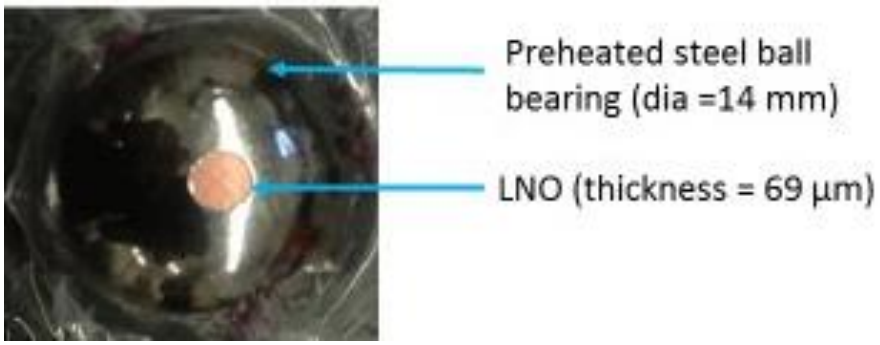

Figure 4.8: Circular disk of LNO of diameter 3mm is pressed on to a steel ball bearing at 75^0C, to form a focused structure. After the ball bearing cooled, a backing layer was cast on the surface. The sample retained the curved structure after it was dismounted from the ball bearing.

4.3.8 Backing Layer

The ultrasound pulses generated by the transducer can be damped efficiently by using lossy backing materials whose acoustic impedances are comparable to that of the active material. The backing layer also provides mechanical strength so it is important that it is present.

The backing layer of the µUS transducers were made from conductive silver epoxy (E-solder 3022, Van Roll, New Haven, CT). The acoustic impedance of the backing layer is 5.9 MRayls with a longitudinal sound velocity of 1850 m/s. This material is made up of silver flakes of 10 µm in size. The silver flakes result in low electrical resistivity and are likely the source of high acoustic attenuation. A second layer of backing layer was applied by mixing 3 µm alumina particles with epoxy, with a 2:1 weight ratio and applying it to the E-solder backing layer.

The back surface of the active element was thoroughly cleaned using isopropanol and distilled water successively before the application of conductive silver epoxy. The thickness of the backing layer was approximately 1 mm. Curing of the backing layer was done for four hours each at 40^0C, 50^0C and 70^0C. Curing at a temperature above ambient provides a more rigid substrate for subsequent processing. The incremental temperature increase increases the glass transition temperature of the silver epoxy and provides a rigid surface for subsequent processing techniques. The conductive silver epoxy provides additional support to the transducer and forms an acoustically lossy but electrically conductive backing layer. Electrical connects were made using low inductance silver wires of diameter 0.5 mm through the backing layer.

4.4 Quarter Wavelength Matching Layer

Matching layers are used to improve the bandwidth and sensitivity of the transducers. Dual λ/4 matching layer designs were considered in this study. The first step is to evaporate a Cu electrode layer of thickness 500 nm onto the front face of the piezoelectric substrate. The metalized layer of the piezoelectric substrate ensures good electrical contact. The matching layer thickness for the transducer operating at 45 MHz was calculated by using Equations *(3.21)* and *(3.22).* A diagram showing the transducer with backing layer, matching layers and the piezoelectric substrate is shown in Figure 4.9.

Figure 4.9: Different layers for λ/4 matched µUS transducer. Thin layers of silver epoxy and parylene approximate a dual λ/4 matching layer on the front face of the piezoelectric substrate.

Conductive silver epoxy (H2OE, Epoxy Technologies, MA, USA) Part A and Part B were mixed in 1:1 weight ratios and cast onto the front face of the electroded piezoelectric substrate. This layer was cured at 60 ^{0}C for four hours and then cured overnight at 40 ^{0}C. The matching layer was then lapped down to λ/4 thickness of 10 µm using the method described in section 4.3.2 the thickness of the substrate was continuously monitored using the contact gauge. The sample was then diced into 3 mm diameter approximately circular disk by using the technique described in Section 4.3.3.

The circular disks were then press focused using the technique described in 4.3.7. A conductive silver epoxy (E-solder 3022, Von Roll Isola Inc., New haven, CT, USA) was then applied as a backing layer and cured overnight. An electrical wire was inserted into the backing layer and was fixed by conductive epoxy. The acoustic stack was placed

into a brass casing and insulating epoxy (Epotek 301, Epoxy Tech., MA, USA) was used to fill the gaps between the housing and the device. A thin layer (500 nm) of Cu electrode was then applied using E-beam evaporation on to the front face. Then a second matching layer of 12 µm parylene was deposited on the front face using the SCS labcoater parylene coater (SCS coating systems, Indianapolis, IN).

4.5 Theory of Mass-Spring Matching Layer

The difficulty in producing conventional matching layers of consistent quality has led to the development of a new acoustic matching layer approach which has been developed recently (Toda & Thompson 2010). This uses thin alternating soft and dense layer materials, similar to "mass-spring" resonators.

The spring layer is a soft layer and the spring's thickness is controlled by adjusting its thickness. The spring stiffness is similar to the mechanical impedance of a quarter wavelength matching layer. In order to create a phase shift across the resonator a dense material is applied to the spring layer to create resonance and is called the "mass". An 180^0 phase shift can therefore be created with any thickness of the spring layer by adjusting the thickness of the mass layer accordingly. As the layer thicknesses are thin, the 360^0 phase shift required for constructive interference generally results from the two 180^0 phase shift in the resonant mass-spring system. In summary any quarter wavelength matching layer thickness and impedance can be very closely approximated with an appropriate mass-spring layer combination. This approach of fabricating mass-spring matched transducers has been used for mass-spring layers with alternating polymer (polyamide) and metal layers (brass) in low frequency ultrasound transducers.

Toda and Thompson suggested that its biggest advantage is that, the ideal acoustic impedance of the first layer in a dual matching layer system can be achieved with alternating layers of polymer and metal. This is significant because materials in the acoustic impedance range of ~ 9 MRayl are not readily available and loaded epoxies tend to be acoustically lossy. In the study of Toda et al., the matching layer approach was experimentally demonstrated at low frequencies by gluing the thin mass-spring matching layers to the PZT substrate. In this thesis a similar matching layer scheme for high frequency transducers was experimentally determined using controlled vacuum deposition (Brown et al. 2014). The model of the mass-spring layer is illustrated in Figure 4.10.

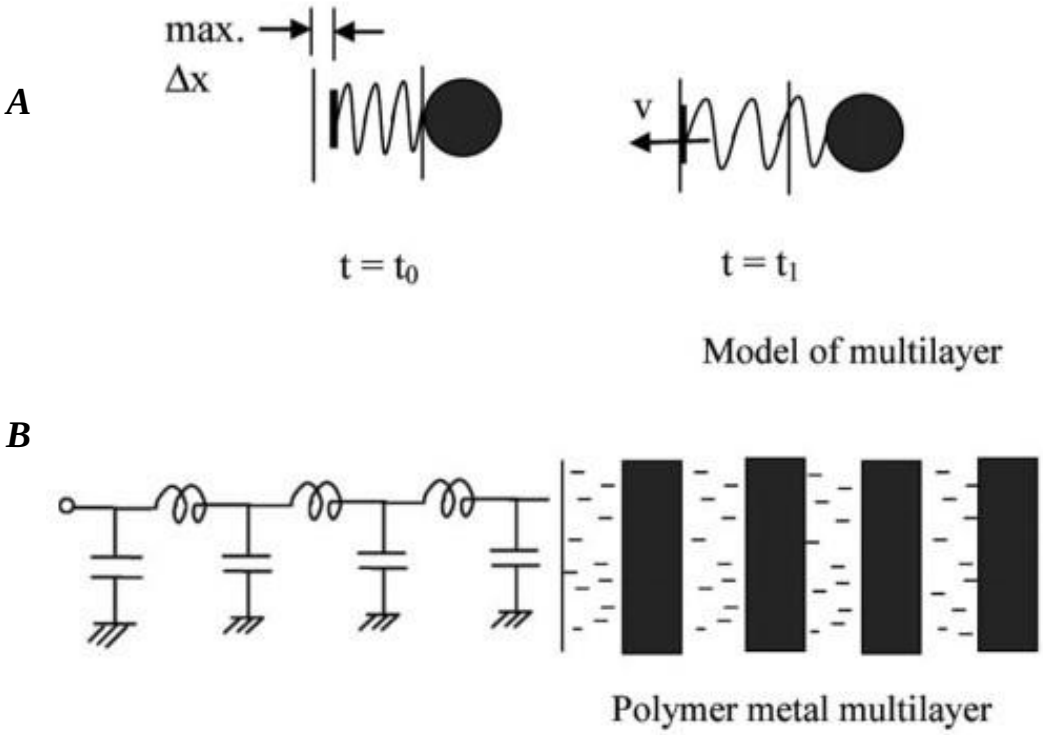

Figure 4.10: ***A.*** *Mass-spring model for polymer (spring) metal layer (mass) showing the timing relation at resonance.* ***B.*** *Equivalent inductance and capacitance (LC) circuit representation of mass-spring layer alongside a multilayer model of metal and polymer (Toda & Thompson 2010).*

In Figure 4.10(A) a spring with length L joined to a mass is displaced through a continuous sinusoidal movement. Resonance occurs when $t = t_o$, due to the spring forcing the mass to accelerate to the right and the force exerted by the spring is maximum. The displacement of the mass is delayed relative to the phase of the applied spring displacement. Due to the phase delay the mass opposes the displacement of the driven end of the spring at $t = t_1$. The impedance of the driven end of the spring is the ratio of force exerted by the spring to its vibration velocity. The amplitude of the mass vibration is maximum at the resonant frequency. This makes the assumption that the soft spring layers are virtually massless in comparison to the dense layer and the dense layer is incompressible in comparison to the spring layer. The resonant frequency of the mass-spring system is determined by Equation *(4.2)*:

$$f_0 = \frac{1}{2\pi}\sqrt{\frac{\frac{\rho_s v^2{}_s}{t_s}}{\rho_m t_m + 0.4\rho_s t_s}} \qquad (4.2)$$

In the equation, f_o is the resonance frequency, ρ_s and ρ_m are the densities of the spring layer and mass layer respectively, t_s and t_m are the thicknesses of the spring layer and mass layer respectively and v_s, is the speed of sound in the spring layer.

Equation *(4.2)* is an expanded form of Hooke's law for a mass-spring system where the resonant frequency is dependent on the spring constant in the numerator and mass in the denominator. In the equation the denominator has been modified with a factor of 0.4 to account for an effective increase in the mass resulting from the polymer layer which is bound to the mass near the boundary between the two. It should be noted that equation in (*4.2)* provides a relationship between the required mass thicknesses for any given thickness of spring layer in order to resonate at a specific frequency.

In the work of Toda and Thompson, they also derived a formula for the mechanical input impedance, Z_{in}, at the driving spring end in a mass-spring layer combination, which is given in (*4.3).* Z_{load} is the load impedance of the layer that is being driven by the mass-spring combination.

$$Z_{in} = \frac{\rho_s {v_s}^2}{t_s Z_{load}} (\rho_m t_m + 0.4 \rho_s t_s) \qquad (4.12)$$

It should also be noted that the input impedance Z_{in} is related to the ideal quarter-wavelength acoustic impedance by:

$$Z_{in} = \frac{{Z^2}_{1/4\lambda}}{Z_{Load}} \qquad (4.13)$$

By combining Equations *(4.3)* and *(4.4),* an expression can be obtained for the ideal quarter wavelength impedance in terms of the thickness and mechanical properties of the mass spring combination:

$${Z^2}_{1/4\lambda} = \frac{\rho_s {v_s}^2}{t_s} (\rho_m t_m + 0.4 \rho_s t_s) \qquad (4.14)$$

By rearranging the terms in Equation *(4.5)*, a relationship between the spring layer thickness, t_s, and mass layer thickness, t_m, can be obtained:

$$(\rho_m t_m + 0.4\rho_s t_s) = \frac{Z^2{}_{1/4\lambda} t_s}{\rho_s {v_s}^2} \qquad (4.6)$$

To obtain an expression for the required thickness of spring layer, we can simply substitute Equation *(4.6)* into Equation *(4.4)* and solve for the required spring thickness, t_s, as a function of the ideal quarter wavelength impedance $Z_{1/4\lambda}$:

$$t_s = \frac{\rho_s {v_s}^2}{Z_{1/4\lambda} 2\pi f_0} \qquad (4.7)$$

The ideal quarter wavelength acoustic impedance could be any λ/4 matching layer in a multiple quarter wavelength scheme. The thickness of the mass layer is given by substituting the value of t_s, in Equation *(4.6)*, and is found to be:

$$t_m = \frac{\rho_s {v_s}^2}{t_s \rho_m (2\pi f_0)^2} - \frac{0.4\rho_s t_s}{\rho_m} \qquad (4.8)$$

As the materials used in this scheme are single-phase metal and polymer, the elastic energy loss will be much less than for multiphase composite materials, which are often used in traditional quarter wavelength matching layers, and therefore a high efficiency transducer with greater sensitivity and bandwidth and low insertion loss is expected. With the use of combined layers of mass and spring model, the low impedance of the propagation medium (e.g. tissue) can be converted to high impedance at a designed centre frequency using Equations (*4.2)* to (*4.8)* by choosing the correct combination of thicknesses.

Prior to the application of this model experimentally to fabricate μUS transducers the theory was compared with data from a KLM model with good agreement. Only single and dual quarter wavelength matching layer designs were considered in this study.

4.5.1 Mass-Spring Matching Layer

In order to overcome these problems with conventional λ/4 matching layers a new scheme of matching layers called the "mass-spring" matching layer was designed, developed and investigated for high frequency applications in this thesis.

The concepts of matching layer designs implemented in this research was described in Section 4.5 and is similar to the designs described by Toda et al., (Toda & Thompson 2010) but with two main differences. Firstly, the matching layers were designed for μUS transducers operating at 45 MHz in order to replace the traditionally matched λ/4 matched transducers as they are cumbersome to fabricate and secondly, controlled vacuum deposition techniques were used to deposit the matching layers. Parylene was used as the "spring" layer and Cu for the "mass" layer. These materials were chosen as they can be readily deposited using a vacuum deposition system. Single and dual λ/4 mass-spring matching layer for single element transducers has been considered in this study.

The first design incorporated a mass-spring matching layer combination approximating to single λ/4 matching layer with the acoustic impedance calculated using Equation (*3.21)*. The λ/4 acoustic impedance was calculated to be 4.25 MRayl. Substituting this impedance into Equation (*4.5)* and using the material properties listed in Table-4.1, the required parylene thickness was determined to be 3.8 μm. The calculated thickness of the parylene was substituted into Equation (*4.6)* to obtain the thickness of Cu or the mass layer. The required thickness of the Cu layer deposited was 1.4 μm. A diagram illustrating the equivalent single λ/4 mass-spring matching layer is shown in Figure 4.11. For coating the mass layer the transducers were first coated with parylene, bonded to a glass substrate and placed in the sample holder of the E-beam evaporation chamber. The chamber was pumped down using a cryo pump. The vacuum pressure for deposition of the mass layer was maintained at 0.8 μtorr.

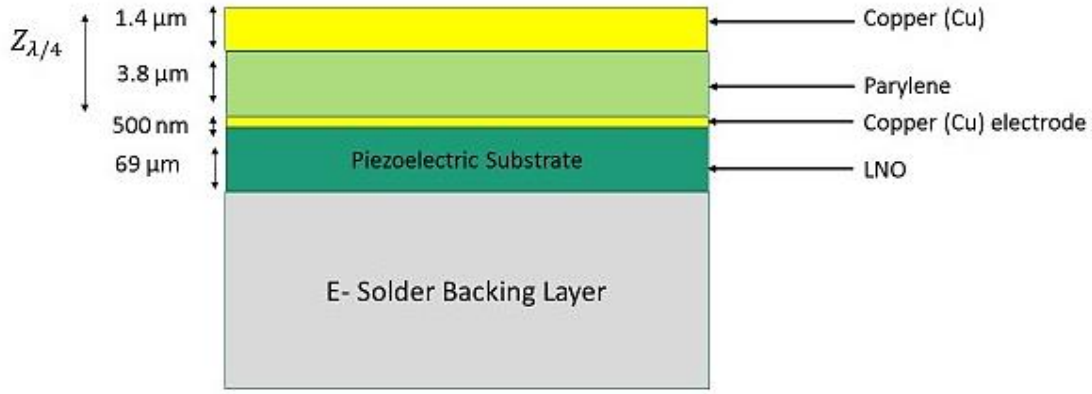

Figure 4.11: A 45 MHz single element LNO µUS transducer with an effective single λ/4 mass-spring matching layer. Thin layer of parylene followed by a thin layer of Cu approximate a single λ/4 matching layer.

The second matching layer system investigated was an effective dual λ/4 matching layer system. The ideal acoustic impedance for λ/4 matching layer in a dual matching system was calculated by substituting the known piezoelectric and tissue impedances in Equation (*3.22).* After substituting the matching layer impedances of: $Z_{1/4\ \lambda\#1}$ = 8.92 MRayl and $Z_{1/4\ \lambda\#2}$ = 2.34 MRayl in Equations *(4.7)* and *(4.8),* the required thicknesses of parylene and Cu were obtained: $ts_{\#1}$ = 1.8 µm, $tm_{\#1}$ = 2.9 µm, $ts_{\#2}$ = 7 µm, $tm_{\#2}$ = 0.42 µm. This multi-layer combination is a good approximation to a dual λ/4 matching layer configuration.

The drawback of this design was that, while testing the transducers, the outer layer of copper, which was deposited onto a smooth parylene layer, either eroded or oxidize after an hour or less of testing. Ideally parylene as the outer layer is preferred as it provides an electrical insulation and acts as a moisture barrier between the transducer and the couplant. As the acoustic impedance of parylene was close to the desired acoustic impedance of the second layer of a dual matching layer system (desired Z1/4λ#2 = 2.34 MRayl and parylene Z = 2.65 MRayl) this allowed a mass-spring matching layer to be used to approximate the first λ/4 matching layer of 1.8 µm parylene and 2.9 µm copper and a conventional λ/4 matching layer of parylene as the second λ/4 layer of thickness ~12 µm parylene. This resolved the issues of erosion and oxidation of the Cu layer being on the top of the transducer stack. The multilayer stack of dual matching layer scheme is shown in Figure 4.12. Both planar and press focused µUS transducers were fabricated with matching layers.

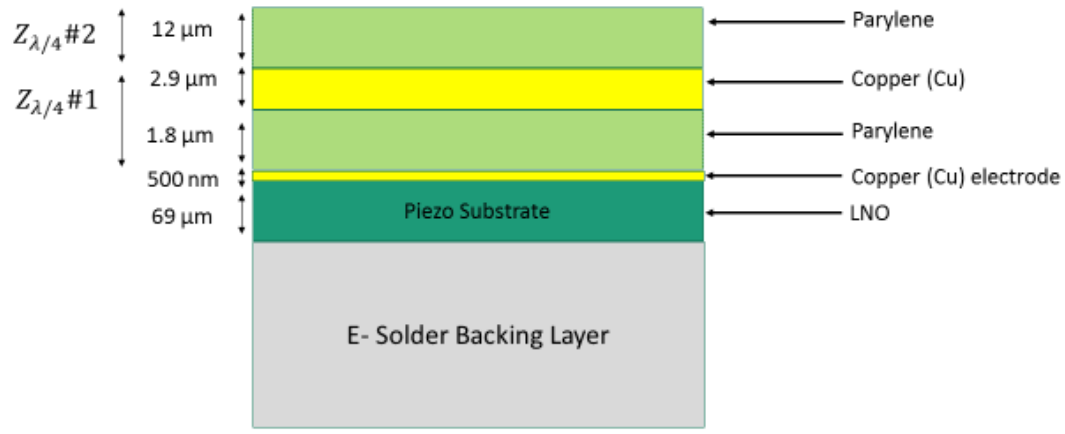

Figure 4.12: A 45 MHz single element LNO µUS transducer with a dual λ/4 mass-spring matching layer.

4.6 KLM Model

Computer modelling is important in design of transducers. Computer models allows prediction of the electrical and acoustic properties of the transducers with a high degree of precision. These predictions allow evaluation of the performance of the transducers. The KLM model has been used extensively for the design of imaging ultrasound transducers (Lockwood & Foster 1994). The KLM model was designed by Krimholtz, Lee and Matthaei in 1970 (Oakley 1997).

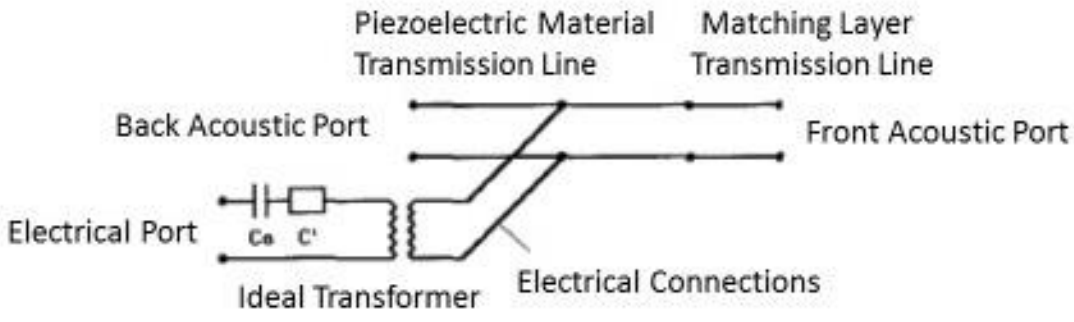

Figure 4.13: A schematic of KLM model (Oakley 1997).

KLM model has been designed as several alternative circuits for piezoelectric transducers, in the form of thickness-expander plates, end-electroded bars and side electroded bars which incorporate the effects of the acoustic transmission line. The

KLM model basically comprises the circuit elements between the pulse generator, V_s, and the impedance load of the water seen at the matching layer Z_W.

All acoustic layers including the active element are treated as transmission lines with lengths that equal the thickness in wavelengths and their impedances as characteristic acoustic impedance. The backing layer and the water interface are represented as impedance loads. Simulation with these models allows the pulse shape at the front face of the transducer to be calculated. The pulse shape, frequency and amplitude of the input can be modified in the KLM model along with the thickness of the active element and the impedance of the backing layer. This allows for the testing of various configurations of transducers prior to fabrication and helps save time and minimises the manufacturing cost.

The main advantage of KLM model is that the electrical and acoustical parts of the transducer can be separated. Three sections can be seen in Figure 4.13, an electrical group and two acoustic groups extending to the left and right from the centre. More detailed explanation of this model can be found in Leedom et al (Leedom et al., 1970).

To assess the performance of μUS transducers and the effects of matching layers an in-house KLM model, developed at Dalhousie University, Canada, built-up using Python script was used. The electrical impedance magnitude and phase along with the two way pulse-echo was measured to evaluate the bandwidth of the transducers. The relevant material parameters of LNO, backing layer and matching layers is listed in Table 4.1 and 4.2. In the KLM model the piezo-material properties are defined by the dielectric loss, h_{33}, $\varepsilon_{33}{}^{T}$, Q_m, density and speed of sound. Coupling coefficient k_t was experimentally measured and was used in the model. The passive materials were defined by density, speed of sound and approximate quality factor, which is the ratio of the stored energy to dissipated energy. An excitation voltage of 10 V and electrical load resistance of 50 Ω were used in the simulations.

4.7 Functional Transducer Characterisation

The transducers fabricated during this project were characterised for electrical impedances, resonant frequency, ultrasound beam profile, insertion loss, pulse shape and line spread function. The experimental values obtained were compared with the

results from the KLM model. The following sections discuss the above mentioned methods that were used for characterisation in detail.

4.7.1 Electrical Impedance Spectroscopy

An Agilent 4395A impedance / network / spectrum analyser (Agilent Technologies, Edinburgh, UK) was used for characterising the transducers. The set-up used is shown in Figure 4.15. For each of the transducers fabricated impedance magnitude and phase was measured. The frequency range chosen was at least $3f_a$, where f_a, is the anti-resonant frequency to enable measurement of harmonic resonance data. The impedance analyser is connected to the computer through a general purpose instrumentation interface bus (GPIB) connection which means that the measurements can be saved on to the computer. The µUS transducers with SMA connection were connected using hook clips to the impedance analyser. Prior to each measurements the impedance analyser was calibrated. A maximum of 801 data points were recorded over the selected frequency range.

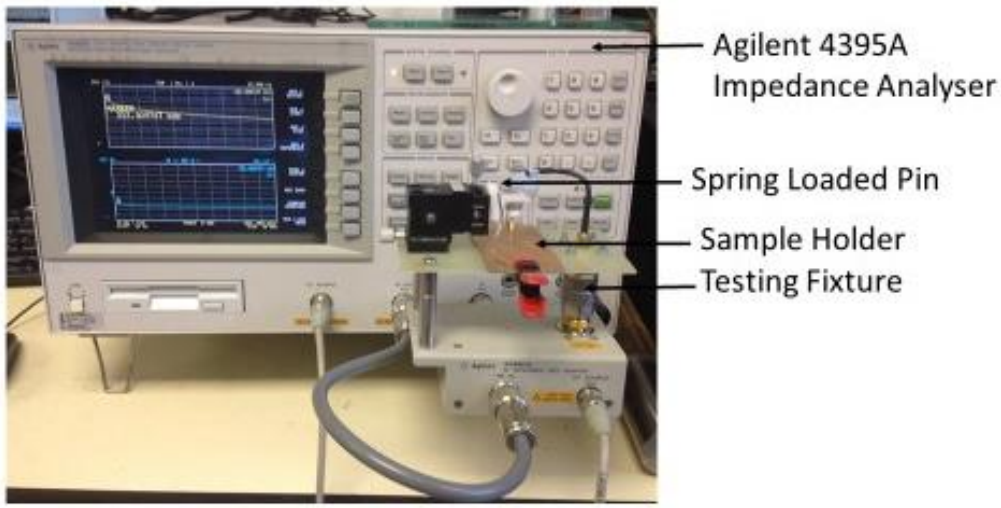

Figure 4.14: Electrical Impedance analyser with fixture for testing the impedance and phase response of µUS transducers and active element.

4.7.2 Insertion Loss Measurements

The two-way insertion loss was calculated from the ratio of the received pulse spectrum to the source spectrum at the output of the pulser. The technique used is similar to the approach reported by Sherar et al., (Sherar 1989) and does not include compensation of

losses due to diffraction. The two way insertion loss of the transducer was performed in pulse-echo mode. Transducer excitation was achieved with a multi-cycle sine wave burst using a pulse generator (BP1, Daxsonics Inc., Halifax, NS) with 50 Ω coupling and reflection off an X-cut quartz flat situated at the focal point of the transducer. The ultrasonic coupling medium was degassed distilled water.

The received waveforms were digitized at 500 MHz and recorded using a Tektronix oscilloscope (MDO 3000, Tektronix, USA). The schematic of the set-up is shown in Figure 4.16. The cable length between the function generator and the oscilloscope was about 15 cm. The signal loss due attenuation in the water bath was compensated as 2.2 x 10^{-4} dB/mm-MHz^2 (Lockwood et al. 1994). The insertion loss for each transducers was determined from the data recorded using the Equation *(4.9).*

$$insertion\ loss = 10\,log\left(\frac{\frac{V^2{}_{out}}{R_{out}}}{\frac{V^2{}_{in}}{R_{in}}}\right) = 20\,log\left(\frac{V_{out}\sqrt{R_{in}}}{V_{in}\sqrt{R_{out}}}\right) \qquad (4.9)$$

In Equation *(4.9), V* denotes voltage, and *R*, is the resistance value used to measure the input or output voltage. $R_{in} = R_{out} = 50\ \Omega$, therefore the insertion loss is measured as the ratio of the input and output voltages.

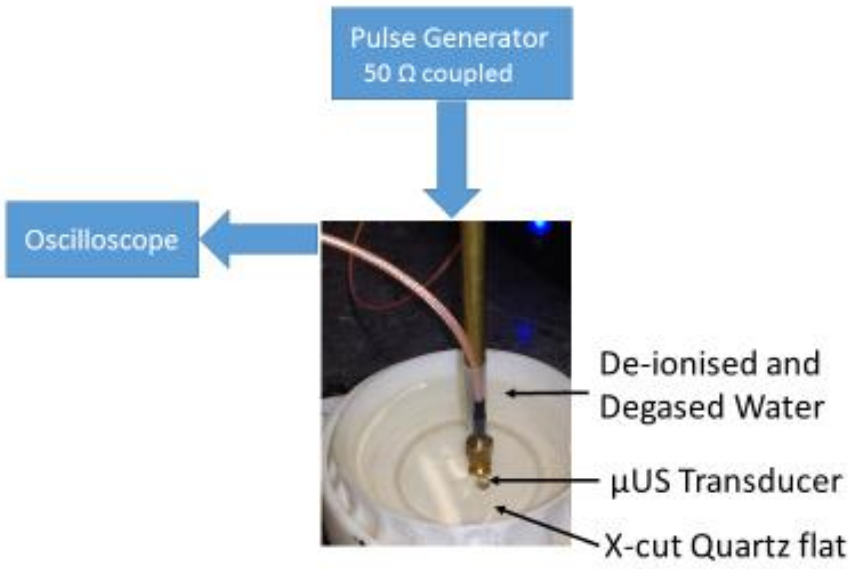

Figure 4.15: Set-up used to measure insertion loss of transducers in pulse echo mode. The Transducer excitation was achieved with multi-cycle sine wave burst using a pulse generator (BP1, Daxsonics Inc., Halifax, NS) with 50 Ω coupling and reflecting pulse from X-cut quartz flat situated at the focal point of the transducer.

4.7.3 Pulse Shape

The pulse shapes of the μUS transducers were examined in pulse-echo mode for all transducers fabricated in this thesis. The echoes were collected by reflection from X-cut quartz flat placed at each transducer's focal point. The experimental focal point was determined by observing the amplitude of the received signal and recording the signal where the signal was maximum. For planar transducers the measurements were recorded at a point beyond the near field boundary. The axial resolution of the transducers were determined from the data recorded using Equation *(4.10)*.

$$R_a = V_t t_p \qquad (4.10)$$

V_t, is the velocity of ultrasound in the tissue and t_p, is the time duration of the decay for the pulse amplitude at -6 dB from its maximum amplitude. The transducers were driven by a DPR500 pulser receiver (JSR, Pittsford, NY, USA). The load impedance of the remote pulser is 100 Ω. The transducer was connected to the remote pulser via SMA connector. The signals were recorded using an Agilent HP 54810A infinium oscilloscope (Santa Clara, CA, USA).

The experimental pulse shapes recorded were then compared with simulated data obtained by KLM modelling. The acoustical parameters of the backing and matching layers used were known and were incorporated in the KLM model. The pulse amplitudes were normalised and expressed in dB using Equation *(4.11)*.

$$Amplitude\ (dB) = 20\ log_{10}\ (normalised\ signal) \qquad (4.11)$$

4.7.4 Tungsten Wire Scanning

A Tungsten wire target of 5 μm diameter were used to measure the line spread function of the transducers. Tungsten was chosen as it has a very high acoustic impedance (101 MRayl) and is thus highly reflective (Cannata et al. 2006). To hold the tungsten wires in place, a wire phantom holder was designed using Solidworks (Waltham, Massachusetts, USA). The wires were placed on the holder in a stepped fashion such that the separation distance between the wires both laterally and axially was maintained at 1 mm (Figure 4.16). The wire phantom was fabricated using a rapid prototyping process. The design of the wire phantom was done using computerised Solidworks software. The 3D model Solidworks file was fed into the Rapid prototyping machine by

creating sliced layers of the model. The first layer of the physical layer is created and then lowered by thickness of the next layer and the process is repeated until the completion of the model. The model is removed from the rapid prototyping machine is cleaned and finished by removing the edges by filing. For the wire attachment, a wire guide was used to hold the tungsten wires on each side of the frame.

The wire phantom was fabricated for the purpose of beam profiling. The reflections from the phantom can be detected up to 12 mm axially, which is large enough to cover the depth of field of a focused transducer. The tungsten wires were carefully fastened into the groves of the wire phantom. The wire phantom was submerged in degassed water and a B-scan of the wires was recorded from a fixed focus of the transducer. Wire scans were performed for focused transducers.

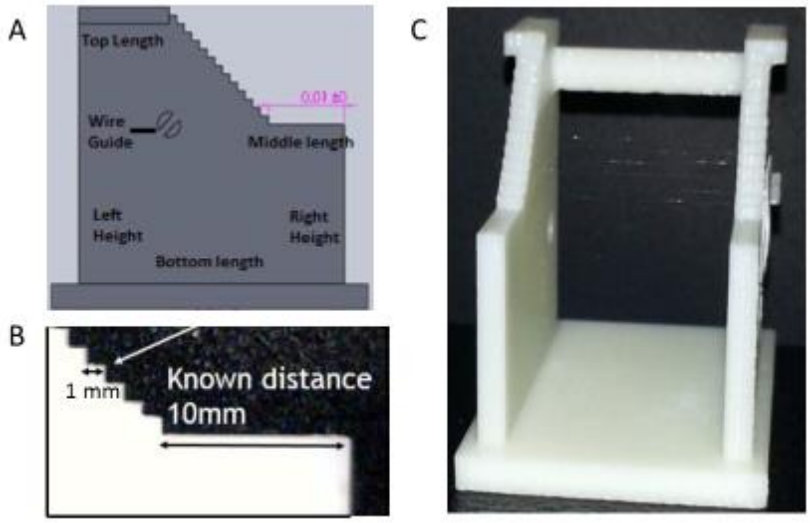

Figure 4.16: Diagram of wire phantom used for the evaluation of beam profile, DOF and point spread function of transducers. ***A.*** *Solidworks design of wire phantom,* ***B.*** *Measurement of separation distance between each step was maintained at 1mm.* ***C.*** *Tungsten wire phantom frame fabricated by rapid prototyping.*

4.7.5 Depth of Field and Line Spread Function

The depth of field (DOF) of the transducers was measured by recording the echoes reflected from an X–cut Quartz surface at a range of axial distances. By altering the height of the stage, in increments of 0.25 mm, the reflected signal amplitude was measured. Measurement of the signal amplitude at each depth was done by taking the averaged peak-to-peak amplitude from the oscilloscope. The reflected amplitude was recorded and plotted versus the axial position of the transducer.

The line spread function (LSF) was recorded by operating the transducers in pulse-echo mode with reflected signals from 5 μm tungsten wire targets suspended in water. Transducer was positioned such that the tungsten wires were at the focal point. The transducer was moved laterally (X-axis) in both positive and negative directions, in steps of 20 μm. until no signal was detectable. The amplitude of the received echoes was then plotted against position. The line spread function provides a measure of the lateral resolution of the transducer.

4.8 Discussion

This chapter presented the materials and methods used for fabrication of high resolution μUS transducers. Three different configurations of transducers were designed, modelled and fabricated namely; high resolution single element μUS without matching layer, with λ/4 matching layer and with novel mass-spring matching layer transducers. The process routes employed for the fabrication of the above mentioned schemes have been explained in this chapter.

The transducers were press focused. Lens focusing was avoided because lens focused devices have lower sensitivity (Cannata et al. 2003). This is most likely due to varying thickness of lens which causes attenuation of ultrasound as the beam passes from the centre to the edges of the active element. Additionally, fabricating epoxy lenses that are bubble free and have uniform surface roughness is challenging.

Conventional ultrasound matching layers comprise one or more λ/4 thick layers of passive materials with acoustic impedances, comparable to the acoustic impedance of the piezoelectric substrate and tissue. The layers of conventional λ/4 matched transducers are very thin and therefore require very precise machining, with any variations in the thickness resulting in degradation of the acoustic beam, band width and sensitivity of the transducer.

One of the layers of conventional λ/4 matching layers is made up of loaded epoxy but the attenuation of ultrasound in epoxies is high due to scattering. The production of conventional λ/4 matched transducers is time consuming and they cannot be fabricated in bulk. To overcome the difficulty in fabricating conventional λ/4 matched transducers a new design approach of matching layer called the mass-spring matching layer was implemented in this thesis.

4.9 Conclusion

The techniques used for fabricating single element 45 MHz μUS transducers with and without matching layers have been discussed. A new technique of matching layer design using vacuum deposition techniques to deposit the matching layers to overcome the difficulties with conventional matching layers has been discussed. This technique provides with distinct advantages. The thicknesses of the matching layers can be precisely controlled and multiple matching layers can be easily deposited through vacuum evaporation. The techniques used for modelling and characterising the transducer were explained. The results of fabrication and transducer performance are presented in Chapter 5.

4.10 References

Abrahams, S. C., Levinstein, H. J., & Reddy, J. M. (1966) "Ferroelectric lithium niobate. 5. Polycrystal X-ray diffraction study between 24° and 1200° C." *Journal of Physics and Chemistry of Solids*, *27*(6), 1019-1026.

Bernassau, A. L., Garcia-Gancedo, L., Hutson, D., Demore, C. E., McAneny, J., Button, T. W., & Cochran, S. (2012) "Microfabrication of electrode patterns for high-frequency ultrasound transducer arrays." *Ultrasonics, Ferroelectrics, and Frequency Control, IEEE Transactions on*, *59*(8), 1820-1829.

Brown, J., Chérin, E., Yin, J., & Foster, F. S. (2009) "Fabrication and performance of high-frequency composite transducers with triangular-pillar geometry." *Ultrasonics, Ferroelectrics, and Frequency Control, IEEE Transactions on*, *56*(4), 827-836.

Cannata, J. M., Chen, W.H., Ritter, T. A., & Shung, K. K. (2010) "Fabrication of high-frequency single element ultrasonic transducers using lithium niobate." *SPIE Proceedings Series*, 86–91.

Cannata, J. M., Ritter, T., Chen, W. H., Silverman, R. H., & Shung, K. K. (2003) "Design of efficient, broadband single-element (20-80 MHz) ultrasonic transducers for medical imaging applications." *Ultrasonics, Ferroelectrics, and Frequency Control, IEEE Transactions on*, *50*(11), 1548-1557.

Cannata, J. M., Ritter, T., Chen, W. H., & Shung, K. K. (2000, October) "Design of focused single element (50-100 MHz) transducers using lithium niobate." In *Ultrasonics Symposium, 2000 IEEE* (Vol. 2, pp. 1129-1133). IEEE.

Cannat, J. M., Williams, J., Zhou, Q., Ritter, T., & Shung, K. K. (2006) "Development of a 35-MHz piezo-composite ultrasound array for medical imaging." *Ultrasonics, Ferroelectrics, and Frequency Control, IEEE Transactions on*, *53*(1), 224-236.

Desilets, C., Fraser, J. & Kino, G. (1978) "The design of efficient broad-band piezoelectric transducers." *Sonics and Ultrasonics, IEEE*, (3), 115–125.

Kino, G. S. (1987) "*Acoustic waves: devices, imaging, and analog signal processing* (Vol. 107)." Englewood Cliffs, NJ: Prentice-Hall.

Garland, P. P., Bezanson, A. B., Adamson, R., & Brown, J. (2011, October). "Experimental and finite element model directivity comparison between PZT and PMN-PT kerfless arrays." In *Ultrasonics Symposium (IUS), 2011 IEEE International* (pp. 365-368). IEEE.

Jeong, S., Lee, H., Cho, H., Lee, S., Kim, H., Kim, S., & Jeong, H. (2010) "Effect of additives for higher removal rate in lithium niobate chemical mechanical planarization." *Applied Surface Science*, *256*(6), 1683-1688.

Knspik, D. A., Starkoski, B., Pavlin, C. J., & Foster, F. S. (2000) "A 100-200 MHz ultrasound biomicroscope." *Ultrasonics, Ferroelectrics, and Frequency Control, IEEE Transactions on*, *47*(6), 1540-1549.

Kossoff, G. (1966) "The effects of backing and matching on the performance of piezoelectric ceramic transducers." *Sonics and Ultrasonics, IEEE Transactions on*, *13*(1), 20-30.

Krimholtz, Richard, David A. Leedom, and George L. Matthaei. (1970) "New equivalent circuits for elementary piezoelectric transducers." *Electronics Letters* 6.13 398-399.

Lockwood, G. R., & Foster, F. S. (1994) "Modeling and optimization of high-frequency ultrasound transducers." *Ultrasonics, Ferroelectrics, and Frequency Control, IEEE Transactions on*, *41*(2), 225-230.

Lockwood, G.R., Turnbull, D.H. & Foster, F.S. (1994) "Fabrication of high frequency spherically shaped ceramic transducers." *IEEE Transactions on Ultrasonics, Ferroelectrics and Frequency Control*, 41(2), 231–235.

Lukacs, M., Yin, J., Pang, G., Garcia, R. C., Cherin, E., Williams, R., & Foster, F. S. (2006) "Performance and characterization of new micromachined high-frequency linear arrays." *Ultrasonics, Ferroelectrics, and Frequency Control, IEEE Transactions on*, *53*(10), 1719-1729.

Nassau, K., Levinstein, H.J. & Loiacono, G.M. (1966a) "Ferroelectric lithium niobate. 1. Growth, domain structure, dislocations and etching." *Journal of Physics and Chemistry of Solids*, 27(6-7), 983–988.

Nassau, K., Levinstein, H.J. & Loiacono, G.M. (1966b) " Ferroelectric lithium niobate. 2. Preparation of single domain crystals." *Journal of Physics and Chemistry of Solids*, 27(6-7), 989–996.

Oakley, C. G. (1997) "Calculation of ultrasonic transducer signal-to-noise ratios using the KLM model." *Ultrasonics, Ferroelectrics, and Frequency Control, IEEE Transactions on*, *44*(5), 1018-1026.

Pinel, S., Tasselli, J., Bailbé, J. P., Marty., A, Puech., P, & Estève., D. (1998) "Mechanical lapping, handling and transfer of ultra-thin wafers." *Journal of Micromechanics and Microengineering*, *8*(4), 338–342.

Qian, Y. & Harris, N.R. (2014) "Modelling of a novel high-impedance matching layer for high frequency (>30 MHz) ultrasonic transducers." *Ultrasonics*, 54(2), 586–91.

Sherar, M., (1989) "The design and fabrication of high frequency poly(vinylidene fluoride) transducers." *Ultrasonic Imaging*, 11(2), 75–94.

Snook, K., Zhao, J. Z., Alves, C. H., Cannata, J. M., Chen, W. H., Meyer Jr, R. J., & Shung, K. K. (2002) "Design, fabrication, and evaluation of high frequency, single-element transducers incorporating different materials." *Ultrasonics, Ferroelectrics, and Frequency Control, IEEE Transactions on*,*49*(2), 169-176.

Toda, M. & Thompson, M. (2010) "Novel multi-layer polymer-metal structures for use in ultrasonic transducer impedance matching and backing absorber applications." *IEEE transactions on ultrasonics, ferroelectrics, and frequency control*, 57(12), 2818–27.

Weis, R. & Gaylord, T. (1985) "Lithium niobate: summary of physical properties and crystal structure." *Applied Physics A*, 203, 191–203.

Chapter 5: Results: µUS transducers

"Theory guides, experiment decides"

Izaak Kolthoff

5.1 Overview

Perhaps the most important component in the work presented in this thesis is the development of high resolution µUS transducer. This chapter presents the results of modelling, fabrication and characterisation of a design for this device including a novel approach for matching layer configuration for high frequency applications previously used at much lower frequencies called the 'mass-spring' matching layer design. This chapter also presents the characterisation results obtained from a commercial single element focused 45 MHz AFM TH-19 µUS transducer. The characterisation results from the fabricated transducers were compared with the commercial transducer.

- In Section 5.2, the results of the process route that was established for ultra-thinning of LNO for high frequency ultrasound transducer applications are described briefly.
- In Section 5.3, characterisation results and comparisons with KLM modelling of single element LNO focused µUS transducers with and without matching layers. For each transducer fabricated and characterised, a table describing the physical characteristics of the transducer is given, followed by graphs showing simulated and experimentally measured electrical spectroscopy data, pulse echo response and insertion loss. The sub-sections present the functional characterisation results.
- In Section 5.3.6, the characterisation results of single element AFM TH-19 focused µUS transducer are presented. The transducer was characterised and a table describing the physical characteristics of the transducer is given, followed by graphs showing experimentally measured electrical impedance data, pulse echo response and beam geometry. The AFM TH-19 µUS transducer was used for imaging and characterisation of murine small intestine.

This Chapter is based on an article published in UFFC-IEEE (J.Brown, S. Sharma et al., 2014)

5.2 Ultra-thinning of LNO

The development of a process route for ultra-thinning of LNO was motivated by the need to produce micro-scale high resolution ultrasound transducer, which requires very thin active elements. A potentially successful process route for high frequency ultrasound transducer applications was established. Two LNO Y-36^0 cut samples were thinned to a thickness of 15 and 10 µm respectively. The samples were thinned on a non-grooved cast iron plate to thicknesses of 23 and 20 µm respectively. The LNO samples were observed under an optical microscope after lapping and it was found that they had pits caused by lapping (Figure 5.1), but no other surface damage such as chipping or micro-fractures were observed. The surface roughness of the lapped samples were measured by using a stylus-based surface profiler (Vecco Dektak 150, Cambridge, UK) to have R_a = 260 ± 2 nm.

In order to obtain a scratch free, specular surface, the samples were polished using expanded polyurethane, a high nap soft pad. The finished thicknesses of the samples after polishing were 15 and 10 µm respectively as noted previously (S.Sharma, & S.Cochran, 2012.). Both lapping and polishing were done at low speeds to reduce surface scratching and vibrations. A surface roughness of R_a = 0.69 ± 2 nm for both the samples was measured after polishing (Figure 5.2). The removal rates and thickness measurements of the samples at every step is summarised in Table-5.1.

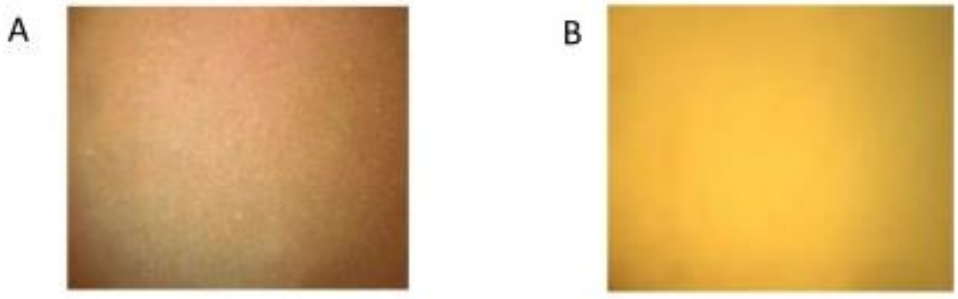

Figure 5.1: Lapped samples of LNO as seen under an optical microscope. A. Lapped LNO sample of thickness 20 µm, exhibits dark spots and a higher surface roughness caused by lapping. B. LNO sample as in A after polishing, shows a specular and smooth surface, free from lapping damages, thickness = 10 µm.

This Chapter is based on an article published in UFFC-IEEE (J.Brown, S. Sharma et al., 2014)

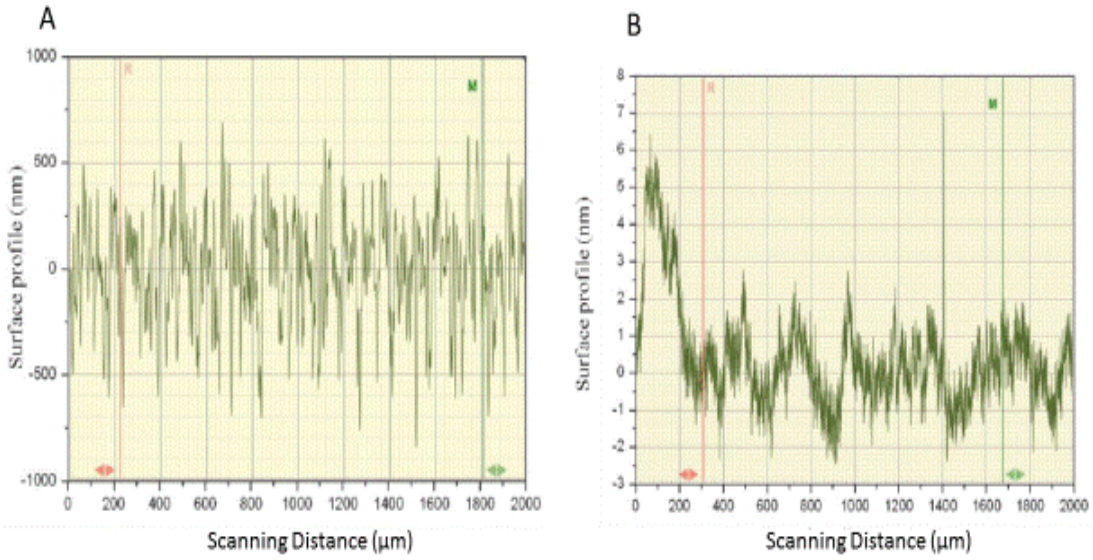

Figure 5.2: The surface roughness of LNO samples measured by a surface profiler. A. After lapping, R_a = 260 nm. B. After polishing, R_a = 0.69 nm. Note that the Y-axis in A and B is scaled differently.

Table 5.1: Summary of thickness measurements and material removal rates for ultra-thinning of LNO.

Material Data	**Sample - 1**	**Sample - 2**
Initial Thickness (µm)	518	519
Mounted Thickness (µm)	519	520
Wax thickness (µm)	1	1
Lapped thickness (µm)	23	20
Material removed (µm)	495	499
Lapping time (min)	124	125
Material removal rate (µm/min)	4.0	4.0
Polished thickness (µm)	15	10
Polishing time (min)	53	66
Material removal rate (µm/min)	0.15	0.15
Final thickness (µm)	15	10

5.3 High Resolution µUS Transducers

The results of the matching layer design presented here are similar to those previously described by Toda et al., (Toda & Thompson, 2010) for much lower operating frequencies. In keeping with the rest of the work described here, the matching layer study was limited to single element transducers. These matching layer designs were designed to replace transducers with traditional quarter wavelength matching layers transducers for the reason that these are difficult to fabricate for both flat and focused µUS transducers. Thus, as part of the work a controlled vacuum deposition technique to deposit the matching layers was developed (J.Brown, S.Sharma, & Adamson, 2014; J.Brown and S.Sharma, 2014). The following sections present the results from:

1. Single element focused and planar µUS focussed and planar transducers without matching layers, which were used as controls.
2. Single element µUS transducer with a conventional quarter wavelength (λ/4) bulk material matching layer used as a control for comparing 'mass-spring' matching layer design.
3. Single element µUS transducer focussed with a single λ/4 'mass-spring' matching layer.
4. Single element focused and planar µUS transducers with dual λ/4 'mass-spring' matching layers.
5. Commercial AFM TH-19 45 MHz piezocomposite focused µUS transducer

µUS transducers of each design were fabricated and characterised. Figure 5.3 shows examples of the different transducers fabricated during this research.

It is known that for focused transducers there is a point in space at which the reflected signal amplitude reaches a maximum value, with a steady drop off beyond this focal point. For each focused transducers the depth of field was measured as described in Chapter 4.7.5. The signal amplitudes obtained were normalised by dividing the amplitudes at each depth by the amplitude obtained at the focal point. The normalised amplitude values were then converted to decibels. The resultant values were plotted against the axial depth to illustrate the depth of field of transducers.

Figure 5.3: µUS transducers with an operation frequency of 45 MHz. A. Single element planar µUS transducer without matching layer. B. Focused single λ/4 wavelength matched µUS transducer. C. Focused µUS transducer with a dual λ/4 'mass-spring' matching layer.

5.3.1 High Resolution µUS Transducer without Matching Layer

A single element 3 mm diameter planar 36^0 Y-cut LNO disk was fabricated with a conductive epoxy backing layer. The technique used for fabricating the single element planar device is similar to the one described by Demore et al.,(Demore, & Weijer, 2011). The piezoelectric layer was lapped to a thickness of 69 µm and then electroded with
500 nm of evaporated Cu using vacuum deposition. A second transducer with the same dimensions was fabricated, however this transducer was press focused to a geometric radius of 7 mm, using the techniques described in Chapter 4.3.7. This transducer was also backed with conductive silver epoxy following press focusing. The electrical impedance magnitude and impedance phase were measured in air for both the planar and press focused transducers in addition to the pulse-echo response and insertion loss in degassed water.

The transducer was modelled using a KLM model in order to be confident of the properties of piezoelectric and backing layers and also to compare the theoretical and experimental results. Figure 5.4 shows the results from measurements and the KLM model for the planar transducer operating at 47 MHz. An electromechanical coupling coefficient, k_t, of 0.49 was experimentally determined from the resonance and anti-resonance frequencies and was used in the model. The KLM model predicted a pulse bandwidth of 26% and an insertion loss of 32.5 dB. The experimental bandwidth and insertion loss were recorded as 25% and 34.1 dB respectively.

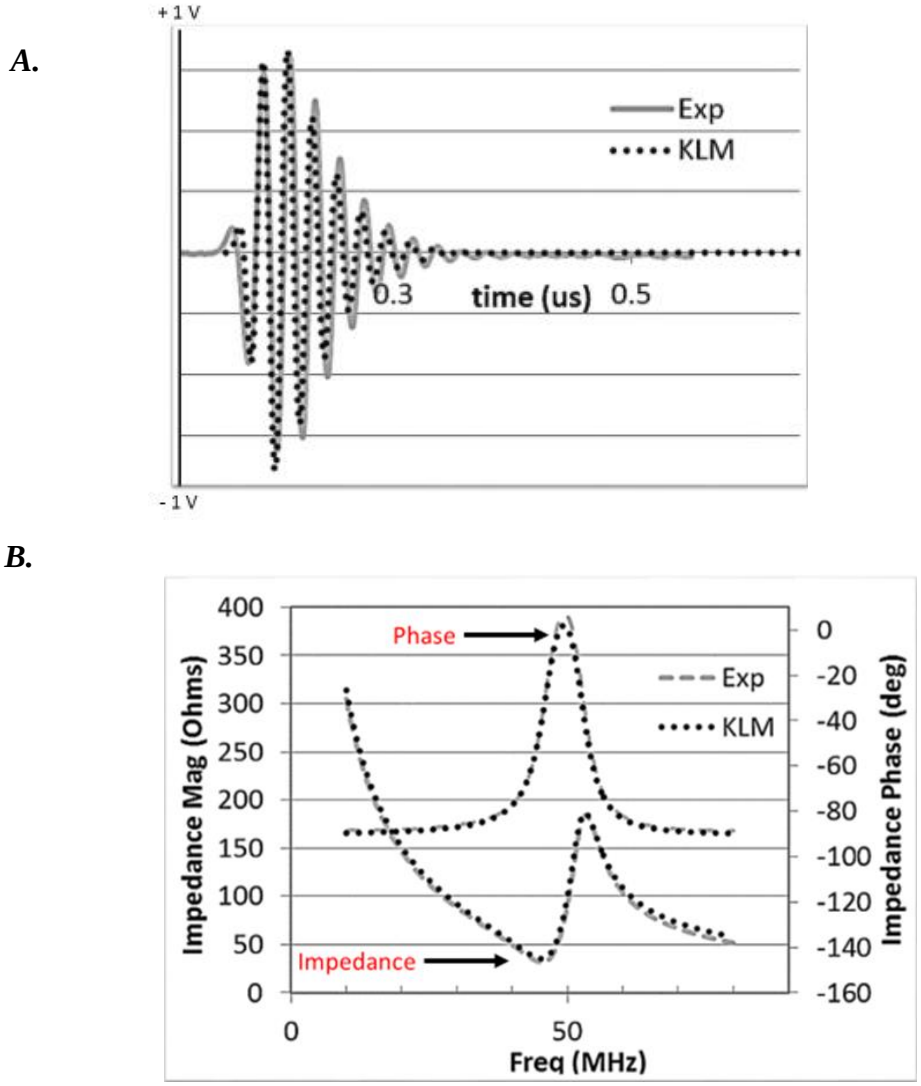

Figure 5.4: Comparison of KLM model to experimental results for a planar transducer without matching layers operating at a centre frequency of 47 MHz. A. Pulse echo response and B. Electrical magnitude and Phase.

Figure 5.5 shows the results from the KLM model and the electrical impedances measured in air for the press focused µUS transducer. An electromechanical coupling coefficient, k_t, of 0.46 was experimentally determined and inserted into the KLM model and a piezoelectric mechanical loss factor was added to the piezoelectric substrate in order to obtain good match for the measured impedances. The decreased k_t, is attributed to micro-cracking of the piezoelectric substrate resulting from press focusing. Previous studies conducted on this have shown that the efficiency of press focused transducers decreases for this reason (Cannata & Shung, 2001). The experimental results show a good match with the KLM model, except for several low frequency modes in the

experimental impedance plots, which may again be a result of micro-fracturing of the piezoelectric substrate.

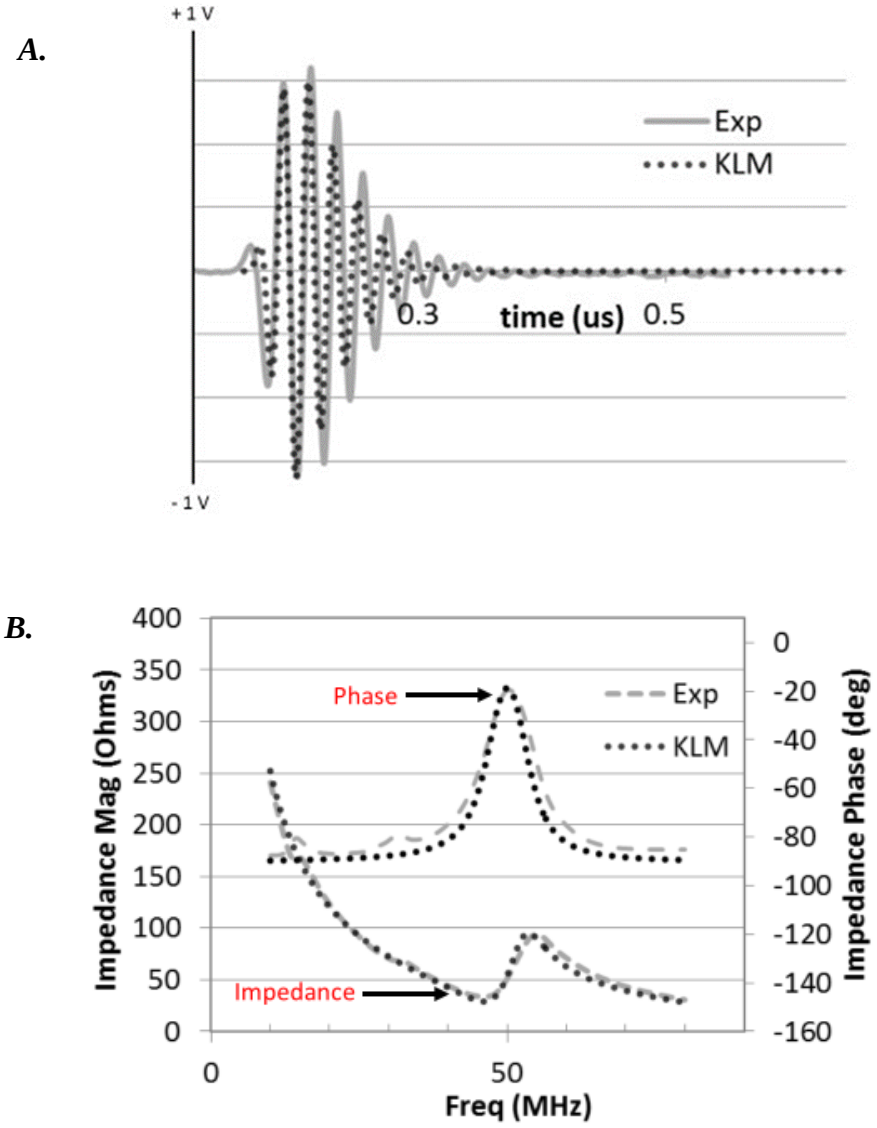

Figure 5.5: The results from the KLM model and experimental electrical impedance measurements for a press focused single element µUS Transducer without matching layers. A. Pulse echo measurements. B. Electrical impedance and phase measurements. Several low frequency modes are seen which could be due to micro-fractures resulting from press focusing.

The focused transducer was characterised for its functionality. The line spread function, axial and lateral resolution of the transducer was evaluated.

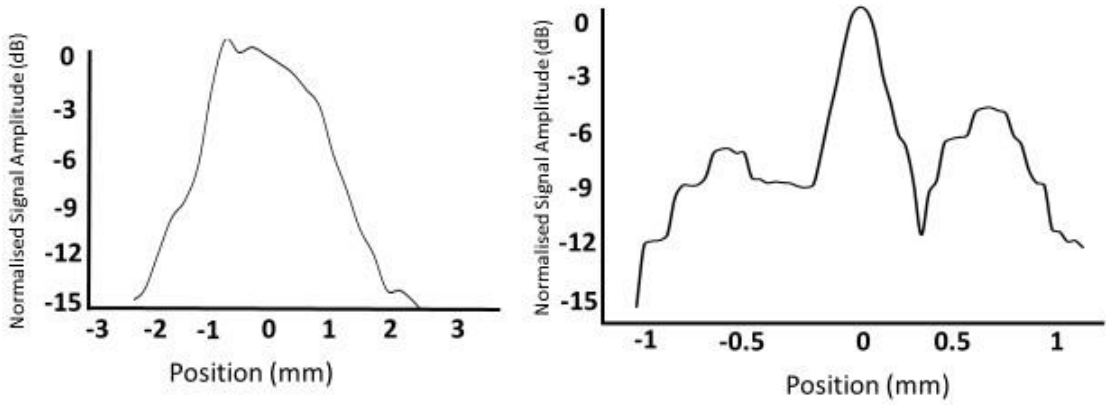

A. ***B.***

Figure 5.6: Functional characterisation of 45 MHz focused µUS transducer without matching layers. A. Depth of field (DOF) measurement, around for a focal at a distance of 7 mm. 0 in the graph on the x-axis represents the focal point at 7 mm. B. Line spread function obtained by pulse-echo from a 5 µm tungsten wire.

From the measurements with the results show in Figure 5.6, the physical characteristics of the transducer is summarised in Table-5.3. The -6 dB bandwidth and resolution of the transducer was determined and is summarised in Table-5.3. For the pulse-echo transmission the -6 dB bandwidth is 12 MHz, giving a Q of 3.9. Axial resolution is 96 µm. The experimental results of bandwidth and insertion loss match well with the theoretical computations.

Table 5.2: Physical characteristics of µUS transducer without matching Layer.

Transducer Parameter	**Value**
Aperture diameter (mm)	3
Shape	Circular - Focused
Thickness (µm)	69
Piezoelectric Material	LNO Y-36^0
Backing Material	Silver Epoxy
Matching Layer	None
Electrodes	Cu
Operational Frequency (MHz)	47
Focal Distance (mm)	5.6
f-number	1.9

Table 5.3: Statistics of focused µUS transducer without matching layer in pulse-echo mode.

Parameter	Threshold	-6 dB
Bandwidth (MHz)	Theoretical	12.2
	Experimental	12
Q	Experimental	3.9
Pulse Length (µs)	Experimental	0.020
Axial Resolution (µm)	Experimental	96
Lateral Resolution (µm)	Theoretical	61
	Experimental	85
Insertion Loss (dB)	Theoretical	32
	Experimental	34.1
Depth of Field	Theoretical	0.90
	Experimental	1.64

The focused transducers were further tested for their functionality in pulse-echo mode. The transducers were used to image a 5 µm Tungsten wire to compute the line spread function of the beam with the results shown in Figure 5.6 (B) generating the data in Table - 5.3.

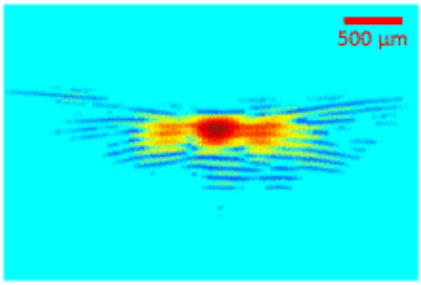

Figure 5.7: B-scan images. B-scan image of a single 5 µm Tungsten wire at the focal point (7mm).

5.3.2 Dual Quarter Wavelength Conventional Matched μUS Transducer

A conventional bulk material λ/4 single matching layer was applied to a 3 mm diameter circular disk using the technique described in Section 4.5.3 after which the circular disks were press focused using the technique described in Section 4.5.4 to a geometrical focal distance of 7 mm. A conductive silver epoxy (E-solder 3022, Von Roll Isola Inc., New haven, CT, USA) was applied as a backing layer and cured overnight. An electrical wire was inserted into the backing layer and fixed by conductive epoxy. The resulting acoustic stack was placed into a brass casing and insulating epoxy (Epotek 301, Epoxy Tech., MA, USA) was used to fill the gaps between the casing and the device. A thin layer (500 nm) of Cu electrode was then applied using e-beam evaporation. Then a second matching layer of 12 μm parylene was deposited on the front face using an SCS labcoater parylene coater (SCS coating systems, Indianapolis, IN).

Figure 5.8 shows good agreement between the KLM model and the experimental results. The theoretical pulse bandwidth and insertion loss were measured to be 44% and 18 dB. The experimental pulse bandwidth and insertion loss was measured to be 43% and 20.2 dB.

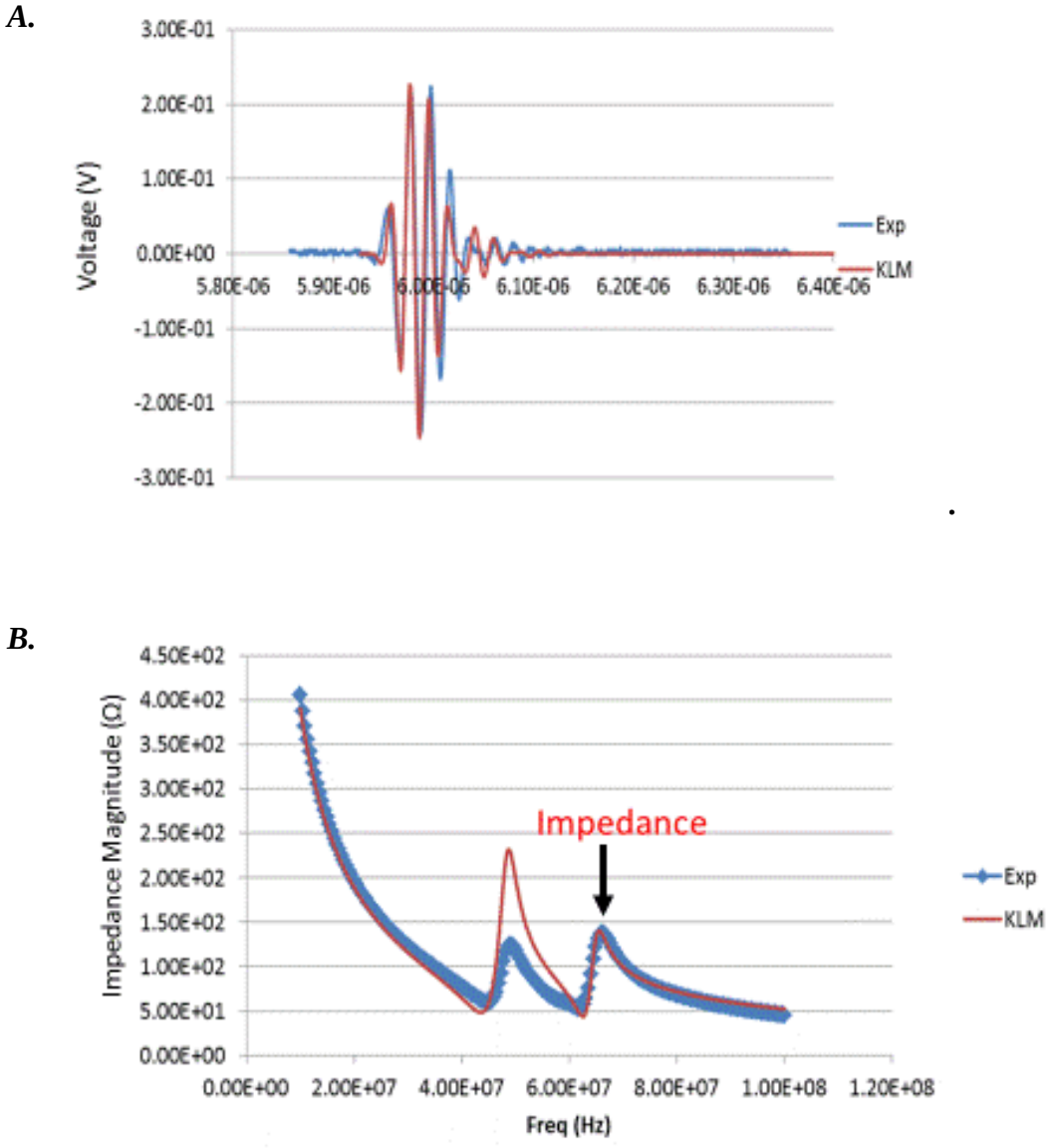

Figure 5.8: Comparison of KLM model to the experimental measurements for a focused single element µUS Transducer with traditional single matching layer. A. Pulse echo measurements. B. Electrical impedance and phase measurements.

The depth of field, line spread function and B-scan imaging could not be performed with this transducer as all the three transducers fabricated stopped working due an electrical short circuit. The shorting happened due to cracking of the LNO during press focusing and the element cracked at the centre after initial tests.

5.3.3 Single Quarter Wavelength 'Mass-Spring' Matched High Resolution μUS Transducer

A mass-spring matching layer combination was applied to a focused single element 45 MHz LNO single element transducer. The results of the planar transducer have been shown in Section 5.2. The matching layer combination approximated with an acoustic impedance $Z_{1/4\lambda}$ = 4.25 MRayl which was calculated using the Equation *(3.21)*. The thickness of parylene was calculated to be 3.8 μm by substituting the results of Equation *(4.7)* into Equation *(4.8)* along with the material properties of parylene and copper. The properties of the materials are listed in Table - 4.1. The required thickness of copper was calculated to be 1.4 μm.

The electrical impedance was calculated using the KLM model and experimentally measured using an impedance analyser. Figure 5.9 shows good agreement between the KLM model and the experimental results. The theoretical pulse bandwidth and insertion loss were measured to be 44% and 21.2 dB respectively and the experimental pulse bandwidth and insertion loss was measured to be 46% and 21.9 dB respectively.

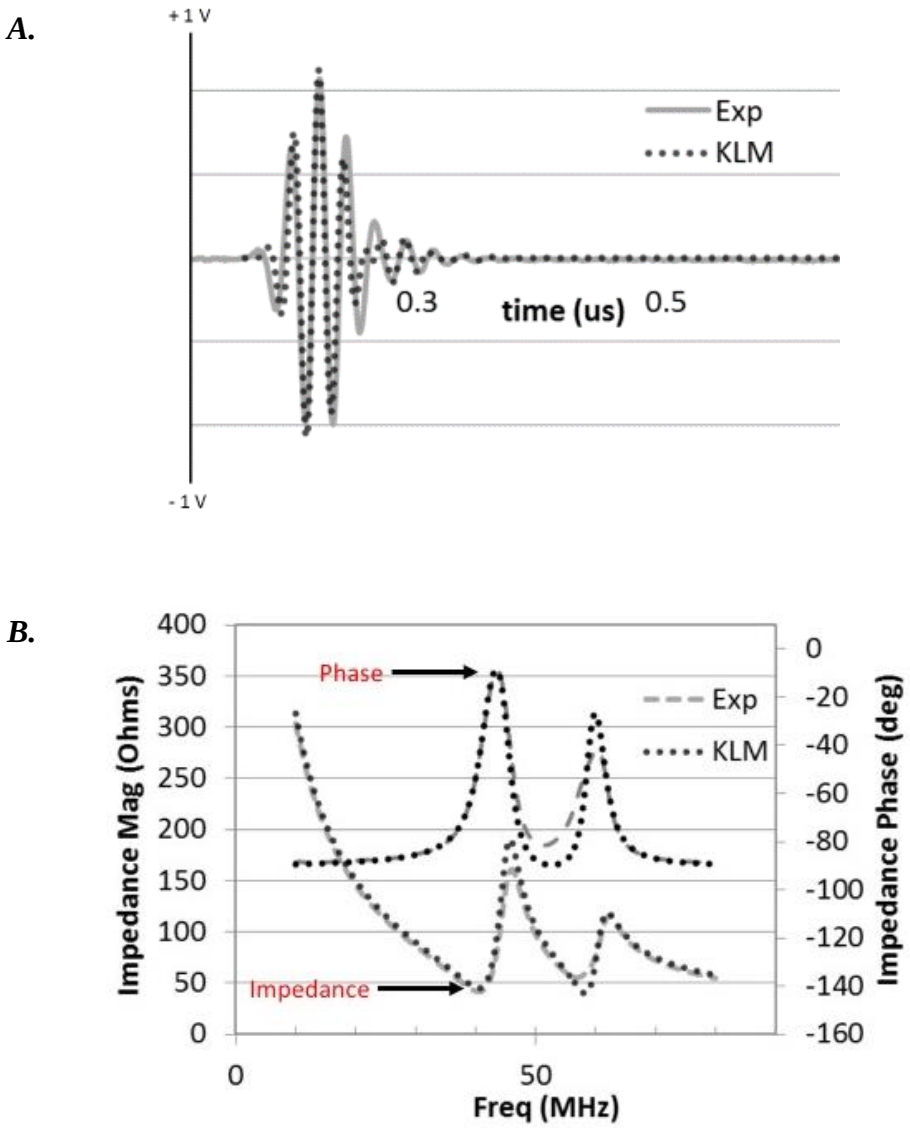

Figure 5.9: Comparison of KLM model to the experimental measurements for a focused single element μUS Transducer with single λ/4 'mass-spring' matching layers. A. Pulse echo measurements. B. Electrical impedance and phase measurements.

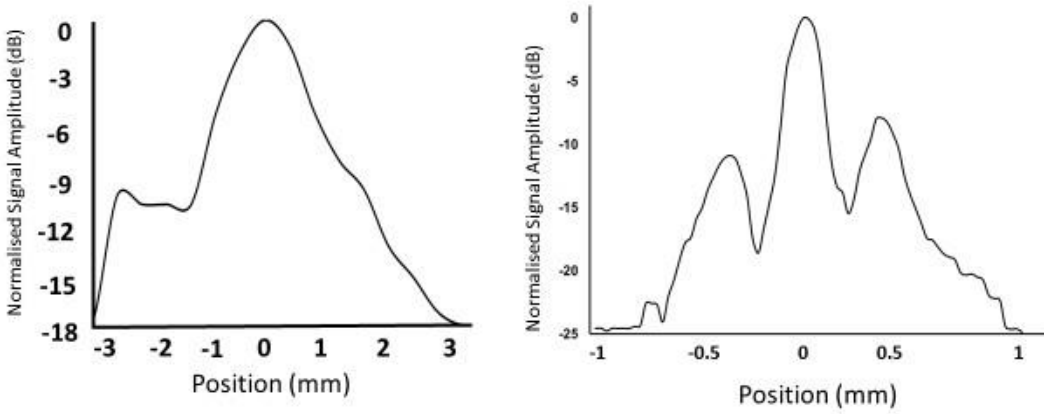

A. ***B.***

Figure 5.10: Functional characterisation of 45 MHz focused µUS transducer with single λ/4 'mass-spring' matching layers. A. Depth of filed (DOF) measurement, the focal point was determined to be at 7 mm. 0 in the graph on the x-axis represents the focal point at 7 mm. B. Line spread function obtained by pulse-echo from a 5 µm Tungsten wire.

With the inclusion of data from Figure 5.10 the complete physical characteristics of the transducer are summarised in Table-5.5. The -6 dB bandwidth and spatial resolution of the transducer in pulse-echo mode were also determined and are summarised in Table-5.6. For the pulse-echo operation the -6 dB bandwidth is 12 MHz, giving Q = 2.1. Axial resolution is 83 µm. The experimental results for bandwidth and insertion loss match well with the theoretical computations. The depth of field measurement showed that the transducer was focused at 6.85 mm compared with an expected focal distance of 7 mm.

Table 5.4: Physical Characteristics of μUS Transducer single λ/4 'mass-spring' Matching Layer.

Transducer Parameter	**Value**
Aperture diameter (mm)	3
Shape	Circular - Focused
Thickness (μm)	69
Piezoelectric Material	LNO Y-36^0
Backing Material	Silver Epoxy
Matching Layer	Parylene, Copper
Electrodes	Cu
Operational Frequency (MHz)	45
Focal Distance (mm)	6.85
f-number	2.3

Table 5.5: Statistics of focused μUS Transducer with single λ/4 'mass-spring' Matching Layer in pulse-echo mode.

Parameter	**Threshold**	**-6 dB**
Bandwidth (MHz)	Theoretical Experimental	19.8 20.7
Q	Experimental	2.1
Pulse Length (μs)	Experimental	0.022
Axial Resolution (μm)	Experimental	83
Lateral Resolution (μm)	Theoretical Experimental	76 75
Insertion Loss (dB)	Theoretical Experimental	21 22
Depth of Field	Theoretical Experimental	1.33 1.65

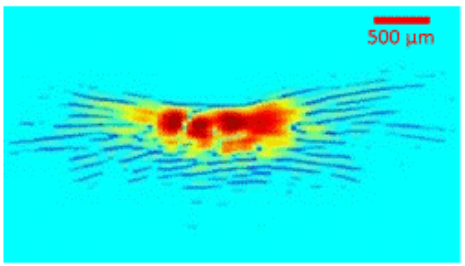

Figure 5.11: B-scan images. A. B-scan image of a single 5 µm Tungsten wire at the focal point (7mm).

The focused transducers were further tested for their functionality for pulse-echo imaging. The transducers were used to image a 5 µm tungsten wire to compute the line spread function of the beam. The lateral resolution was measured to be 76 µm which is a close match to the theoretical value of 75 µm. The B-scan image of in figure 5.11 shows reverberation effects of the transducer, which is due to multiple reflections of ultrasound from the wire target. Multiple reverberations occur as tungsten has large acoustic impedance (101 MRayl) and is highly reflective of ultrasound.

5.3.4 Dual Quarter Wavelength Matched High Resolution µUS Transducer

The second matching layer scheme investigated was the dual λ/4 matching layer system for a single element planar 45 MHz LNO transducer. The known piezoelectric and tissue impedance was substituted into Equation *(3.29)* to calculate the acoustic impedances for λ/4matching layer in a dual matching layer system. The required thickness (t) of Copper and Parylene for two layers was calculated to be: $t_{\#1parylene}$= 1.8 µm, $t_{\#1Cu}$ = 2.9 µm, $t_{\#2parylene}$= 7 µm and, $t_{\#2Cu}$ = 0.42 µm respectively. As the outer layer of Cu is very thin, Cu layer tended to rub off or got oxidised when testing the transducers. Ideally an outer layer of parylene is preferred as this would act as a barrier between the transducer and the water or ultrasound coupling gel. To overcome this issue 1.8 µm of parylene and 2.9 µm of Copper which approximates to the first λ/4 matching layer and 12 µm of parylene was deposited on this stack to provide us a transducer with a dual matching layer. All of the deposition was done using vacuum deposition techniques as described in 4.3.4 and 4.3.5.

The electrical impedance magnitude and phase was simulated using KLM model and was measured experimentally. Figure 5.11 shows the two-way pulse echo response and impedance magnitude and phase. The KLM model predicted a pulse bandwidth of 63% and an insertion loss of 19.3 dB respectively. The experimental pulse bandwidth and insertion loss was measured to be 59% and 18.2 dB. The measured insertion loss was better than the theoretical values.

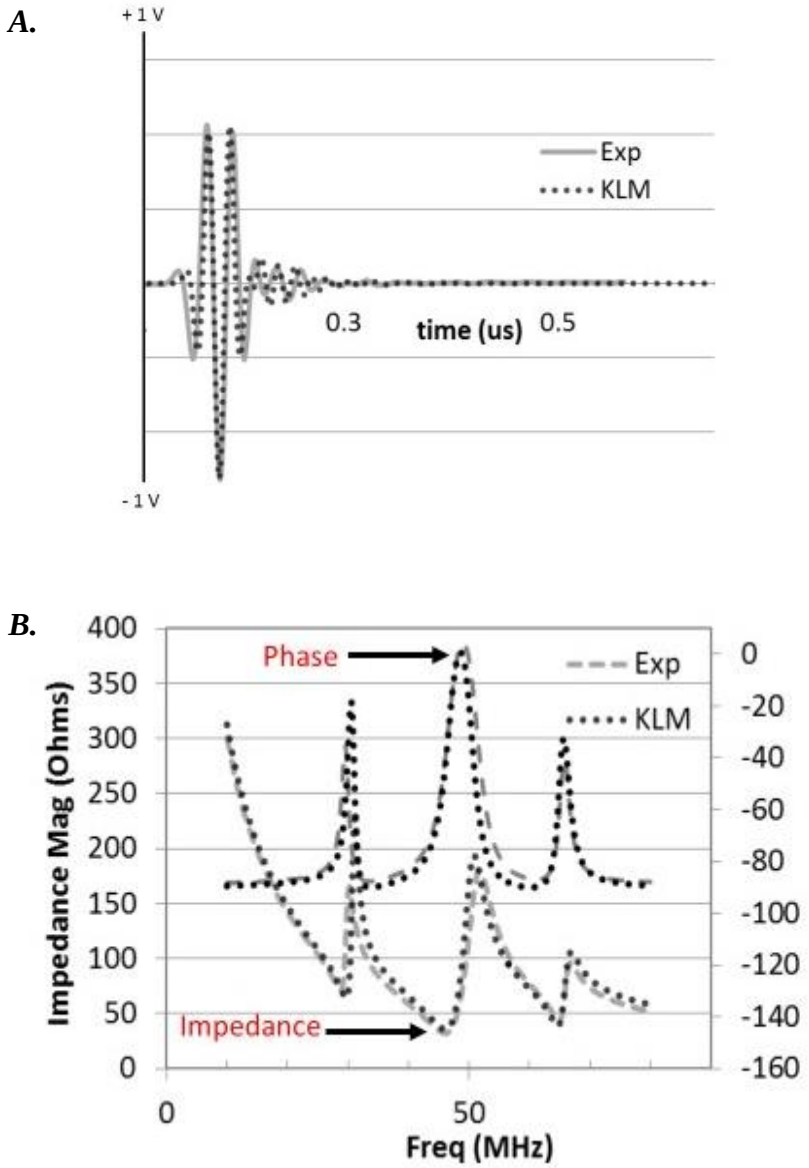

Figure 5.12: Comparison of KLM model and experimentally measured electrical impedance magnitude for LNO planar transducer with dual 'mass-spring' matching layer. A. Pulse echo measurements. B. Electrical impedance measurements.

Table 5.6: Physical Characteristics of µUS Transducer with dual matching Layer.

Transducer Parameter	**Value**
Aperture diameter (mm)	3
Shape	Circular - Planar
Thickness (µm)	69
Piezoelectric Material	LNO Y-36^0
Backing Material	Silver Epoxy
Matching Layer	Parylene and Copper
Electrodes	Cu
Frequency(MHz)	45

Table 5.7: Statistics of planar µUS Transducer with dual λ/4 'mass-spring' Matching Layer in pulse-echo mode.

Parameter	**Threshold**	**-6 dB**
Bandwidth (MHz)	Theoretical Experimental	28.4 26.6
Q	Experimental	1.69
Pulse Length (µs)	Experimental	0.031
Insertion Loss (dB)	Theoretical Experimental	19.3 18.2

The physical characteristics of the transducer are summarised in Table - 5.7. The -6 dB bandwidth and resolution of the transducer was determined and is summarised in Table - 5.8. For the pulse-echo transmission the -6 dB bandwidth is 26.6 MHz, with Q = 1.69. The experimental results of bandwidth and insertion loss match well with the theoretical computations.

5.3.5 Dual Quarter Wavelength Matched Focused High Resolution µUS Transducer

The final transducer configuration comprised a 45 MHz press focused transducer fabricated with the matching layer scheme similar to that described in Section 4.4. The results from a KLM model for this configuration were compared with experimental electrical impedance and two way insertion loss was calculated. The KLM model

predicted a pulse-echo bandwidth of 62% and an insertion loss of 21.5 dB. The measured pulse bandwidth and insertion loss was 68% and 26 dB respectively.

The reduced insertion loss is due to the reduction of the coupling coefficient, k_t, which was measured experimentally to be 0.46. As before, a possible reason for this is the occurrence of micro-fractures due to press focusing. In damping the natural resonance of the transducer, the backing material of the transducer may contribute to the thickness mode lateral mode apparent in the electrical impedance. Such lateral modes cannot be modelled using the unidimensional KLM approach and therefore the simulated impedance does not necessarily match well with the experimental data in the case of focused transducer geometry. However the functional performance of the transducer does not seem to be degraded and this is verified by the pulse echo measurements shown in Figure 5.13.

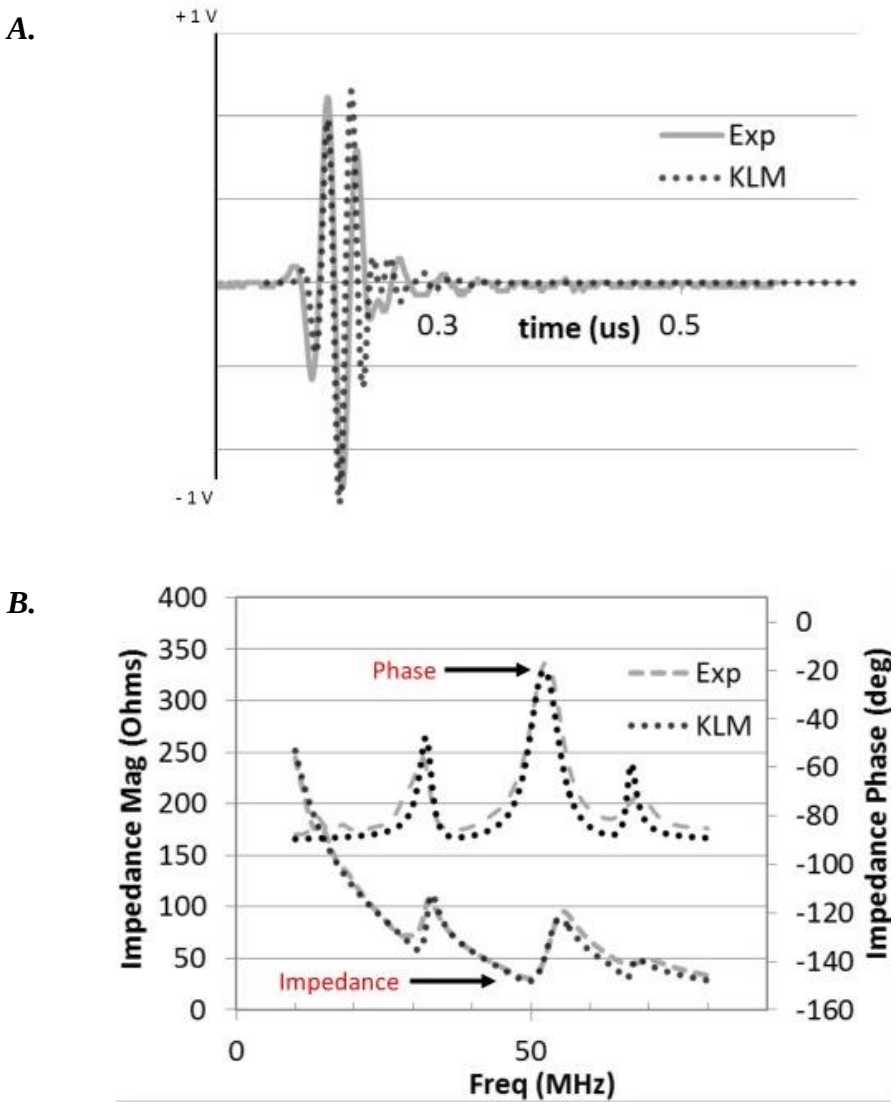

Figure 5.13: Comparison of KLM model to the experimental measurements for a focused single element µUS transducer with dual λ/4 'mass-spring' matching layers. A. Pulse-echo measurements. B. Electrical impedance and phase measurements.

The focused transducer was also characterised for functionality with the line spread function, axial and lateral resolution of the transducer evaluated. From the measurements with the results shown in Figure 5.14 (A) the physical characteristics of the transducer is summarised in Table-5.8. The -6 dB bandwidth and resolution of the transducer was determined and is summarised in Table-5.12. For the pulse-echo transmission the -6 dB bandwidth is 30.6 MHz, giving a Q of 0.68. The experimental results of bandwidth and insertion loss match well with the theoretical computations.

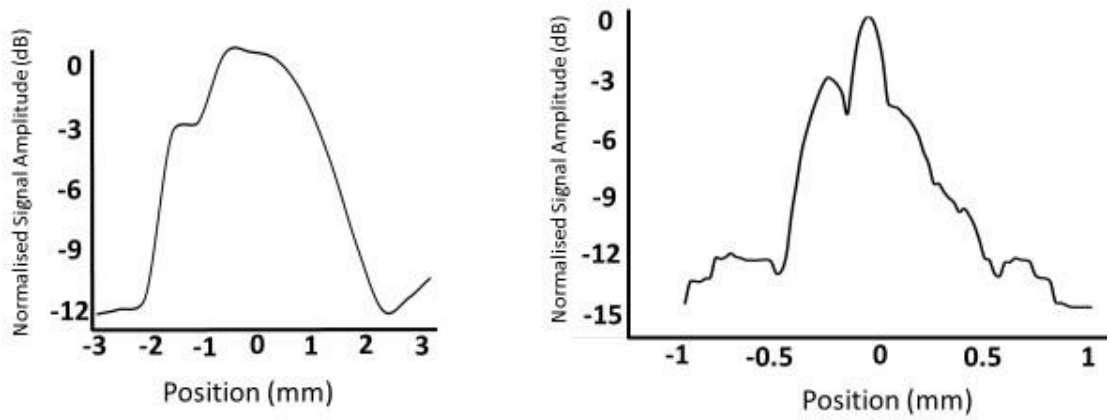

A. ***B.***

Figure 5.14: Functional characterisation of 45 MHz focused µUS transducer with dual λ/4 'mass-spring' matching layers. A. Depth of field (DOF) measurement relative to a focal depth of 7 mm. 0 in the graph on the x-axis represents the focal point at 7 mm. B. Line spread function obtained by pulse-echo from a 5 µm Tungsten wire.

Table 5.8: Physical Characteristics of µUS Transducer with dual λ/4 'mass-spring' matching Layer.

Transducer Parameter	**Value**
Aperture diameter (mm)	3
Shape	Circular - Focused
Thickness (µm)	69
Piezoelectric Material	LNO Y-36^0
Backing Material	Silver Epoxy
Matching Layer	Parylene and Copper
Electrodes	Cu
Operational Frequency (MHz)	45
Focal Distance (mm)	6.75
f-number	2.08

Table 5.9: Statistics of focused µUS Transducer with dual λ/4 'mass-spring' Matching Layer in pulse-echo mode.

Parameter	**Threshold**	**-6 dB**
Bandwidth (MHz)	Theoretical Experimental	27.9 30.6
Q	Experimental	0.68
Pulse Length (µs)	Experimental	0.023
Axial Resolution (µm)	Experimental	81
Lateral Resolution (µm)	Theoretical Experimental	76 75
Insertion Loss (dB)	Theoretical Experimental	21.5 26
Depth of Field (mm)	Theoretical Experimental	1.09 2.01

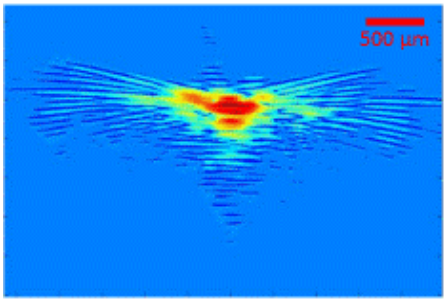

Figure 5.15: B-scan images. A. B-scan image of a single 5 µm Tungsten wire at the focal point (7mm).

The measured lateral resolution of the transducer is 76 µm and is in close match to theoretical value of 75 µm. The B-scan image of the tungsten wire shows slight misalignment of the transducer with the tungsten wire and there are reverberations seen in the image which could be an effect of the presence of lateral modes. The lateral modes are due to micro fractures of the LNO element due to press focusing. The B-scan image is shown of 5 µm tungsten wire and murine intestine is shown in Figure 5.15. The image quality is good and the dynamic range of the B-scan image is 40 dB giving a greater signal to noise ratio as expected due to lesser insertion loss.

5.3.6 Commercial µUS Transducer

A commercially available 45 MHz composite transducer (AFM Ltd. Birmingham, UK) was used in this study. The transducer used in the experiments is shown in Figure 5.16 and for ease will be referred to as AFM TH-19. The active element of AFM TH-19 is 1.5 mm diameter, the operating frequency is 45 MHz, with a wavelength, $\lambda = 35$ µm. It is focused with an f-number of 2.85 providing an experimental lateral resolution of 107 µm at the focus and is a close match to the theoretical value of 100 µm. The physical properties of the transducer are listed in Table - 5.10. The transducer was characterized prior to being used as an imaging device and the results of the functional characterisation are reported. In pulse echo mode the same transducer transmits and receives the backscattered echoes from the tissue and converts them into electrical signals that can be detected using a digitiser. The quality of the echoes is dependent on the properties of the transducer. Commercially available composite transducers have large bandwidths and less noise when compared to transducers based on other materials such as lead zirconate titanate (PZT).

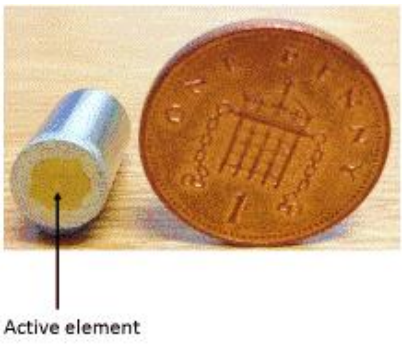

Figure 5.16: AFM TH-19 µUS transducer. This device operates at 45 MHz with an f# = 2.85 and provides a beam width of 107 µm at the focus.

Table 5.10: Physical Characteristics of the AFM TH-19 µUS transducer

Parameter	Value
Piezoelectric Material	Composite – 29% piezoceramics volume fraction with hexagonally packed 25 µm pillars at 75 µm pitch
Element diameter (mm)	1.5
Element Thickness (µm)	46
Operating Frequency (MHz)	45
Focal Distance (mm)	4.25
f-number	2.85

5.3.7 Commercial µUS Transducer Characterisation

Prior to using AFM TH-19 for imaging of murine intestine, the transducer was characterised and tested for its functionality. Pulse-echo measurements from quartz flat and electrical impedance spectroscopy measurements are shown in Figure 5.17. The active element of the transducer is 1.50 mm in diameter. It operates at a centre frequency of 45 MHz and is focused with an f-number of 2.85. The experimental bandwidth of the transducer was measured as 26.0 MHz. The beam geometry data were obtained using a phantom consisting of 5 µm tungsten wires representing ideal line reflectors.

The -6 dB bandwidth, resolution and Q of the transducer were determined and are summarised in Table 5.11. For the pulse-echo transmission, the -6 dB bandwidth is 26.0 MHz, gives a Q = 1.73. The line spread function and depth of field for the transducer was measured and is shown in Figure 5.18. Depth of field was measured by recording the echoes from a quartz flat of thickness = 500 µm, at a range of axial distances from the quartz flat, and plotting amplitude against the axial position. The line spread function was measured by recording the data in pulse-echo mode from a 5 µm tungsten wire target in water. The transducer was positioned such that the focal point coincided with the wire target. The transducer was then moved laterally in positive and negative directions, in steps of 15 µm, until there was no detectable signal. The amplitude of the echoes was then plotted against position. From the line spread function the lateral

resolution of the transducer was determined. The beam geometry of the transducer obtained by reflecting the ultrasound signals from a 5 µm tungsten wire target is shown in Figure 5.19. A theoretical lateral resolution of 94.0 µm and an experimental lateral resolution of 107 µm at the focal distance of 4.25 mm were measured. The reduced experimental lateral resolution is due to an extended ringing in the axial pulse. The depth of field was measured to be 1.92 mm.

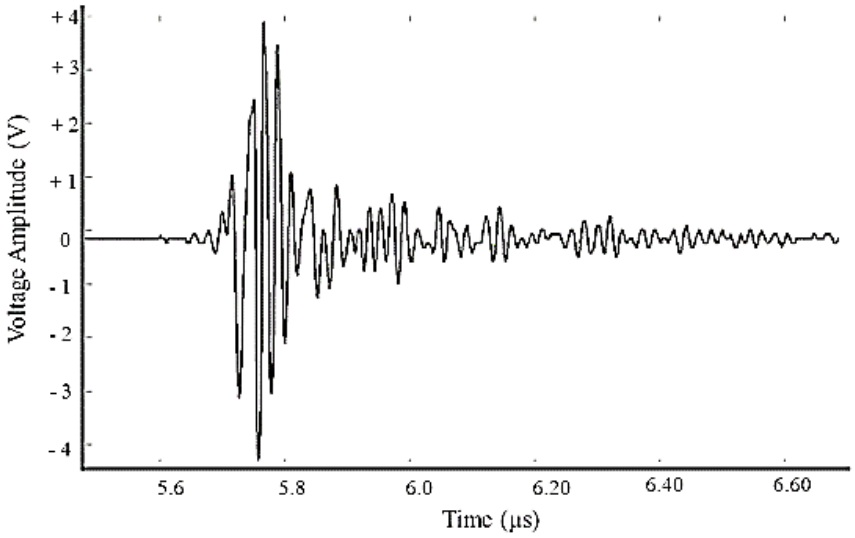

A.

B.

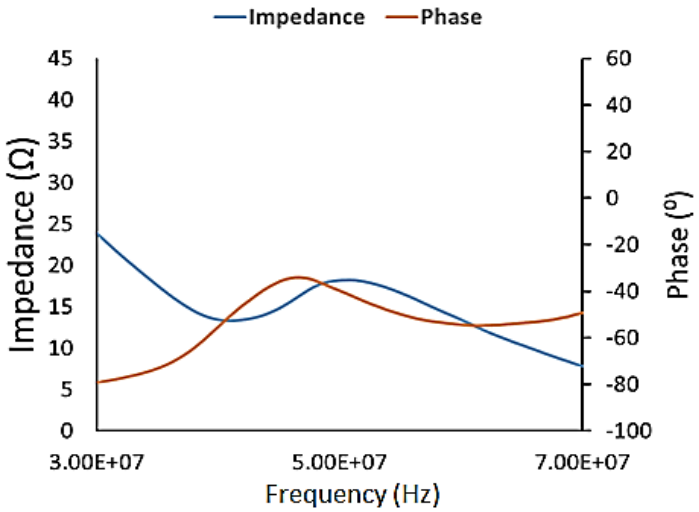

Figure 5.17: Functional characterisation of AFM TH-19 focused µUS transducer. ***A.*** *Pulse echo measurement, from a quartz flat of thickness 500 µm at the focal distance of 4.25 mm.* ***B.*** *Electrical impedance spectroscopy measurement shows a resonance in the region of 45 MHz.*

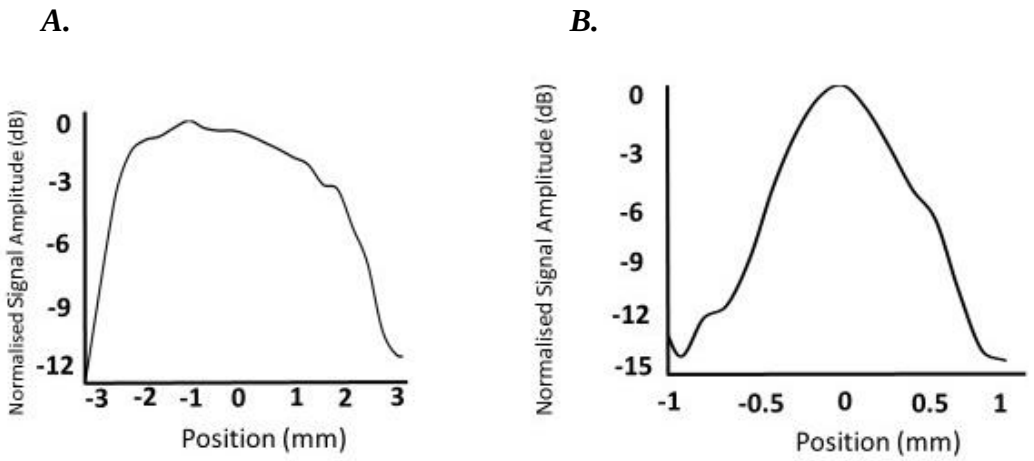

Figure 5.18: Functional characterisation of AFM TH-19 µUS transducer. ***A****. Depth of field (DOF) measurement, with the focal distance determined to be at 4.25 mm. 0 in the graph on the x-axis represents the focal point at 4.25 mm.* ***B****. Line spread function obtained by pulse-echo from a 5 µm tungsten wire.*

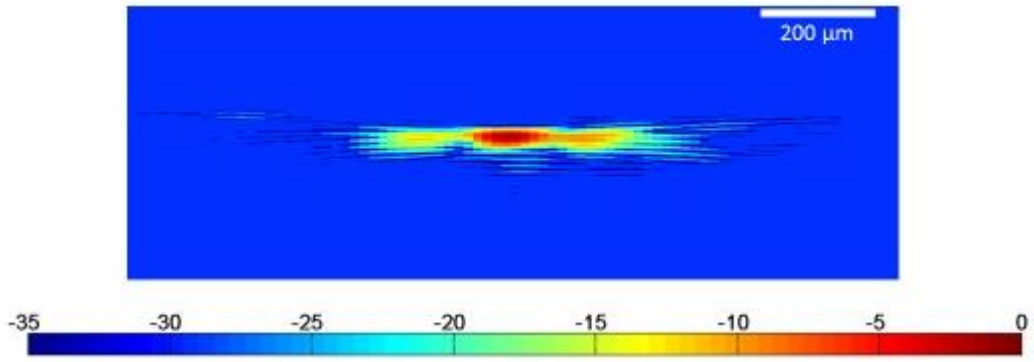

Figure 5.19: B-scan image of a single 5 µm tungsten wire at the focal point to determine the beam geometry of AFM TH-19 transducer, dynamic range = 35 dB.

Table 5.11: Characteristics of focused AFM TH-19 µUS transducer in pulse-echo mode.

Parameter	**-6 dB**
Frequency (MHz)	45
Bandwidth (MHz)	26.0
Cycles per Pulse	06
Pulse Width (µm)	0.140
Q	1.77
Pulse Length (µs)	0.022
Axial Resolution (µm)	98.0
Lateral Resolution (µm)	107.0
Insertion Loss (dB)	22.1
Depth of Field (mm)	2.01

5.4 Summary of Results

Three configurations of 'mass-spring' model of matching layers were evaluated by fabricating 3 mm diameter LNO transducers operating at a resonant frequency of 45 MHz. The summary of the performance of the transducers is shown in Table 5.12. The first transducer design evaluated was a control without any matching layers. The second design fabricated had a single λ/4 'mass-spring' matching layer. The results from this configuration showed that the bandwidth increased from 28% without matching layer to 44% with matching layer and the insertion loss of the transducer decreased from 34 dB without matching layer to 21 dB with matching layer. The third model investigated was a dual λ/4 'mass-spring' matching layer. The experimental results showed that the bandwidth of the transducer increased from 28% without matching layer, to 59% with dual matching layers. The insertion loss was seen to decrease from 34 dB without matching layer to 18 dB with dual matching layers. The dual matching layers were finally applied to geometrically focused transducer to test the efficacy of the design (Brown et al., 2014).

The bandwidth of the transducer with a single λ/4 matching layer was calculated to be 44%, which was an improvement of 19% when compared to an equivalent transducer without matching layer. The results from the single 'mass-spring' layer are close to achieving the qualitative benchmarks for bandwidth, but the insertion loss of this design

is low. Another relevant issue is that the transducers outlined here were not tuned electrically; implementing passive electrical tuning could significantly improve their bandwidth and insertion loss.

Table 5.12: Summary of experimentally determined characteristics of µUS transducers tested in pulse echo mode.

Transducer	**Insertion Loss (dB)**	**Bandwidth (MHz)**
AFM TH-19 (Focussed)	22.1	26.0
Single element without matching layer (Planar)	34.1	12
Dual λ/4 'mass-spring' Matching Layer (Focussed)	30.6	26
Single quarter wavelength 'mass-spring' (Planar)	20.7	22
Dual λ/4 'mass-spring' Matching Layer (Planar)	18.2	26.6

The dual λ/4 'mass-spring' matching layer design showed that; the theoretical insertion loss of less than 20 dB and bandwidth greater than 50% can be achieved. The experimental bandwidth for this device was measured to be 59% with an insertion loss of 18 dB. The dual λ/4 matching layer was first designed for a planar configuration for the ease of fabrication. After the initial success with this arrangement, focused transducers with dual λ/4 matching layers were investigated to demonstrate that vacuum deposition of matching layers is effective on geometrically curved transducers. For the focused transducers a bandwidth of 68% was achieved. The insertion loss was measured to be 26 dB, the desired insertion loss was not met and the experimental values were not a close match with theoretical KLM model. The most likely reason for this is the presence of micro-fractures of the LNO substrate that occurred while press focusing. The electromechanical coupling coefficient, k_t, dropped from 0.49 to 0.46 and there was a subsequent increase in the piezoelectric loss factor. The loss factor obtained experimentally was used in the KLM model to obtain the best fit impedance graphs. For the AFM TH-19 transducer a bandwidth of 26 MHz and an insertion loss of 22.1 dB were experimentally measured. It can be concluded from the above results that a wide bandwidth, low insertion loss µUS transducers can be fabricated with dual matching

layers. Wide bandwidth μUS transducers are preferred for clinical imaging systems as they give us the flexibility to work over a range of frequencies.

5.5 Discussion

The development of the process route of for ultra-thinning of LNO was motivated by the need to produce micro-scale ultrasonic transducers for operation at high frequency. The success of this process was demonstrated by the fabrication of single element high resolution transducers. Conventional λ/4 matching layers consists of one or more λ/4 thick layers of material usually bonded to the piezoelectric surface. The layers are 10 – 15 μm thick and require precise lapping and bonding techniques to maximise bandwidth and sensitivity of the transducer. The conventional matching layers usually comprise of loaded epoxy, on the basis that the attenuation of loaded epoxies at high frequencies is mostly due to scattering of the ultrasound wave. The fabrication of conventional matching layers is cumbersome due the difficulty in maintaining uniform thickness and to produce bubble free epoxies. It is also adds to the difficult to produce matched transducers in large numbers.

As an alternate to conventionally matched transducers the use of ‘mass-spring’ matching layers using vacuum deposition was described. A parylene coater was used to deposit the ‘spring’ layer and an evaporator to deposit Cu as the ‘mass’ layer. The issue of delamination in the mass-spring matched transducers is something that needs to be addressed and will be dealt with in the future.

The results in this chapter have shown that the insertion loss of a μUS transducer can be improved significantly by depositing specific thicknesses of parylene and Cu (e.g. 3.8 μm of parylene and 1.4 μm of Cu in the case of single λ/4 matched transducer operating at 45 MHz). The fabrication of these matching layers employs vacuum deposition technique.

The bandwidth required for high resolution ultrasound applications is difficult to quantify as it is dependent on the imaging application. However the literature suggests that an insertion loss of 20 dB and a bandwidth greater than 50% are adequate for high resolution ultrasound imaging for frequencies in the range 30 – 70 MHz. KLM modelling of AFM TH-19 transducers could not be performed as the appropriate materials parameters for backing layers and the piezoelectric element were not provided by the company that manufactured these transducers.

The graphs obtained experimentally for the dual quarter wavelength mass-spring matched transducer showed three resonant peaks similar to the KLM model, but the experimental curves indicated higher damping. The effect of damping suggests that there is trade-off between sensitivity and bandwidth. In order to overcome this in the future, focused transducers could be fabricated with less dense backing material. The use of less dense backing material may reduce the two-way fractional bandwidth but will provide greater sensitivity. Future transducers could use series inductive tuning to improve the sensitivity.

Another way to improve transducer performance would be to use greater number of matching layers. The problem with adding more layers with this configuration reported here is that the sample would have to be moved back and forth between the separate parylene coating machine and the evaporator for the Cu. This is time consuming as the system needs to be pumped down and ramped up for deposition. The total time taken for the deposition of three matching layers was approximately 10 hours. On the other hand the distinct advantage of using vacuum deposition for matching layers is that the transducers can be fabricated in bulk at the same time providing near identical performance if the evaporation process of parylene and copper is parallelised.

5.6 Conclusion

A potentially reliable, repeatable and cost effective process route for ultra-thinning of LNO has been demonstrated. In the future it is expected that this process route will prove viability for wafer scale bulk thinning of LNO, but in wafer repeatability needs further investigation. The vacuum deposition technique developed during this research has many advantages over conventionally matched transducers, while maintaining performance. With the vacuum deposition technique µUS transducers can be produced uniformly in large volume without adhesion of matching layers. As the use of loaded epoxy was avoided, this gives us the advantage of fabricating µUS transducers with low attenuation and versatile material selection based on the specific functionality of the transducer. The application of matching layers to single element probes in this work was demonstrated. The technique developed here could be easily implemented to with high frequency arrays because the acoustic characteristics of PZT ceramics are quite similar to LNO single crystal.

The focused mass-spring matched transducers fabricated were used for imaging and tissue characterisation of murine small intestine initially, but the transducer matching

layer delaminated over a period of time and the performance of these µUS transducers deteriorated. Hence a decision was made to use the commercial AFM TH-19 µUS transducers for tissue imaging and characterisation as the transducers showed uniform performance.

5.7 References

Brown, J., Sharma, S., Leadbetter, J., Cochran, S., & Adamson, R. (2014, September). "Vacuum deposition of mass-spring matching layers for high-frequency ultrasound transducers." In *Ultrasonics Symposium (IUS), 2014 IEEE International*, 101-104, IEEE.

Brown, J., Sharma, S., Leadbetter, J., Cochran, S., & Adamson, R. (2014) "Mass-spring matching layers for high-frequency ultrasound transducers: a new technique using vacuum deposition." *Ultrasonics, Ferroelectrics, and Frequency Control, IEEE Transactions on*, *61*(11), 1911-1921.

Cannata, J. M., Ritter, T. A., Chen, W., & Shung, K. K. (2001) "Design of focused single element (50-100 MHz) transducers using lithium noibate". In M. F. Insana & K. K. Shung (Eds.), *Medical Imaging 2001* (pp. 28–35). International Society for Optics and Photonics.

Demore, C., Sharma, S., Cochran, S., Hughes, D. a., & Weijer, K. (2011) "Multi-wavelength ultrasonic standing wave device for non-invasive cell manipulation and characterisation." *2011 IEEE International Ultrasonics Symposium*, (c), 188–191.

Sharma, S., Mcaneny, J. J., Mccrossan, J., & Cochran, S. (2011) "Ultra thinning of Lithium Niobate (LNO) for High frequency Ultrasonic Medical Imaging." In *EMFFT- Munich*.

Toda, M., & Thompson, M. (2010) "Novel multi-layer polymer-metal structures for use in ultrasonic transducer impedance matching and backing absorber applications." *IEEE Transactions on Ultrasonics, Ferroelectrics, and Frequency Control*, *57*(12), 2818–27.

Chapter 6: Materials and Methods for µUS Imaging and Tissue characterisation

"True method of knowledge is experiment"

William Blake

6.1 Overview

The work presented in this Chapter explains the materials and methods employed to test the hypothesis that, the murine intestinal tissue morphology of WT and $Apc^{Min/+}$ diverge with progressing age.

- In Section 6.1, the different aspects such as; clinical need and rationale behind design of µUS system for imaging and tissue characterisation in pulse-echo mode is explained. Furthermore, fundamental properties of the µUS transducer and the two ultrasound scanning systems developed during this project are explained in Sections 6.2.2 and 6.2.3. The algorithms developed for visualisation of data collected from the µUS scanners are explained in Sections 6.2.4 and 6.2.5.

- In Section 6.3, the methods used to monitor the progression of CRC using ultrasound tools for early detection and classification murine small intestine at varying ages is explained. The methods used for preparing murine tissue for scanning are explained in Section 6.3.1. Sections 6.3.2 - 6.3.5 explains the methods used for measuring acoustical properties of tissue such as: acoustic impedance, attenuation and BSC.

- In Section 6.4, the control experiments designed to measure acoustic impedance of tissue phantoms using through-transmission method and in order to verify the acoustic impedance measurements performed on tissue in pulse-echo mode using the ultrasound transducer are explained and also BSC measurements using polystyrene beads of varying sizes at different concentrations were made to understand how size and concentration of beads contributes to the variance of BSC in tissue.

6.2 High Resolution Ultrasound Scanning System

A µUS scanning system was developed to image and measure the ultrasound tissue properties of murine small intestine to aid diagnosis of CRC. The µUS system is based on the concept of acoustic microscopy (Shung, 2009). This section describes the development of µUS imaging system used in this work for qualitative and quantitative tissue characterisation to detect early stages of CRC by employing mouse models.

The development of a custom design system has several reasons, principally that commercial ultrasound imaging systems operating at frequencies greater than 35 MHz are not commonly available. Moreover, commercial systems have limitations when it comes to characterisation of tissues. For characterisation studies the raw backscatter signals are required and not just final images. Commercial systems lack the flexibility required for tissue characterisation. In commercial systems, it may not be possible to correct for diffraction effects and attenuation through axial scanning as correction curves may not be available. Hence a decision was made to build a custom designed system on a research platform in the laboratory. Two systems with increasing functionality and complexity were constructed.

A single element commercial ultrasound probe operating at 45 MHz (AFM Ltd. Birmingham, UK) was mechanically scanned over the tissue to collect echo signals at various positions. Apart from the ultrasound transducer, such systems requires mechanical scanning stages to accurately position and move the transducer, a pulser-receiver to excite the transducer and amplify the received signals, a digitizer to collect the backscattered echoes and a PC to control and automate the hardware. The first system was a simple step-repeat LabView controlled automated system. The imaging time for this system was large and there were limitations with the bit depth of the data being acquired. In order to overcome these limitations a second system with a capability to scan faster and superior bit depth resolution was designed.

At the heart of both the systems is the µUS transducer that generates acoustic waves and collects the backscattered echoes. In medical ultrasound applications where a pulsed wave is used it is common to use the centre frequency of the transducer. The frequency characteristics of the transducer are important in determining the characteristics of the imaging system. The axial and lateral resolution determines the quality of B-scans and is also important for tissue characterisation. For example, to compute the attenuation and BSC, the average spectra from adjacent lateral resolutions must be computed. The

lateral resolution determines how far the transducer has to be moved to record independent echoes. The axial resolution determines the distance along an echo line required for measurements. The depth of focus is also an important quantity as it provides an indication of the extent over which any features can change due to diffraction. Therefore it is important to understand the functional properties of the transducer.

6.2.2 Step-Repeat Scanning System

A single element µUS transducer is scanned at right angles to the propagating beam to obtain 2D images. To demonstrate the capability of µUS to image and characterize murine small bowel *in vitro,* a computer-controlled automated scanning system operating in pulse echo mode was designed. The LabVIEW (National Instruments, Newbury, UK) controlled scanning system was used to acquire the data, based on the the block diagram shown in Figure 6.1. Two stepping motors, (Shot 602, Sigma Koki, Tokyo, Japan) mounted on an optical breadboard (Thorlabs, Ltd. Ely, UK) for stability, moved the transducer across the sample in X- and Y-axes. The stepping motors have a 5-phase stepper motor that uses the "half drive step" method to drive the scanning stages. The scanning stages were connected to the computer via RS232 connection. The scanning stages have a minimum programmable increment of 2 µm and the scanner was programmed to return to its origin after completing the scan. The movement of scanning stages and data acquisition was automated using a LabView script. The scanning system was programmed to do raster scans to produce 2D data, which were post processed using imaging algorithms to produce 3D images.

The transducer was fitted to the remote pulser-receiver (DPR 500, JSR electronics, NY, USA). The remote pulser-receiver was mounted on a goniometer and then this was mounted on the stages using M4 screws. The transducer angle was maintained at 90^0 using the goniometer to avoid oblique incidence, i.e. the transducer not being at 90^0. Since the interaction of the waves with the tissue comprises more scattering than specular reflections, the effect of oblique incidence is very small (Waag, 1984). The tissue sample to be scanned is placed on a 3-axis micro-block flexure stage (Thorlabs, Ltd. Ely United Kingdom). The sample can be positioned accurately at the focal point of the transducer using the three translational axes X, Y, and Z. The sample holder provides a flat surface to support the sample and is a stable setup. A user friendly GUI

enables the users to input the sampling frequency, averaging, step sizes and total scan length (Appendix-I).

Pulsing and receiving was done using a commercial pulser-receiver (DPR 500, JSR Electronics, NY, USA). The pulser-receiver was connected via RS232 port to a PC, from which the control parameters for transducer excitation and reception are set using the JSR software. The settings were fixed at the following values for all the scans: *Trigger*: internal; *Pulse repetition frequency:* 200 Hz; *Pulse energy:* 12.40 μJ; *Voltage: 143 V; Damping:* 100 Ω; *Receiver Bandwidth:* 5 - 300 MHz and the receiver gain were set at 40 dB.

At each scan point, the RF data was obtained from a digital oscilloscope (HP 54810A, Agilent Technologies, Santa Clara, USA) at a sampling frequency of 1 GHz. Each A-scan stored was the temporal average of 128 echoes to decrease noise enabling weak signals from the epithelial layer to be recorded. The 9-bit data from the oscilloscope were transferred to the computer via a general purpose interface bus (GPIB). The oscilloscope was chosen to operate in multiple record capture mode, wherein it could be triggered continuously to capture and stack a number of waveforms in its memory. The number of samples to be recorded can be defined by the user. This feature was useful in collecting just the portion of waveform corresponding to the area of interest. This reduced the memory requirements. The LabView interface showed B-scan images acquired as the scans were in progress. The flow chart for the LabVIEW controlled step-repeat scanner is shown in Figure 6.2. All of the tissue imaging and characterization studies reported in this thesis were performed using this system.

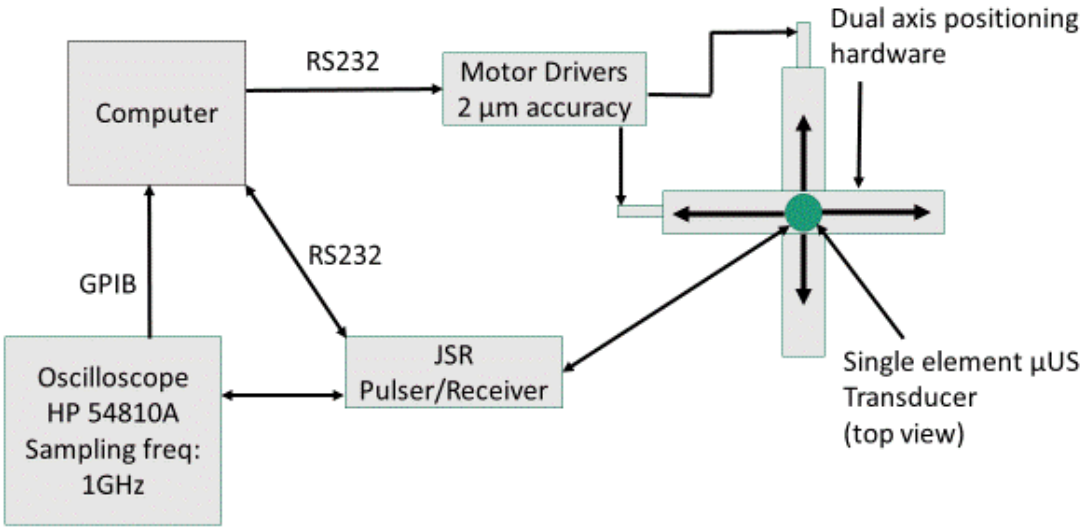

Figure 6.1: Block diagram of the step-repeat scanner used for scanning of tissue. A computer controls the motion of the transducer and an oscilloscope collects the peak amplitude data which is transferred to the computer to generate B-scan images.

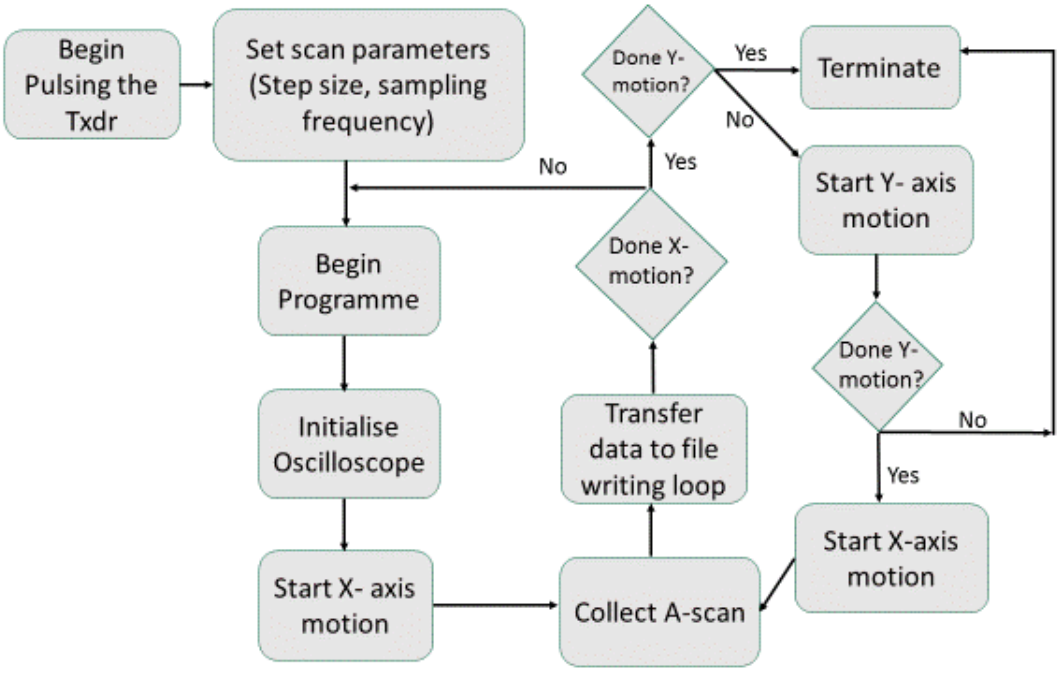

Figure 6.2: Flow chart for the LabView controlled step-repeat scanning system. The scanner is automated to collect RF data from the tissue which is post processed to produce B-scans and measure tissue properties.

The total time taken to record a single B-scan from a tissue sample measuring 12 mm in width was approximately 18 minutes. The reason for the long imaging time of the

system was that the scanning system used a step-repeat scanning process and did not have position encoders which decreased the lateral positioning accuracy of the scanning stages. Also the data transfer rate from the oscilloscope to the computer using the GPIB interface was too slow. GPIB communication protocols can handle high data transfer rates up to 1.5 MB/sec, but these were not achieved in the present system.

The increased time taken by the digitising oscilloscope to parse commands sent by the computer reduced the data transfer rates. For example: assuming, that the data are collected at regular intervals during step-repeat motion of the transducer, then the inter-sampling distance should be smaller than half the lateral resolution of the transducer to avoid aliasing artefacts due to beam overlapping. Data from one echo line should be transferred to the computer during the time it takes the transducer to move to the next location. If the transducer moved in steps of 20 μm, then 0.31 s will be the time taken to transfer a waveform from the oscilloscope to the computer approximately this was determined by benchmark experiments conducted.

The other drawback of this system was that, while recording each echo line (A-scan), the vertical scale on the oscilloscope had to be adjusted manually in order to record strong signals like surface reflections from the muscle free of clipping, as well as weak signals backscattered from mucosa and epithelial layer of the murine intestine without quantization effects. For example, if a vertical scale of +1 to -1 V is set, a weak signal with amplitude of 20 mV will be quantized to zero, due to the number of bits which was limited to eight. On the other hand if the scale is set to a low value of +10 mV to -10 mV, the strong signal from the muscle surface will be clipped.

As there was no prior way of knowing the magnitude of signals to be recorded, the scaling on the vertical axis of the oscilloscope was set by trial and error for each echo sequence to ensure signals were recorded without degradation due to quantization and clipping effects.

The step-repeat scanner was used for most of the work presented here but to overcome its drawbacks in terms of time and improve the bit depth of the data being recorded, a high speed scanner was designed.

6.2.3 High Speed Scanning System

The drawbacks of the step-repeat scanning system explained in Section 6.2.2 were addressed with this new design. A LabVIEW controlled fast scanning system was used to acquire the data, the block diagram is shown in Figure 6.4. The mechanical scanning of the transducer in the X and Y-axes across the specimen was achieved using two Maxon brushless servo motors (ML series 3000, Motionlink Ltd. Berkshire, UK) that uses the ball screw drive method to drive the scanning stages. The scanning stages had inbuilt position encoders (HEDS 500ppr, Motionlink, Ltd, Berkshire, UK) that enabled measurement of the position accurately in the lateral axis at the time of pulsing. This is critical in designing a fast scanner. The scanning stages were mounted on an optical breadboard (Thorlabs, Ltd. Ely United Kingdom) for stability.

The scanning stages were controlled by a two axis motion controller (Galil DMC 4132, Motionlink, Ltd, Berkshire, UK). The motion controller was connected to the computer via USB connection. The scanning stages have a minimum programmable increment of 0.5 µm and a total travel length of 25 mm. They can be controlled either through the manufacturer supplied software or a LabView script, that had to be developed. Pulsing and receiving was again done using a commercial pulser-receiver (DPR 500, JSR Electronics, NY, USA). The transducer was mounted onto the scanning stages, and pulsed in a similar way to that described in Section 6.2.2. The flow chart of the LabView-based FPGA high speed scanner is shown in Figure 6.4.

For the high speed scanning system, to perform a continuous scan, the speed of the motion should be as high as possible which leads to two problems. Firstly the time required to capture waveforms. The transducer that is in continuous motion should have moved by only a small fraction of the distance, otherwise the waveforms being averaged do not correspond to the same tissue location. Secondly during the time the transducer moves to the next location, where another A-scan is recorded, two tasks should be completed: 1.all the waveforms from the previous location should be recorded and 2. the averaged waveforms have to be transferred to the PC's memory.

Pulsing and receiving was done using a commercial pulser-receiver (DPR 500, JSR Electronics, NY, USA). The pulser-receiver was connected via RS232 port to a PC, from which the control parameters for transducer excitation and reception are set using the JSR software. The settings were fixed at the following values for all the scans: *Trigger*: internal; *Pulse repetition frequency:* 20 KHz; *Pulse energy:* 12.40 µJ;

Damping: 100 Ω; *Receiver Bandwidth:* 5 - 300 MHz and the receiver gain were set at 40 dB. For a PRF of 20 KHz the interval of pulses is 50 µs, high PRF ensures that all the waveforms were acquired from the same position for a set scanning speed of 2 mm/sec.

At each scan point, the RF data were obtained from a 12-Bit FlexRIO oscilloscope adapter module (NI 5772, National Instruments, Newbury, UK) at a sampling frequency of 800 MS/s. The oscilloscope module has a 50 Ω AC-coupled input. The FlexRIO adapter module is paired with a field-programmable gated array (FPGA). The FPGA module communicates with the computer via a PCI (peripheral component interconnect) Express bus. PCI Express overcomes the data transfer limitations of the GPIB interface that was used in the step-repeat scanner. The PCI Express bus operates at a theoretical bandwidth of 132 MB/s. Each A-scan stored was the temporal average of 128 echoes to decrease noise, and the 12-bit data from the digitiser was transferred to the computer via PCI Express. The number of samples in waveforms could be specified beforehand. The FPGA board captures the specified number of data points and re-arms itself to capture successive waveforms.

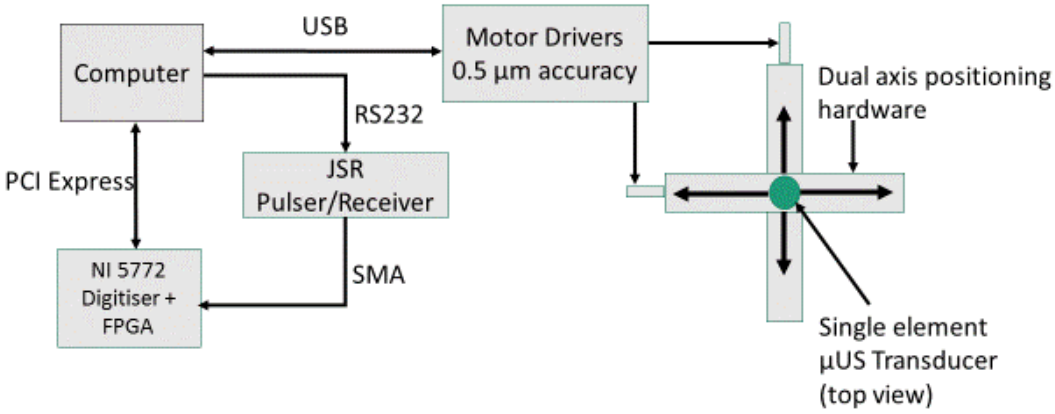

Figure 6.3: Block diagram of high speed scanner used for scanning of tissue. A LabView controlled FPGA module controls the motion of the transducer and a FlexRIO digitiser collects the peak amplitude data which is transferred to the computer via a high speed PCI express card to generate B-scan image.

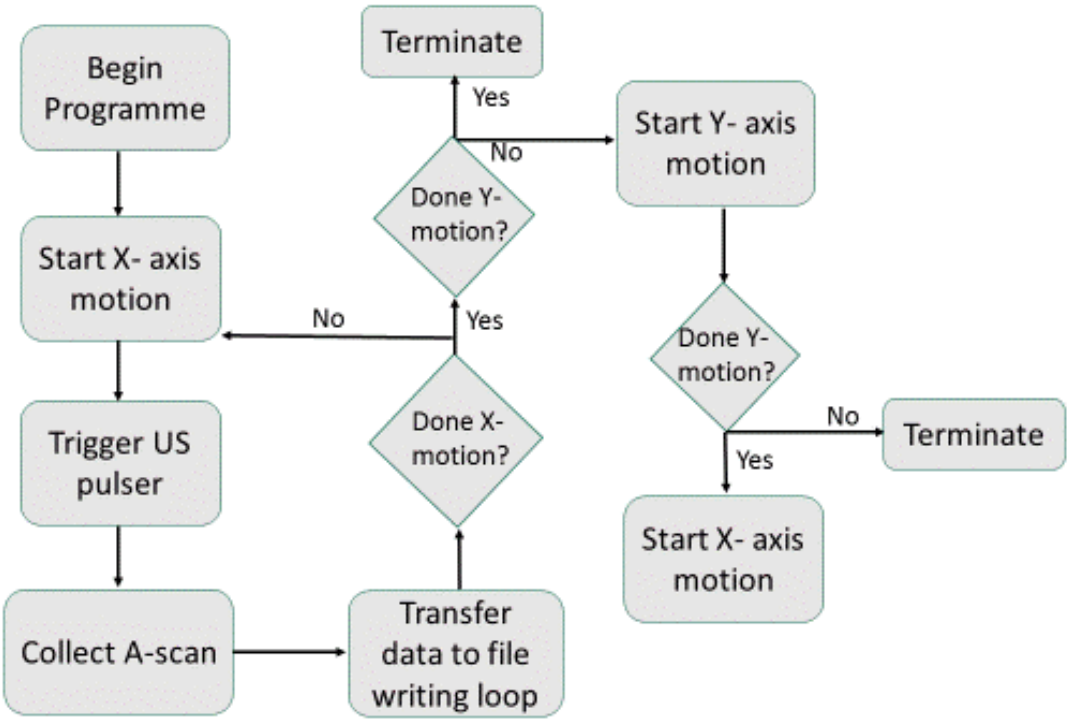

Figure 6.4: Flow chart for the LabView controlled high speed scanning system. FPGA controls the motion of the scanner and the digitiser to collect RF data from the tissue which is post processed to produce B-scans and measure tissue properties.

6.2.4 Visualisation of Data

The primary aim of this work was tissue characterisation but it is often advantageous to visualise B-scan images. Tissue characterisation and Imaging have different requirements, in case of tissue characterisation there is no need to collect A-scans that are spaced closed together, in fact the echo lines need to be spaced larger than the lateral resolution to collect independent echoes. For imaging the echo lines should be spaced less than one half of the lateral resolution of the transducer, to construct an image by combining all the echo lines. Therefore tissue characterisation can be done on the data collected from imaging experiments but not vice versa.

In this work data was collected using the AFM TH-19 transducer using the step-repeat µUS scanning system. Echo lines were recorded from 600 to 700 independent lateral locations and 10 axial locations for each of the tissue specimens by scanning the transducer along X and Y axes in a raster format. The separation distance between scans in Y direction was 1 mm. The lateral stepping distance of the transducer was set to 20 µm, which corresponds approximately to $1/5^{th}$ of the lateral resolution of the transducer.

The A-scans recorded were post processed to obtain B-scan images. They represent a 2D slice from a volume of a tissue, with scan depth and scan step size forming the two axes of the image. The data collected from the ultrasound scanning system were stored in a .txt format in the form of an *m* x *n* array, where *m* corresponds to the number of individual A-scans collected, and *n* corresponds to the number of points in an A-scan. Metadata such as the sampling frequency, scan step size and number of averages were included in the RF data. Each of the points in the matrix represents a voltage measurement recorded from the oscilloscope or the digitiser. The RF data was processed using MatLab (Natick, MA, USA; www.mathworks.com) to produce B-scan images of the tissue sample for visual inspection and, acoustic parameters of the tissue such as: acoustic impedance, *Z*, attenuation coefficients, α, and BSC were computed from the RF data.

The flowchart for producing B-scan images and an example of a B-scan image is shown in Figure 6.5. A Hilbert transform is performed on each individual A-scan to find the envelope of each pulse. The Hilbert transformed data is then converted to a dB scale and represented as a colour map. The features in the image are displayed as a modulation in the displayed intensity (i.e. colour) for each pixel in the image.

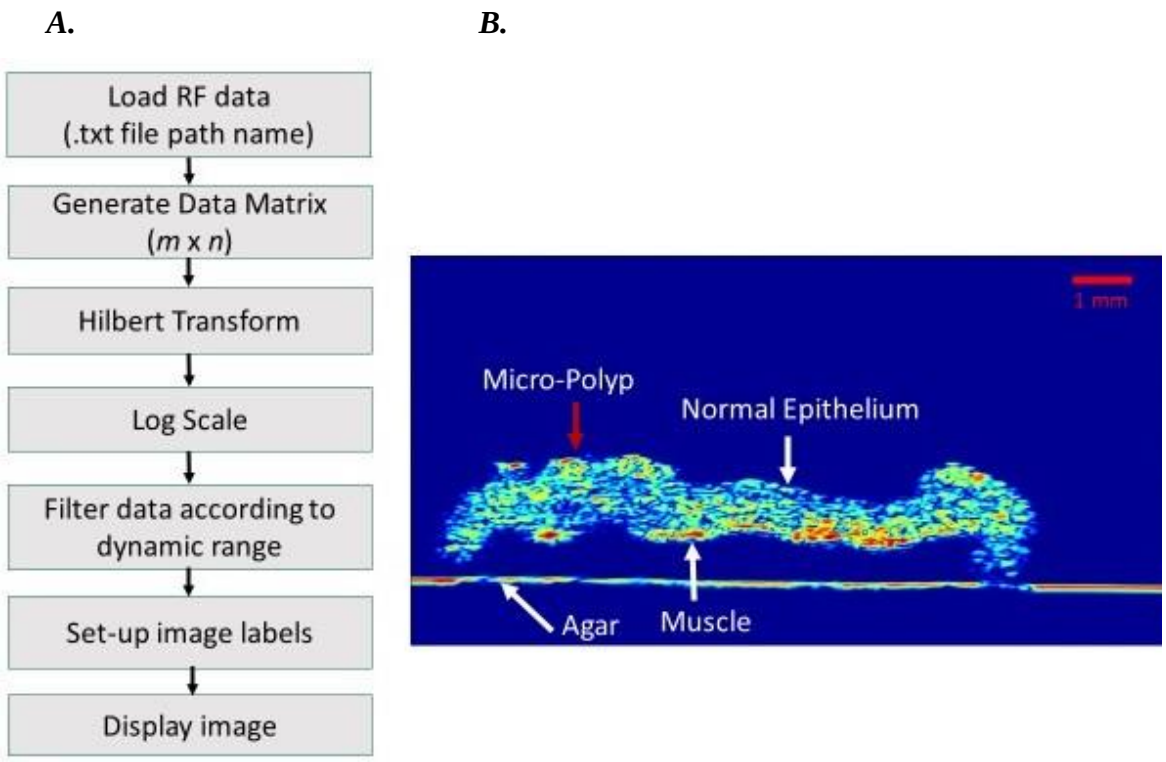

Figure 6.5: Procedure to produce B-scan images from RF data. ***A.*** *Flow chart showing the steps involved in producing a B-scan from the recorded A-scans at different positions across the tissue.* ***B****. An example of a B-scan image produced by scanning the transducer across a murine small intestine with micro polyps using the 45 MHz probe. Dynamic range of the image = 30 dB.*

6.2.5 3D Imaging

Three dimensional (3D) ultrasound imaging is an advancement of ultrasound technology. To produce 3D images of the tissue samples, a continuous series of B-scan images (2D) was acquired as explained in the previous section, across the entire volume of the tissue. The B-scan images were 'stitched' together by manipulating the data via the stacks menu in a public domain imaging software package (ImageJ, NIH, Maryland, USA). The method used for creating 3D images is shown in Figure 6.6. This method of visualising the data allowed projection of the data in the Z direction, which permitted visualisation of 3D data in one slice. The volumetric data presents a SNR lower than 2D data, and image processing such as de-speckling was used to enhance the contrast of the images. The reason for lower SNR is that during the reconstruction of 3D images from 2D slices, the 2D slices are misaligned and some processing is required for proper alignment during this process some of the original pixel values may be lost and some processing using median filters is required. The process of producing a series of B-scans from a volumetric scan was automated using a custom made MatLab programme

(Appendix II). 3D images allow inspection of the images in Z-axis, which is important as it allows visualisation of the extent of polyp invasion and muscle damage caused by polyps in the murine small bowel.

In the present work, the B-scans were recorded from the murine intestine in the XY plane with a step size of 20 µm, and the adjacent B-scans were recorded in steps of 50 µm. The total area scanned was 14 mm in the X-axis and 12 mm in the Y-axis, giving a total scan area of 168 mm^2. After the data was collected, each B-scan was manually visually inspected, to ensure that the muscle layer in the tissue was clearly visible. ImageJ was then used to produce a rotating projection of the murine intestinal surface in RGB format, showing the morphology of the intestinal surface.

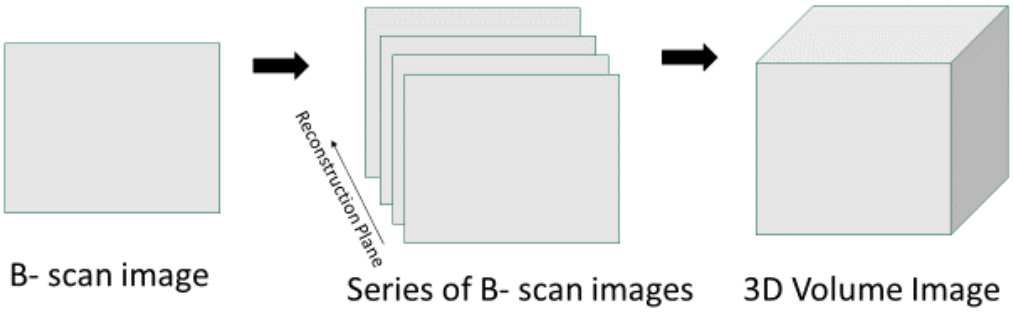

Figure 6.6: Illustration of method used for creating 3D volumetric images from a series of B-scan images, using the ImageJ imaging software.

6.3 Ultrasound Tissue Characterisation

The hypothesis that, the intestinal tissue morphology of WT and $Apc^{Min/+}$ diverge with progressing age, has been investigated by attempting to answer the question: Can varying structural differences be identified between WT and $Apc^{Min/+}$ mice at varying ages by qualitative and quantitative US characterization? The hypothesis was confirmed by using a specially designed µUS system, which is capable of producing B-scan images and measuring three important ultrasound characteristics such as: attenuation, acoustic impedance and BSCs. The acoustic principle of µUS scanning system is schematically shown in Figure 6.7.

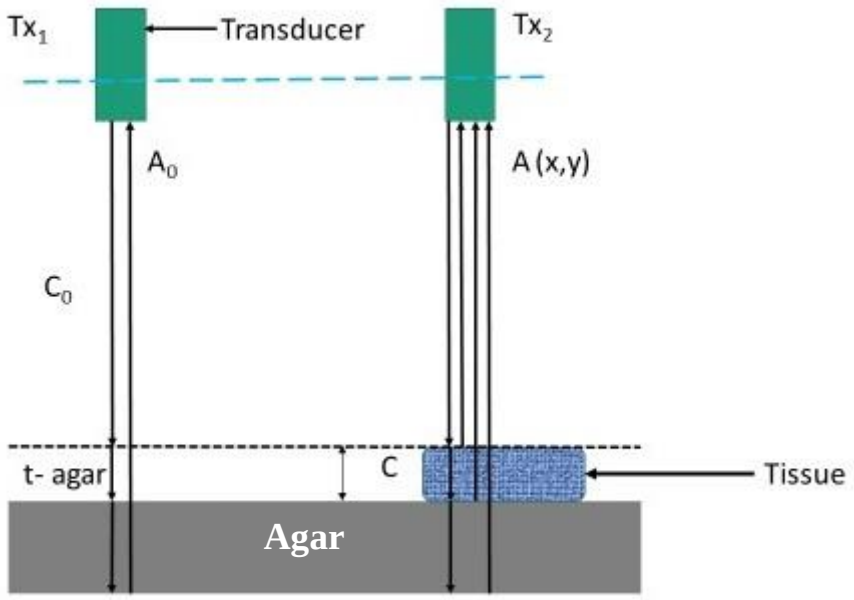

Figure 6.7: Pulse-echo measurement conditions to determine attenuation, BSC's and acoustic impedance of murine small intestine. A 45 MHz transducer is mechanically scanned across the tissue sample pinned on agar (thickness = 2 mm) at a distance of 5 mm, close to the focal distance. The reference signal from agar has peak amplitude of A_0 and time of arrival t_0, while the sample returning from the tissue sample at position (x, y) has a peak amplitude of A(x, y) and time of flight of t(x, y). A_0 is used as the reference signal for calculating α.

The tissue sample under examination is pinned on agar close to focal plane of the transducer and the motion of the transducer is controlled by high precision mechanical stages and is constrained to follow a raster pattern generating an array of measurements across the tissue. Agar was chosen as the substrate, as it was easy to pin the tissue and the reflection of the ultrasound signal from the agar substrate was free of reverberations. The backscattered signal from the tissue is recorded and processed to compute the acoustical properties of the tissue. An example of the backscattered A-scan from tissue pinned on agar is shown in Figure 6.8. The methods used for computing the acoustical properties to determine the differences between normal and pre-cancerous murine small intestine are explained in the following sections.

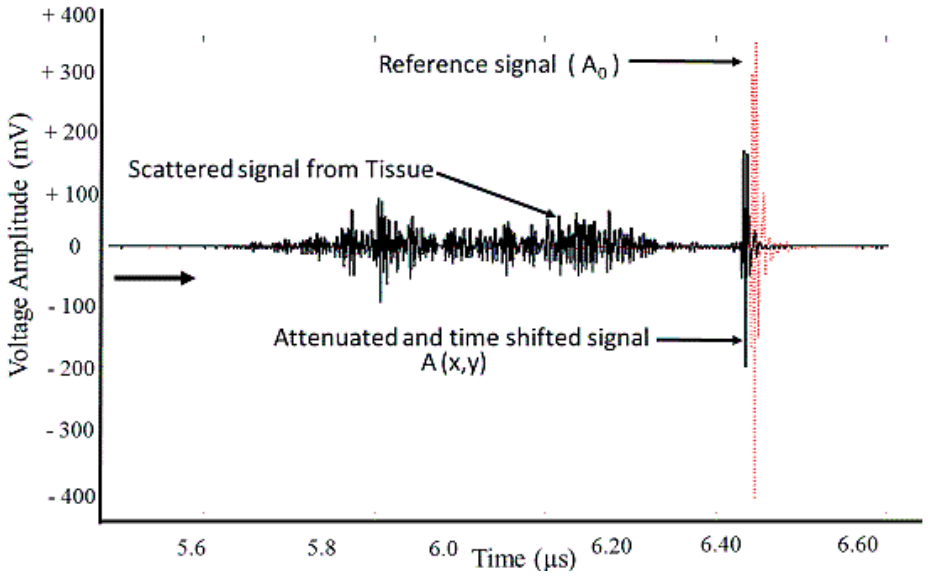

Figure 6.8: A-scan ultrasound signal measured by scanning AFM TH-19 probe over murine intestine in pulse-echo mode. The signal in red is the reference signal (A_0) reflected back from agar without tissue and the signal in black is an example of the signal A(x,y) obtained when the transducer moves across and scans the tissue. Notice the reduced amplitude and time shifted signal due to attenuation of sound after interaction with the tissue.

6.3.1 Preparation of Murine Small Intestine

All experiments were performed in accordance with the UK Home Office guidelines. Mice used for this study were WT or $Apc^{Min/+}$ of the C57BL/6 genetic background (Su & Kinzler, 1992). Five males and five females of WT and $Apc^{Min/+}$ genotype were used for each time point of 60, 90 days and for an older cohort comprising mice greater than 95 days old that carried a significant polyps load. The $Apc^{Min/+}$ mice is heterozygous for mutations in adenomatous polyposis coli (APC) and has been used as a model for familial adenomatous polyposis (FAP) as the individuals affected develop polyps in the small intestine. The murine intestine samples for ultrasound scanning were provided by Dr. Scott Nelson and Dr. Aliya Fatehullah , Nathke Lab, Wellcome Trust, University of Dundee.

The mice were sacrificed using CO_2 asphyxiation. The small intestine was removed and 3 cm long sections from Region 2 as shown in Figure 6.9 were washed with cold phosphate buffer solution (PBS) and fixed using 4% para-formaldehyde (PFA, pH = 7.4), overnight at 4°C. The tissue was removed from the 4% PFA solution and allowed to equilibrate to room temperature in degassed PBS prior to scanning. The tissue was

pinned on an agar plate to prevent it curling up. However, it was difficult to pin the tissue completely flat as the tissue samples are thin (thickness = ~ 550 - 750 µm) and have a strong tendency to curl. Conventional B-scan images use only the magnitude of the envelope and have limited value as it is difficult to difficult to distinguish between features such as tumours and benign lesions (Turnbull & Ramsay 1996; Hoffman et al., 1992). Hence it becomes vital to study methods that attempt to classify the tissues based on their ultrasonic properties.

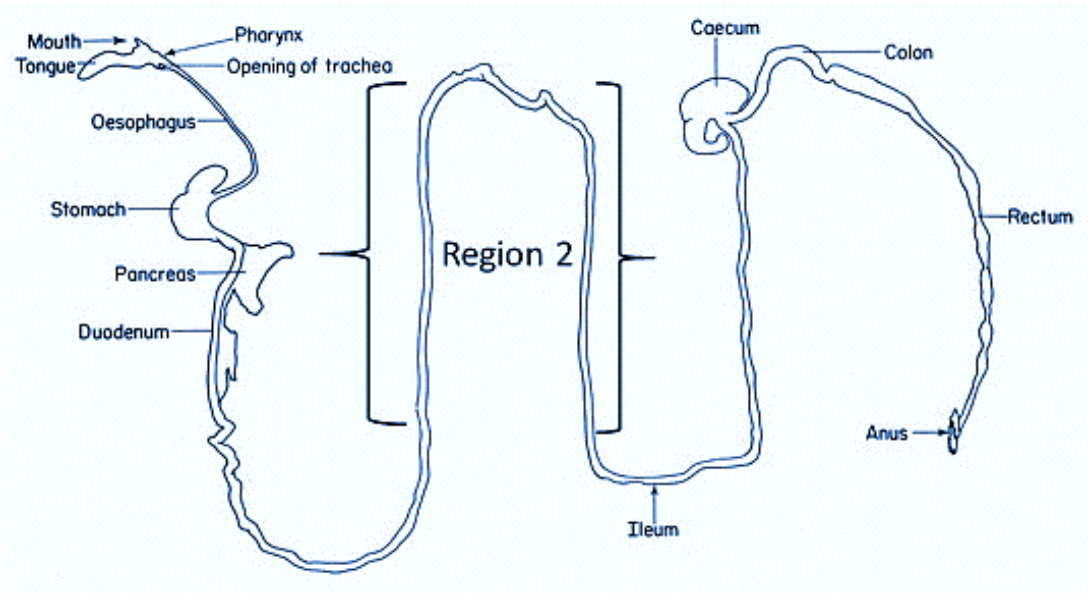

Figure 6.9: Anatomy of murine GI tract. The portion of small intestine marked as Region-2 measuring approximately 3 cm in length was used for ultrasound imaging and characterisation studies.

6.3.2 Image Processing

The experiments were performed on murine intestinal tissue by following the experimental protocol described in Section 6.3.1. Understanding ultrasound interaction in the top layer of the tissue where the polyp is usually seen is necessary and a technique to characterize the top layer of the tissue from the muscle is required as the tumours develop from the crypt and grow towards the lumen. Detecting tissue changes in the top layer is a prerequisite for early detection of colon cancer.

An image processing algorithm to classify the top and bottom layer of the tissue was developed in MatLab (Appendix II) to classify the tissue as top or bottom layer. The RF

data from the top layer was used for measuring the ultrasound tissue properties. This is important because understanding the mechanical properties of the polyp and the neighboring tissue, enables classification of normal and abnormal tissue quantitatively. This approach of image segmentation delineated the lumen (crypt, villi, epithelial layer and mucosa) from the muscle layer.

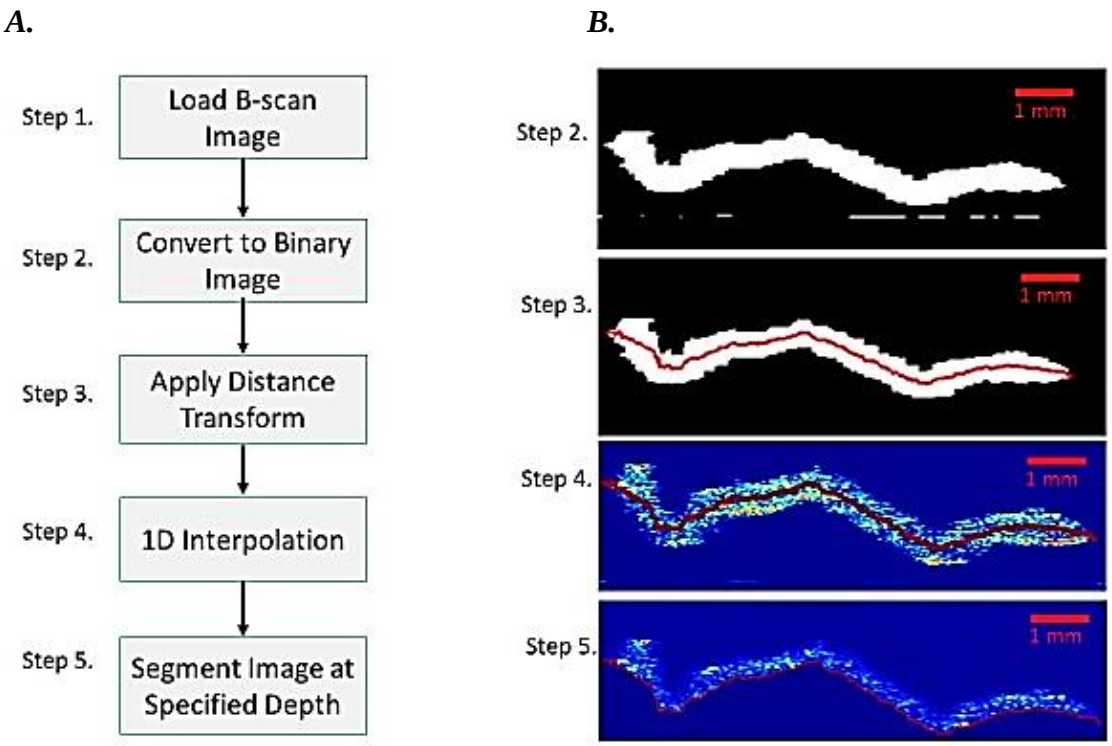

Figure 6.10: Illustration of tissue segmentation algorithm. ***A.*** *Step wise procedure used for segmenting the B-scan image at desired depth of the tissue.* ***B.*** *Shows the application of image segmentation algorithm to a B-scan image. Step .5 shows the final image, the RF data from this segmented image were used for quantitative analysis of tissue data.*

The algorithm segments the tissue at required depths. The algorithm is a five-step procedure as shown in Figure 6.10, which works on various shapes of tissue. The approach is based on Euclidean distance transform (EDT). EDT is the straight line distance between two adjacent pixels in a gray scale image. The gray scale B-scan image was converted to a binary image and EDT was applied to the binary image. The midpoints of the binary image were used to fit a best fit mathematical line through the middle of the tissue. The MatLab function used for segmentation of the image was 'bwdist'. This function computes the EDT of the binary image. For each pixel in the binary image, the distance transform assigns a number that is the distance between that pixel and the nearest nonzero pixel of the binary image. The mid-band fit was then

superimposed on the RF image using 1D linear interpolation. In Figure 6.10 (B) the red line passing through the middle of the B-scan images is the best fit line. The RF data from either the top layer or the bottom layer can then be selected for further analysis. The algorithm also allows accurate thickness measurement of the tissue which was required for accurate measurement of attenuation coefficients. The tissue can be segmented at user defined depths using the EDT approach. Acoustic parameters such as attenuation coefficients, acoustic impedance and BSC's were measured from the top half layer of the murine intestine.

6.3.3 Attenuation Coefficients

Attenuation of ultrasound is a result of absorption and scattering. Absorption occurs due to conversion of energy into heat is due to relaxation mechanisms. Scattering loss is attributed to incident wave being partially redirected in many directions and thus reducing the energy of the propagating wave. The computation of attenuation coefficients from pulse echo measurements requires comparison of the recorded signals from several depths of the tissue specimen. The attenuation at various depths in the tissue will differ because of attenuation, and also due to the changes in backscatter coefficients between depths (Raju & Srinivasan, 2001). This difficulty was overcome by assuming that the region over which attenuation is being computed to be in homogenous continuum. The attenuation coefficients reported here represent the signal loss as recorded by the transducer with respect to a reference measuring point.

Figure 6.7 shows the schematic representation of the system used for the measurement of attenuation, $\alpha(x, y)$. Attenuation depends upon two signals received by the µUS transducer. The reference signal, obtained from agar with an acoustic path which, does not pass through the tissue has a peak amplitude, A_0, while the signal returning from tissue at the position (x, y) has a peak amplitude of, $A(x, y)$. The attenuation coefficient, α, at (x, y) is computed using Equation *(6.1)*:

$$Attenuation\ (\alpha) = -\frac{20}{2l} * log_{10}\frac{A(x,y)}{A_0}\, db\ mm^{-1} \qquad (6.1)$$

l, is the thickness of the sample in mm. The equation does not consider frequency dependent attenuation and in effect, computes the attenuation coefficient at the centre frequency of the transducer, i.e. 45 MHz. The attenuation coefficient has contributions from both absorption and scattering effects. The sources of errors due to refraction of the ultrasound beam between the coupling medium and the sample and interface errors need to be given consideration. The two specific sources of error due to refraction when the sample is placed perpendicular to the beam diameter will be due to a non-parallel specimen and misalignment of the specimen with respect to the transducer (Moran, Bush, & Bamber, 1995). The goniometer on which the transducer was fixed ensured that the acoustic reflection from the sample surface was optimised. The calculation of attenuation coefficient for every A-scan was fully automated by developing an algorithm in MatLab (Appendix II).

6.3.4 Acoustic Impedance

The acoustic impedance of the tissue, $Z_{T,}$ was computed in pulse echo mode. The technique is similar to that proposed by Strohm and Kolios and (Gururaja & Schulze, 1985; Strohm & Kolios, 2009). Strohm et al., measured the mechanical properties of cells in pulse-echo method and Guruaja et al., measured the acoustic impedances of composite materials in pulse-echo mode. The acoustic impedance of tissue, $Z_{T,}$ was computed by first recording the magnitude of the reflected amplitude, A_{ref}, from a quartz optical flat. An x-cut quartz flat of thickness 500 µm was placed on 3% agar at the focal point of the transducer and the reflected signal amplitude was recorded. Quartz flat was used as it has a uniform surface and well calibrated thickness. The reflectance, *R*, of the quartz and water interface was then computed using Equation *(6.2)*.

$$R = (Z_{quartz} - Z_0)/(Z_{quartz} + Z_0) \qquad (6.2)$$

Z_{quartz}, and Z_0, are the known acoustic impedances for quartz and coupling medium respectively. Z_{quartz} = 12.48 MRayl and Z_o = 1.48 MRayl.

The incident amplitude (PI) from the transducer is then found from Equation *(6.3)*.

$$PI = A_{ref}/R \tag{6.3}$$

The acoustic impedance of the tissue, Z_T, is then measured using Equation 6.4:

$$Z_T = -Z_0 \frac{(A_{ref}+PR)}{(PR-PI)} \tag{6.4}$$

PR is the magnitude of reflected voltage amplitude recorded from the tissue at any given position, *x*. The acoustic impedance is calculated over the entire sample of tissue and then averaged to obtain the mean acoustic impedance of the tissue. The acoustic impedance measurements were automated by using an algorithm developed using MatLab (Appendix II). Approximately 6000 A-scans were collected across a single tissue specimen and the individual acoustic impedances for the A-scans were computed and then averaged to obtain the mean acoustic impedance.

The acoustic impedance measurements are accurate when the transducer is positioned perpendicular (90^0) to the tissue. Practical limitations arise from the fact that the transducers have a finite size, so the waves emitted from it is spread out or diffracted. Secondly, the tissue is heterogeneous and the acoustic parameters such as density and velocity vary from one point in the tissue to another, due to which the amplitude varies and part of the wave is scattered in various directions. For the calculation of Z_T, only the wave reflected back at 90^0 to the transducer was considered.

6.3.5 Backscatter Coefficient (BSC)

Backscatter coefficient is one measure of tissue properties. BSC is defined as the differential scattering cross section per unit volume of tissue at angle of 180^0. The BSC was computed by following the approach originally described by Nicolas et al (Nicholas, Hill, & Nassiri, 1982) with the exception that a strongly focused transducer geometry is used which simplifies the equation for the BSC by eliminating a complex directivity factor. The method of computing BSC is similar to the one used by Foster et al.,(D'Astous & Foster, 1986; Foster & Austin, 1984).

The steps involved in computing BSC are shown in Figure 6.11. The averaged and gated RF echo signal was recorded from the tissue at the focal point of the transducer.

To improve the estimate of BSC the averaged RF signal divided by the RF signal by a calibration spectrum to remove system dependent effects and then compensated for attenuation effects. The calibration spectrum was obtained by placing an x-cut quartz flat (thickness = 500 µm) at the focal point of the transducer. The width of the signal is gated to eliminate specular reflections from Agar substrate on which the tissue is pinned. A gate length was adjusted for every tissue sample under investigation, the gate corresponded to the thickness of the tissue. The gate length varied for different specimens and was dependant on the thickness of the top layer of the tissue which was variable. The typical thickness was found to be between 250 – 350 µm. Equation *(6.5)* was used to compute BSC.

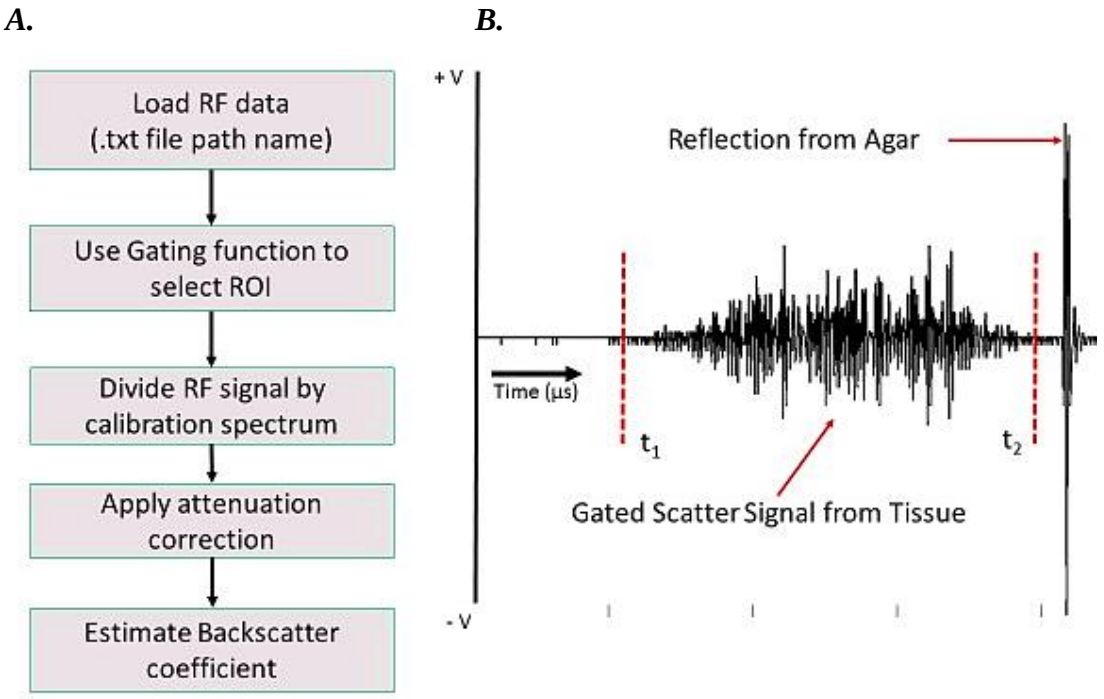

Figure 6.11: Steps involved in computation of BSC from RF data. ***A.*** *Flow chart of the algorithm used to measure BSC from tissue data.* ***B.*** *A-scan of the tissue to illustrate the gating procedure used for computation of BSC, the signals from agar and muscle were omitted and only the reflections from the top layer of the tissue were considered.*

$$BSC = \frac{R}{2\pi(1-cos\theta_T)} * \frac{\int_{t1}^{t2} |v_{tissue}|^2 dt}{\int_{-\infty}^{\infty} |v_{reference}|^2 dt} * \frac{2\alpha'}{(e^{-2az_1})(-e^{-2az_2})} \qquad (6.5)$$

R, is the intensity reflection coefficient of the water and quartz interface calculated using Equation *(6.2)*, V_{tissue}, is the measured scatter signal from tissue and $V_{reference}$, is the signal measured from the quartz interface measured. θ_T, is the half angle subtended by the transducer aperture at the focus and z_1 and z_2 are the axial distances that corresponds to the gates times t_1 and t_2 respectively. The unit of BSC is steradians per mm ($sr^{-1}mm^{-1}$). α', is the intensity attenuation coefficient, calculated using Equation *(6.6):*

$$\alpha' = \frac{2\alpha}{8.686}\ mm^{-1} \qquad (6.6)$$

The magnitudes of errors associated with BSC measurements are unclear due to the definitive lack of standard of BSC measurements. The errors associated with BSC can be deduced from the individual components of in Equation 6.5. This approach has been adopted by Nassiri and Moran et al., (Moran et al., 1995; Nicholas et al., 1982) to analyse the sources of errors. Sources of errors which have been considered are: neglecting the attenuation coefficients in the coupling medium, and determining the exact thickness of the sample. The uncertainties in the measurement of the attenuation coefficients dominate the measured BSC values, as the attenuation coefficients were used as a correction factor for estimating BSC.

6.4 Control Experiments

To validate the quantitative results obtained from pulse echo measurements on tissue, control experiments using agar phantoms and polystyrene beads were designed to measure acoustic impedance and BSc's. Insertion technique was used for characterising agar. Using this technique attenuation coefficient, α, and acoustic impedance, Z, were computed. The technique used is similar to one described by Zell and Haisch, (Zell & Haisch, 2007). The BSC was computed from known sizes and concentrations of polystyrene beads mixed in 0.5% agar using the AFM TH-19 probe operating at 45 MHz. Control experiments to evaluate BSC were performed to understand the spectral content of echoes, in turn to understand the physical characteristics and the distribution of scatterers in murine intestinal tissue. The method used for control experiments is explained in the following sections.

6.4.1 Acoustic Impedance

Measurements of acoustic impedance of varying concentrations of agar by mass were made at 5 MHz using the non-contact-through transmission set-up (figure). Six samples of agar with varying mass concentrations of 0.5%, 1%, 1.5%, 2%, 2.5% and 3% were used. As an example the ratio of agar powder (Agar, Fisher Scientific, Loughbourgh, UK) to deionised and degassed water for a 0.5% agar phantom was 0.5 g agar: 99.5 ml water. The agar was mixed in the water using a magnetic stirrer and heated to 70 ^{0}C while still stirring to ensure all of the powder dissolved. Heating ensured there were no air bubbles in the mixture. The mixture was then gently poured onto a petri dish and allowed to cool to room temperature. The agar phantom was then gently removed from the petri dish and cut into 12 mm^2 square samples of thickness 11 mm, which were then placed inside the water tank for characterisation as shown in Figure 6.12.

Two 5 MHz flat immersion transducers (Sonatest INC, Texas, USA) were used as the transmitter and receiver respectively and clamped into position facing each other and separated by a distance of 15 cm to ensure both the transducers were not in the near field (Figure 6.13). The measured physical parameters and signal statistics of the 5 MHz ultrasound planar transducers are listed in Table 6.1.

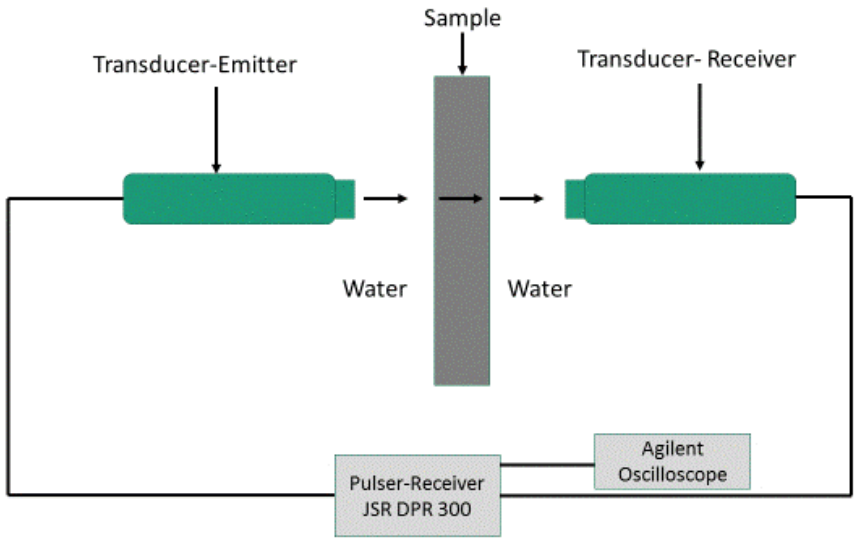

Figure 6.12: Schematic of the Through-Transmission set-up for measurement of attenuation coefficients and acoustic impedances of varying concentrations of agar using a 5 MHz ultrasound probe.

Table-6.1: Physical parameters and signal statistics for 5 MHz transducers used in through-transmission measurements.

Parameter	**Value**
Piezo Material	Lead Metaniobate
Shape	Circular / Planar
Size (mm)	12.5
Frequency (MHz)	5.18
Pulse Width (ns)	100
Pulse Impedance (Ohms)	50
Near Field Length (mm)	140
Pulse Duration (µs)	0.84
-6 dB Bandwidth (MHz)	2.73

Both the transducers were connected to a DPR 300 pulser-receiver and an oscilloscope (Agilent 54641 A, Agilent Technologies, South Queensferry, UK). A pulse was transmitted by one transducer upon excitation by the pulser-receiver and the time scale on the oscilloscope was adjusted so that the pulse from the receiving transducer was clear and the edge could be seen, ensuring that the time taken for the wave to travel between the transducers could be recorded accurately. The agar sample was then carefully placed between the transducers, ensuring the transducers were not moved. The pulse transmitted through the sample could then be compared with the original pulse and the time difference Δt, was recorded. Δt, is the difference in time of arrival between the two signals, i.e. signal without the sample to signal when the sample is in place. Between each measurement the reference pulse was checked to ensure the transducers were not moved. The speed of sound in the material, attenuation and acoustic impedance of varying concentrations of agar were measured. The density of agar was calculated by dividing the mass of agar, by the volume of displacement of water when the agar sample was submerged in a measuring cylinder.

The speed of sound in agar was calculated by using Equation *(6.7):*

$$v_s = \left(\frac{1}{v_w} - \frac{\Delta t}{\Delta x}\right)^{-1} \qquad (6.7)$$

$v_{s,}$ is the velocity of sound in agar, v_w, is the speed of sound in water at room temperature and was taken as 1482.3 ms^{-1} (Duck, 2010). Δx, is the thickness of the sample which was calculated by using a non-contact thickness monitor.

The acoustic impedance, *Z*, was calculated by multiplying the velocity of sound in agar, v_s, and density of agar, ρ, using Equation *(6.8)*.

$$Z = \rho v_s \qquad (6.8)$$

The attenuation coefficients of the agar samples were measured using Equation *(6.9)*:

$$\alpha = 8.686 * \left(\alpha_w - \frac{1}{\Delta x}[lnA_s - lnA_w - 2\,ln(1-R)]\right) \qquad (6.9)$$

$\alpha_{w,}$ is the attenuation of ultrasound in water having a book value of 0.0022 dB cm^{-1}. 8.686 is the conversion factor from Np cm^{-1} to dB cm^{-1}.

A_s, is the peak voltage amplitude with the sample in between the transducers. A_w, is the peak voltage amplitude recorded without the sample.

R, is the acoustical reflection coefficient of the water and sample interface, for the transition of the ultrasound wave from one medium (water) to the other medium (Agar) with a change in impedance $Z_i = {}_{1,2..}$, *R* was calculated using Equation *(6.10)*.

$$R = \frac{(Z_{Agar} - Z_{water})}{(Z_{Agar} + Z_{water})} \qquad (6.10)$$

Z_{water} = 1.48 MRayl and Z_{Agar} is computed for various concentrations of agar.

The acoustic impedances of agar obtained by the through-transmission method were compared with the acoustic impedance measurements obtained by pulse echo measurements which were performed using the AFM TH-19 probe.

6.4.1.1 Results: Acoustic Impedance

Tissue mimicking phantoms are an important tool for testing the performance and optimising an ultrasound transducer. The ideal phantom material should possess acoustic properties similar to that of tissue. Given the heterogeneity of tissue it is often difficult to find suitable materials to mimic the properties of tissue. The reason to conduct this control experiment was to test for the validity of measurements, the experiments with agar were conducted in pulse-echo and through transmission mode and then compared.

Agar was chosen as a tissue mimicking material as the acoustical properties of agar is similar to biological tissue. In pulse-echo mode μUS transducer (AFM TH-19) was used to evaluate the acoustic impedance of agar at varying concentrations. The results obtained from the pulse echo mode were cross validated in through transmission mode using a 5 MHz planar ultrasound probe. The methods used for this experiment are explained in Chapter 6. Acoustic parameters such as Z and α, were calculated in through transmission mode. This section summarises the results.

Measurements in pulse-echo mode was obtained by scanning the agar phantom at five different regions, in through transmission mode the same agar phantom used in pulse echo experiments was used and ultrasound signals from five different regions were recorded. It was found that the acoustic impedance calculations using the two modes were in good agreement (Figure 6.13). The Z, for agar increases with concentration as expected due to increase in the density. Z does not seem to increase linearly as expected and the possible reasons for this could be misalignment of the sample, thickness variation of sample and air bubbles in the agar samples. Table 6.1 summarises the measured acoustic properties of agar from through transmission experiments.

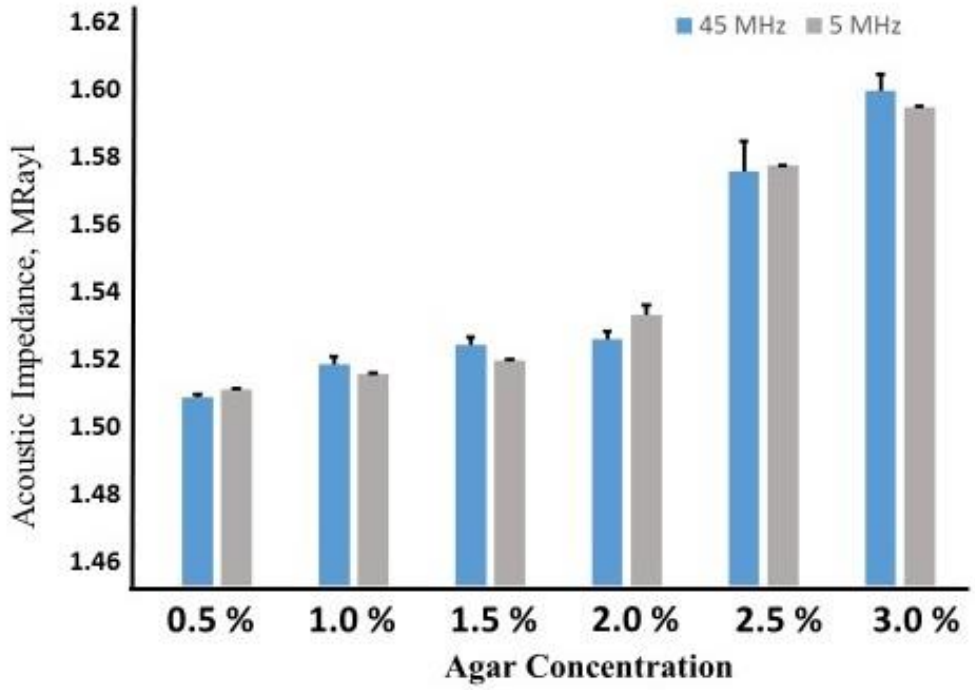

Figure 6.13: Acoustic impedance measurements. Comparison of acoustic impedances of agar at varying concemtrations using pulse-echo measurements (at 45 MHz) and through-transmission measurements (at 5 MHz).

Table 6.1: Acoustical parameters of Agar measured in through transmission mode using 5 MHz planar ultrasound transducer.

Agar Concentration	**Speed of Sound (ms^{-1})**	**Density (Kgm^{-3})**	**Acoustic Impedance (MRayl)**
0.5%	1486.2	1005.5	1.4943
1%	1487.1	1008.7	1.5000
1.5%	1488.8	1011.1	1.5053
2%	1490.4	1021.6	1.5223
2.5%	1491.7	1058.4	1.5788
3%	1498.7	1072.6	1.610

The uncertainties in the measurements of acoustic impedance were calculated using the resolutions of the equipment used to weigh and measure the sample dimensions and the difference in the densities of individual samples. The experimental error with respect to velocity and attenuation measurement was taken into account in terms of the temporal

resolution of the oscilloscope. The maximum velocity was calculated using the smallest path length and shortest time and the minimum velocity was calculated using the longest path length and longest time. The collective errors involved in measuring density and velocity were combined to account for errors in acoustic impedance in through-transmission mode using the 5 MHz transducer.

The attenuation coefficients, α, of agar was measured in through-transmission mode using 5 MHz transducer (Figure 6.14). It can be seen that the attenuation coefficient increases with increasing density of agar as expected.

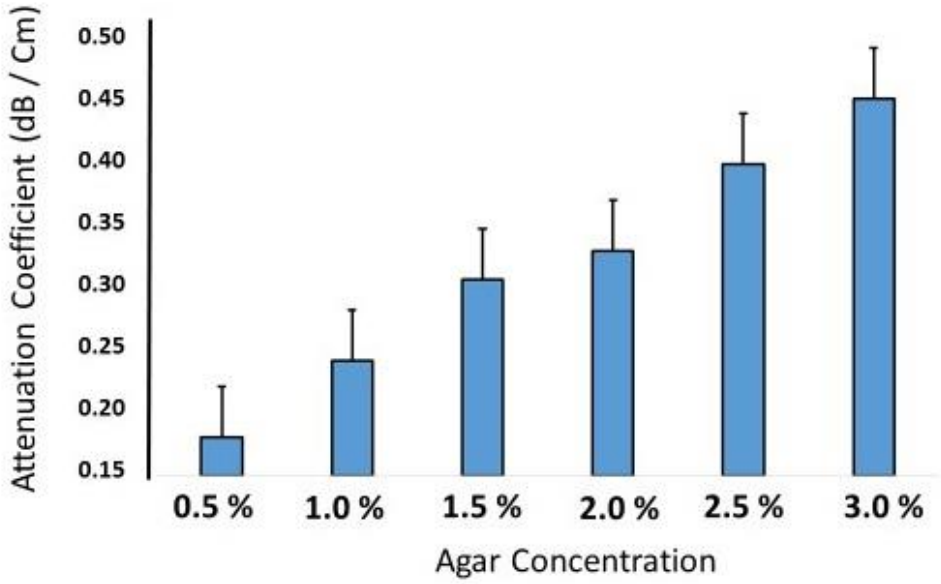

Figure 6. 14: Attenuation coefficient measurements. Atteunation coefficients for varying concentrations of agar measured in through-transmission mode. The greaph shows a linear relationship between attenautaion and density.

6.4.2 BSC Measurements using Beads

The BSC control experiments using beads were designed to determine how concentration and size of beads contributes to BSC. BSC from polystyrene beads (Polyscience, Warrington, PA, USA) at sizes of 10 µm, 20 µm and 45 µm dispersed in 3 ml of 1 % agar were scanned using the AFM TH-19 probe. The transducer was moved in the x-axis in steps of 20 µm over a range of 1.5 mm and then stepped in y-axis by 50 µm. A total of three B-scans were recorded and the BSC coefficient was measured.

The polystyrene beads have a density, ρ = 1050 kg m^{-3} and speed of sound of, c = 2400 ms^{-1}. The concentration of beads in the agar was varied by 5 and 10 fold, e.g. 1 ml of 10 µm polystyrene beads were pipetted out and mixed in 3 ml of 1 % agar, from this mixture 10 µl, 50 µl and 100 µl were pipetted out into a three individual wells of an eight well plate and cooled down rapidly in an ice bath. The numbers of polystyrene beads in the agar mixture at varying concentrations are shown in Table 6.1. Ice bath was used to ensure the beads did not settle down to the bottom of the well. BSC was determined similar to methods described in Section 6.3.5.

Table-6.2: Polystyrene bead concentrations and number of beads in the agar mixture for the measurement of BSC.

Bead Size	**Volume (µl)**	**Final Concentration (particles / µl)**
10 µm	10	1.52×10^5
10 µm	50	7.57×10^5
10 µm	100	1.52×10^6
20 µm	10	1.89×10^4
20 µm	50	9.47×10^4
20 µm	100	1.89×10^5
45 µm	10	1.66×10^3
45 µm	50	8.31×10^3
45 µm	100	1.66×10^4

6.4.2.1 Results: BSC

Backscatter coefficients from ensembles of polystyrene beads (Polyscience, Fisher Scientific, USA) at diameters of 10 µm, 20 µm and 45 µm at varying concentrations were measured. Polystyrene beads were used as they are homogenous (ρ = 1.05 g/ml, c = 2350 m/s) and are available in calibrated sizes (diameter tolerances of ± 0.5%). The beads were suspended in 1% agar and scanned using µUS transducer AFM TH-19 across three different regions in a well plate. PBS was used as a coupling medium. Smaller sizes of beads were chosen as they are in the same size range as of cells and crypts in intestinal tissue.

The graph shows an increase in BSC as the concentration of the beads increases (Figure 6.15). However when the scatterer becomes large, as for the 45 µm beads the intensity levels of BSC were lower than the rest of the measured results as the number of scatterers for larger diameter of beads was less and the beads were sparsely distributed. This is because the surface to volume ratio decreases with increasing particle size, therefore the BSC is expected to peak at higher volume fractions with smaller particle sizes.

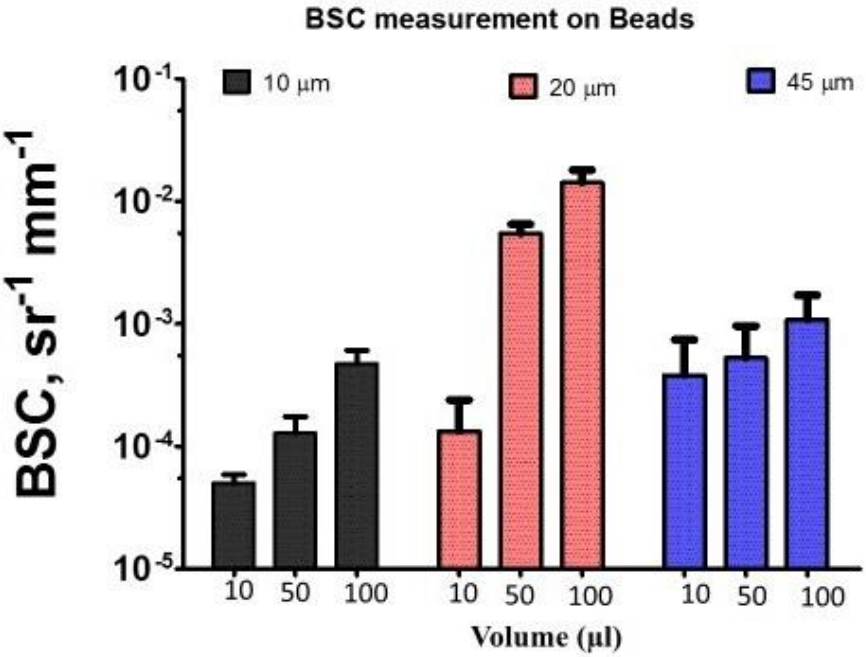

Figure 6. 15: BSC measurements on polystyerene beads. Beads of varying sizes and concetration suspended in agar were scanned and average BSC is shown.

The BSC from beads is strongly dependent on the echoes received from the micro-spheres. The loss in the amplitude of the signal will be due to absorptive and radiative losses. BSC measurements on beads confirmed that the size and concentration are contributing factors that lead to an increase in BSC in $Apc^{Min/+}$ tissue.

6.4.3 Tissue Fixation

Histological tissue samples are usually preserved using aldehydes, alcohols, etc. Bamber et al., reported that fixation of tissue with potassium dichromate and formalin affects the acoustical properties of tissue (Bamber,& Dunn, 1979). They demonstrated

that the acoustic parameters such as BSC and *Z*, were different in fixed and unfixed tissue. The authors suggested 4% formalin and 5% potassium dichromate are good for consistently preserving the ultrasonic properties of tissue. To establish how fixation changes the ultrasonic propagation in tissue, the effects of paraformaldehyde (PFA) fixation on acoustical properties of the murine intestinal tissue were investigated.

To ensure there was no degradation of acoustical properties with PFA fixation, murine intestinal tissue was prepared as described in Chapter 6 and scanned in two different physical positions of the tissue by µUS prior to fixation and at indicated times after fixation (Figure 6.16). The fresh tissue was scanned immediately after excision and phosphate buffer solution (PBS, pH = 7.3) was used as coupling medium in all the scans. Gaseous inclusions in the sample were removed before measurements by manual manipulation under the fluid and all the measurements were made at room temperature. The temperature was measured using a thermocouple and was noted to be 21 ± 1 ^{0}C. The average of two readings at each time point is plotted against time to illustrate that there were no effect of fixation with 4% PFA. The results indicate that the acoustic impedance of the tissue remained constant over the period of scans indicating that there was no degradation in the acoustic properties of PFA fixed tissue specimens.

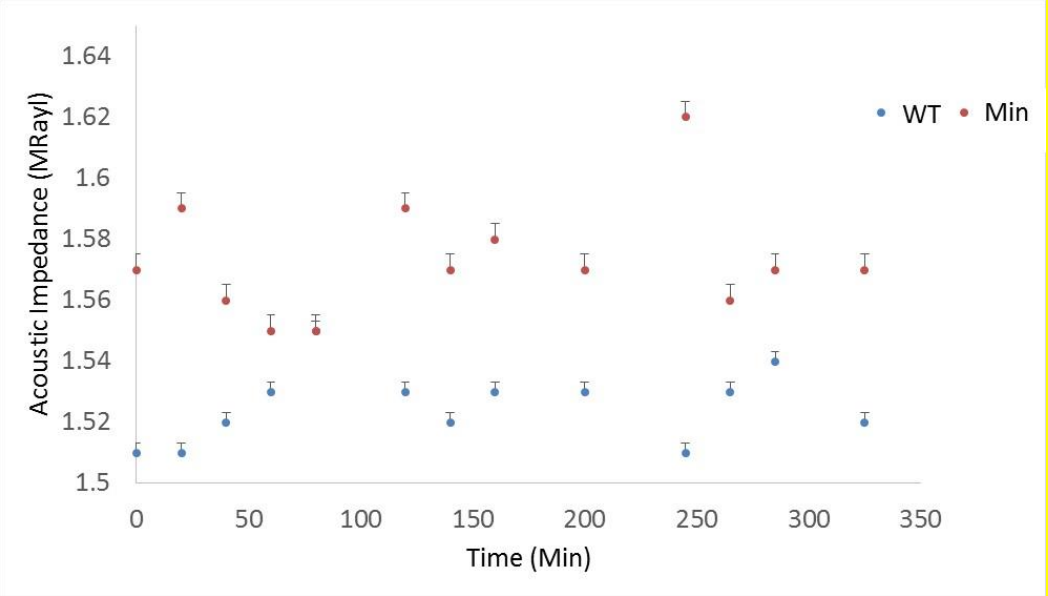

Figure 6. 16: Effect of fixation on acoustical properties of tissue. The tissue was scanned over a period of time after fixation to determine the effect of fixation on acoustical properties.

6.5 Conclusions

This Chapter has presented the materials and methods to build two µUS scanning system for imaging and tissue characterisation of murine small intestine. A number of design constraints had to be addressed while designing the scanning systems, due to the conflicting requirements between duration of imaging, image quality, limitations in hardware, ease of building the system, simplicity in use and overall cost. The primary aim of the work was tissue characterisation, but it is advantageous to visualise tissue through conventional B-scans.

Control experiments were designed to understand the effects/contributions of variables. Better understanding the variables increases the reliability of the results by providing a standard of comparison between control experiments and actual experiments. The variables investigated were effect of fixation on acoustic properties of tissue, testing of method used for computing Z in pulse-echo and through-transmission modes and estimation of backscatter coefficients using an ensemble of beads of known concentration and sizes. The results obtained from the control experiments helped to understand some key concepts especially BSC. The results from BSC then helped to answer the question as to why and what contributes to an increase in BSC in $Apc^{Min/+}$ tissue.

The methods to compute the specific acoustic properties of tissue i.e. acoustic impedance, attenuation and BSC at the centre frequency of the transducer were explained. BSC is a fundamental property of the material, from which size, shape, organisation, concentration and impedance mismatch between the normal and dysplastic tissue can be estimated. This can be used to quantify the tissue properties and classify diseased tissue from normal. The results from µUS imaging and tissue characterisation are presented in Chapter 7.

6.6 References

D'Astous, F., & Foster, F. (1986) "Frequency dependence of ultrasound attenuation and backscatter in breast tissue." *Ultrasound in Medicine & Biology, 12*(10), 795–808.

Duck, F. (2010) "Tissue non-linearity." *Proceedings of the Institution of Mechanical Engineers, Part H: Journal of Engineering in Medicine*, *224*(2), 155–170.

Foster, F. S., Strban, M., & Austin, G. (1984) "The ultrasound macroscope: initial studies of breast tissue." *Ultrasonic imaging*, *6*(3), 243-261.

Moran, C. M., Bush, N. L., & Bamber, J. C. (1995) "Ultrasonic propagation properties of excised human skin." *Ultrasound in medicine & biology*, *21*(9), 1177-1190.

Nicholas, D., Hill, C. R., & Nassiri, D. K. (1982) "Evaluation of backscattering coefficients for excised human tissues: Principles and techniques." *Ultrasound in Medicine & Biology*, *8*(1), 7–15.

Raju, B. I., & Srinivasan, M. A. (2001) "High-frequency ultrasonic attenuation and backscatter coefficients of in vivo normal human dermis and subcutaneous fat." *Ultrasound in medicine & biology*, *27*(11), 1543-1556.

Shung, K. K. (2009) "High Frequency Ultrasonic Imaging." *Journal of Medical Ultrasound*, *17*(1), 25–30.

Strohm, E. M., & Kolios, M. C. (2009, September) "Measuring the mechanical properties of cells using acoustic microscopy." In *Engineering in Medicine and Biology Society, 2009. EMBC 2009. Annual International Conference of the IEEE* (pp. 6042-6045). IEEE.

Waag, R. C. (1984). "A review of tissue characterization from ultrasonic scattering." *IEEE Transactions on Bio-Medical Engineering*, *31*(12), 884–93.

Zell, K., Sperl, J. I., Vogel, M. W., Niessner, R., & Haisch, C. (2007) "Acoustical properties of selected tissue phantom materials for ultrasound imaging." *Physics in Medicine and Biology*, *52*(20), 475–84.

Chapter 7: Results: Early Detection of Colon Cancer by µUS

"There can be life after cancer, the prerequisite is early detection"

Ann Jillian

7.1 Overview

Ultrasound has been used as a clinical tool to detect tissue abnormalities usually at frequencies that permit deep tissue penetration. Using higher frequency (45 MHz) provides increased resolution which can help visualising micro-structures in tissue. This chapter presents the results of imaging and tissue characterisation of WT and $Apc^{Min/+}$ female and male, murine small intestine at ages of 60, 90 and 120 days. The results were correlated with optical images to establish the efficacy of the findings. The key concepts covered in this chapter are:

- In Section 7.2, B-scan images are presented of murine small intestine tissue obtained by µUS scanning of murine small intestine *ex vivo* to detect early tissue dysplasia.
- In Section 7.3, 3D ultrasound images are correlated with high resolution optical images to prove the clinical relevance of ultrasound images. Data from ultrasound and high resolution optical imaging are presented.
- In Section 7.4, the RF data obtained by ultrasound scanning of murine intestine analysed and quantitative measurements on WT and $Apc^{Min/+}$ tissue are presented. The results were correlated with high resolution optical measurements.

Biological tissue samples and optical images were contributed to this thesis by Dr. Aliya Fatehullah and Dr. Paul Appleton, CLS, UOD.

7.2 B-Scan Imaging of Early Tissue Dysplasia

Detection of pre-malignant changes in tissue is of key importance as this corresponds with early detection of colon cancer. To determine if tissue changes could be detected using µUS, tissue samples at 60, 90 and 120 days from female and male murine small intestine were investigated *ex vivo* with AFM TH-19. Examples of B-scan images of murine small intestine of WT and $Apc^{Min/+}$ at different ages are shown in Figure 7.1. The dynamic range was set at -35 dB and no time gain compensation was used.

The B-scan images show typical 'speckle' pattern of medical ultrasound images, which is due to superimposition of diffusely backscattered coherent echoes. The B-scans produced from ten different axial positions of the tissue were manually visually inspected to ensure that the muscle layer was clearly visible and distinguishable. From the ten B-scans produced from a single tissue specimen five B-scans were selected and the data was used for tissue characterisation. The B-scan images have sufficient resolution for anatomical features of the intestine i.e. mucosa and muscle to be clearly identified as shown in Figure 7.1 (B). The other important features than can be recognised in the images from $Apc^{Min/+}$ tissue are increased backscatter and high amplitude features corresponding to micro-polyps of size less than 500 µm in the scan plane.

The B-scan images shown in Figure 7.1 are representative results from a cohort of mice aged 60, 90 and 120 days. For each of the age groups, excised small intestine from ten of each, WT and $Apc^{Min/+}$ mice were scanned using the 45 MHz AFM TH-19 probe and B-scan images were produced, using a MatLab script and MatLab function 'imagesc'. The images are shown in RGB format rather than in grey scale. In RGB format the colours can be specified based on the signal strength which helps in identify the anatomical features. For e.g. Red colour represents maximum signal intensity and Blue represents minimum intensity, in the displayed B-scan images.

The minimum size of polyps that can be detected using present imaging techniques such as endoscopy and CT is 6 - 10 mm (Summers, 2010). The B-scan images show that the backscatter of ultrasound is increased in pre-cancerous tissue suggesting that the pre-cancerous tissue is more irregular compared to WT tissue. From the B-scan images micro-polyps could be identified as early 60 days. B-scan images of the murine small intestine deliver information about the size, extension and depth of polyps which appear as hyper-echoic areas within the hypo-echoic regions of the surrounding tissue. B-scan

images from human tissue were obtained to determine if similar changes in backscatter and density of tissue could be visualised.

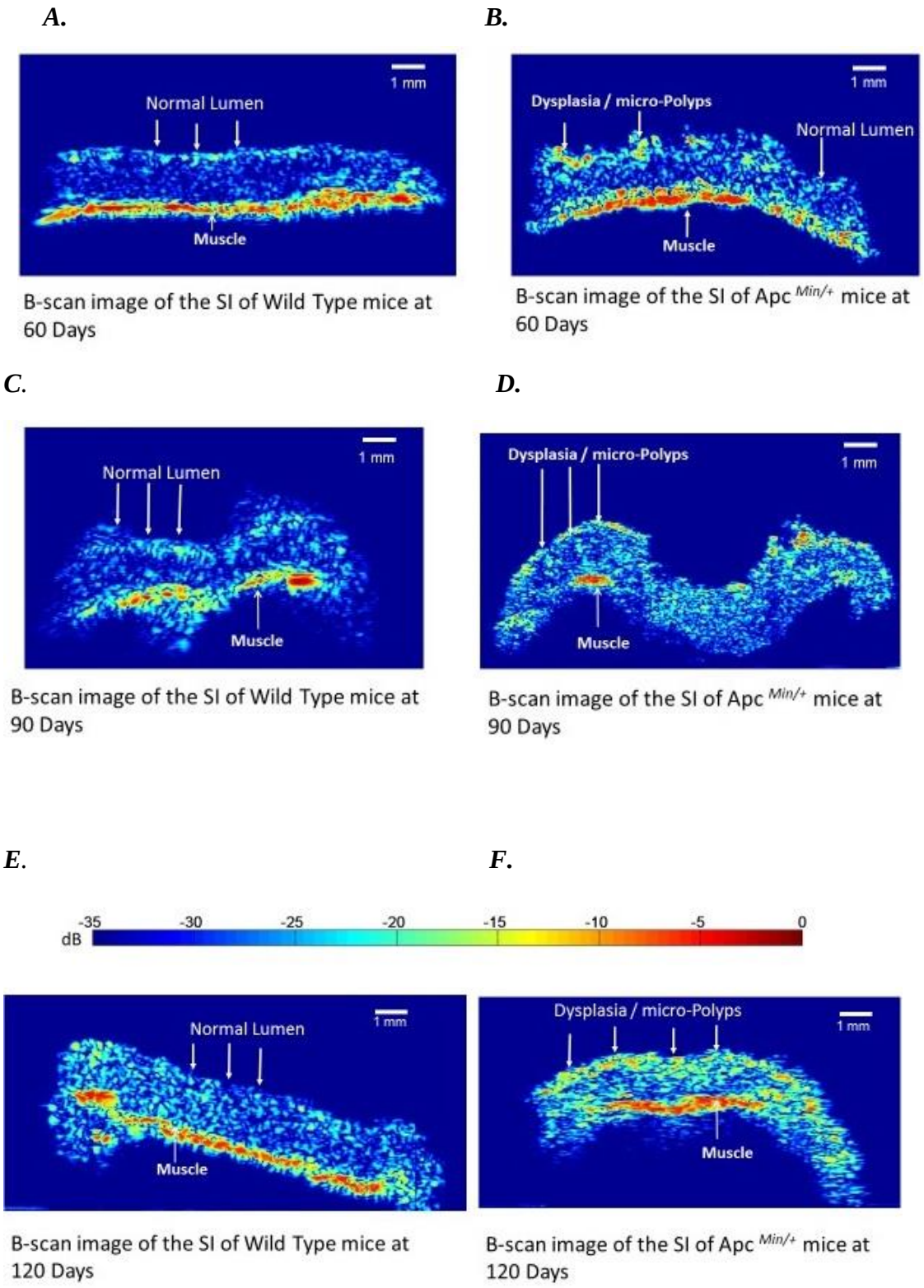

Figure 7.1: HRUS scans of murine small bowel. ***A.*** *WT mouse intestine aged 60 days.* ***B****. Apc$^{Min/+}$ mouse intestine aged 60 days, arrows shows increased backscatter indicating tissue dysplasia.* ***C.*** *WT mouse intestine aged 90 days.* ***D****. Apc$^{Min/+}$ mouse intestine aged 90 days, arrows shows increased backscatter indicating tissue dysplasia and the number of micro polyps is more than in image B.* ***E****. WT mice intestine aged 60 days.* ***F****. Apc$^{Min/+}$ mouse intestine aged 120 days, note increased backscatter and high amplitude features corresponding to polyps on the top surface. Scale bar = 1mm, dynamic range = 35 dB.*

7.2.1 Ultrasound Imaging of Human Tissue

A human polyp was imaged using the AFM TH-19 µUS transducer and correlated with high resolution optical images as shown in Figure 7.2.

The Tayside Tissue bank subcommittee of the local research ethics committee approved the collection of the human tissue samples. Normal human samples were obtained after surgical resections for hemi-colectomy. After specimen removal, samples with macroscopically normal appearance were excised by a consultant pathologist and divided into 5 mm long sections. Normal colonic biopsies from FAP (familial adenomatous polyposis) patients were obtained during routine colonoscopy surveillance. All specimens were fixed in 4% paraformaldehyde at pH 7.4 and stored overnight at 4 ^{0}C and brought to room temperature prior to imaging.

The B-scan images showed layered tissue organisation including indications of FAP polyps. The backscatter varied in between layers which are due to the differences in the acoustic impedance. The layered tissue architecture was confirmed by optical image. This suggests that µUS can be used as a potential tool to characterise the overall tissue organisation.

The significant increase in variability of tissue organisation in precancerous mouse intestine and human tissue was further validated by comparing 3D ultrasound images with high resolution optical images.

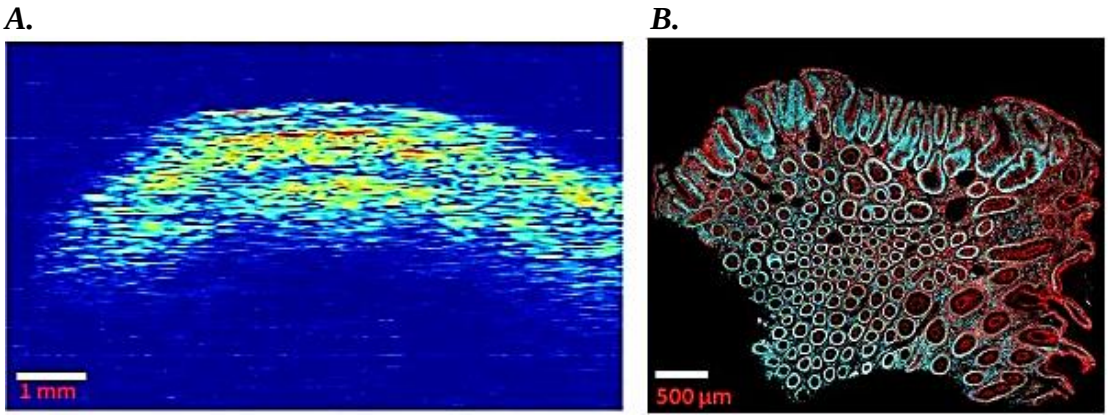

Figure 7.2: Correlation of µUS scan of human polyp from FAP patient with optical image. ***A****. B-scan image of the human polyp showing three different tissue organisational layers with varying scattering intensity within the structure.* ***B****. Cross section of the same polyp stained with DAPI and phalloidin to reveal F-actin (red) and nuclei (blue) showing the overall structure of the polyp. (Optical image was taken by Dr. Paul Appleton).*

7.3 3D Ultrasound Imaging of Early Tissue Dysplasia

Conventional B-scan images have certain limitations. The conventional ultrasound images of internal organs are in 2D yet the anatomy is 3D. Interpretation of 2D images thus needs experience and may lead to variability and incorrect diagnosis. To improve the diagnostic capabilities of µUS transducers, 3D ultrasound images of the murine intestine were obtained and compared with confocal images of the tissue (Figure 7.3). Echogenicity, tissue morphology and thickness of polyps and structures can be assessed much better in 3D ultrasound images.

The polyps in the 3D image are seen as hyper-echogenic regions with respect to surrounding tissue. The 3D ultrasound image provides depth information and the extent of polyp invasion and the extent of muscle damage can be visualised. The information on depth of polyp invasion towards the muscle layer is important for preoperative planning of polyp excision and follow up studies of bowel cancer.

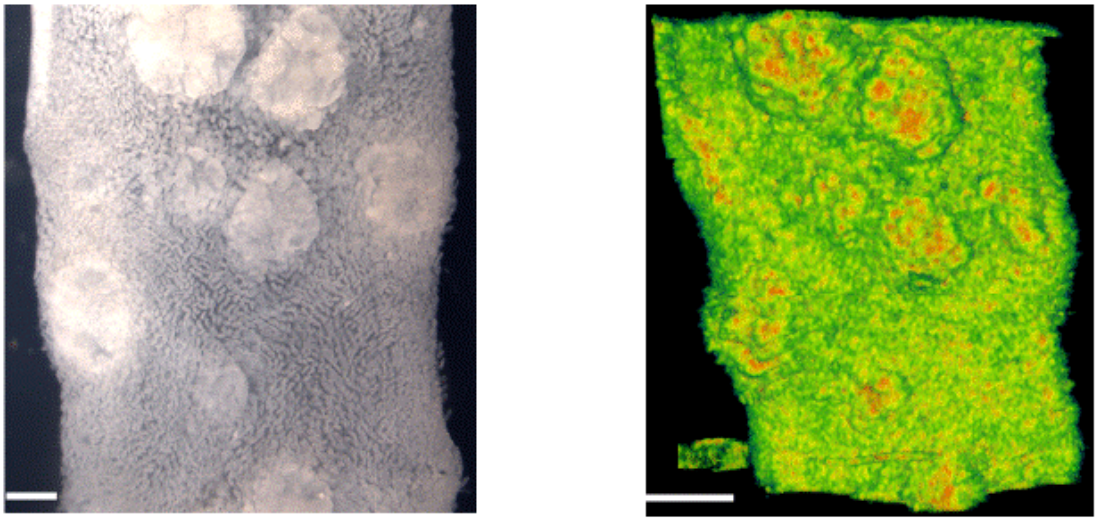

A. ***B.***

Figure 7.3: 3-D ultrasound imaging. A. Confocal image of $Apc^{Min/+}$ tissue pinned on agar to prevent from curling viewed at 10X magnification. B.3-D ultrasound intensity image of tissue shown in A, imaged with AFMTH-19 shows correlation with the optical image. Scale bars = 1mm. (Optical image in A was taken by Dr. Paul Appleton).

7.3.1 Correlation of µUS Images with Optical Images

The polyps on the tissue marked by arrows and labelled ‘i’ and ‘ii’ in Figure 7.4 were resected and sectioned with a vibratome. A B-scan image of the vibratome section of the polyp was produced. This B-scan image shows the resected polyps in ‘i’ and ‘ii’ as bright red spots indicating increased backscatter and density from the polyp. The B-scan image of the resected polyp was then correlated with bright field and confocal images (Figure 7.4). Histology of the murine small intestine was not performed and the only evidence is correlation of ultrasound images with optical images. Not all the tissue imaged was correlated with B-scan images. The images shown in figure 7.4 are representative images, showing the relation between ultrasound and optical images.

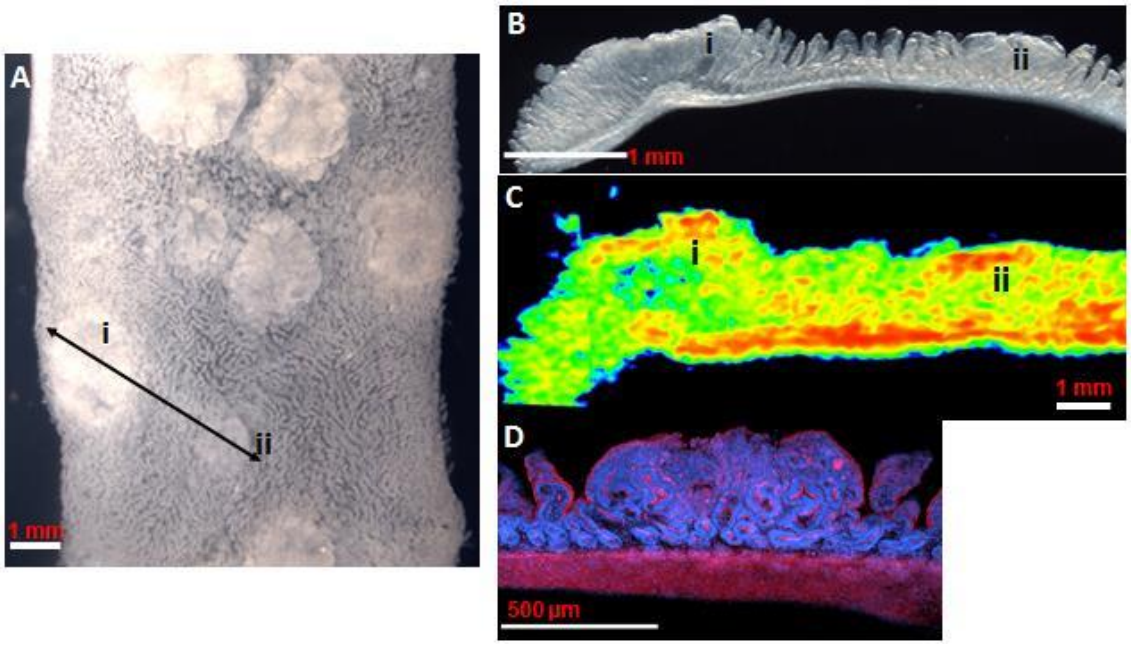

Figure 7.4: Correlation of µUS images with optical images. A. intestinal tissue from Apc $^{Min/+}$ mouse pinned on agar viewed under stereomicroscope at 10X magnification. The arrow marked as ‘i’ and ‘ii’ shows the region of polyp that was resected and vibratome sectioned. B. Bright field optical image of the cross section of the resected polyp. C. B-scan image of the resected polyp, regions ‘i’ and ‘ii’ are marked and seen as bright red spots indicating increased backscatter and density of the tissue in the polyp. D. Confocal image of the resected polyp in region ‘ii’ stained with phalloidin and DAPI to visualise F-actin (red) and nuclei (blue). (Optical images were taken by Dr. Paul Appleton).

The B-scan image shows good correlation with the optical images and confirms that the µUS transducer can be used for early detection of colon cancer. The other important

finding of the studies is the success in detection of micro-polyps of size less than 500 µm in width which is not possible with current imaging techniques.

7.4 Quantitative Ultrasound Tissue Characterisation

Quantitative ultrasound tissue characterisation deals with measurements, which can yield quantitative tissue properties that, are independent of operator and instrumentation, thus eliminating bias. The quantitative parameters have the potential to be used to differentiate between normal and cancerous tissue. In this research, RF data obtained by scanning the µUS transducer over WT and $Apc^{Min/+}$ mouse intestinal tissue was used to establish whether the differences in tissue architecture could be detected quantitatively. Parameters such as *Z*, and BSC were measured to determine if tissue changes that precede polyp formation could be detected. Scanned tissue samples from male and female mice at different ages (60 - 120 days) were scanned. The B-scan images from tissue were segmented using the approach described in Chapter 6. The segmented tissue data was used for computing *Z* and BSC. Paired t-tests were performed to compare the two groups (WT vs $Apc^{Min/+}$) and the differences between groups were considered statistically significant at a p value of 0.05.

The quantitative results obtained from µUS experiments and measurements from high resolution optical imaging are explained in the following sections.

7.4.1 Backscatter Coefficient Measurements

Ultrasound in tissue is a propagating wave that interacts with the medium as a function of mechanical properties of the tissue. Analysing BSC allows us to infer various properties of the tissue. Mamou et al., reported to have differentiated between neoplastic and healthy tissue by studying the frequency dependent backscatter from *in vivo* rat mammary tumours (Oelze, 2002). BSC measures the scattering strength of a randomly distributed scattering objects when insonated by a plane wave. In isolated cells the most effective scatterers are nuclei and scattering is caused by differences in the density and compressibility of the intercellular structures (Cobbold, 2007; Kolios & Czarnota, 2008).

Using the µUS transducer, differences in the values of BSC in histologically normal Apc$^{Min/+}$ and WT tissue (Figure 7.5) were measured. WT and Apc$^{Min/+}$ tissue specimens from male and female mice at varying ages were prepared and scanned. Tissue from 3-5 male and female mice were used and the width of each tissue was scanned at ten different positions that were 1 mm apart along the tissue axis in a raster format, as shown in Figure 7.5. The graph shown in Figure 7.6 represents the average values of BSC for male and female mice from at least three - five B-scans recorded from each tissue. The BSC for Apc$^{Min/+}$ tissue are seen to have a relatively high BSC while the BSC measured for WT murine tissue is lower.

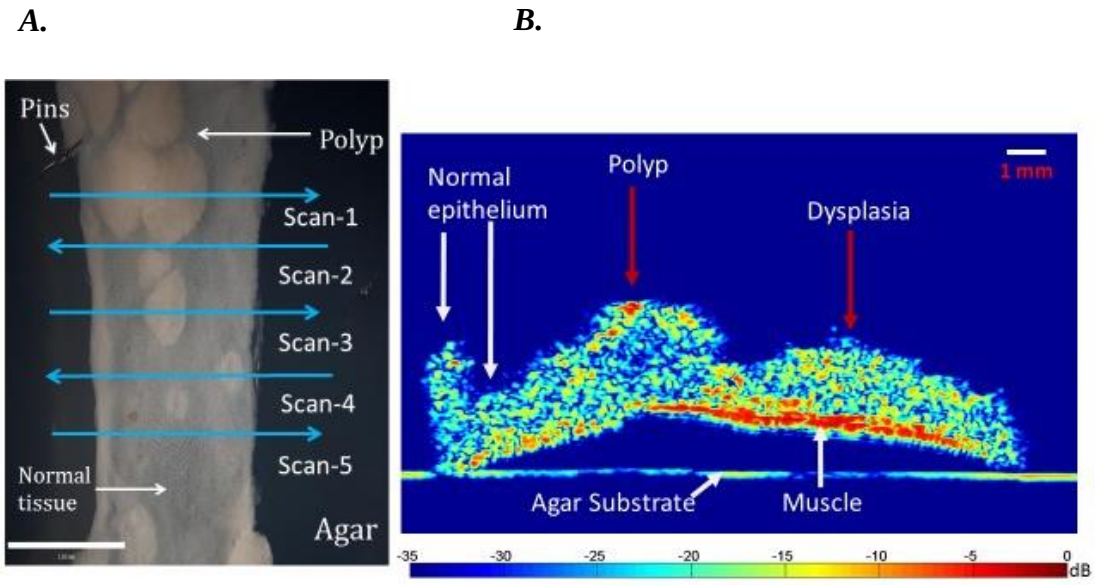

Figure 7.5: A. Apc heterozygous murine intestinal tissue showing the scanning path taken by the µUS transducer to produce B-scan images. B. B-scan image of tissue in A, showing the histological features of the tissue.

The calculation of backscatter coefficients is based on the energy spectrum of the scattered radiation from the tissues, relative to the energy spectrum of plane interface reflection, i.e. quartz The results show differences between scatterer acoustic concentration, size and distribution in WT and Apc$^{Min/+}$ tissue. For the frequency used in the present studies, the scatterers must be effectively in the range of 5 – 90 µm in dimension. This size range of scatterers places them between the diffractive and Rayleigh scattering regions, for the frequency investigated. Diffractive scattering in principle occurs, when the scattering structures are similar in size and spacing to the wavelength of the ultrasound beam. Rayleigh scattering occurs from structures that are smaller than the wavelength of the ultrasound beam The size range of scatterers in the

tissue corresponds to cellular and tissue structures that include the nuclei, cells and crypts, enabling detection of irregularly packed crypts, cells and nuclei in precancerous tissue (Fatehullah et al., 2014).

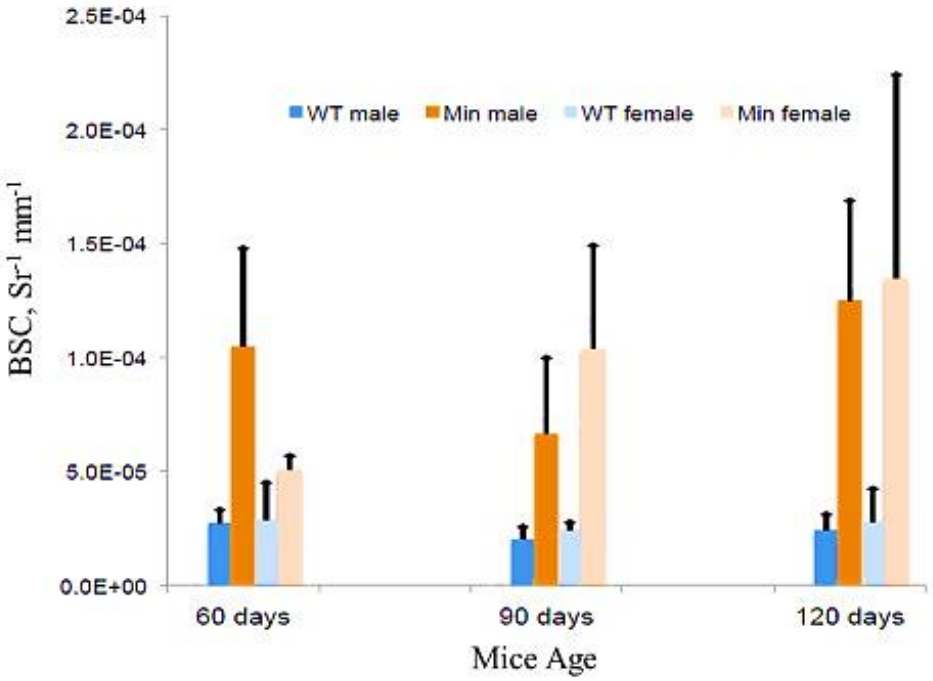

Figure 7.6: Backscatter Coefficients. WT and Apc$^{Min/+}$ tissue specimens from male and female mice at varying ages were prepared for µUS scanning. In male mice an increase in BSC is detectable at 60 days whereas female mice show a significant increase only at 90 days.

To determine how the quantitative differences detected by µUS relate to tissue organisation, collaborating researchers in the College of Life Sciences, University of Dundee (CLS, UOD) measured the packing, shape and size (length, width and number of cells) of crypts and the distribution of mitotic cells within crypts using high-resolution optical imaging. Fatehullah et al., reported an increase in the variability in the physical properties of crypts. In Apc$^{Min/+}$ tissue crypts were found to be curved suggesting that the cells were randomly distributed along the crypt axis. The random distribution of cells in Apc$^{Min/+}$ tissue could be a contributing factor to increased BSC. The measured p-values showed that the results obtained were significant.

The measured distances between the neighbouring crypts showed that the distance between crypt centres varied by a factor of 3.1 between WT and Apc$^{Min/+}$ tissue (Figure 7.7) (Fatehullah et al., 2014). The differences is due to the mean crypt diameter which is

smaller in Apc$^{Min/+}$ tissue. In most region of the intestinal tract, crypts occupy a greater proportion of the total area in WT tissue than in Apc$^{Min/+}$ tissue suggesting more space is occupied by cryptal cells in precancerous tissue. The end points in the graph indicate maximum and minimum distances between the neighbouring crypts.

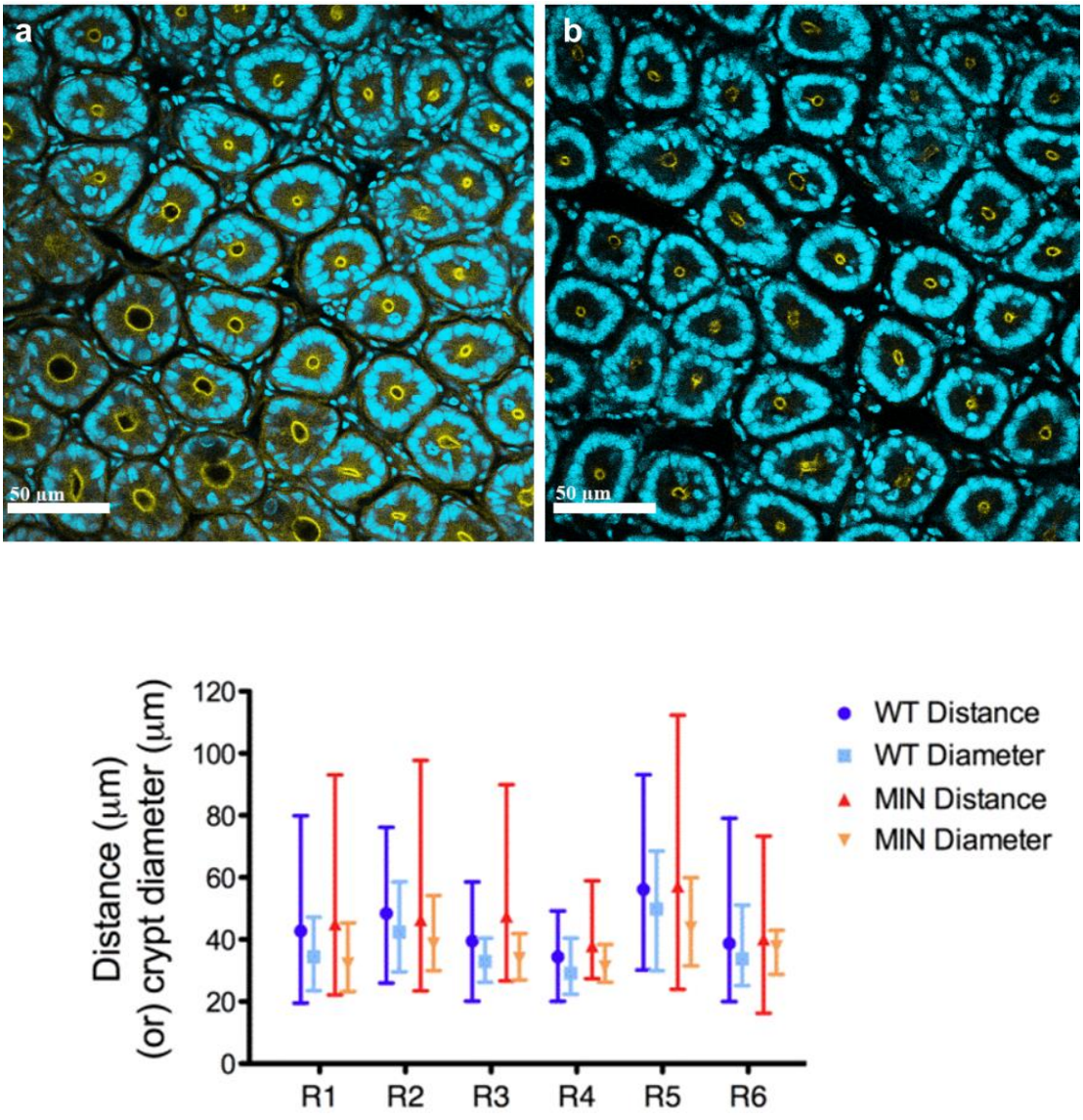

Figure 7.7: Images of crypts. a. WT and b. Apc$^{Min/+}$ tissue from region 2 of murine small intestine stained with DAPI to visualise nuclei (cyan) and phalloidin (yellow) to mark F-actin at the apical surface of cells revealing the packing of crypts in tissue. ***c.*** *Crypt packing and size in human tissue were determined by measuring diameters of crypts and the distances between a selected crypt and its six closest neighbouring crypts. (Fatehullah et al., 2014).*

7.4.2 Acoustic Impedance Measurements

Measuring the mechanical properties of tissue, such as the density, is important in understanding the changes that occur in pre-cancerous tissue. Studying the changes in acoustic impedance, *Z*, of WT and $Apc^{Min/+}$ tissue can assist in monitoring the changes in density that accompany pre-malignant tumour initiation in murine small intestine.

The mean values of *Z* were determined in WT and $Apc^{Min/+}$ intestinal tissue from 3-5 mice for male and female genders at ages of 60, 90 and 120 days and are shown in Figure 7.8. The average values in the graph represent 30 – 50 data points collected from each tissue by scanning µUS transducer in 20 µm steps across the width of the tissue at three to five different positions separated by 1 mm along the tissue axis. The graphs show an increase in *Z* for $Apc^{Min/+}$ tissue indicating that precancerous tissue is more dense than WT tissue. Optical images of polyps show that there is an increased density of epithelial cells and myofibroblasts could lead to increased density and therefore produce increased *Z* in Apc heterozygous tissue. The measured p-values showed that the results obtained were significant.

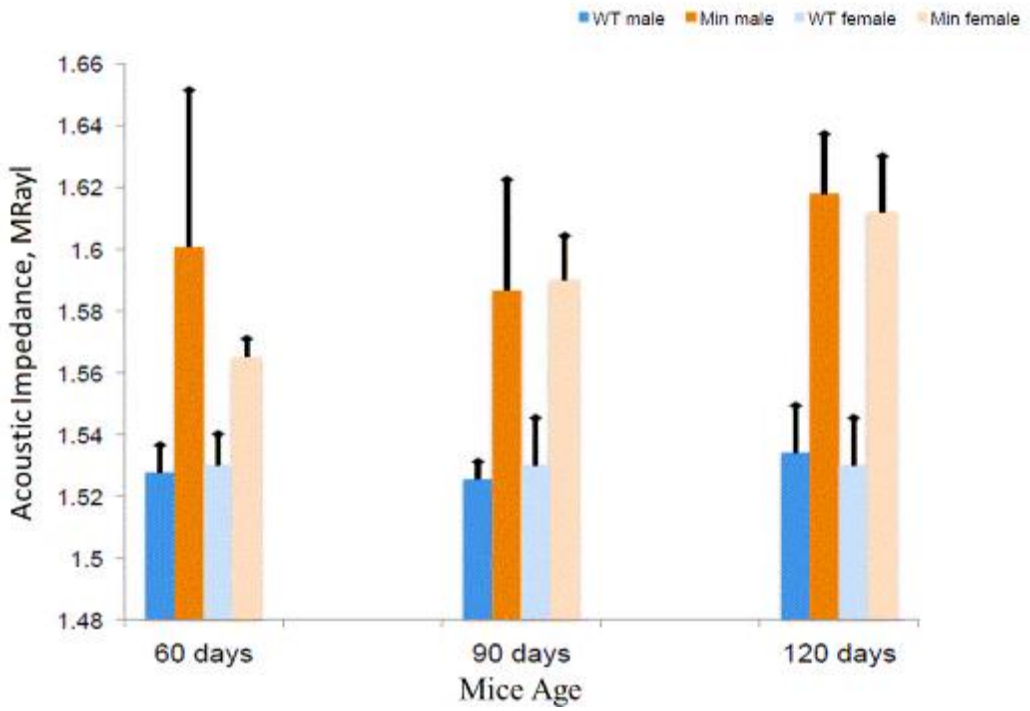

Figure 7.8: Acoustic impedance measurements. Mean acoustic impedance from the tissue was determined for WT and $Apc^{Min/+}$ tissue using µUS transducer. In male mice there is an increase in Z at 60 days. The increase in Z for $Apc^{Min/+}$ mice at varying ages indicates differences in density and acoustical properties.

7.4.3 Attenuation Coefficients

Figure 7.10 shows the attenuation coefficients of the lumen of murine intestinal tissue obtained using 45 MHz AFM TH-19 µUS transducer. The lumen is heterogeneous in nature comprising of epithelial layer, mucosa and villi. The B-scan images depicted areas in $Apc^{Min/+}$ tissue having varying amount of bright spots, depicting high attenuation. The data represented here is at the centre frequency of the transducer i.e. 45 MHz. It is seen that the attenuation coefficients of the $Apc^{Min/+}$ mice increases with respect to age for both male and female mice. The attenuation values for the $Apc^{Min/+}$ tissue varied from 2.15– 2.32 dB/mm for male mice and from 2 – 2.35 dB/mm for female mice, for ages between 60 – 120 days. The attenuation coefficients for the WT male mice was in the order of 1.09 – 1.46 dB/mm and 1.18 – 1.75 dB/mm for female mice. The attenuation coefficients were used as a correction factor for estimating BSC. The collective mean values of Z, BSC and α, for male, female WT and $Apc^{Min/+}$ is summarised in Tables 7.1 – 7.2 respectively. The measured p-values showed that the results obtained were not significant for female mice at all ages. The p-values of male mice were non-significant at 90 days for male mice but significant at 60 and 120 days.

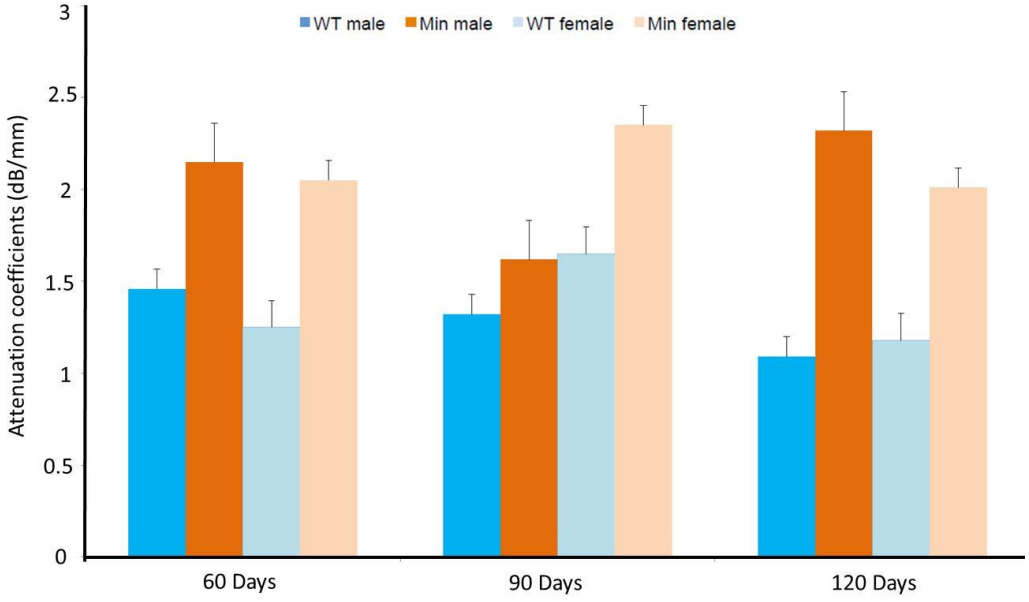

Figure 7.9: Attenuation coefficient measurements. Mean attenuation coefficients from the tissue was determined for WT and $Apc^{Min/+}$ tissue using µUS transducer at the centre frequency of 45 MHz. Indicated on the x-axis are the age of mice, the error bars indicate the positive range of the data.

Table 7.1: Summary of ultrasound tissue parameters measured from male murine intestine.

Age	**60 days**		**p-value**	**90 days**		**p-value**	**120 days**		**p-value**
Parameter	WT (n =4)	$Apc^{Min/+}$ (n = 4)		WT (n=4)	Apc^{Min+} (n = 4)		WT (n = 5)	$Apc^{Min/+}$ (n = 5)	
Acoustic Impedance (Z) MRayl	1.52	1.60	0.025	1.53	1.58	0.044	1.53	1.61	0.003
Attenuation coefficients (α) dB/mm	1.45	2.15	0.017	1.26	1.62	0.27	1.09	2.32	0.034
BSC (Sr^{-1} mm^{-1})	0.0000274	0.00001054	0.040	0.0000202	0.000066	0.050	0.0000242	0.000125	0.008

Table 7.2: Summary of ultrasound tissue parameters measured from female murine intestine.

Age	**60 days**		**p-value**	**90 days**		**p-value**	**120 days**		**p-value**
Parameter	WT (n = 3)	$Apc^{Min/+}$ (n = 5)		WT (n = 5)	$Apc^{Min/+}$ (n = 5)		WT (n = 5)	$Apc^{Min/+}$ (n = 5)	
Acoustic Impedance (Z) MRayl	1.53	1.56	0.031	1.53	1.59	0.003	1.53	1.61	0.001
Attenuation coefficients (α) dB/mm	1.15	2.05	0.064	1.65	2.35	0.062	1.18	2.01	0.072
BSC (Sr^{-1} mm^{-1})	0.000029	0.00005	0.080	0.0000242	0.000104	0.017	0.0000279	0.000135	0.058

7.5 Discussion

Detection of early tissue changes is a crucial step for detection and monitoring of CRC to deliver effective treatment. µUS was used to detect early tissue abnormalities. The scanning systems built during this research allowed the formation of images based on ultrasonic properties of tissue. One important finding of this study is that we are able to differentiate $Apc^{Min/+}$ tissue from WT tissue through visual inspection of B-scans and also based on the measured ultrasound parameters. Results for ultrasound attenuation,

acoustic impedance and BSC for excised murine intestine at a center frequency of 45 MHz have been presented.

The quantitative data pertains directly to ultrasound images which are of prime importance in clinical diagnostics. The quantitative results obtained from ultrasound were validated by high resolution optical measurements. The optical studies revealed that the $Apc^{Min/+}$ tissue was altered structurally and the physical properties of crypts were highly variable. The increased and irregular packing of nuclei which is a common feature of dysplastic tissue is likely to contribute to an increase in BSC. The measured differences in Z and BSC between WT and $Apc^{Min/+}$ suggest the possibility of making a diagnosis of early bowel cancer on the basis of scatterer information. The increase in the attenuation coefficients of the precancerous tissue is because, the cellular distribution is dense. This dense arrangement of the cells makes the tissue stiffer and results in the absorption of ultrasound. The increased stiffness of the tissue was recorded as increased values of acoustic impedance were measured in the precancerous tissue. The result shown here suggests that, the structure and arrangement of the cellular components in the tissue influence the acoustic properties.

The future goal of this project will be develop a probe that will aid in detecting early tissue dysplasia based on the ultrasound parameters in pseudo real time. The development of µUS transducers that can be incorporated into devices that can be swallowed will allow imaging of diseases of the small intestine. Quantitative tissue measurements will enable computer aided diagnosis of diseases which will limit bias and significantly improve interpretation times. Thus, µUS is a versatile and a powerful tool for analysing diseases in normal and genetically engineered animal models and can also be extended to human studies.

One of the limitations of this system is that it neglects frequency dependent effects and it is therefore important to extend the measurements over a wide range of frequencies, to understand the frequency dependent variation of ultrasonic properties in tissue. The velocity of sound in the tissue was assumed to be 1540 m/s. Estimation of the velocity in soft tissue could further help in understanding the changes in density across the whole murine intestinal tissue more accurately. This will help in differentiating between WT and $Apc^{Min/+}$ tissue based on density and bulk modulus. Estimating BSC using other methods and comparing them with the present technique will prove the sensitivity of the measurements. Incorporating diffraction correction into the BSC equation will improve the accuracy of the calculations. Further understanding the relationship between

histological detail and quantitative parameters by µUS using mathematical modelling will be required to validate µUS as a useful tool for detecting early tissue dysplasia.

The intestinal tissue pinned on agar substrate was not completely flat as it has fine folds and sometimes would be raised at certain points; therefore it was necessary to check the ultrasound signals continuously during scanning, to ensure the sample was in the focal region of the transducer. Use of washers or weights to hold the sample down was not useful either as a portion of the sample would lift up as the under surface of the polyps created air pockets which would make the tissue float. Also using weights to hold the tissue down is not advisable as it destroys the villi and other micro-structures in the tissue. Therefore manually adjusting the height of the transducer was time consuming and many experiments had to be repeated several times. To overcome this problem, modifying the scanning system with automatic height adjustment based on the signal received by the system can incorporate in the future. This would save time and ensure the sample is always in the focal region.

The current ultrasound imaging method used is based on a relatively simple mechanical scanning system that has a limited image acquisition rate, which will limit its clinical use. A key improvement in the imaging rate for *in vivo* application will be required to progress further. Higher frame rates can be achieved by the development of electronically scanned phased arrays but they pose technical challenges in terms of fabrication. The use of arrays will improve the depth of field of imaging which is currently limited by using a fixed focus single element transducer.

Quantitative parameters obtained by micro-ultrasound transducers need specialised algorithms and prior knowledge to use these algorithms is required. If the present available system can achieve an ease of use and a level of functionality similar to clinical ultrasound scanners the routine use of µUS in a clinical setting will be greatly enhanced. µUS can also potentially be used for measuring changes in tissue from patients suffering from other diseases such as: inflammatory bowel disease, coeliac disease, etc.

7.6 Conclusion

The results from ultrasound imaging and quantitative ultrasound tissue characterisation proved the hypothesis that: the intestinal tissue morphology of WT and $Apc^{Min/+}$ murine small intestine diverges with increasing age.

High resolution images produced by the AFM TH-19 µUS transducer allowed identification of structures within the murine intestine. The 2D and 3D ultrasound images showed that µUS detect polyps < 500 µm in the scan plane, which is currently not possible using conventional endoscopes and CT. The ultrasound images showed excellent correlation with high resolution optical images. µUS was further used to image human polyps and the images showed a layered organisation similar to the appearance of optical images. From an imaging point of view it is therefore possible to suggest that 2D and 3D ultrasound imaging is a potential tool for early detection and longitudinal growth analysis of polyps in colon cancer. Different layers of the murine intestine were distinguishable showing that the image quality of the B-scans is acceptable. The p-values calculated for BSC showed that the results for male mice were significant when compared to the female mice. The p-values computed for acoustic impedance showed that the results are significant in both male and female mice.

7.7 References

Baddour, R. E., Sherar, M. D., Hunt, J. W., Czarnota, G. J., & Kolios, M. C. (2005) "High-frequency ultrasound scattering from microspheres and single cells." *The Journal of the Acoustical Society of America*, *117*(2), 934.

Bamber, J., Hill, C., King, J., & Dunn, F. (1979) "Ultrasonic propagation through fixed and unfixed tissues." *Ultrasound in Medicine & Biology*, *5*(1977), 159–165.

Cobbold, R. S. C. (2007). *Foundations of Biomedical Ultrasound*. *Oxford University Press* (pp. 45–51). Oxford University Press, Inc.

Fatehullah, A., Sharma, S., Newton, I. P., Nelson, S. A., Mcmahon, R. K., Mcilvenny, N.,Näthke, I. S. (2014) "Microultrasound detects microscopic variations in precancerous intestinal tissue". *Nature Medicine (Manuscript under Consideration)*.

Brand, S., Weiss, E. C., Lemor, R. M., & Kolios, M. C. (2008) "High frequency ultrasound tissue characterization and acoustic microscopy of intracellular changes." *Ultrasound in Medicine & Biology*, *34*(9), 1396–407.

Moran, C. M., Bush, N. L., & Bamber, J. C. (1995) "Ultrasonic propagation properties of excised human skin." *Ultrasound in medicine & biology*, *21*(9), 1177-1190.

Nicholas, D., Hill, C. R., & Nassiri, D. K. (1982) "Evaluation of backscattering coefficients for excised human tissues: Principles and techniques." *Ultrasound in Medicine & Biology*, *8*(1), 7–15.

Oelze, M. L., Zachary, J. F., & O'Brien, W. D. (2002) "Parametric imaging of rat mammary tumors in vivo for the purposes of tissue characterization." *Journal of ultrasound in medicine*, *21*(11), 1201-1210.

Summers, R. M. (2010) "Polyp size measurement at CT colonography: what do we know and what do we need to know?" *Radiology*, *255*(3), 707–20.

Chapter 8: Conclusions and Future Work

"Do you have the patience to wait until your mud settles and the water is clear?"

Lao Tzu

8.1 Overview

The overall contribution of this thesis has been the implementation of 'mass-spring' matching layers for high resolution µUS transducers using vacuum deposition and the development of µUS scanning methods for detection of colon cancer in its early stages using mouse models.

The research reported in this thesis was driven by two reasons. First, novel matching layers were designed for high frequency µUS transducers to overcome the difficulty posed by conventional λ/4 matching layers. Secondly, the present imaging modalities to detect micro polyps of sizes 500 µm or less is currently not possible. The original aims stated in Chapter 1 of this thesis were answered. µUS qualitative and quantitative techniques and the results were compared with high resolution optical imaging to detect early stages of CRC. All of the studies were performed on murine small intestine *ex vivo*. The specific contributions of this thesis and suggestions for future work are explained in the following Sections.

8.2 Discussion

Conventional matching layers comprise of one or more quarter wave thick layers of materials with acoustic impedance intermediate between those of the piezoelectric substrate and wafer. The layers are typically only of the order of 10 µm in thickness and therefore require precise thickness control and bonding techniques to avoid degradation of the acoustic matching, the bandwidth and the uniformity of element response. In addition, to obtain good impedance matching, typically at least one layer consists of loaded epoxy. The attenuation of such loaded epoxies at high frequencies is large due to scattering losses (Cannata & Shung 2003). The necessary material processing techniques are also relatively slow and are difficult to scale up to large batch production with high yield because of the difficulty in maintaining thickness uniformity over large sample during lapping/grinding and adhesion.

The vacuum deposition techniques researched and developed in this thesis, have many benefits over the conventional quarter wavelength resonant cavity approach. It maintains an equal or better acoustic matching performance. In fact there is no noticeable difference when comparing KLM simulations of quarter wavelength matching and the mass spring matching network resulting from the increased thickness. Aside from the slight improvement in the performance, the main advantages of 'mass-spring' matching layers are a result of the ability to vacuum deposit the layers at high frequencies. This allows for large volume production, low attenuation, versatile material selection, excellent uniformity and straight forward application to curved surfaces without the need for any adhesion layers.

One of the limitations noticed was that, over a period of time the thin parylene matching layer eroded from the surface of the transducer. The reasons for this are yet to be ascertained and will be looked into in the future.

Quantitative µUS measurements in WT and precancerous $Apc^{Min/+}$ mice tissue that was correlated with high resolution 3D optical data from crypts in small and large murine intestine and corresponding human FAP patient tissue. Heterozygosity in Apc is predicted to produce subtle effects on cells including decreased cell migration and cytoskeletal changes which in turn changes the crypt structure. These changes were observed by quantitative µUS and high resolution 3D optical, whole tissue imaging.

The primary difference in the tissue architecture of WT and Apc heterozygous mice tissue measured using optical techniques was that, the packing of crypts in Apc heterozygous tissue was less regular. The distribution of the inter-crypt distance was skewed in human FAP tissue. These differences were attributed to increased crypt curvature. It was noticed that the curved crypts occupy larger cross sectional area in the plane of the tissue when examined in x-y as shown in Figure 8.1. An important factor that could contribute to crypt shape is the compliance of cells in crypts and the surrounding tissue. Changes in the mechanical properties of tumour cells have been detected in other epithelial cancers (Plodinec et al., 2012).

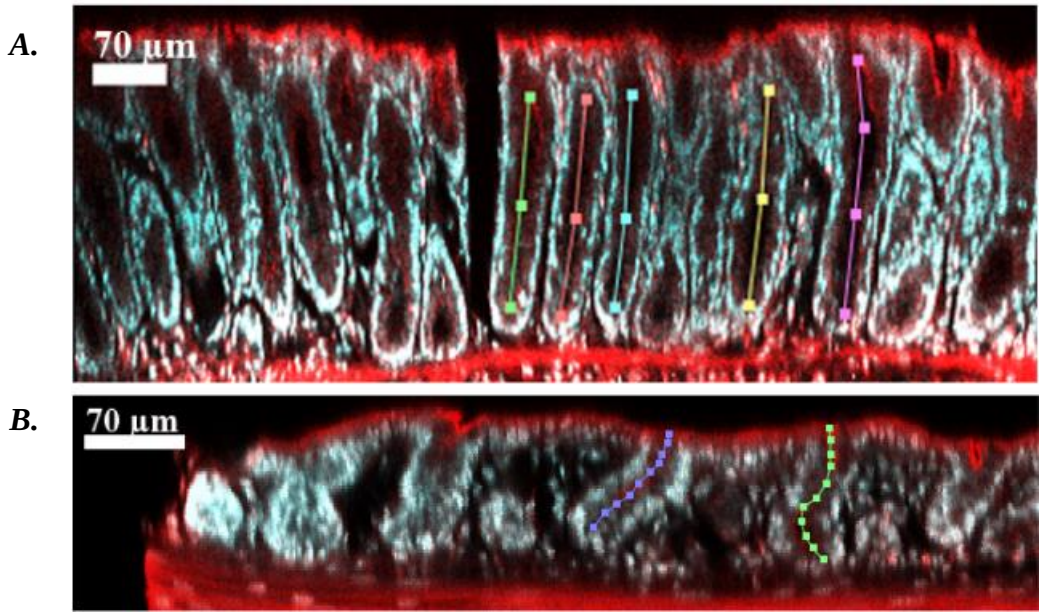

Figure 8.1: Tissue from human small intestine. A. Normal human small intestine. B. FAP tissue. Straight crypts are seen in normal tissue and the crypts are curved in FAP tissue as indicated by coloured lines. The curvature index was calculated as the ratio between the length and depth of the crypts. (Picture taken by Dr. Paul Appleton) (Fatehullah et al., 2014).

If the cells are stiffer, they may fail to accommodate the required conformations causing aberrant crypt shapes. The decline in the regularity of the tissue structure suggests the effect of multiple cellular defects caused by reduced availability of Apc protein. All of the optical measurements were performed in collaboration with Wellcome Trust, College of Life Sciences (CLS), University of Dundee.

Ultrasound parameters were combined with confocal imaging measurements, taking into account that the optical measurements provide different information about the tissue architecture. It was noticed that the µUS measurements complement the optical measurements giving an insight into changes in tissue morphology that accompany premalignant initiation. Adding quantitative imaging modalities to histological examination has enormous potential to improve the ability to detect the relatively subtle tissue abnormalities that were discovered *ex vivo*. Ultrasound has been successfully used to detect tissue abnormalities in clinical settings, usually at frequencies that permit deep tissue penetration but lacks resolution to measure detailed changes in the tissue structure.

Using higher frequencies provides increased resolution and allows tissue characterisation at the level of crypts (diameter > 50 µm) making it suitable for

identifying precancerous changes in patients. Importantly µUS could detect polyps of diameter 500 µm, which is not possible with current imaging modalities. Using µUS, significant changes in values of BSC and *Z* in histologically normal Apc heterozygous tissue were measured. BSC reports on the distribution, concentration and size of scattering objects whereas *Z* suggests increased density of tissue or increased mechanical stiffness.

Increased BSC is caused by an increase in concentration of scatterers and also relates to the spatial distribution of scatterers. Specifically BSC measured the scattering strength of a distribution of scattering objects when insonated with a plane wave. In isolated cells the most effective scatterers are nuclei and scattering is caused by the differences in density and compressibility compared with other cellular structures (Kolios & Czarnota, 2008).

For the frequency of µUS used in this study, objects that scatter effectively are in the range of 5 - 90 µm. This range corresponds to cellular and tissue structure including nuclei, cells and crypts enabling the detection of more irregularly packed crypts, cells and nuclei in precancerous tissue. The reporter of altered precancerous tissue detected by optical imaging was an increased variability in almost all physical properties of crypts examined. The increased and more irregular packing of nuclei common to hyperplastic tissue is likely to contribute to the increased BSC, together with irregular packing and shape of crypts. The steps involved in measuring quantitative parameters and imaging the murine intestine have been explained in this thesis through the chapters.

At present the µUS device is limited to *ex vivo* studies. This is a serious limitation as the ultimate aim of tissue characterisation methods is to evaluate tissues in clinical setting. Further designs of the ultrasound probe to make the device accessible for *in vivo* studies would be useful.

The solutions to challenges encountered in measuring these parameters were not fully answered during the duration of this project but have been recommended as future work. Nevertheless, a good starting point has been established for methods to quantify acoustic properties of tissue to detect early stages of CRC.

8.3 Conclusion

The potential of novel ‘mass-spring’ matching layers developed during this research have contributed to the ease with which broad bandwidth, high resolution µUS transducers can be made and thus to improve their availability by using carefully controlled vacuum deposition alone. Novel ‘mass-spring’ matching layers was implemented by adapting the scheme for high frequency transducers using vacuum deposition processes (J.A.Brown & R.Adamson, 2014). The matching layers developed have the potential to replace conventional λ/4 matching layers. This would improve the speed with which high resolution µUS transducers can be fabricated.

The hypothesis that, the intestinal tissue morphology of WT (wild type) and $Apc^{Min/+}$ diverges with progressing age of mice was tested and proved. The divergence was successfully proved using quantitative and qualitative ultrasound methods. High resolution images produced by the AFM TH-19 µUS transducer allowed identification of structures within the murine intestine. The 2D and 3D ultrasound images showed that µUS detect polyps < 500 µm in the scan plane, which is currently not possible using conventional endoscopes and CT. The ultrasound images showed excellent correlation with high resolution optical images. µUS was further used to image human polyps and the images showed a layered organisation similar to the appearance of optical images. Measuring the acoustic parameters in the murine small intestine has provided a wealth of information and considerable amount of knowledge has been gained about CRC leading to recommendations for further work and opening up opportunities for future research for early detection of cancer.

8.4 Future Work

The work presented here represents only an initial attempt at characterising murine intestinal tissue for early detection of CRC with numerous avenues to explore.

The data collected in this work could be analysed further to extract additional parameters such as the mean scatterer size in the intestinal tissue. The scatterer size could be determined from the frequency dependence of BSC. The previous studies have shown the potential in characterising breast tissues (D’Astous & Foster, 1986). The determination of mean scatterer size could further improve our understanding of ultrasound interaction in tissue. This will improve the prediction of diseased tissue from normal (Kanzler & Oelze, 2008).

Ultrasound data collected from various intestinal lesions could be used to create a database of ultrasonic properties. The specificity and the sensitivity of the parameters to identify and differentiate could then be tested using independent tissue samples. Ultrasound can also be used for determining the tumour margins in terminal mice to determine if biopsies are needed.

Fully developing the correlation between the quantitative parameters provided by µUS and histological detail will be required to validate µUS as a useful complement to existing modalities for detecting early lesions in patients. For instance, comparing µUS biopsies from non-FAP patients reported as normal with those with dysplastic change is required to establish how well µUS data correlates with histological evaluation.

Measurements in tissue from patients suffering from other conditions that pre-dispose them to cancer may show how tissue properties identified by µUS relates to other disease markers. Furthermore, the development of µUS transducers that are sufficiently small to permit incorporation into devices that can be swallowed will permit investigating diseases even of the small intestine, which is currently difficult to reach routinely with endoscopy.

In the future for array design, the technique of ‘mass-spring’ matching layers has the advantage of the first layer consisting of parylene which is an insulating polymer and avoids shorting of the active array electrodes in the front face.

8.5 References

Brown, J. A., Sharma, S., Leadbetter, J., Cochran, S., & Adamson, R. (2014) "Mass – Spring Matching Layers for High- Frequency Ultrasound Transducers : A New Technique Using Vacuum Deposition." *IEEE Transactions on Ultrasonics Ferroelectrics and Frequency Control*, *61*(11), 1911–1921.

Cannata, J. M., Ritter, T. a, Chen, W.-H., Silverman, R. H., & Shung, K. K. (2003) "Design of efficient, broadband single-element (20-80 MHz) ultrasonic transducers for medical imaging applications." *IEEE Transactions on Ultrasonics, Ferroelectrics, and Frequency Control*, *50*(11), 1548–57.

D’Astous, F., & Foster, F. (1986) "Frequency dependence of ultrasound attenuation and backscatter in breast tissue." *Ultrasound in Medicine & Biology*, *12*(10), 795–808.

Fatehullah, A., Sharma, S., Newton, I. P., Nelson, S. A., Mcmahon, R. K., Mcilvenny, N., Näthke, I. S. (2014) "Microultrasound detects microscopic variations in precancerous intestinal tissue." *Nature Medicine (Manuscript under Consideration)*.

Kanzler, S. G., & Oelze, M. L. (2008) "Improved scatterer size estimation using backscatter coefficient measurements with coded excitation and pulse compression." *The Journal of the Acoustical Society of America*, *123*(6), 4599–607.

Baddour, R. E., Sherar, M. D., Hunt, J. W., Czarnota, G. J., & Kolios, M. C. (2005) "High-frequency ultrasound scattering from microspheres and single cells." *The Journal of the Acoustical Society of America*, *117*(2), 934.

Plodinec, M., Loparic, M., Monnier, C. A., Obermann, E. C., Zanetti-Dallenbach, R., Oertle, P., Schoenenberger, C.-A. (2012) "The nanomechanical signature of breast cancer." *Nature Nano*, *7*(11), 757–765.

Toda, M., & Thompson, M. (2010) "Novel multi-layer polymer-metal structures for use in ultrasonic transducer impedance matching and backing absorber applications." *IEEE Transactions on Ultrasonics, Ferroelectrics, and Frequency Control*, *57*(12), 2818–27.

Appendix – I

1. Script to Produce B-scan Images

Matlab SCRIPT file: Bscan_srikanta.m%

Bscan, offline programme to analyse data collected by the LabVIEW programme and create 2D Images (B-Scans),

Author: S.Sharma, PhD Student, Medical Ultrasound Group

Institute for Medical Science and Technology, University of Dundee

The programme uses the voltage amplitude data collected by scanning an Ultrasound transducer over a sample of interest, using a fully automated scanning system controlled by LabVIEW. The data collected is saved in a text file format and contains the voltage amplitude and also the basic information such as the scan step size, averaging, sampling frequency and the start time in first line.

```
Savefile=('/Volumes/Srikanta/labView Data'); %Command to save the data in the desired folder%
clear all;
close all;
clc;
workspace;
V=1540; %Velocity of ultrasound in tissue%
DR=-30;
DataC=dlmread('H:\04NOV14\04NOV14\beads\file_3control1.txt');
 [a,b]=size(DataC);
Imagedata=DataC(2:a,1:b);
hil1=abs(hilbert(DataC(2:end,:)));
SF=1e9;
%Sampling Frequency%
ST=1/SF;
%SF=Sampling Time%
SS=DataC(1,3);
%Scanning step sizes%
t1=DataC(1,2);
```

```
%start time,i.e the time recorded on the scope from where the signal of
%interest is being recorded%
Imagedata=abs(hilbert(Imagedata));
%Envelope detection using the Hilbert transform, Hilbert is a built in function in
%Matlab%
Imagedata=20*log10(Imagedata/(max(max(Imagedata))));
%after Hilbert the next step is to find the dynamic range of the
XY=find(Imagedata<DR);
Imagedata(Imagedata<DR)=DR;
 [f,g]=size(Imagedata);
X=1:g;
Y=1:f;
Time=Y*ST; % seconds %
Time1=Q*ST1;
%now we need to calculate the actual time taken to collect n number of
%samples, which is done by multiplying the sampling time with the number of data
samples collected in an A-scan%
Absolutetime=Time+t1;
%Absolute time is the time taken to collect the time plus the X-origin on
%the oscilloscope, this is recorded while recording the data in LabView%
Depth=Absolutetime*V*1000/2;
% mm %
%Distance is calculated using the absolute time, which determines the
%distance of the sample of interest from the face of the transducer%
%%
figure
Z=(Imagedata(Y,X));
imagesc(SS*X,Depth,Z);
colormap(gray)
```

2. Script to Produce Series of B-scan images for 3D Imaging

```
clear all;
nfiles      = input('Number of tissue files available: ');
fileheader  = ('C:\\Users\\user\\Desktop\\Feb-Scans-PhD\\30days\\');
tissueID ='181593';
fileext= '\\file_%d.txt';
for j = 1:nfiles
DataC = dlmread(sprintf(strcat(fileheader,tissueID,fileext),j));
%DataC = dlmread(sprintf('/Users/srikantasharma/Desktop/Sept-
scan/Male/106904(40db)/position-%d.txt',j));
[rsize, colsize] = size(DataC(2:end,:));
[a,b]=size(DataC);
cols = b;
SF=DataC(1,1);
%Sampling Frequency%
ST=1/SF;
%SF=Sampling Time%
SS=DataC(1,3);
%Scanning step sizes%
t1=DataC(1,2);
%start time,i.e the time recorded on the scope from where the signal of
%interest is being recorded%
Imagedata=DataC(2:a,1:b);
hil1=abs(hilbert(DataC(2:end,:)));
Imagedata=abs(hilbert(Imagedata));
%Envelope detection using the Hilbert transform, Hilbert is a built in function in
%Matlab%
Imagedata=20*log10(Imagedata/(max(max(Imagedata))));
DR = -25;
V = 1540;
XY=find(Imagedata<DR);
Imagedata(Imagedata<DR)=DR;
[f,g]=size(Imagedata);
X=1:colsize;
Y=1:rsize;
```

```
Time=Y*ST; % seconds %
%now we need to calculate the actual time taken to collect n number of
%samples, which is done by multiplying the sampling time with the number of data
samples collected in an A-scan%
Absolutetime=Time+t1;
%Absolute time is the time taken to collect the time plus the X-origin on
%the oscilloscope, this is recorded while recording the data in LabView%
Depth=Absolutetime*V*1000/2;
% mm %
%Distance is calculated using the absolute time, which determines the
%distance of the sample of interest from the face of the transducer%

imageTitle=sprintf(strcat('Colour-',tissueID,'-%d'),j);
Z=(Imagedata(Y,X));
h1=figure('name',imageTitle,'numbertitle','off','units','normalized','outerposition',[0 0 1
1]);
imagesc(SS*X,Depth,Z);
Z=(Imagedata(Y,X));
Imagetitle=sprintf(strcat('Gray-',tissueID,'-%d'),j);
h2=figure('name',Imagetitle,'numbertitle','off','units','normalized','outerposition',[0 0 1
1]);
imagesc(SS*X,Depth,Z);
colormap(gray(128));
brighten(0.5);
temp=sprintf(strcat('Colour-',tissueID,'-%d'),j);
print(h1,'-dtiff',temp);
temp2=sprintf(strcat('Gray-',tissueID,'-%d'),j);
print(h2,'-dtiff',temp2);
close all
end
```

3. Script to Compute Attenuation Coefficients

```
%MATLAB SCRIPT FILE: attenuation.m
```

Author: S.Sharma,PhD student, medical ultrasound group institute for medical science and technology, university of Dundee estimation of attenuation

```
Agar=dlmread('C:\Users\srikanta\Desktop\Mouse-1feb\minfix-t0.txt');
Beads = dlmread('C:\Users\srikanta\Desktop\Mouse-1feb\minfix-t0.txt');
Column=[];
Attvector=[];
Atttruncvector=[];
hil3 = abs(hilbert(Agar(4593:5011,1:58)));
hil3=max(max(hil3));
hil4 = abs(hilbert(Beads(4593:5011,125:end)));
l=1;
tic;
for j=2:460
Column=[Column j];
e=(max(max(hil4(2:end,j))));
attenuation= (-20)*log10(e/hil3);
attenuation=attenuation/2*l;
Attvector=[Attvector attenuation];
end
%sortedcol,sortedattntrunc;
        average_attn = mean(Attvector);
        stde_attn = std(Attvector);
        maximum_attn = max(Attvector);
        minimum_attn = min(Attvector);
        med_attn = median(Attvector);
        meanlabel=mean(Attvector);
        imageTitle=sprintf('Attenuation Coefficients');
        figure('name',imageTitle,'numbertitle','off');
        plot ( Column*SS,Attvector,'LineWidth',1.5,'Color',[0.8 0 0]);
        legend(['Mean = ' num2str(meanlabel)]);
         xlabel ('lateral position (mm)'); ylabel('dB / mm')
```

4. Script to Compute Acoustic Impdance

```
MATLAB SCRIPT FILE: Acousticimpedance.m
AUTHOR: S.SHARMA,PHD STUDENT, MEDICAL ULTRASOUND GROUP
INSTITUTE FOR MEDICAL SCIENCE AND TECHNOLOGY, UNIVERSITY OF
DUNDEE  ESTIMATION OF Acosutic Impedance
clc;
DataQ=dlmread('C:\Users\srikanta\Desktop\quartz\4.5mm\file_3.txt');
hil2 = abs(hilbert(DataQ(2:end,:)));
hil2=max(max(hil2));
Column1=[];
znormalvector=[];
PRnvector=[];
z1=1.48; %Acoustic impedance of PFA: (MRayl; Kg/s/m)%
z2=12.48; %Acoustic impedance of Quartz, Prokop et al 2003%
R=(z2-z1)^2./(z2+z1)^2;  %Reflectance%
PR= (max(max(hil2)));%maximum reflected volatage amplitude from Quartz %
PI= R-PR; %PI= incident voltage amplitude %
For
 j=125:589
Column1=[Column1 j];
PRn=(max(hil1(2:end,j))); %PRn= Reflected maximum volatge amplitude from normal
Tissue%
znormal = -z1*(PI+PRn)./(PRn-PI); %znormal= acoustic impedance of Tissue
(MRayl)%
znormalvector=[znormalvector znormal];
PRnvector= [PRnvector PRn];
end
        ws = Column1(1);
        rs = znormalvector(1);
        ws1 = Column1(20);rs1 = znormalvector(1);
        ws2 = Column1(12);rs2 = znormalvector(1);
        meanlabel=mean(znormalvector);
        stdlabel=std(znormalvector);
        maxlabel=max(znormalvector);
        imageTitle=sprintf('Acoustic Impedance');
```

```
figure('name',imageTitle,'numbertitle','off');
plot(znormalvector);
plot (ws,rs,'.w',ws1,rs1,'*w',ws2,rs2,'<w', Column1,znormalvector,'k');
legend(['Mean = ' num2str(meanlabel)], ['Std='  num2str(stdlabel)], ['Maximun='
num2str(maxlabel)]);
ylabel 'Acosutic impedance (MRayl)', xlabel 'Column number';
```

5. Script to Compute BSC

```
%MATLAB SCRIPT FILE: backscatter_coefficeint.m%
%AUTHOR: S.SHARMA, PHD STUDENT, MEDICAL ULTRASOUND GROUP
INSTITUTE FOR
%MEDICAL SCIENCE AND TECHNOLOGY, UNIVERSITY OF DUNDEE%
% ESTIMATION OF BACKSCATTER COEFFICIENT.

ColumnBSC=[];
BSCvector=[];
z_1=t1*1480*1000/2;
z_2= Absolutetime1(2006)*1540*1000/2;
t2=DataW(1,2);
[s,t]=size(DataW);
SF1=DataW(1,1);
%Sampling Frequency%
ST1=1/SF1;
P=1:t;
Q=1:s;
Time1=Q*ST1;
Absolutetime1 = Time1+t2;
TissueID = 97101-1;
average_attn=mean(Attvector);
[b, m]= size(Attvector);
for j=b:m
AT=2*average_attn./8.686;
```

```
ColumnBSC=[ColumnBSC j];
BSC= R./(2*pi*(1-cos(0.59)))*(trapz(t1:(Absolutetime(end)-
t1)/5009:Absolutetime(end),abs(hil1(2:end,j)).^2));
BSC=BSC./trapz(t2:(Absolutetime(end)-
t2)/5010:Absolutetime(end),(abs(hilbert(DataQ(2:end,20)).^2)));
BSC=BSC*(2*AT./(exp(-2*AT*z_1)-(exp(-2*AT*z_2))));
BSCvector= [BSCvector BSC];
end
        meanlabel=mean(BSCvector);
        avg_bsc = mean(BSCvector);
        stde_bsc = std(BSCvector);
        maximum_bsc = max(BSCvector);
        minimum_bsc = min(BSCvector);
        med_bsc = median(BSCvector);

imageTitle=sprintf('BackScatter Coefficients');
figure('name',imageTitle,'numbertitle','off');
semilogy(ColumnBSC*SS,BSCvector,'k');
xlabel('lateral postion');ylabel('Back scatter coefficeint:Sr/mm');
```

6. Script to to Segement B-scan Images

```
workspace;  % Make sure the workspace panel is showing.
format longg;
format compact;
fontSize = 20;
% Read in a standard MATLAB gray scale image.
folder = ('');
baseFileName = 'C:\Users\user\Desktop\Bscans\30-days\128766\tif\Gray-128766-4.tif';
% Get the full filename, with path prepended.
fullFileName = fullfile(folder, baseFileName);
% Check if file exists.
if ~exist(fullFileName, 'file')
    % File doesn't exist -- didn't find it there.  Check the search path for it.
```

```
    fullFileName = baseFileName; % No path this time.
    if ~exist(fullFileName, 'file')
        % Still didn't find it.  Alert user.
        errorMessage = sprintf('Error: %s does not exist in the search path folders.',
fullFileName);
        uiwait(warndlg(errorMessage));
        return;
    end
end
grayImage = imread(fullFileName);
% Display the original RGB image.
subplot(2, 2, 1);
imshow(grayImage, []);
title('Original Grayscale Image', 'FontSize', fontSize);
% Convert it to gray scale and Crop it.
grayImage = rgb2gray(grayImage);
grayImage = imcrop(grayImage, [   157          74        931      726]);
% Get the dimensions of the image.
% numberOfColorBands should be = 1.
[rows, columns, numberOfColorBands] = size(grayImage);
% Display the cropped gray scale image.
subplot(2, 2, 2);
imshow(grayImage, []);
title('Cropped Grayscale Image', 'FontSize', fontSize);
% Enlarge figure to full screen.
set(gcf, 'units','normalized','outerposition',[0 0 1 1]);
% Give a name to the title bar.
set(gcf,'name','Image Analysis','numbertitle','off')
% Let's compute and display the histogram.
[pixelCount grayLevels] = imhist(grayImage);
% Suppress the 0 bin:
pixelCount(1) = 0;
subplot(2, 2, 3);
bar(pixelCount);
```

```
grid on;
title('Histogram of original image', 'FontSize', fontSize);
xlim([0 grayLevels(end)]); % Scale x axis manually.
% Get the binary image
binaryImage = grayImage > 50;
% Display the original gray scale image.
subplot(2, 2, 4);
imshow(binaryImage, []);
title('Binary Image', 'FontSize', fontSize);
% Smooth it out some and clean it up.
binaryImage = imclose(binaryImage, true(5));
binaryImage = imfill(binaryImage, 'holes');
figure;
subplot(2, 2, 1);
imshow(binaryImage, []);
title('Cleaned Binary Image', 'FontSize', fontSize);
% Find and keep just the largest blob.
labeledImage = bwlabel(binaryImage);
measurements = regionprops(labeledImage, 'area');
allAreas = [measurements.Area];
[sortedAreas indexes] = sort(allAreas, 'descend');
% Get justthe largest blob.
largestBlob = ismember(labeledImage, indexes(1));
binaryImage = largestBlob > 0; % Binarize the labeled image.
subplot(2, 2, 2);
imshow(binaryImage, []);
title('Cleaned Binary Image', 'FontSize', fontSize);
% Get the midpoints
topRow = zeros(columns, 1);
bottomRow = zeros(columns, 1);
midpoints = zeros(columns, 1);
for column = 1 : columns
    oneColumn = binaryImage(:, column);
    if sum(oneColumn) > 0
```

```
        topRow(column) = find(binaryImage(:, column), 1, 'first');
        bottomRow(column) = find(binaryImage(:, column), 1, 'last');
        midpoints(column) = (topRow(column) + bottomRow(column)) / 2;
    end
end
hold on;
% Get rid of points that are not in the object.
x = 1:columns;
noObjectIndexes = midpoints == 0;
midpoints(noObjectIndexes) = [];
x(noObjectIndexes) = [];
plot(x, midpoints, 'r-', 'LineWidth', 2);
% Now show over original image
% Display the cropped gray scale image.
subplot(2, 2, 3);
imshow(grayImage, []);
title('Cropped Grayscale Image', 'FontSize', fontSize);
hold on;
plot(x, midpoints, 'r-', 'LineWidth', 2);
% Now make measurements.
area = sum(binaryImage); % Blob area in pixels.
% Calculate the Euclidean distance transform.
edt = bwdist(~binaryImage);
subplot(2, 2, 4);
imshow(edt, []);
title('Euclidean distance transform', 'FontSize', fontSize);
% Get the half-widths by extracting the EDT along the spine.
% Compute the average RF gray level of the original image along the spine also.
numberOfPoints = length(midpoints);
halfWidths = zeros(numberOfPoints, 1);
sumOfGrayLevels = 0;
for k = 1 : numberOfPoints
    row = int32(midpoints(k));
    col = int32(x(k));
```

```
    halfWidths(k) = edt(row, col);
    sumOfGrayLevels = sumOfGrayLevels + double(grayImage(row, col));
end
averageWidth = 2 * mean(halfWidths);
averageGrayLevel = sumOfGrayLevels / numberOfPoints;
message = sprintf('The average width = %.4f\nThe average RF signal along the spine =
%.4f\n', averageWidth, averageGrayLevel)
uiwait(msgbox(message));
```

7. Script for 1D interpolation of B-scan Images

```
workspace;
yy = ceil(midpoints*5011/735);
xx = ceil(1:length(midpoints))*607/602;
YY= interp1(xx,yy,X);
le = length(YY);
data =zeros(size(DataC(2:end,:)));
dat = zeros(size(hil1));
dat1 = zeros(size(Imagedata));
for i=2:le;
data(2:YY(i),i)=DataC(2:YY(i),i);
dat(1:YY(i),i)=hil1(1:YY(i),i);
dat1(1:YY(i),i) =Imagedata(1:YY(i),i);
end
figure
imagesc(Z)
hold on
plot(YY,'LineWidth',3,'color',[.9 0 0])
```

Appendix – II- Manual HRUS

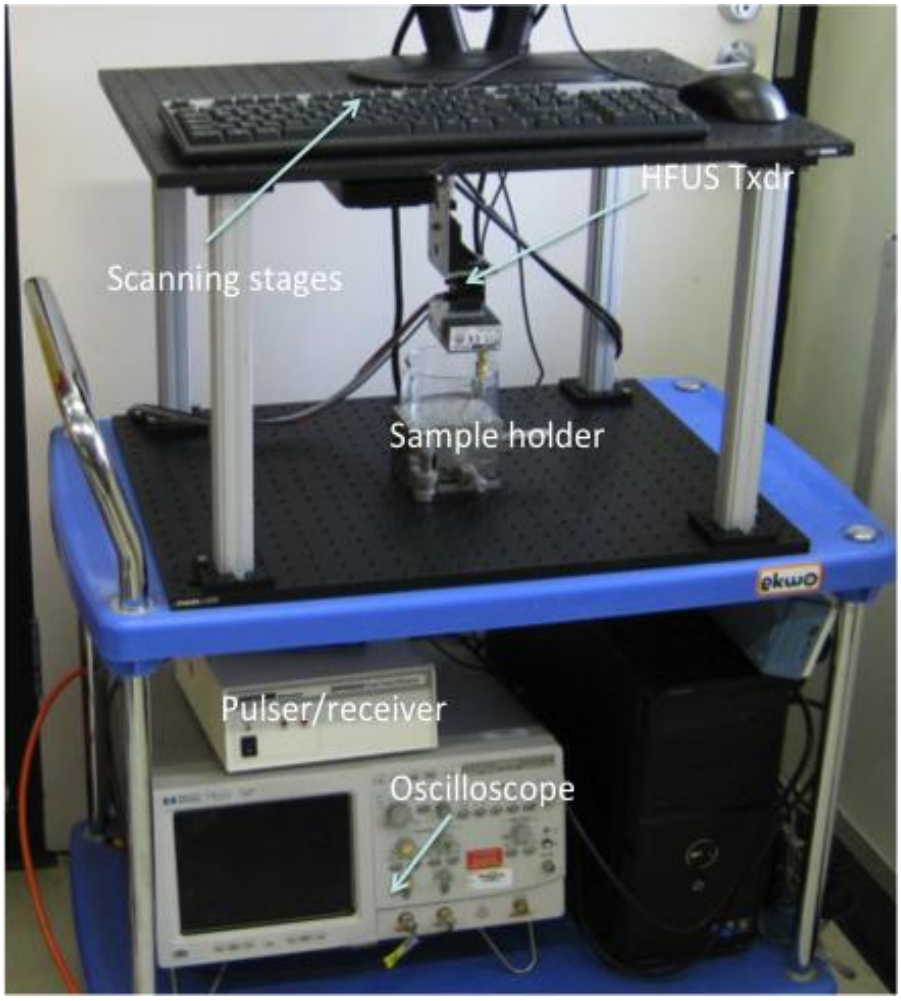

Fig 1: **High Frequency Ultrasound Scanning Bio-Microscope**

Key features:

- Image displayed during scanning for on-line imaging
- Stable scanning set-up to reduce noise and vibration
- System is capable of 2D and 3D image acquisition
- 2 µm scan resolution in X and Y direction

NOTE: System check should be performed before beginning to scan: switch on Oscilloscope, Scanning stages, DPR 500 Pulser/receiver and Computer.

Block Diagram of the Set-up:

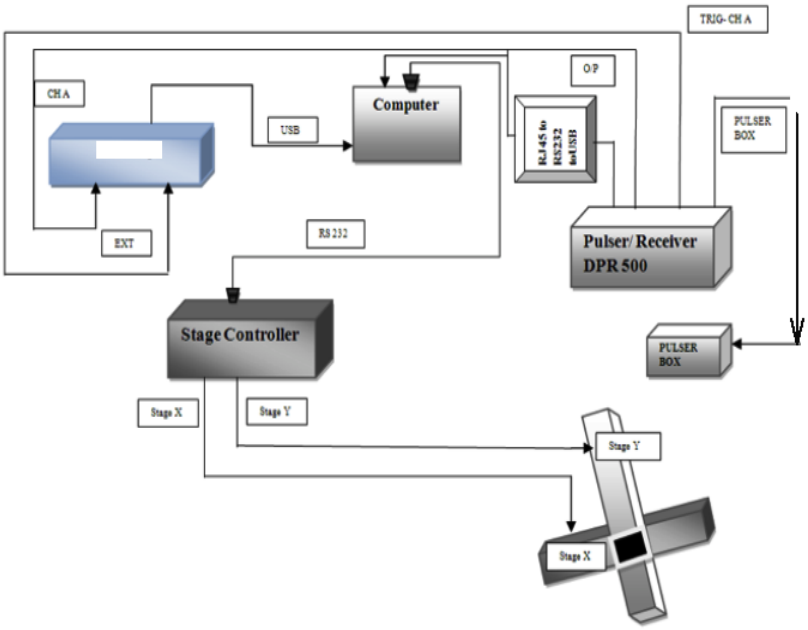

Fig 2: Block diagram of the Scanning system

1. Mechanical Hardware

Item	Description
1. Frame	Optical breadboard assembly, with custom made Aluminum pillars to minimize vibration in scanner by securely fastening the scanning stages to the base of the frame.
2. Scanner	The SHOT-602 is an intelligent two axis driver, the SHOT-602 provides a resolution of 2 μm in X and Y direction. Shot-602 is connected to the personal computer using the RS232C interface; the commands written in LabVIEW can accurately move the stages. A 5-phase stepper motor uses the "half drive" step method to move/drive the scanner stages. The scanner returns to its original position after completing a scan in any given direction.
3.Sample holder	3-Axis micro block flexure stage. The sample can be positioned accurately using the three translational axes x, y and z. The maximum height of the stage is 75 mm from the base. To move the stages the coarse adjustment screw is to be turned. The sample holder provides a flat surface for imaging the sample and is a very stable setup, which can be screwed to the optical breadboard using M3 screws.

2. Electronic Hardware

Item	Description
Pulser/Receiver (DPR/500)	The DPR500 Dual Pulser-Receiver is a modular instrument consisting of two Pulser-Receiver systems in one unit. It is operate under the control of a computer. DPR500 produces a high voltage electrical excitation pulse on the remote pulser's ECHO connector. The DPR-500 is connected to the computer using the USB interface. Settings such as the Damping, receiver gain in db, damping, pulse energy, high pass and low pass filter frequency (Hz), of the Pulser receiver can be controlled using the JSR GUI. The trigger is always set to internal, and the pulse can be observed on channel 2 of the oscilloscope. The pulse from the Transducer is connected to channel 1 of the scope.
HP54810A Oscilloscope	Agilent Oscilloscope is a two channel, 500 MHz bandwidth, 1 GSa/s is connected to the computer through the GPIB interface. The oscilloscope when scanning is controlled by the LabVIEW programme. The key features such, as the horizontal time base, low pass filter, and voltage amplitude are set-up manually before the scan. The sampling frequency and averaging can be selected from a range of values from the drop down menu and is set-up on the LabVIEW front panel to match the frequency of the Transducer and is user dependent.
Monitor	One 15" flat panel monitor, for online viewing of the acoustical and GUI

3. Graphical User Interface (GUI)

Item	Description
LabVIEW ('HFUS scan')	An intuitive LabVIEW GUI controls the functions of the Bio-microscope; the control program is called 'HFUS scan' and is an .exe file. The user interface is friendly and easy to learn. GUI displays A, B and C- scans online images while scanning. The GUI records the RF data and processed data for offline processing in the pre-allocated location. The GUI is capable of performing signal processing such as FFT and Hilbert transforms and displaying data online.
B-scan.m (MATLAB script)	The dynamic range is set through user interface while scan step size, total path, number of samples, and average times are loaded form the selected .txt file. The B-scan image is produced in ~15 seconds after scanning.
Gate Configuration for C- Scan	The gate width, gate delay, thresholding, time of flight information can be optimized to obtain a online C-scan display of the sample in 3D.

4. JSR Pulser/Receiver Front panel settings

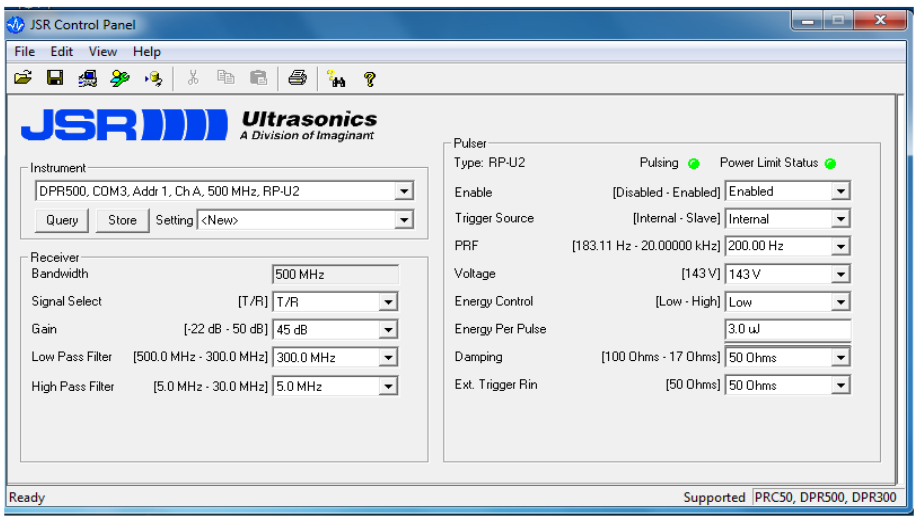

Fig 3: JSR front panel

The JSR pulser receiver is used to trigger the transducer. The settings for 45 MHz, 60 MHz and 150 MHz transducers are stored. The settings can be accessed by clicking: file>recall setting>'desired transducer'.

The stored settings have been optimized and need no further changes unless your application calls for it.

The enable box on the right hand side should be **enabled** and the trigger source should be set to **internal.**

Once this has been done two green LED's will glow on the right hand side of the front panel indicating the pulser is triggering and receiving signal from the transducer.

This can be confirmed by observing the signal on the oscilloscope.

5. LabVIEW front panel description

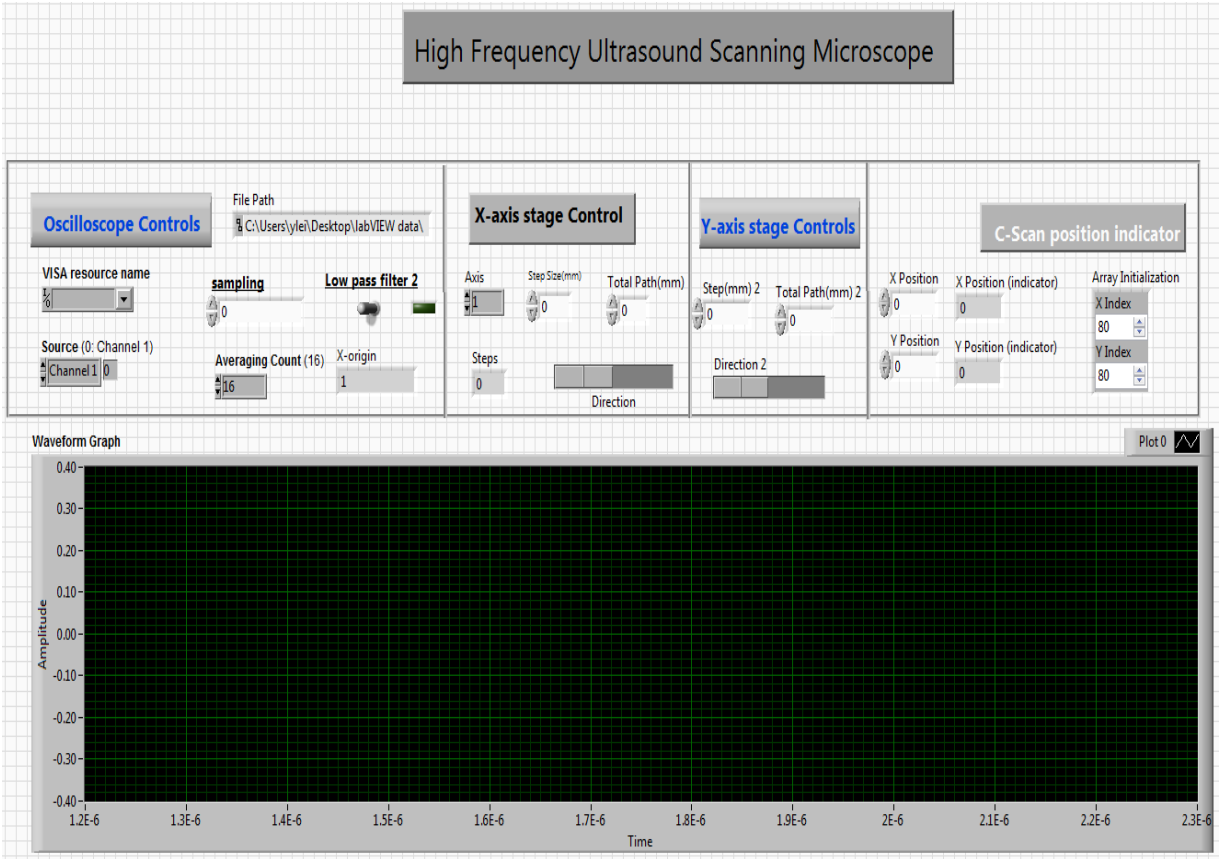

Fig 4: LabVIEW front panel for HFUS scanning

A. Oscilloscope Set-Up:

The user settings listed below provides a guide to set-up the system methodically and avoids system crashes.

- VISA resource name: GPIB instr
- Source: Channel 1
- File path: 'User defined'
- Sampling: 'Choose from drop down menu', the options are: 150 MSa/s, 250 MSa/s, 500 MSa/s, 1GSa/s
- Averaging: 'choose from drop down menu', you can choose your averaging to be 8, 16, 64, 128, 256 and 512 (number of averages depends on your application)
- View pulse echo signal on the Oscilloscope and use the time base dial (Horizontal scale) to zoom in on the signal of interest.

B. User setting for 1D scanning

- Use primary axis control for 1D scanning
- Enter Axis 1 for scanning in X-axis, Axis 2 for Y-axis.
- Enter the step size for the scan, (depends on the beam width of the Txdr)
- Enter Total path length
- Choose direction of scan by sliding the direction control, the positive and negative axis is mentioned on the scanner and in the LabView programme

C. User setting for 2D scanning

- Enter the step sizes in the Secondary axis column
- Enter path length in the Secondary axis column
- Set direction
- Set Gate configuration
- Set up threshold (Voltage)
- Setup Time of Flight mode or Voltage amplitude mode
- Setup signal of interest (back wall or front wall)

D. Image acquisition and Processing

- After following steps A to C press run, B-Scan Images are displayed on-line.
- B-scan images displayed online are Hilbert transformed and log scaled.
- C-scan images will be displayed only if 2D scanning mode has been chosen.
- The RF data is stored in the LabVIEW data folder; the data can be viewed after the scanning.
- The data is stored in .txt format and contains all the scanning parameters entered in the front panel and the voltage amplitude data in M x N format.
- For 2D scanning the data can be directly exported from the C-scan graph on to a excel sheet for further processing.